DIEGO ROMERO ABUJETAS

NANOPHOTONICS OF HIGH REFRACTIVE INDEX DIELECTRIC STRUCTURES:

OPTICAL RESONANCES IN METASURFACES AND SEMICONDUCTOR NANOWIRES

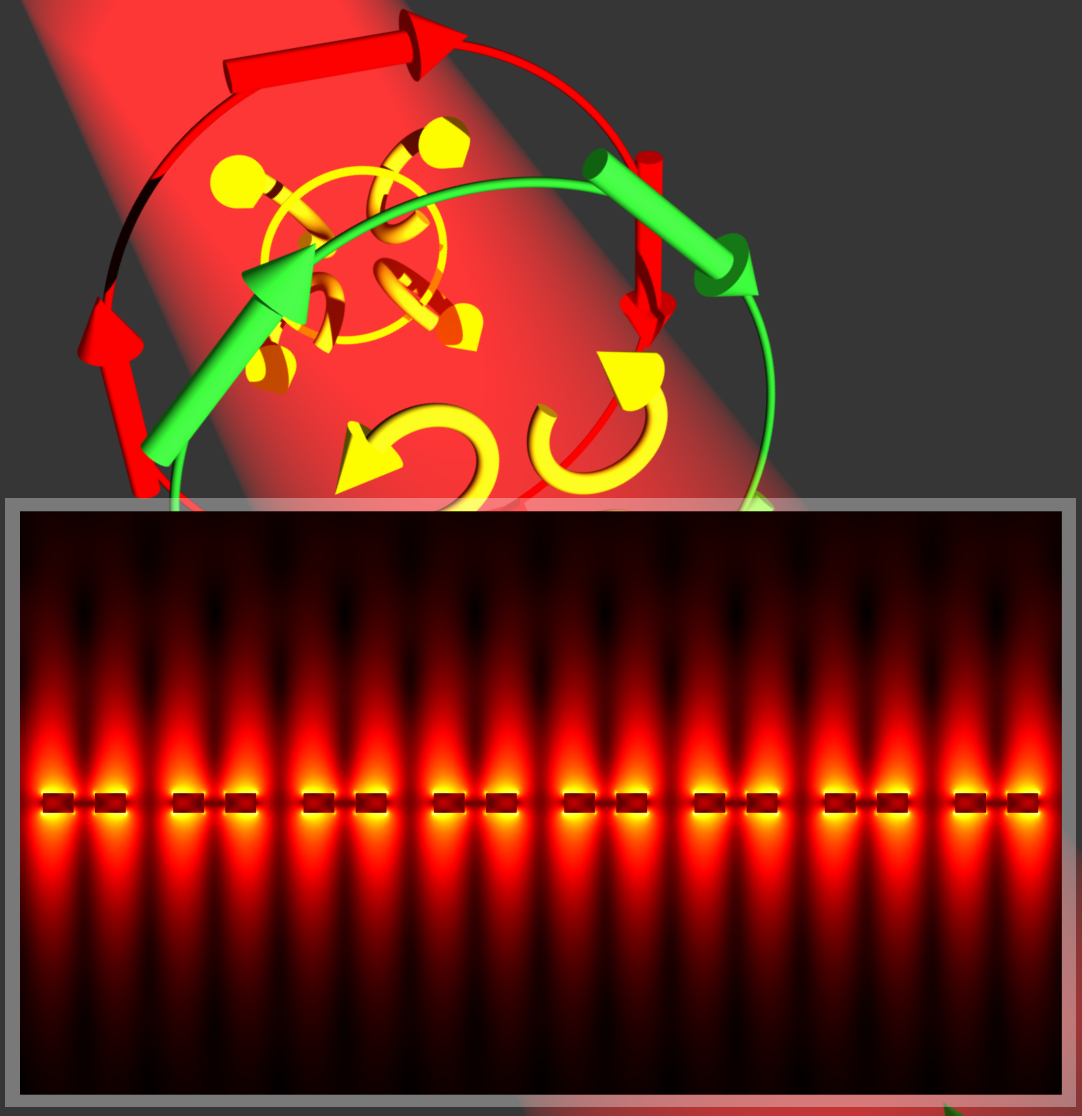

UAM
Universidad Autónoma de Madrid

CSIC
Consejo Superior de Investigaciones Científicas

UNIVERSIDAD AUTÓNOMA DE MADRID

Facultad de Ciencias

Departamento de Física de Materiales

Nanophotonics of high refractive index dielectric structures: optical resonances in metasurfaces and semiconductor nanowires

Nanofotónica de estructuras dieléctricas de alto índice de refracción: resonancias ópticas en metasuperficies y nanohilos semiconductores

Diego Romero Abujetas

Memoria presentada para optar al grado de

Doctor en Ciencias Físicas

supervisada por el Dr. José A. Sánchez Gil, en el

INSTITUTO DE ESTRUCTURA DE LA MATERIA (CSIC)

CSIC

Consejo Superior de Investigaciones Científicas

UAM

Universidad Autónoma de Madrid

He derrochado más vida de las que tengo
y las seguiré malgastando

Cada gesto, cada palabra,
son ecos de un insondable latido

Acknowledgements

No se puede escribir una tesis sin estar agradecido a multitud de personas. porque durante este largo camino, de duro esfuerzo, me he rodeado de gente maravillosa que de un modo u otro, me ha ayudado a seguir hacia delante. Intentaré estampar aquí su marca del mismo modo que ellas me han dejado sus huellas en mi. Me olvidaré, y lo sé, de muchos nombres. No os preocupéis, que estáis ahí.

Primero quería mencionar la situación que me encontré cuando llegué al CSIC en bicicleta, allá en el verano de 2012. Junto con mi supervisor, que terminaría siendo mi director de tesis, había cinco personas trabajando en física: Jose, Luis, Fernando, Nuno (aunque estaba de "infiltrado" de la UAM) y Ramón. Pero poco depués, cuando volví para comenzar la tesis en 2014, ya sólo quedaban Jose y Ramón, y no pasó mucho tiempo hasta que me quedé a solas con el boss. Esta ha sido la herencia de la gestión científica que se ha llevado en este país. Me habría gustado haber estado más tiempo con mis hermanos mayores, y haberlo compartido con alguien más pequeño.

Ahora comenzando con los agradecimientos de la tesis, tengo que empezar con la persona con la que he pasado el mayor tiempo de mi periplo, y posiblemente el que más lo ha sufrido. Jose A. Sánchez Gil, aquel que también firma la portada, mi director de tesis. Nada más terminar la JAE-Intro me dió una oportunidad pero descubrir este mundo y desde entonces ha hecho todo lo posible para que siguera este camino. No fue fácil la primera etapa hasta que conseguimos la FPU, pero fue mucho más sencillo haciéndolo con Jose. Se avanza con delicadeza, sin darte cuenta de lo lejos que has llegado hasta que, con vertigo, echas la vista atrás. Cuántas veces no te volvería a elegir como director. Muchas gracias Jose.

Gran parte del día a día lo he compartido con los compañeros del grupo. Por parte de los seniors, Sagrario, Santiago, Jose Vicente, Luis, Paz, Mercedes y Vincenzo. Respecto a los pocos estudiantes: Moises y Adi. Aunque han pasado bastantes más de estancia: Alba, Xuanyi, Iker, Laura, Giulia, Camilo, Elizabeth, Miguel, Gabriela, Silvia, Teresa, Rafa, Sole, Nacho... espero no saltarme a nadie! No conozco mejor forma para despejar la mente que tomar un café con ellos. Tampoco me puedo olvidar de los estudiantes del Instituto de óptica, de Soto, Juan Diego, Giusseppe, J-Low, Nuño, Guillermo, Rosa y del gran elenco de TeatrIEM con sus triunfos en el escenario. Más allá del instituto pero aun en Madrid me gustaría mencionar a Antonio, Manuel, Gil, Nuno, Manolo, Johannes, FJ, Luis Enrique, Paula, Rosa y Rebeca. Last but not least, no se podía salvar la pachanga de los viernes (LDLV), compañeros de fútbol y birras.

Quisiera hacer una mención especial a Txiki por ser un encanto y a Mole, alias Juan José Sáenz, quien me acogió en el DIPC durante los tiempos difíciles y me ha vuelto a acoger todas

las veces que se lo he pedido. Y volveré, porque en Donosti siempre me he sentido como en casa, gran parte gracias a Cristina y Jorge, que literalmente siempre me han dejado su casa. Ya me puedo buscar un sitio bien bonito para pagarles todo lo que me han dado. El norte sería más triste sin la felicidad incondicional de Sofía y el machaca de Ion. Gracias a Aitzol por esa tabla de surf y encontrarnos mÃąs cerca cada día. Además quisiera recordar de mis días en Donosti a Mireia, Maritito, Gabriel, Maia, Mari Mar, Aiora, Irene, Raquel, Jorge Hita, Nieves, Oihana y Bernhard.

Otra parte importante se lo quiero agradecer a Jaime Gómez Rivas, que me hizo un hueco en DIFFER cuando aun no lo tenía asegurado en Madrid, gracias por confiar en mi. En Eindhoven Niels y Alex me recibieron con los brazos abiertos, Stas me acogió como a un holandes que no sabe llevar un sofá en la bici, llevándome los jueves al Borrel y enseñándome la cultura local; mientras que Miriam me ayudaba a escapar del curro los findes y días festivos.

Por último tengo que hablar de Ramón, siempre disponible para echarte una mano y tomarte una cerveza. Gracias a él, junto con Irene, he estado tres meses en Singapur como si estuviera en Donosti, o como si estuviese en casa. Desde el minuto uno me ayudó para que me sintiera cómodo, introduciéndome en el trabajo, con sus amigos y en su equipo de fútbol de los domingos. Me ha encantado terminar las semanas reponiendo líquidos en el tercer tiempo después de sudar bien la camiseta en el terreno de juego. Además Ramón actuó como mi aval, y aunque ya pagué mi deuda nunca le podré pagar lo que le debo. También se lo quiero agradecer a Arseniy por recibirme tan bien en su grupo, su interés por mi trabajo y su compañía durante las comidas. A Dima, por dar tanto sin esperar nada a cambio. A Franky por pasarme un poco con él. A Vitas y a Seb por ser los mejores, ya fuera bajando un melón o compartiendo una cerveza.

Finalmente muchas gracias a las constantes de mi vida. Gracias a mi familia por estar siempre ahí, aunque yo no lo esté tanto. Sin su apoyo nunca habría sido posible llegar tan lejos. Gracias a mis amigos que nada de lo que diga les puede hacer justicia.

Gracias

Contents

List of Figures

Chapter 1

Introduction

1.1 Short overview of light

Around 400000 years after the Big Bang the matter cooled down enough to give light the "freedom" to propagate. Before that, matter was highly ionized and there were too many charged particles to allow light to freely travel. Since then light has covered a long path, propagating in free space, bending by the force of gravity, diffracting by apertures, scattering by objects, being absorbed and emitted, creating and annihilating particles. Nonetheless, 13.7 billion years later the first vestige of light is still observable, retaining the secrets of the early universe.

The first efforts to unravel the nature of light can be tackled back to the 5th century BC in the Hindu schools of Samkhya and Vaisheshika, followed by the Chinese philosopher Mozi and the philosophical Greek schools. Samkhya school considered light as one of the five fundamental elements which set up the universe, together with fire, air, water and earth. Opposite, Vaisheshika school and Empedocles postulated that there are only four elements, while light is consequence of fire. Beyond philosophical ideas about the building blocks of nature, the pillars of optics can be attributed to Socrates, Plato and Aristotle that established the foundations of disciplines as astronomy, physics, biology and mathematics. Nonetheless, the contributions of Mozi to optics should be noted as the first written record of the camera obscura. Indeed, some authors consider that Aristotle was a follower of his ideas. Finally, all the previous ideas were summarized by Euclid in a formal scientific text called "Optica", where the fundamental knowledge of optic were settled and the laws of reflection, diffusion and vision were studied mathematically.

Art and Science developed a flourishing evolution that was suddenly cut down at the Middle Ages. During this long period, small advances were made in all scientific areas and Optics/Physics was not an exception. The main contribution was done by the Persian scholar Ibn al-Haytham in the 10th and 11st centuries, considered the first theoretical physicist. Also, his rigorous use of theory, the application of mathematical methods and his experimental designs served as the base for modern science. In relation with light, he wrote the "Book of Optics", where he proposed experiments and observation through the use of lenses and mirrors to explain optical phenomenons like reflection and refraction.

With the advent of the modern period science began to grow again, starting a new era that has not stopped until now. In the early 17th century Johannes Kepler deepened into Ibn al-Haytham's works, explaining the working principles of lenses and setting down the principles of geometrical optics. Willebrord Snellium and René Descartes derived independently the law of refraction, and Descartes theorized that light behaves as a mechanical wave, implying that light was a particle. Also, Pierre Gassendi followed these ideas and proposed a particle theory of light. Although there are evidences that Leonardo da Vinci noted it before, Francesco Grimaldi did the first accurate observation of the diffraction of light and coined the word "diffraction". These observations manifested the wave nature of light, starting at the middle of the 17th century the struggle between waves and particles.

On the side of particles was Sir Isaac Newton, that expanded Descartes' theory and develop the corpuscular theory of light. He described light as a stream of particles moving in straight lines at high speed, and demonstrate that light is a mixture of various colors through the famous prism experiment. On the other side, Robert Hook and Christiaan Huygens integrated the wave team. They considered light as a high-speed wave that propagates in aether, a medium that permeates the whole universe, and through the wavefront concept they explained light reflection and refraction phenomenons. Also, Leonhard Euler followed Huygens' ideas and reinforced the wave theory of light, although Newton's concept still prevailed.

In the 18th century the flourish of experiments and theories about electricity and magnetism took place. The most notable scientists in this field were Charles-Augustin de Coulomb, Hans Christian Ørsted, Carl Friedrich Gauss, Jean-Baptiste Biot, Félix Savart, André-Marie Ampère, and Michael Faraday. Their experimental observation and mathematical equations culminated with the formulation of the Maxwell's equations, by James Clerk Maxwell in the 19th century. Originally there were 20 equations, but Oliver Heaviside compacted and rewrote them in the famous four equations that we study nowadays, with the aid of George Francis FitzGerald, Oliver Lodge, Heinrich Hertz and Nikola Tesla who clarified and confirmed the meaning of Maxwell's equations.

These equations predict the generation (by charges and currents) and propagation of polarized waves composed of rapid oscillations of electric and magnetic fields. Surprisingly, the speed of these waves coincided with the experimental values of the speed of light, and another properties of light, like the Snell's law, are derived from Maxwell's equations. In this regard, Albert Abraham Michelson and Edward Williams Morley can be highlighted for their precise measurement of the speed of light, task stated centuries ago by Galileo Galilei. It was believed that light traveled in aether and the relative motion of earth with this medium yielded different speeds of light if light propagated in the earth rotation or antirotation direction, as sound waves. However, Michelson and Morley showed that the speed of light was always the same. In addition, at the beginning of 19th century Thomas Young and Augustin-Jean Fresnel conducted the double slit-experiment that further showed that light behave like a wave. These evidences confirmed the wave behavior of light, concluding, apparently, the battle over the interpretation of light with the defeat of Newton's theory.

However, in 1899 Max Plank solved the blackbody radiation problem following the suggestion by Ludwig Boltzmann that the energy exchange between matter and light is done by discrete

quantities of energy, called quanta. Although Plank solved the problem, he believed that this assumption was mindless and also some authors tried to abate the idea, but later Albert Einstein showed the quantization of light through the explanation of the photo-electric effect. Thus, light is made of particles. Gilbert Newton Lewis coined the term "photon" for this quanta, that derives from the Greek word light, $\phi\widetilde{\omega}\zeta$. This led into some fundamental questions because light behaves at the same time as particle and wave. Nonetheless, the development of Quantum Mechanics in the 20th century embraced this dual interpretation, where particularly Louis de Broglie suggested that every particle is transported by a wave. Also, Einstein developed the Special relativity, a theory that relies on the basis that the speed of light is invariant, and it was shown that Maxwell's equations too implied this fact.

After finishing the wave/particle struggle, where nobody was defeated, the theory of light was developed yielding the Quantum Electrodynamics by In-Itiro Tomonaga, Julian Schwinger and Richard Phillips Feynman. However, it is fascinating to note that the technologies used in our daily life are still based on the classic theory of light given by Maxwell's equations, helped sometime with a quantum description of matter. Radio frequencies are used to broadcast radio and television, and to image through the magnetic resonance. Microwaves for cooking and sending signals by the radar and by telephone. New advances at Terahertz sources and detection allow us to benefit from this previously unused frequency band for detecting defects, material characterization and new ways of bioimaging. Lasers and leds operate principally at Infrared and Visible frequencies, being indeed very versatile applications. At this point, I would like to emphasize the discovery of Laser (and Maser), which was a milestone on the development of optics, opening new fields of research. At that frequencies, bioimaging techniques and telecommunication based on fiber optics that connect the entire world can be highlighted. The ultraviolet is used for growth techniques and to avoid counterfeit. With X rays radiation we study the crystallographic structure of matter and the condition of our bones. Even Gamma rays are used for medical imaging, as PET and SPECT techniques.

The perpetual challenge of Photonics from the technological point of view is to improve the efficiency and decrease the size of actual devices. In addition, new technologies are coming from the optoelectronic field, in which the electronic systems must be coupled to and/or replaced by pure photonics devices. In this regard, Nanophotonics plays a relevant role and new fundamental studies must be done to understand the properties of light and its interaction with matter at the nanoscale. The wavelength of visible light is of the order of hundredths of nanometers, thus optical resonances will be relevant at that scale. Moreover, at this size quantum effects start to arise, and it is necessary to determine when the classical description of light suffices to describe the underlining physics or fails in the attempt. In addition, although the study of light interaction with small structures dates back to the 19th century (or even earlier!), the advances in the fabrication techniques allow us to grow a great variety of nanostructures. Thus, we are in an exceptional age to develop and test new theories, playing around with their size, shape, arrangement and composition that determine their properties. Playing, like a good physicist.

1.2 Maxwell's equations

In this section we will present Maxwell's equations and the basic concepts to understand and solve electromagnetic problems in continuous media. For a deeper knowledge on classical electromagnetic theory the reader can visit the books that I have used along the thesis.[1–7]

The microscopic Maxwell's equations relate the electric and magnetic fields to the total charge and current. The distribution of charge and current can be complicated at the atomic scale and it is common to use an average version of the equations, the macroscopic Maxwell's equations:

$$\nabla \cdot \mathbf{D}(\mathbf{t}) = \rho, \tag{1.1a}$$

$$\nabla \times \mathbf{E}(\mathbf{t}) = -\frac{\partial \mathbf{B}(\mathbf{t})}{\partial t}, \tag{1.1b}$$

$$\nabla \cdot \mathbf{B}(\mathbf{t}) = 0, \tag{1.1c}$$

$$\nabla \times \mathbf{H}(\mathbf{t}) = \mathbf{J}(\mathbf{t}) + \frac{\partial \mathbf{D}(\mathbf{t})}{\partial t}, \tag{1.1d}$$

where the spatial dependence will be in general assumed through the text. Here, $\mathbf{E}$ and $\mathbf{H}$ denote the electric and magnetic fields, $\mathbf{D}$ and $\mathbf{B}$ the electric displacement and magnetic induction, and ρ and $\mathbf{J}$ the charge and current densities, respectively. With charge and current densities we refer to the free sources, while the effect of induced charge and current are included in $\mathbf{D}$ and $\mathbf{H}$. These macroscopic quantities are local spatial averages over the exact microscopic fields associated to the discrete nature of matter. The charges and fields (so, the space) are considered a continuous function of the position that can be polarized by the electromagnetic field. The size of atoms are on the order of angstroms, so it is expected that Eqs 1.1 work above the range of tens of nanometer.

The polarization of the medium defines the electric displacement and the magnetic induction

$$\mathbf{D}(\mathbf{t}) = \epsilon_0 \mathbf{E}(\mathbf{t}) + \mathbf{P}(\mathbf{t}), \tag{1.2a}$$

$$\mathbf{B}(\mathbf{t}) = \mu_0 \left[\mathbf{H}(\mathbf{t}) + \mathbf{M}(\mathbf{t})\right], \tag{1.2b}$$

where $\mathbf{P}$ and $\mathbf{M}$ are the polarization and the magnetization, while ϵ_0 and μ_0 are the vacuum permittivity and permeability, respectively. Also, Eqs 1.1 are self-consistent. For example, they imply the conservation of charge

$$\nabla \cdot \mathbf{J} + \frac{\partial \rho}{\partial t} = 0, \tag{1.3}$$

and they are relativistically invariant, where the speed of light is constant, $c_0 = 1/\sqrt{\epsilon_0 \mu_0}$. However, to solve the equation it is necessary to define how matter is polarized and magnetized in the presence of an electromagnetic field. This relation is called constitutive relations and in general can be an intricate relation of both electromagnetic fields neither isotropic, linear nor local.

Non-linear terms become relevant at high intensity electric fields, when the applied field is of the order of the characteristic atomic electric field strength. For an electron in its orbit in a hydrogen atom the electric field is around $\mathbf{E} \approx 5 \times 10^{11}$ V/m. To achieve this field one needs typically a picosecond laser. Although feasible, in principle we will consider the matter as a linear

medium. In addition, when we pass from the microscopic to the macroscopic Maxwell's equations any non-locality in the media is smeared out. Thus, the most general relation of $\mathbf{P}$ and $\mathbf{M}$ for a local and linear media can be written in the integral form

$$\mathbf{P}(\mathbf{t}) = \epsilon_0 \int_0^\infty \bar{\bar{f}}_e(\tau)\mathbf{E}(t-\tau)\mathrm{d}\tau + \int_0^\infty \bar{\bar{f}}_{em}(\tau)\mathbf{H}(t-\tau)\mathrm{d}\tau, \tag{1.4a}$$

$$\mathbf{M}(\mathbf{t}) = \int_0^\infty \bar{\bar{f}}_m(\tau)\mathbf{H}(t-\tau)\mathrm{d}\tau + \int_0^\infty \bar{\bar{f}}_{me}(\tau)\mathbf{E}(t-\tau)\mathrm{d}\tau/\mu_0. \tag{1.4b}$$

The functions $\bar{\bar{f}}_\alpha(\tau)$ are the response functions, that in general are tensors. They describe how the polarizations depend on the value of the field at any previous time (the response must obey causality). For example, in a lossless medium, an electric field applied up to a time t_0 will drive the electrons and will induce a polarization even at long times $t \gg t_0$. Nonetheless, the fundamental radiation of accelerated charges will damp out the polarization.

Any variable can be expanded into a series of components of a single frequency, in which all quantities depend on time though the factor $e^{-\mathrm{i}\omega t}$, being ω the angular frequency of the field. Recall that the magnitude with physical meaning is the real part, $\Re\left[\mathbf{A}(t)e^{-\mathrm{i}\omega t}\right]$. Using this Fourier expansion, Eqs. 1.4 become

$$\mathbf{P}(\omega) = \epsilon_0 \bar{\bar{\chi}}_e(\omega)\mathbf{E}(\omega) + \bar{\bar{\xi}}(\omega)\mathbf{H}(\omega), \tag{1.5a}$$

$$\mathbf{M}(\omega) = \bar{\bar{\chi}}_m(\omega)\mathbf{H}(\omega) + \bar{\bar{\zeta}}(\omega)\mathbf{E}(\omega)/\mu_0, \tag{1.5b}$$

where

$$\bar{\bar{\chi}}_\alpha(\omega) = \int_0^\infty \bar{\bar{f}}_\alpha(\tau)e^{\mathrm{i}\omega t}\mathrm{d}\tau, \tag{1.6a}$$

$$\bar{\bar{\xi}}(\omega) = \int_0^\infty \bar{\bar{f}}_{em}(\tau)e^{\mathrm{i}\omega t}\mathrm{d}\tau, \tag{1.6b}$$

$$\bar{\bar{\zeta}}(\omega) = \int_0^\infty \bar{\bar{f}}_{me}(\tau)e^{\mathrm{i}\omega t}\mathrm{d}\tau. \tag{1.6c}$$

The electric susceptibility, $\bar{\bar{\chi}}_e$, the magnetic permeability, $\bar{\bar{\chi}}_m$, and the magnetoelectric crosspolarization terms, $\bar{\bar{\xi}}$ and $\bar{\bar{\zeta}}$, describe the response of the medium for monochromatic waves. For a reciprocal system, $\bar{\bar{\xi}} = -\bar{\bar{\zeta}}^T$, those materials in which the polarization (magnetization) depend on the magnetic (electric) field are called bianisotropic, although in general we can safely take $\bar{\bar{\xi}} = \bar{\bar{\zeta}} = 0$. For simplicity in the mathematical description we consider that the matter is isotropic, but the only difference is the tensor or scalar nature of the material properties. Under these considerations, using Eqs. 1.5 on Eqs. 1.2 we arrive to the usual expression for $\mathbf{D}$ and $\mathbf{B}$ for common media

$$\mathbf{D}(\omega) = \epsilon_0\epsilon(\omega)\mathbf{E}(\omega), \tag{1.7a}$$

$$\mathbf{B}(\omega) = \mu_0\mu(\omega)\mathbf{H}(\omega). \tag{1.7b}$$

In the expression above we define the dimensionless quantities relative electric permittivity, $\epsilon =$

$1+\chi_e$, and relative magnetic permeability, $\mu = 1+\chi_m$. They are usually called material constants, but they are dispersive, i.e., depend on the frequency. These constants collect the response of matter to electromagnetic fields, that ultimately are related to the motion of the electrons and their electronic, vibrational and rotational transitions. Although the response can be complicated, there are two simple models, the Drude and Lorentz models, that describe fairly well their dispersive character. Along the text, we will consider the matter as non-magnetic, i.e., $\chi_m = 0$.

Upon decomposing the electromagnetic field into its Fourier components and using constitutive relations, Maxwell's equations can be rewritten as

$$\nabla \cdot [\epsilon \mathbf{E}] = \rho/\epsilon_0, \tag{1.8a}$$
$$\nabla \times \mathbf{E} = \mathrm{i}\omega\mu_0\mu\mathbf{H}, \tag{1.8b}$$
$$\nabla \cdot [\mu \mathbf{H}] = 0, \tag{1.8c}$$
$$\nabla \times \mathbf{H} = \mathbf{J} - \mathrm{i}\omega\epsilon_0\epsilon\mathbf{E}. \tag{1.8d}$$

From now on, the dependence on the frequency will be assumed. These equations only depend on $\mathbf{E}$ and $\mathbf{H}$. Rearranging the equations, we arrive at two equations that only depend on one of the electromagnetic fields

$$\nabla \times \left[\mu^{-1}\nabla \times \mathbf{E}\right] - k_0^2\epsilon\mathbf{E} = \mathrm{i}\omega\mu_0\mathbf{J}, \tag{1.9a}$$
$$\nabla \times \left[\epsilon^{-1}\nabla \times \mathbf{H}\right] - k_0^2\mu\mathbf{H} = \nabla \times \left[\epsilon^{-1}\mathbf{J}\right], \tag{1.9b}$$

where $k_0 = \omega/c_0$ is the propagation constant in vacuum. The propagation constant is inversely proportional to the wavelength, $\lambda_0 = 2\pi/k_0$. Generally, the material constants are homogeneous over the media, where discontinuities are located at the boundaries between different homogeneous regions. Thus, if we divide the space in every homogeneous subdomains with material constants ϵ_i and μ_i, Eqs. 1.9 in each media reduce to

$$\nabla \times [\nabla \times \mathbf{E}] - k_i^2\mathbf{E} = \mathrm{i}\omega\mu_0\mu_i\mathbf{J}, \tag{1.10a}$$
$$\nabla \times [\nabla \times \mathbf{H}] - k_i^2\mathbf{H} = \nabla \times \mathbf{J}, \tag{1.10b}$$

with $k_i = \omega/c_i$, the propagation constant in the medium, while $c_i = c_0/\sqrt{\epsilon_i\mu_i}$ is the speed of light in the medium.

Finally, to solve any problem we need to know what happens at the boundary between two media. Using Maxwell's equations it can be shown that the discontinuity of the fields is related to the surface free charge and current density, σ and $\mathbf{K}$ respectively, at the surface. For two media with material constants ϵ_i, μ_i and ϵ_j, μ_j (medium i and j, respectively), the discontinuities of the

electromagnetic fields are

$$\mathbf{n} \times [\mathbf{E}_i - \mathbf{E}_j] = 0, \tag{1.11a}$$

$$\mathbf{n} \times [\mathbf{H}_i - \mathbf{H}_j] = \mathbf{K}, \tag{1.11b}$$

$$\mathbf{n} \cdot [\epsilon_i \mathbf{E}_i - \epsilon_j \mathbf{E}_j] = \sigma/\epsilon_0, \tag{1.11c}$$

$$\mathbf{n} \cdot [\mu_i \mathbf{H}_i - \mu_j \mathbf{H}_j] = 0. \tag{1.11d}$$

Here, $\mathbf{E}_i$ ($\mathbf{E}_j$) and $\mathbf{H}_i$ ($\mathbf{H}_j$) are the fields at the surface in medium i (j), and $\mathbf{n}$ is the normal vector to the surface, pointing from medium j into medium i. Although these discontinuities are an idealization, consequences of the macroscopic description that we use, in general they are an accurate approximation. However, at the nanoscale each nanometer matters! For example, at visible frequencies bad conducting metals can display values for the skin depth in the order of nanometers that must be considered.

With Maxwell's equations, the constitutive relations and the boundary conditions, together with the Sommerfeld radiation condition, we have the key ingredients to solve any electromagnetic problem. Nonetheles, nobody assures you that it is an easy task.

1.3 Point dipole sources and Green function

Every charge and current in the universe creates an electromagnetic field in the space surrounding it. Maxwell's equations are linear, thus from the Principle of Superposition the total electromagnetic field is simply the sum of the fields created by any individual source. Therefore, it is interesting to know how the field is created by a point electric current source. We will focus only on the electric field, while the magnetic field can be calculated from the electric one.

We consider a point current source in a homogeneous, linear and isotropic space. The current can be interpreted as an electric dipole, represented by two charges q of opposite sign oscillating at a frequency ω and separated by an infinitesimal vector $\mathrm{d}\mathbf{u}$. The dipole is located at $\mathbf{r} = \mathbf{r_n}$, with amplitude A and oscillating in an arbitrary direction $\hat{\mathbf{u}}$. Since the source is concentrated at one point, we can safely use the identity $\nabla \times [\nabla \times \mathbf{E}] = -\nabla^2 \mathbf{E}$, i.e., $\nabla \cdot \mathbf{E} = 0$. Thus, Eqs 1.10 reduces to

$$\nabla^2 \mathbf{G}_{\hat{\mathbf{u}}}(\mathbf{r} - \mathbf{r_n}) + k^2 \mathbf{G}_{\hat{\mathbf{u}}}(\mathbf{r} - \mathbf{r_n}) = -A\hat{\mathbf{u}}\delta(\mathbf{r} - \mathbf{r_n}), \tag{1.12}$$

where we have substituted $\mathbf{E}$ by $\mathbf{G}_{\hat{\mathbf{u}}}$, the Green function of the linear differential operator defined by $\mathcal{L} = \nabla^2 + k^2$, the Helmholtz operator. For $\mathcal{L}\mathbf{E} = 0$ we recover the homogeneous Helmholtz equation. The unit vector $\hat{\mathbf{u}}$ can be projected on three axes for any coordinate system, so Eq 1.12 discloses three equations that can be written in closed form as

$$\nabla^2 \overleftrightarrow{\mathbf{G}}(\mathbf{r} - \mathbf{r_n}) + k^2 \overleftrightarrow{\mathbf{G}}(\mathbf{r} - \mathbf{r_n}) = -A \overleftrightarrow{I}\, \delta(\mathbf{r} - \mathbf{r_n}), \tag{1.13}$$

$\overleftrightarrow{I}$ being the unit dyad and $\overleftrightarrow{\mathbf{G}}$ the dyadic Green's function. The only physical solution to this

equation is

$$\overleftrightarrow{\mathbf{G}}\left(\mathbf{r}-\mathbf{r_n}\right)=\left[\overleftrightarrow{I}+\frac{1}{k^2}\nabla\nabla\right]G_0\left(\mathbf{r}-\mathbf{r_n}\right), \tag{1.14}$$

where we set $A=1$, $\nabla\nabla$ is the dyadic product between ∇ operators and G_0 is the scalar Green's function, defined as the solution of the scalar Helmholtz equation

$$\nabla^2 G_0\left(\mathbf{r}-\mathbf{r_n}\right)+k^2 G_0\left(\mathbf{r}-\mathbf{r_n}\right)=-\delta(\mathbf{r}-\mathbf{r_n}). \tag{1.15}$$

The dyadic Green's function is the propagator of the electromagnetic field, rendering the field at $\mathbf{r}$ produced by a single point source at $\mathbf{r_n}$. For example, in Cartesian coordinates the first column vector of $\overleftrightarrow{\mathbf{G}}$ is the electric filed due to a point current source $\mathbf{J}=(\mathrm{i}\omega\mu_0)^{-1}\delta(\mathbf{r}-\mathbf{r_n})\hat{\mathbf{u}}_\mathbf{x}$. From the properties of the Green's function, the field created by an arbitrary current distribution $\mathbf{J}$ located in a volume V_n is

$$\mathbf{E}\left(\mathbf{r}\right)=\mathrm{i}\omega\mu_0\mu\int_{V_n}\overleftrightarrow{\mathbf{G}}\left(\mathbf{r}-\mathbf{r_n}\right)\mathbf{J}\left(\mathbf{r_n}\right)\mathrm{d}V_n,\qquad \mathbf{r}\notin V_n. \tag{1.16}$$

This is a particular solution of the electromagnetic field, and for the total field we need to add any homogeneous solutions $\mathbf{E_0}$ of the Helmholtz equation.

The scalar Green's function in 3D is

$$G_0\left(\mathbf{r}-\mathbf{r_n}\right)=\frac{e^{+\mathrm{i}kr}}{4\pi r},\quad r=|\mathbf{r}-\mathbf{r_n}|. \tag{1.17}$$

This solution denotes a spherical wave that propagates out of the origin, where the plus sign in the exponential is explicitly written to distinguish between an ingoing spherical wave, written with a minus sign. For 2D systems the scalar Green's function is shown in Appendix A and B.

Following the description in the book of Novotny and Hecht,[3] the Green's function has terms in $(kr)^{-1}$, $(kr)^{-2}$ and $(kr)^{-3}$, called far, intermediate and near-field, respectively

$$\overleftrightarrow{\mathbf{G}}=\overleftrightarrow{\mathbf{G}}_{NF}+\overleftrightarrow{\mathbf{G}}_{IF}+\overleftrightarrow{\mathbf{G}}_{FF}. \tag{1.18}$$

For $r\gg\lambda$, only the terms with $(kr)^{-1}$ survive, i.e., the far-field ($\overleftrightarrow{\mathbf{G}}_{FF}$) is the dominant one. However the opposite, that the near-field dominates ($\overleftrightarrow{\mathbf{G}}_{NF}$) for $r\ll\lambda$, is not totally true. For $kr\to 0$ the real part of $\overleftrightarrow{\mathbf{G}}_{NF}$ dominates, but the imaginary part has contributions from all terms. The imaginary part of the Green's function is connected with the electromagnetic local density of states. If only the near-field term is considered, the conservation of the energy is not ensured because the imaginary part of the inverse of the polarizability must be equal to the imaginary part of the Green's function at $r=0$. We will talk later about the polarizability. Therefore, to study the near-field we have two options: (i) take only the real part of $\overleftrightarrow{\mathbf{G}}_{NF}$ and use the quasi-static polarizability (without radiative corrections); (ii) take the real part of $\overleftrightarrow{\mathbf{G}}_{NF}$ and add it the imaginary part of the total Green's function at $r=0$.

Another interesting way to deal with the Green's function is decomposing it into their homogeneous and evanescent parts on the basis of proper half-space field representation.[8] The homo-

geneous part contains the information related to the propagating components and is finite at the origin, $r = 0$. Opposite, the evanescent part carries the exponential decaying waves, vanishes at the far field and diverges at $r = 0$.

From Eq. 1.17 we easily know the field created by a current distribution. However, the current density and the electromagnetic field are connected by the constitutive relations, $\mathbf{J} = (-\mathrm{i}\omega)(\epsilon - 1)\mathbf{E}$, and the problem becomes more complex. The current in a specific location is affected and modified by the adjacent currents, building up a self-consistent problem. Typically, these systems are solved by expressing the problem as a Lippmann-Schwinger equation. A common problem to solve is the scattering of an electromagnetic wave from an arbitrary object. One way to face this problem is the discrete dipole approximation (DDA), in which the media is discretized in small pieces of polarizable material. Also, it is normal to use a multipole analysis to describe their scattering properties.

Charges and currents are located in finite regions, but the field scattered by an arbitrary particle can be decomposed by fields created by point sources. This decomposition is called a multipolar expansion of the field. Although the formalism can be expressed as a function of the current density, it is more frequent to find the problem written as a function of the polarization, $\mathbf{P}$. In the case of monochromatic fields, the current density is related to the polarization through the relation $\mathbf{P} = \mathrm{i}\omega\mathbf{J}$. The multipolar decomposition is normally done in a Cartesian base, expanding the current (polarization) distribution inside the particle; or in a spherical base, projecting the far-field into spherical harmonics.

To expand the polarization in the Cartesian base, we use the naive expression

$$\mathbf{P}(\mathbf{r}) = \int \mathbf{P}(\mathbf{r}')\,\delta(\mathbf{r} - \mathbf{r}')\,\mathrm{d}V', \tag{1.19}$$

and then expand the Dirac delta function in Taylor series. It is recommended to expand it with respect to the electromagnetic center of mass of the particle. We set this point $\mathbf{r_n}$. Then, we can write the polarization as

$$\mathbf{P}(\mathbf{r}) \approx \mathbf{p}\delta(\mathbf{r} - \mathbf{r_n}) - \frac{1}{6}\hat{Q}\nabla\delta(\mathbf{r} - \mathbf{r_n}) + \frac{\mathrm{i}}{\omega}\left[\nabla \times \mathbf{m}\delta(\mathbf{r} - \mathbf{r_n})\right] + \cdots, \tag{1.20}$$

being $\mathbf{p}$, $\mathbf{m}$ and $\hat{\mathbf{Q}}$ the electric dipole, magnetic dipole and electric quadrupole moments, respectively, whose expressions are

$$\mathbf{p} = \int \mathbf{P}(\mathbf{r}')\,\mathrm{d}V', \tag{1.21a}$$

$$\mathbf{m} = \frac{\mathrm{i}\omega}{2}\int \left[(\mathbf{r}' - \mathbf{r_n}) \times \mathbf{P}(\mathbf{r}')\right]\mathrm{d}V', \tag{1.21b}$$

$$\hat{\mathbf{Q}} = 3\int \left[(\mathbf{r}' - \mathbf{r_n})\,\mathbf{P}(\mathbf{r}') + \mathbf{P}(\mathbf{r}')\,(\mathbf{r}' - \mathbf{r_n})\right]\mathrm{d}V'. \tag{1.21c}$$

Here, $(\mathbf{r}' - \mathbf{r_n})\,\mathbf{P}(\mathbf{r}')$ represents the dyadic product between corresponding vectors. We have stopped the expansion at $\hat{\mathbf{Q}}$, but depending on the symmetry and the size of the particle, higher multipoles can be needed to describe its properties.

At large wavelengths compared to the particle size, all (non-magnetic) particles behave as an electric dipole. The field is essentially constant inside the particle and retardation effects can be neglected. The field scattered (outside the own particle), $\mathbf{E_{sca}}$, by a particle located at $\mathbf{r_n}$ can be approximated by the field radiated by a point electric dipole:

$$\mathbf{E_{sca}}\left(\mathbf{r}\right) = k^2 \overleftrightarrow{\mathbf{G}}\left(\mathbf{r}-\mathbf{r_n}\right)\mathbf{p}/\epsilon_0. \tag{1.22}$$

Note that this equation is formally identical to Eq. 1.17 if the current distribution reduces to a point source. As the particle becomes bigger, even for non-magnetic particles, a contribution arises formally equivalent to the emission of a magnetic dipole given by $\mathbf{m}$. Although in nature there are no magnetic charges, we can calculate the field radiated by a point magnetic current $\mathbf{J_m}$ represented by two oscillating magnetic charges of opposite sign. The solution is similar to Eq. 1.17

$$\mathbf{H}\left(\mathbf{r}\right) = \mathrm{i}\omega\epsilon_0\epsilon \int_{V_n} \overleftrightarrow{\mathbf{G}}\left(\mathbf{r}-\mathbf{r_n}\right)\mathbf{J_m}\left(\mathbf{r_n}\right)\mathrm{d}V_n, \qquad \mathbf{r}\notin V_n, \tag{1.23}$$

where the Green's function is the same as that of an electric dipole. For bigger particles, more multipoles are needed to describe the scattering of the particle and the expressions for the far field become more complex.

Since it is a scattering problem, Eq. 1.22 is often written as a function of the incident external field, $\mathbf{E}^{(0)}$,

$$\mathbf{E_{sca}}\left(\mathbf{r}\right) = k^2 \overleftrightarrow{\mathbf{G}}\left(\mathbf{r}-\mathbf{r_n}\right)\overleftrightarrow{\alpha_e}\mathbf{E}^{(0)}\left(\mathbf{r_n}\right), \tag{1.24}$$

where $\overleftrightarrow{\alpha_e}$ is its electric polarizability, that in general can be a tensor. The polarizability tells us how the particle is polarized in the presence of an electromagnetic field, relating the dipole moment to the electric field

$$\mathbf{p^{(s)}} = \epsilon_0 \overleftrightarrow{\alpha_e}\mathbf{E}\left(\mathbf{r_n}\right). \tag{1.25}$$

Note the superscript is added to the dipole moment to distinguish from $\mathbf{p}$. $\mathbf{p^{(s)}}$ is the electric dipole moment in the spherical base, while $\mathbf{p}$ is the expansion in a Cartesian base.

For long wavelengths the value of the field inside the particle is practically constant and $\mathbf{E}\left(\mathbf{r_n}\right)$ is well defined. However, at wavelengths in the order of the particle size (and smaller) the field is no longer constant. Thus, the dipole moment depends on the origin of coordinates $\mathbf{r_n}$, opposite to Eq. 1.21a, for which $\mathbf{p}$ does not depend on $\mathbf{r_n}$. This fact makes a clear distinction between the different approaches that follow from different interpretations. Of course, both ways must yield the same results and must be a bridge between them. For example, $\mathbf{p^{(s)}}$ is in general a function of $\mathbf{p}$ and also of higher multipoles that do depend on the origin of coordinates. For more details about the multipolar expansion see.[9–12]

Similar to the electric dipole, we can define a magnetic polarizability, $\overleftrightarrow{\alpha_m}$, and write the field radiated by a magnetic dipole as

$$\mathbf{H_{sca}}\left(\mathbf{r}\right) = k^2 \overleftrightarrow{\mathbf{G}}\left(\mathbf{r}-\mathbf{r_n}\right)\overleftrightarrow{\alpha_m}\mathbf{H}^{(0)}\left(\mathbf{r_n}\right). \tag{1.26}$$

Equations 1.24,1.26 and the expansion in the spherical (or cylindrical) base will be the pillars of

our coupled dipole theory developed in Chapter 2.

1.4 Scattering and propagation on infinitely long cylinders

Now we will show two electromagnetic problems in 2D systems: (i) the scattering of infinitely long cylinders upon the incidence of plane waves; (ii) the propagation of electromagnetic waves in a waveguide. Both problems are solved using Maxwell's equations, the constitutive relations and the boundary conditions. For this section we will follow refs.[5–7] .

We have seen that the electromagnetic field in a linear, isotropic and homogeneous medium satisfies Eqs. 1.10. In the absence of charges and currents the fields are divergence-free, and Eqs. 1.10 simplify to the wave equation

$$\nabla^2\mathbf{E} + k^2\mathbf{E} = 0, \tag{1.27a}$$

$$\nabla^2\mathbf{H} + k^2\mathbf{H} = 0. \tag{1.27b}$$

Assume that we design a vector function $\mathbf{M}$ from the curl of a given scalar function ψ multiplied by an arbitrary constant vector $\mathbf{v}$:

$$\mathbf{M} = \nabla \times (\mathbf{v}\psi)\,. \tag{1.28}$$

Since $\nabla \cdot (\nabla \times \mathbf{M}) = 0$ for any vector function, our function is automatically divergence-free. Introducing $\mathbf{M}$ into the wave equation, after some algebra we can show

$$\nabla^2\mathbf{M} + k^2\mathbf{M} = \nabla \times \left[\mathbf{v}\left(\nabla^2\psi + k^2\psi\right)\right]. \tag{1.29}$$

Thus, $\mathbf{M}$ has the properties of the electromagnetic field if ψ satisfies the scalar wave equation. Although we have used $\mathbf{M}$ for the magnetization, since we consider the matter as non-magnetic we will take this convention to follow the usual textbooks. From $\mathbf{M}$ we can derive another another vector function in analogy with the electromagnetic field

$$\mathbf{N} = \frac{\nabla \times \mathbf{M}}{k}, \tag{1.30}$$

that also satisfies the wave equation and is divergence-free. Therefore, the problem of finding solutions to the wave equations simplifies by finding solutions to the scalar wave equation, although we must find an appropriate constant vector $\mathbf{v}$. The scalar function ψ is usually called the generating function for the vector harmonics $\mathbf{M}$ and $\mathbf{N}$, while vector $\mathbf{v}$ is sometimes called the guiding or pilot vector.

Before studing the scattering from infinitely long cylinders we will take a look at the vector harmonics in 3D. If we take as constant vector $\mathbf{v} = \hat{\mathbf{u}}_\mathbf{r}$, where $\hat{\mathbf{u}}_\mathbf{r}$ is the radius vector, then $\mathbf{M}$ is a solution to the vector wave equation in spherical polar coordinates. The vector harmonics generated in this way are the so called vector spherical harmonics, $\mathbf{M_{elm}}$, $\mathbf{M_{olm}}$, $\mathbf{N_{elm}}$ and $\mathbf{N_{olm}}$.[5] Any electromagnetic field can be expanded in these functions, being an orthogonal multipolar expansion. For instance, at $m = 1$ we recover the field scattered by a point dipole. Moreover,

the spherical harmonics are another way to write down the Green's function. As an illustrative example, $\mathbf{N_{e11}}$ is related to the following components:

$$G_{xx} = -\frac{\mathrm{i}k}{4\pi}\mathbf{N_{e11}}\cdot\hat{\mathbf{u}}_\mathbf{x}, \quad G_{xy} = -\frac{\mathrm{i}k}{4\pi}\mathbf{N_{e11}}\cdot\hat{\mathbf{u}}_\mathbf{y}, \quad G_{zx} = -\frac{\mathrm{i}k}{4\pi}\mathbf{N_{e11}}\cdot\hat{\mathbf{u}}_\mathbf{z}. \tag{1.31}$$

1.4.1 Scattering from infinitely long cylinders

The scattering from infinitely long cylinders is comparable to the Mie problem (scattering by a sphere). Both problems can be found in details in the classical textbooks.[5,7] Taking into account the symmetry of the system, we consider the scalar wave equation in cylindrical coordinates r, ϕ, z,

$$\frac{1}{r}\frac{\partial}{\partial r}\left(r\frac{\partial\psi}{\partial r}\right) + \frac{1}{r^2}\frac{\partial^2\psi}{\partial\phi^2} + \frac{\partial^2\psi}{\partial z^2} + k^2\psi = 0, \tag{1.32}$$

where the z axis coincides with the axis of the cylinder. Separable solutions that are single-valued functions of ϕ are of the form

$$\psi_m = Z_m(\rho)\, e^{\mathrm{i}m\phi} e^{\mathrm{i}hz}, \quad m = 0, \pm1, \cdots, \tag{1.33}$$

where $\rho = r\sqrt{k^2 - h^2}$, Z_m is a solution to the Bessel equation that matches the boundary condition and h is unrestricted. The appropriate constant vector for this geometry is $\mathbf{v} = \hat{\mathbf{u}}_\mathbf{z}$ and the cylindrical harmonics are generated by

$$\mathbf{M_m} = \nabla\times(\hat{\mathbf{u}}_\mathbf{z}\psi_m), \quad \mathbf{N_m} = \frac{\nabla\times\mathbf{M_m}}{k}. \tag{1.34}$$

$\mathbf{M_m}$ and $\mathbf{M_m}$ are the vector cylindrical harmonics, forming an orthogonal multipolar expansion of the field. Upon inspection of the fields, it is clear that h is the component of the propagation constant along z and ρ/r its projection on the xy plane. At normal incidence for $m = 0$ and 1 we recover the field scattered by a single point dipole out-of- and in-plane, respectively. Since there is translational symmetry along the z-axis, some authors call monopole to the out of plane mode $m = 0$.

Lets us now consider an infinite circular cylinder of radius R, with material properties ϵ_1 and μ_1, embedded in a homogeneous media characterized by ϵ_2 and μ_2. The cylinder is illuminated by a plane wave, $\mathbf{E_i}$, propagating along the direction $\hat{\mathbf{u}}_\mathbf{i} = -\sin\theta\hat{\mathbf{u}}_\mathbf{x} - \cos\theta\hat{\mathbf{u}}_\mathbf{z}$, where θ is the angle between the incident wave and the cylinder axis. The problem can be divided into two different polarizations, electric field parallel or perpendicular to the incident zx plane, but the procedure is the same.

As an example, we consider an incident electric field parallel to the zx plane

$$\mathbf{E_i} = E_0\left(\sin\theta\hat{\mathbf{u}}_\mathbf{z} - \cos\theta\hat{\mathbf{u}}_\mathbf{x}\right) e^{-\mathrm{i}k_2(r\sin\theta\cos\phi + z\cos\theta)}. \tag{1.35}$$

This incidence is usually called transverse magnetic (TM) because the magnetic field has no z component. The first step is to expand the total field in the vector harmonics. Also, we expand the field as the scattered field ($\mathbf{E_s}$,$\mathbf{H_s}$), internal field ($\mathbf{E_{int}}$,$\mathbf{H_{int}}$) and incident field. For $\mathbf{E_{int}}$, in

order for the expansion to be finite at $r = 0$, the appropriate Bessel function for the radial part must be $Z_m = J_m$. Also, to match the dependence on z, from $\mathbf{E_{int}}$ we note that h must be equal to $-k_2 \cos\theta$. Projecting the incident field on the cylindrical harmonics we find that the incident fields can be written as

$$\mathbf{E_i} = \sum_{m=-\infty}^{\infty} E_m \mathbf{N_m^{(1)}}, \tag{1.36}$$

where $E_n = E_0(\mathrm{i})^m / k_2 \sin\theta$ and the superscript $^{(1)}$ means that J_m is taken as the radial dependence.

For the internal and the scattered field an arbitrary expansion is also proposed

$$\mathbf{E_{int}} = \sum_{m=-\infty}^{\infty} E_m \left[f_m \mathbf{N_m^{(1)}} + g_m \mathbf{M_m^{(1)}} \right], \tag{1.37a}$$

$$\mathbf{E_s} = -\sum_{m=-\infty}^{\infty} E_m \left[b_{m\mathrm{I}} \mathbf{N_m^{(3)}} + \mathrm{i} a_{m\mathrm{I}} \mathbf{M_m^{(3)}} \right]. \tag{1.37b}$$

The field is finite at $r = 0$, hence the radial dependence in the inner field must be J_m. The scattered field must be an outgoing wave at large distances from the cylinder, thus $Z_n = H_n^{(1)}$ is the appropriate generation function, indicated by the superscript $^{(3)}$. The dependence on z is also given by the incident field, then h is the same for all fields ($h = -k_2 \cos\theta$). However, ρ is different in- and out-side due to the different value of the wavevector k.

Once all fields are defined, the last step is to apply the boundary condition at the cylinder surface, $r = R$,

$$(\mathbf{E_i} + \mathbf{E_s} - \mathbf{E_{int}}) \times \hat{\mathbf{u}}_\mathbf{r} = (\mathbf{H_i} + \mathbf{H_s} - \mathbf{H_{int}}) \times \hat{\mathbf{u}}_\mathbf{r} = 0, \tag{1.38}$$

that yields a linear system of equations with $4 \times m$ equations and $4 \times m$ unknowns, $f_m, g_m, a_{m\mathrm{I}}$ and $b_{m\mathrm{I}}$. Luckily, from the orthogonality of the vector harmonics the equations can be split into m sets of 4 linear equations, solving for each m independently. The orthogonality can look natural, but, for example, if the scattering problem is solved for elliptical cylinders (in elliptical coordinates), all equations from the boundary condition are entangled.[13,14]

For the other polarization, called transverse electric (TE), the same steps are followed. The only change is the inhomogeneous term (given by the incident field) in the continuity relation equations. In this case, the incident field is

$$\mathbf{E_i} = E_0 \hat{\mathbf{u}}_\mathbf{y} e^{-\mathrm{i}k_2(r\sin\theta\cos\phi + z\cos\theta)} = -\mathrm{i} \sum_{m=-\infty}^{\infty} E_m \mathbf{M_m^{(1)}}. \tag{1.39}$$

Finally, to distinguish between the terms of the other polarization, the scattered field is written with different coefficients:

$$\mathbf{E_s} = \sum_{m=-\infty}^{\infty} E_m \left[b_{m\mathrm{II}} \mathbf{N_m^{(3)}} + \mathrm{i} a_{m\mathrm{II}} \mathbf{M_m^{(3)}} \right]. \tag{1.40}$$

The expressions for the coefficients are given in the books.[5,7] They are related to important magnitudes as the amplitude scattering matrix and the scattering, extinction and absorption cross sections.

It is interesting to note that at normal incidence ($\theta = 90^{\circ}$), $a_{m\mathrm{I}} = b_{m\mathrm{II}} = 0$, and we simply write $a_{m\mathrm{II}}\left(\theta = 90^{\circ}\right) = a_m$ and $b_{m\mathrm{I}}\left(\theta = 90^{\circ}\right) = b_m$. Do not confuse with the coefficients for the scattering from a sphere, in which the same notation is used. To differentiate them in the text we will add the superscript $^{(s)}$ to indicate the scattering terms from a sphere (although this notation will be only used in this section). Moreover, the nature of the coefficients is different. For a sphere, $a_m^{(s)}$ is related only to electric multipoles, while $b_m^{(s)}$ represents magnetic multipoles. The lowest-oder response of the particle is given by $a_1^{(s)}$, governing at low frequencies and associated to the electric polarizability, $\alpha_e = i6\pi/k^3 a_1^{(s)}$. Nonetheless, for high refractive index dielectric spheres the lowest frequency resonance is given by $b_1^{(s)}$, connected to the magnetic polarizability, $\alpha_m = i6\pi/k^3 b_1^{(s)}$. In both cases, the polarizability can be considered as a scalar.

Opposite, for cylindrical particles both coefficients, a_m and b_m, are related to electric and magnetic responses. In addition, the polarizability is a diagonal tensor, with different response in the xy plane and in the z axis. The lowest-order terms $m = 0, 1$ are related to the polarizability of the cylinder.[15] b_0 and a_1 are identified with the electric polarizabilty out and in the xy plane, respectively. The magnetic polarizabilty in the xy plane is given by b_1, while the out of plane response is dictated by a_0.

1.4.2 Propagation along circular cylinders

Let us now study the propagation of guided modes in cylindrical waveguides. We consider again an infinite circular cylinder of radius R, with material properties ϵ_1 and μ_1, embedded in a homogeneous medium characterized by ϵ_2 and μ_2. The idea is similar to that in our scattering problem, but in this case we solve the electromagnetic field that satisfies Maxwell's equations in the absence of an external incident field. The fields are again expanded in vector cylindrical harmonics. However, to follow previous textbooks,[6] instead of expanding the field as in Eqs. 1.37, the fields are written as

$$E_r = \sum \left[\frac{\imath k_z}{k_t} Z_m'\left(k_t r\right) a_m - \frac{\mu\omega m}{k_t^2 r} Z_m\left(k_t r\right) b_m\right] F_m, \tag{1.41a}$$

$$E_\theta = -\sum \left[\frac{m k_z}{k_t^2 r} Z_m\left(k_t r\right) a_m + \frac{\imath\mu\omega}{k_t} Z_m'\left(k_t r\right) b_m\right] F_m, \tag{1.41b}$$

$$E_z = \sum \left[Z_m\left(k_t r\right) a_m\right] F_m, \tag{1.41c}$$

$$H_r = \sum \left[\frac{m k^2}{\mu\omega k_t^2 r} Z_m\left(k_t r\right) a_m + \frac{\imath k_z}{k_t} Z_m'\left(k_t r\right) b_m\right] F_m, \tag{1.41d}$$

$$H_\theta = \sum \left[\frac{\imath k^2}{\mu\omega k_t} Z_m'\left(k_t r\right) a_m - \frac{m k_z}{k_t^2 r} Z_m\left(k_t r\right) b_m\right] F_m, \tag{1.41e}$$

$$H_z = \sum \left[Z_m\left(k_t r\right) b_m\right] F_m. \tag{1.41f}$$

Nonetheless, the expansion is equivalent to a linear combination of $\mathbf{M_m}$ and $\mathbf{N_m}$, as it was done before. In these expressions, k_z and k_t are the longitudinal and transverse components of the wavevector, respectively, and $k = |\mathbf{k}| = \sqrt{k_z^2 + k_t^2}$ is the modulus of the wavevector. k_z is the same for both media, then k_t is different in/out the guide. Since the dielectric waveguide is intended to guide the light, the propagation constant k_z has to be in the range $n_2/n_1 < ck_z/\omega < n_1$. Recall that under these conditions, k_t is imaginary for guided modes outside the waveguide. Upon using functions Z_m, we collapse the electromagnetic fields inside ($Z_m = J_m$) and outside ($Z_m = H_m$) the waveguide into formally identical equations. In this regard, recall that a_m, b_m, ..., obey different expressions inside/outside. The function $F_m = e^{\imath(m\theta + k_z z - \omega t)}$ is the phase of the wave, the subscript m being an integer related to its azimuthal order. Bear in mind that the longitudinal and transverse components of the wavevector depend on m, but we dropped the subscript for simplicity. The fields of the waveguide written in Eqs. 1.41 are expressed as the sum over different guided modes, encoded in the subindex m.

Applying the continuity relations at the boundary $r = R$, Eq. 1.38 constitutes a homogeneous system of $4 \times m$ linear equations, where a_m and b_m are the $4 \times m$ unknowns (remember a_m and b_m are different inside/outside). Similar to the scattering problem, the system can be divide for each m in sets of 4 independently linear equations, although for guided modes, the system of equations is homogeneous. Hence, each system admits a nontrivial solution only in the case in which its determinant is zero, yielding the condition for the propagation factor k_z. Expansion of this determinant leads to the transcendental equation

$$\left[\frac{\mu_1}{u}\frac{J_m'(u)}{J_m(u)} - \frac{\mu_2}{v}\frac{H_m'(v)}{H_m(v)}\right]\left[\frac{\epsilon_1}{u}\frac{J_m'(u)}{J_m(u)} - \frac{\epsilon_2}{v}\frac{H_m'(v)}{H_m(v)}\right] = m^2\frac{(k_z R)^2}{(\omega R/c)^2}\left(\frac{1}{v^2} - \frac{1}{u^2}\right)^2, \tag{1.42}$$

where $u = k_1 R, v = k_2 R$, and m an integer. For non-metallic media, solutions of Eq. 1.42 can be associated to each guided mode, labeled by a pair index *ml*, where $m = 0, \pm 1, \pm 2, \ldots$ is the azimuthal index and $l = 1, 2, 3, \ldots$ the radial index. For guided modes with $m = 0$, the field is symmetric about the axis, exhibiting a pure transverse character, either electric (TE_{0l}, $E_r = E_z = H_\theta = 0$, with $a_m = 0, b_m \neq 0$) or magnetic (TM_{0l}, $H_r = H_z = E_\theta = 0$, with $a_m \neq 0, b_m = 0$). These modes are decoupled, satisfying each set the following dispersion relations:

$$\frac{\epsilon_1}{u}\frac{J_m'(u)}{J_m(u)} - \frac{\epsilon_2}{v}\frac{H_m'(v)}{H_m(v)} = 0, \text{for TE modes;} \tag{1.43a}$$

$$\frac{\mu_1}{u}\frac{J_m'(u)}{J_m(u)} - \frac{\mu_2}{v}\frac{H_m'(v)}{H_m(v)} = 0, \text{for TM modes.} \tag{1.43b}$$

Hybrid modes arise for $m \neq 0$ (HE_{ml}), where in general all field components are non-zero and their phases accumulate a factor of $2\pi m$ in a closed loop around the cylinder axis.

Regarding the nature of the mode, they can be divided into guided and leaky modes. Modes with $k_z > \omega/c_2$ are guided, while modes with $k_z < \omega/c_1$ are leaky. The propagation constant

of guided modes is higher than the propagation constant of the free radiation in the surrounding media. Thus, for conservation of the momentum they cannot couple to the external continuum of radiation and guided modes are confined in the waveguide. However, k_z is smaller for leaky modes that the propagation constant in the surrounding media and coupling to the continuum of radiation is allowed: part of the propagating wave is radiated outside the guide. More specifically, $k_z = k_z' + \imath k_z''$ is real for guided modes ($k_z'' = 0$), so that k_{t2} is purely imaginary for a lossless dielectric cylinder (the mode is confined inside the cylinder); by contrast, both k_z, k_{t2} are complex for leaky modes, with $k_z'' > 0$ ($k_{t2}'' < 0$) accounting for radiative losses along the propagation direction.[16]

As a final note, for solving the dispersion relation a constant and stationary field/energy distribution along the cylinder axis is assumed. However, leaky modes radiate energy into the far-field, and its energy should decay along its propagation. This conflict implies that the field at $r \to \infty$ diverges. Despite the mathematical inconsistence, these modes are physically meaningful and have been observed.[16]

1.5 Synopsis

The present thesis collects the main results along my years on my pre-doctoral period about the theoretical scattering properties of semiconductor nanowires and their collective response in periodic arrays (metasurfaces). The study has been focused at the nanoscale and optical frequencies, where the non-negligible losses of metallic particles difficult their use and deteriorate their performance. Metals are replaced by semiconductors and new paths must be explored to mimic the magnetic properties of metals. Incidentally, for the sake of the insight provided by our theoretical study, we will also include two experimental results based on systems that could escape from this description: an array of high refractive index disks at Gigahertz; and an array of metallic rods at Terahertz. These experiments represent pioneering approaches to engineer the so called bound states in the continuum; besides, our theoretical conclusions will allow us to extrapolate them to the nanoscale and the optical regime.

The thesis's chapters are structured as follow:

In Chapter 2, the reflection and transmission properties of an all-dielectric array consisting of high refractive-index (HRI) cylinders whose scattering properties can be described by their two lowest-order Mie resonances are theoretically studied. To this aim, we derive a coupled electric and magnetic dipole (CEMD) formulation that, through the explicit expressions for the Fresnel reflection amplitudes, unravels the interference and coupling between electric and magnetic dipolar fields (Section 2.1). Based on the multiple scattering approach, we discuss the nature of reflection resonances and generalized Brewster conditions induced by the coupling of electric and magnetic dipoles with the lattice periodicity (Section 2.2). Also, the results derived from our analytical approach are compared to numerical results obtained from commercial full wave electromagnetic solvers, being in full agreement and validating our model. Finally, based on the narrow resonances found in the reflection spectra, the performance of the metasurface as a refractive index sensor is studied (Section 2.3). These results have been done in collaboration with our colleagues at the

Donostia International Physics Center (DIPC).

The concept of bound state in the continuum (BIC) is formally introduced in Chapter 3, and it is explored in to metasurfaces (Section 3.1). The CEMD formulation is extended to 2D metasurfaces and used to analyze the conditions to confine waves in a periodic array. Then, BICs are theoretically and experimentally studied in two systems, in which their underlying physics is different. First, a periodic array of extremely high reflective index disks is investigated at Gigahertz. This work has been done in collaboration with our colleagues of the Institut Fresnel (Marseille) and the Universidad de Cantabria. When the emission of the parallel dipoles is in phase, due to a destructive interference effect, they cannot emit into the far field; and it is shown that close to the resonant condition of the parallel dipole, a BIC can be excited in the system (Section 3.2). Also, rotating the disks we modify the axis direction of the parallel dipole, allowing the coupling to the far field. Later, it is shown that an array of detuned dipoles supports robust BICs (Section 3.3). This BIC arises from the out-of phase oscillation of rods within the unit cell. The symmetry protection of these BICs is not destroyed by displacements of the dipoles within the unit cell, which increase the tolerance of these systems to imperfections. Also, it is demonstrated experimentally that such BICs emerge at THz frequencies in Au-rod dimer metasurfaces formed by two rods per unit cell by observing the vanishing linewidth in the THz-transmission spectra, accompanied by the pronounced increase of the resonance lifetime, when rods are made identical. The experimental work has been carried out by our colleagues at the Technological University of Eindhoven.

The scattering properties of dielectric cylinders are studied in Chapter 4. First we established the connection between Mie resonances and leaky/guided modes in infinitely long cylinders (Section 4.1). It is shown that the poles of both resonant processes (scattering and propagation) are given by the same fundamental equation (in fact, Eq. 1.42), although the interpretation is slightly different. For Mie resonances, the poles are found as a function of complex frequencies, while propagating modes are characterized by a complex wavevector. Later, the role of leaky and guided modes on the absorption in finite nanowires is investigated, showing the relevance of guided modes at grazing angles of incidence. Finally, we study the scattering at normal incidence of shorter nanowires, with lengths in the order of the incident wavelength. The interplay between Mie resonances and guided modes leads to strong asymmetric narrow Fano resonances in this simple configuration (Section 4.2). The nanowire acts as a Fabry-Perot cavity that supports guided modes. Depending on the symmetry of the modes and on the incoming polarization, the scattering cross section presents either strongly or weakly asymmetric (Fano) line shapes with a large contrast over the background. The corresponding higher or lower degree of interference is explained through a theoretical model as a result of the far-field overlap of broad Mie modes with narrow Fabry-Perot resonances.

In Chapter 5, we deepen into the fundamental properties of guided modes. The peculiar structured wavefield arising inside waveguides has not been addressed in detail. Thus, the spin and orbital angular momenta of confined light inside waveguides is theoretically studied (Section 5.1). This is done for two cases: simplest (planar) waveguide geometry with transverse electric/magnetic modes; and a cylindrical (nanowire) geometry (much more involved), which supports not only pure transverse modes but also hybrid modes with intrinsic helicity. It is shown that the

transverse spin density inside waveguides does not vanish and depends on the transverse momentum. Thus, subwavelength waveguides are amenable to spin-orbit interaction (SOI) phenomena. In addition, the appearance of strong coupling regimes in a system consisting of a semiconductor nanowire embedded in an excitonic medium, by means of the interplay between guided modes and excitonic states, is theoretically investigated (Section 5.2). Upon exploiting the evanescent tail of various weakly guided modes outside the semiconductor nanowire, the coupling to excitonic modes of an organic dye surrounding the nanowire is plausible. A quantum model is developed (in collaboration with our colleagues at the Universidad Autónoma de Madrid) to determine the polaritonic modes revealed through an avoided crossing with expectedly large enough Rabi splittings, showing that a strong coupling regime can be accomplished.

Finally, Chapter 7 (and Chapter 6 in Spanish) presents the main conclusions of the work developed in preceding chapters and future perspectives are disclosed.

Chapter 2

Metasurfaces

From the beginning of the century, there has been a great deal of attention devoted to metamaterials.[17–20] Metamaterials are artificial materials that can be described in terms of their effective medium behavior that depends on the geometry and properties of their basic constituents. From the parallelisms with natural media, in which their properties depend on constitutive chemical components, the basic constituents of metamaterials are called meta-atoms. These new degrees of freedom have allowed to design new materials with exotic and not naturally attainable properties along the electromagnetic spectrum.

The process of deducing the effective properties of metamaterials, ϵ_{eff} and μ_{eff}, from the properties of their meta-atoms is known as homogenization. The simplest homogenization model is the well known Clausius-Mossotti equations, applied to a random arrangement of dipolar particles. They retrieve the permittivity and permeability from the polarizabilities, α_e and α_m , of the constitutive particles

$$\frac{\epsilon_{\text{eff}}-1}{\epsilon_{\text{eff}}+2}=\frac{N}{3}\alpha_e, \quad \frac{\mu_{\text{eff}}-1}{\mu_{\text{eff}}+2}=\frac{N}{3}\alpha_m, \tag{2.1}$$

where N is the number of particles per unit volume. Interesting properties arise from double negative materials, i.e., $\epsilon_{\text{eff}} < 0$ and $\mu_{\text{eff}} < 0$. To achieve a magnetic response, $\mu_{\text{eff}} \neq 1$, our meta-atoms must present a non-zero magnetic polarizability, but since there are no magnetic charges, in general matter is considered non-magnetic. Nonetheless there are ways to induce a magnetic response from non-magnetic materials. For example, a close current loop has an associate magnetic moment. Thus, the first attempts to induce negative responses, and to build metameterials, were done with metals, modeling "current circuits".

This approach was very successful at gigahertz frequencies, designing magnetic metals $\mu_{\text{eff}} \neq 1$, zero and negative refraction index materials ($n \sim 0, n < 0$), and hyperbolic media, among others. Maxwell's equations are scalable so that the same concepts can be applied to different sizes. However, material properties are not. Although at low frequencies, for example at Gigahertz, metals behave like lossless conductors, the absorption increases with frequency and is no longer negligible at infrared and optical wavelengths. The inevitable increase of light absorption and the subsequent conversion into heat impeded the use of metals in many practical applications at the

nanoscale.

Recently, a different approach to nanophotonics has emerged, based on all-dielectric materials.[21] In the same way that electric currents are related to magnetic moments, it was shown that the circulation of the displacement current, $\mathbf{D}$, in dielectric materials can also induce a magnetic response.[22–25] In addition, dielectrics present no (or low) losses at the optical regime. In this regard, semiconductor particles posses strong magnetic dipole resonances in the visible and infrared frequencies, which make them especially appealing to tailor light at the nanoscale, as an alternative to plasmonic (metallic) nanostructures. The main drawback with respect to plasmonics is the near field enhancement, much higher in the surrounding media for metallic particles. Also, despite the constituents are lossless, all-dielectric metamaterials present ultimately propagation losses from incoherent scattering that deteriorate their performance. This effect can be seen in Eq. 2.1, where the inherent imaginary part of the polarizability yields to effective properties with losses. Moreover, in order to induce stronger responses, the meta-atoms are designed to be on resonance. Thus, propagation losses are enhanced due to the high scattering cross sections of individual particles.

However, for many applications we are interested only in the final state of the field. Following the classical Huygens' principle, each point on a wavefront acts as a source of secondary wavelets and the new wavefront is found by constructing the surface tangent to the secondary wavelets. A single or few meta-atom layers can be arranged in such a way that the interference of secondary waves can create any arbitrary wavefront. Therefore, the shape, phase, polarization and intensity of the transmitted wave can be broadly engineered using a thin planar structure by the control of the phase difference between meta-atoms. This elegant 2D version of metamaterials is called metasurfaces.[19,26,27] Metasurfaces have been shown to be relevant in a variety of applications,[28–36] taking up less physical space and offering the possibility to reduce losses.

Among all-dielectric metasurfaces, one of the simplest geometries considered thus far is an array of dielectric wires. In the next sections, we analytically study the reflection and transmission of all-dielectric metasurfaces consisting of high refractive-index cylinders. The results presented in this chapter are the fruit of long discussions with Prof. Juan José Sáenz,[37,38] at the Donostia International Physics Center (DIPC).

2.1 Coupled electric and magnetic dipole (CEMD) formulation

The properties of metasurfaces are usually described using a coupled electric model. However, it has been pointed out that dielectric particles can present strong magnetic responses, that must be accounted for. Thus, we will first derive a coupled electric and magnetic dipole (CEMD) formulation to incorporate the magnetic dipole response and to understand the complex interference, scattering and resonant phenomena arising in simple geometrical arrangements such one-dimensional arrays of parallel cylinders.[37]

2.1.1 Scattering properties of a single HRI cylinder

Let us consider a dielectric cylinder with its axis along the x-axis, radius R, electric permittivity ε and centred at $\boldsymbol{r}' = (y', z')$ in an otherwise homogeneous medium (which, for simplicity, we assume to be vacuum or air). The infinitely long cylinder is illuminated by an external plane wave with a wave vector $\boldsymbol{k}_0$ (with $|\boldsymbol{k}_0| = k = 2\pi/\lambda$, λ being the wavelength of the incident field in the surrounding media) perpendicular to the cylinder axis. We describe the electromagnetic field as a 6-dimensional vector field $\boldsymbol{\Psi}(\boldsymbol{r})$ as

$$\boldsymbol{\Psi}(\boldsymbol{r}) = \begin{bmatrix} \boldsymbol{E}(\boldsymbol{r}) \\ Z\boldsymbol{H}(\boldsymbol{r}) \end{bmatrix}, \qquad \boldsymbol{E}(\boldsymbol{r}) = \begin{bmatrix} E_x(\boldsymbol{r}) \\ E_y(\boldsymbol{r}) \\ E_z(\boldsymbol{r}) \end{bmatrix}, \qquad \boldsymbol{H}(\boldsymbol{r}) = \begin{bmatrix} H_x(\boldsymbol{r}) \\ H_y(\boldsymbol{r}) \\ H_z(\boldsymbol{r}) \end{bmatrix}, \tag{2.2}$$

$\boldsymbol{E}(\boldsymbol{r})$ and $\boldsymbol{H}(\boldsymbol{r})$ being the electric and magnetic vector fields defined in Cartesian coordinates and $Z = (\mu_0/\epsilon_0)^{1/2}$ the vacuum impedance ($Z\boldsymbol{H}(\boldsymbol{r})$ and $\boldsymbol{E}(\boldsymbol{r})$ have the same units). We assume that the cylinder's electrodynamics response can be fully described by its lowest electric and magnetic multipoles in terms of a 6×6 polarizability tensor,[39–41] $\overleftrightarrow{\boldsymbol{\alpha}}$,

$$\overleftrightarrow{\boldsymbol{\alpha}} = \begin{pmatrix} \boldsymbol{\alpha}^{(e)} & 0 \\ 0 & \boldsymbol{\alpha}^{(m)} \end{pmatrix}, \tag{2.3}$$

where $\boldsymbol{\alpha}^{(e)}$ and $\boldsymbol{\alpha}^{(m)}$ are the electric and magnetic polarizabilities

$$k^2\boldsymbol{\alpha}^{(e)} = \begin{pmatrix} 4ib_0 & 0 & 0 \\ 0 & 8ia_1 & 0 \\ 0 & 0 & 8ia_1 \end{pmatrix}, \qquad k^2\boldsymbol{\alpha}^{(m)} = \begin{pmatrix} 4ia_0 & 0 & 0 \\ 0 & 8ib_1 & 0 \\ 0 & 0 & 8ib_1 \end{pmatrix}, \tag{2.4}$$

and a_n and b_n are the (dimensionless) Mie coefficients.[5] For convenience in this chapter, the 3x3 matrices are written in bold letter like vectors. Full 6x6 matrices are written with a double arrow, as done for matrices in the introduction. For homogeneous and isotropic cylinders, the polarizability is diagonal and, to this end, we define:

$$\alpha_x \equiv \alpha_{xx}, \qquad \alpha_y = \alpha_z = \alpha_{y,z} \equiv \alpha_{yy} = \alpha_{zz}. \tag{2.5}$$

The multipoles associated to $\alpha_x^{(m)}$ and $\alpha_x^{(e)}$ (i.e. a_0 and b_0, respectively) can be seen as magnetic and electric dipoles along the cylinder axis. We will refer to them as longitudinal dipoles. Strictly speaking, a dipole along the axis is meaningful and it can be considered as a (polarization) current line. The multipoles $\alpha_{y,z}^{(e)}$ and $\alpha_{y,z}^{(m)}$ (i.e. a_1 and b_1, respectively) are dipoles in the transversal yz plane, and we will call them transverse dipoles.

In Fig. 2.1 we plot the first Mie coefficients of an isolated HRI dielectric cylinder with real permittivity $\varepsilon = 12.25$ and radius $R = 50$ nm as a function of the frequency of the incoming field ($\omega = ck = 2\pi c/\lambda$, c the speed of light in the surrounding media). As the incident field is normal to the cylinder axis, the TE and TM waves are decoupled and can be treated independently. Notice

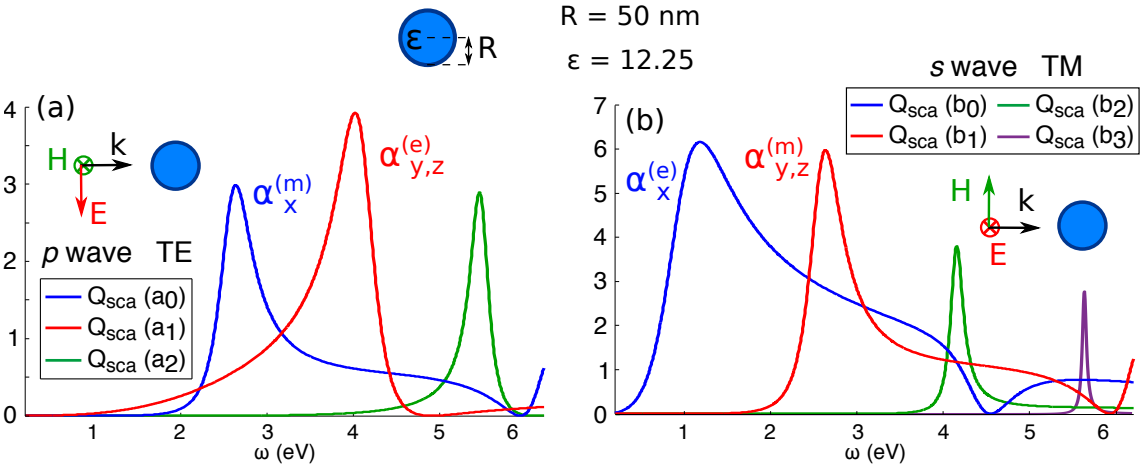

Figure 2.1: Contributions of the first terms in Mie theory to the scattering efficiency, Q_{sca}, for (a) p-polarized TE and (b) s-polarized TM waves of a dielectric cylinder of radius $R = 50$ nm and relative permittivity $\varepsilon = 12.25$ as a function of the energy ω. The second order terms a_2, b_2 are also shown to indicate the limit of validity of the dipolar approximation.

that, in contrast with the Mie theory for spheres, for cylinders at normal incidence (in general for 2D objects) the coefficients a_n are related to the response to TE (p-polarized) waves -with the magnetic field parallel to the cylinder axis-, while b_n describes the response upon TM (s-polarized) waves -with the electric field parallel to the cylinder axis-.

The field scattered by the cylinder, $\mathbf{\Psi}_{\text{sca}}$, at the position $\boldsymbol{r} = (y, z)$ can then be expressed in a closed form from Eqs 1.24, 1.26 as a function of the polarizing (incoming) field, $\mathbf{\Psi}_{\text{inc}}(\boldsymbol{r}')$, at the cylinder position, $\boldsymbol{r}' = (y', z')$, as

$$\mathbf{\Psi}_{\text{sca}}(\boldsymbol{r}) = k^2 \begin{pmatrix} \mathbf{G}(\boldsymbol{r},\boldsymbol{r}') & \mathbf{G}_{EM}(\boldsymbol{r},\boldsymbol{r}') \\ -\mathbf{G}_{EM}(\boldsymbol{r},\boldsymbol{r}') & \mathbf{G}(\boldsymbol{r},\boldsymbol{r}') \end{pmatrix} \overleftrightarrow{\boldsymbol{\alpha}} \mathbf{\Psi}_{\text{inc}}(\boldsymbol{r}') = k^2 \overleftrightarrow{\mathbf{G}}(\boldsymbol{r},\boldsymbol{r}') \overleftrightarrow{\boldsymbol{\alpha}} \mathbf{\Psi}_{\text{inc}}(\boldsymbol{r}'), \quad (2.6)$$

where $\mathbf{G}(\boldsymbol{r},\boldsymbol{r}')$ and $\mathbf{G}_{EM}(\boldsymbol{r},\boldsymbol{r}')$ are the Green functions of the cylinder (see Appendix A)

$$\mathbf{G}(\boldsymbol{r},\boldsymbol{r}') = \left\{\mathbf{I} + \frac{\boldsymbol{\nabla}\boldsymbol{\nabla}}{k^2}\right\} g(\boldsymbol{r}-\boldsymbol{r}'), \quad (2.7)$$

$$\mathbf{G}_{EM}(\boldsymbol{r},\boldsymbol{r}') = \mathrm{i}\frac{\boldsymbol{\nabla}}{k} \times \left(g(\boldsymbol{r}-\boldsymbol{r}')\,\mathbf{I}\right), \quad (2.8)$$

where $g(\boldsymbol{r}-\boldsymbol{r}') \equiv (\mathrm{i}/4)H_0(\boldsymbol{r}-\boldsymbol{r}')$ is the two-dimensional scalar Green function (with H_0 the Hankel function of order zero) and $\mathbf{I}$ the (3×3) unit dyadic. For a single, isolated, cylinder the incoming field is simply given by the external plane wave $\mathbf{\Psi}^{(0)}(\boldsymbol{r}')$ (see below).

In the far field, the intensity I_{ff} of the light scattered is, in general, asymmetric due to the interference between electric and magnetic contributions[5]

$$\begin{aligned} I_{\text{ff}}^{(TE)}(\omega,\phi) &\propto |a_0 + 2a_1\cos\phi|^2 \propto \left|\alpha_x^{(e)} + \alpha_{y,z}^{(e)}\cos\phi\right|^2, \\ I_{\text{ff}}^{(TM)}(\omega,\phi) &\propto |b_0 + 2b_1\cos\phi|^2 \propto \left|\alpha_x^{(e)} + \alpha_{y,z}^{(m)}\cos\phi\right|^2, \end{aligned} \quad (2.9)$$

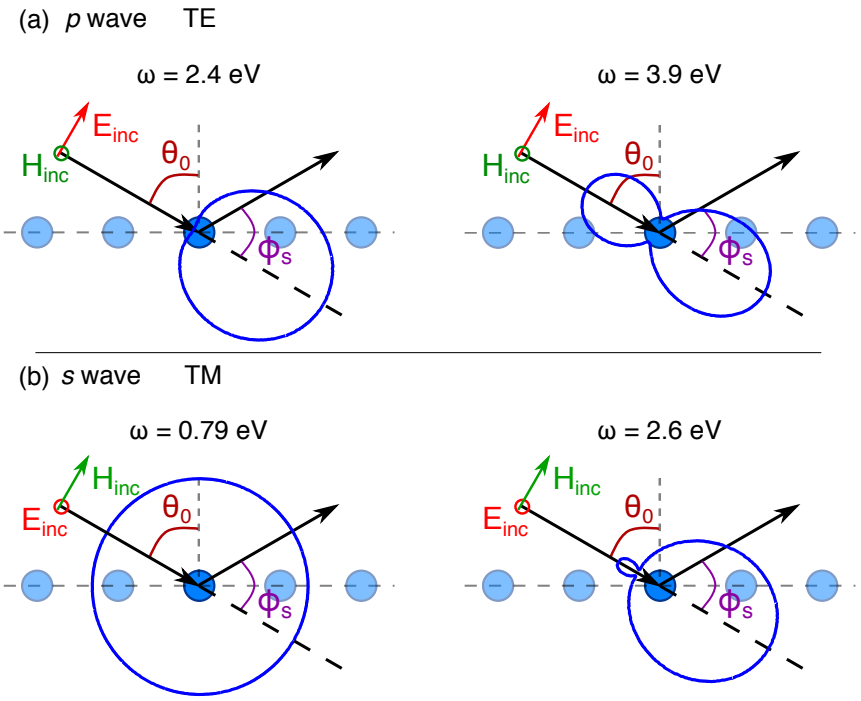

Figure 2.2: Sketch of the metafilm based on an array of parallel nanorods and scattering geometry for both s and p polarizations of the incoming light. Continuous blue lines correspond to radiation intensity diagrams of a single HRI cylinder for different frequencies and polarizations (same parameters as in Fig. 2.1).

where the scattering angle, ϕ, is the angle between the incident and scattered waves. Figure 2.2 illustrates typical radiation patterns at different frequencies and polarizations (see also Fig. 2.3). Although at specific wavelengths the scattering backwards can be almost suppressed, the Optical Theorem precludes the existence of *zero backscattering*: The conservation of energy for 2D lossless objects implies[41]

$$\mathrm{Re}\left[1/a_n\right] = \mathrm{Re}\left[1/b_n\right] = 1 \;\rightarrow\; \left\{\mathrm{Im}\left[1/\left(k^2\alpha_x\right)\right] = -1/4, \quad \mathrm{Im}\left[1/\left(k^2\alpha_{y,z}\right)\right] = -1/8\right\}, \tag{2.10}$$

or, equivalently,

$$\mathrm{Im}\left\{\overleftrightarrow{\boldsymbol{\alpha}}^{-1}\right\} = -k^2 \mathrm{Im}\left\{\overleftrightarrow{\mathbf{G}}(\boldsymbol{r}_0)\right\}, \tag{2.11}$$

so Eq. 2.9 can not vanish for the backward wave ($\phi = 180°$). Unlike spheres, in cylinders the degrees of freedom of the electric the magnetic fields are different and there is a mismatch between the local density of states of each multipole. Nonetheless, when $2\alpha_x = \alpha_{y,z}$, Eq. 2.9 can be zero at $\phi = \pm 120°$.

2.1.2 Periodic array of HRI nanorods: formal scattering theory and general results

Let us now consider an infinite set of parallel cylinders with the same radius R placed at $\boldsymbol{r}_n = (y_n = na, z_n = 0), n = 0, \pm 1, \pm 2, ...$ where a is the lattice constant, illuminated by an

external plane wave, $\mathbf{\Psi}^{(0)}(\boldsymbol{r})$, perpendicular to the cylinder axis with an incident angle θ_0 with respect to the normal to the cylinders' plane, as shown in Fig. 2.2. The spatial dependence of the plane wave can be taken as $\exp(\mathrm{i}\boldsymbol{k}_0\cdot\boldsymbol{r}) = \exp(\mathrm{i}K_0 y)\exp(-\mathrm{i}q_0 z)$ where

$$K_0 = k\sin\theta_0, \qquad q_0 = k\cos\theta_0, \qquad k^2 = K_0^2 + q_0^2, \tag{2.12}$$

with $k = |\boldsymbol{k}_0|$, while the time dependence $\exp(-i\omega t)$ will be assumed for all the fields. Therefore, the external plane wave travels from the upper to the lower half plane. The upper half plane ($z > 0$) is considered as the reflected region, while the lower half plane ($z < 0$) is the transmitted region.

Single scattering versus full wave numerical calculations

In order to emphasize the relevance of interference and multiple scattering effects (even for subwavelength gratings), we have ploted in Fig. 2.3a,c the reflected intensity in the specular direction in a 'a/λ vs. θ_0' (or ω vs. θ_0) map assuming non-interacting cylinders, i.e. a plot of $I_{\mathrm{ff}}(\omega, \pi - \theta_0)$ normalized to its maximum value. The Q_{sca} plots on top serve to identify frequency regions where only the first two Mie coefficients are relevant and do not overlap with higher order multipoles. The results for I_{ff} include all relevant multipoles and reduce to Eq. 2.9 with $\phi_s = \pi - \theta_0$ when only the first two terms are relevant. These results summarise the different intensity radiation patterns of a single cylinder as a function of the ratio a/λ (each pattern in Fig. 2.2 corresponds to a vertical line in the $I_{\mathrm{ff}}(\omega, \pi - \theta_0)$ map).

The maps in Fig. 2.3d,f correspond to the full wave numerical calculation of the specular reflection $R_0(\omega, \theta_0)$ obtained from a well established electromagnetic solver (COMSOL Multiphysics). The regions with

$$0 \leq |\sin\theta_0| \leq \frac{\lambda}{a} - 1, \tag{2.13}$$

correspond to a subwavelength, 'zero order', grating (the black solid line delimits the onset of diffraction in the bottom half of Fig. 2.3). Upon comparing upper and lower graphs in Fig. 2.3, it becomes evident that most relevant features in the full wave numerical simulations cannot be reproduced by the scattering from single, non-interacting cylinders.

Formal scattering theory

Formal scattering theory can help us to understand the strong influence of the lattice on the optical properties of the metafilm observed in Fig. 2.3. The discussion below follows the notation introduced in Ref.[42] which is now extended to include electric and magnetic responses.

Let us consider an external plane wave, $\mathbf{\Psi}^{(0)}$ (with wave vector $\boldsymbol{k}_0 = K_0\hat{\boldsymbol{y}} - q_0\hat{\boldsymbol{z}}$), as:

$$\boldsymbol{E}^{(0)}(\boldsymbol{r}) = \left(E_{s_0}\hat{\boldsymbol{x}} + E_{p_0}\left[(K_0/k)\hat{\boldsymbol{z}} + (q_0/k)\hat{\boldsymbol{y}}\right]\right)e^{\mathrm{i}\boldsymbol{k}_0\cdot\boldsymbol{r}}, \tag{2.14a}$$

$$Z\boldsymbol{H}^{(0)}(\boldsymbol{r}) = \left(-E_{s_0}\left[(K_0/k)\hat{\boldsymbol{z}} + (q_0/k)\hat{\boldsymbol{y}}\right] + E_{p_0}\hat{\boldsymbol{x}}\right)e^{\mathrm{i}\boldsymbol{k}_0\cdot\boldsymbol{r}}, \tag{2.14b}$$

where $\mathbf{\Psi}^{(0)}$ is divided into s (E_{s_0}) and p (E_{p_0}) wave contributions.

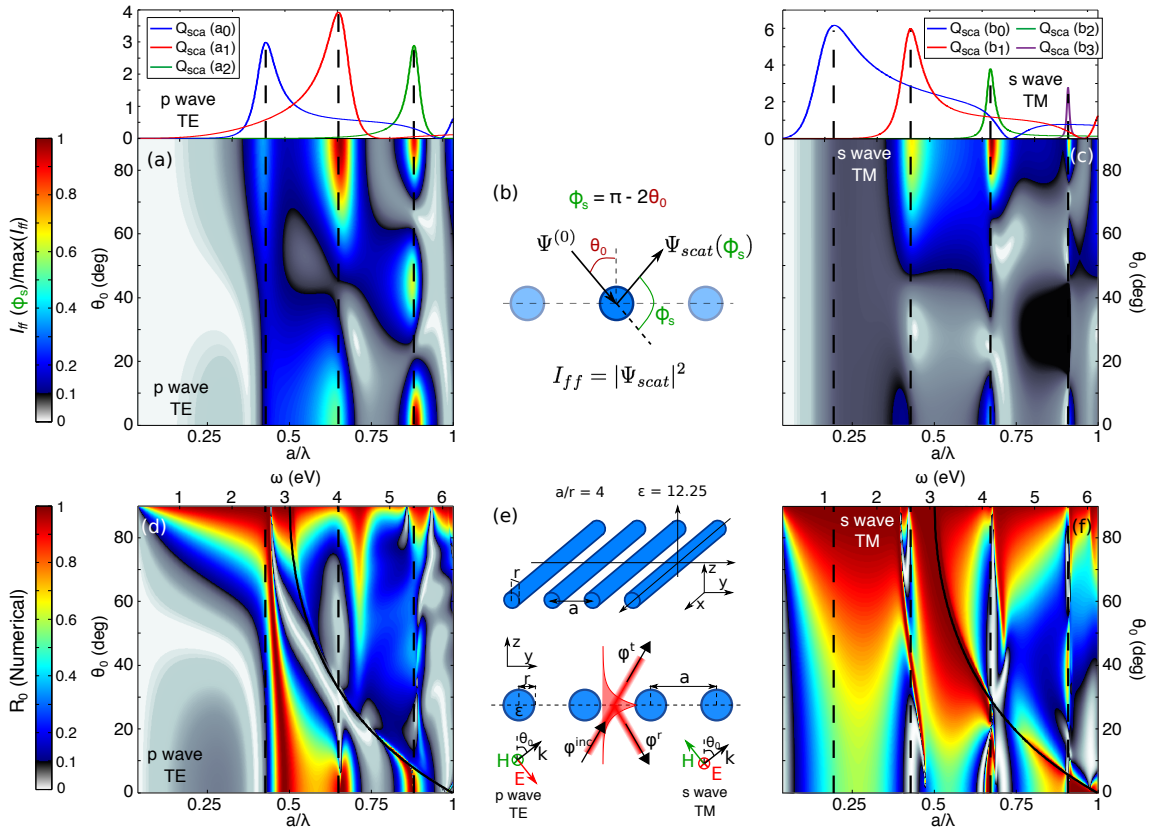

Figure 2.3: The two-dimensional maps correspond to the metafilm normalized specular reflection versus angle of incidence θ_0 and frequency ω (or $a/\lambda = \omega/(2\pi c)$). (a,c) Maps calculated from single scattering and neglecting interference effects corresponding to the asymmetric and resonant scattering from a single cylinder. (b) Schematic of the single scattering geometry. (d,f) Results of a (COMSOL) full wave numerical solution. Black solid lines delimit the onset of diffraction. Notice that we use two different color palettes to emphasise both transparent and total reflection regions. (e) Illustration of the metafilm and the scattering configuration.

Each nanorod is excited by the external plane wave plus the waves scattered from the rest of the grating.[43] The self-consistent incident field, on the $n = 0$ rod ($|\boldsymbol{r}_0| = 0$), is then given by the solution of

$$\boldsymbol{\Psi}_{\text{inc}}(\boldsymbol{r}_0) = \boldsymbol{\Psi}^{(0)}(\boldsymbol{r}_0) + \sum_{n\neq 0} k^2 \overleftrightarrow{\mathbf{G}}(\boldsymbol{r}_n) \overleftrightarrow{\boldsymbol{\alpha}} \boldsymbol{\Psi}_{\text{inc}}(\boldsymbol{r}_n). \tag{2.15}$$

For a periodic array and plane wave illumination the Bloch's theorem holds. The periodicity is given by the incident plane wave, $\boldsymbol{\Psi}_{\text{inc}}(\boldsymbol{r}_n) = \boldsymbol{\Psi}_{\text{inc}}(\boldsymbol{r}_0)\exp(\mathrm{i}K_0 na)$, and the self-consistent incident field can be written as

$$\begin{aligned}\boldsymbol{\Psi}_{\text{inc}}(\boldsymbol{r}_0) =& \boldsymbol{\Psi}^{(0)}(\boldsymbol{r}_0) + k^2 \left\{ \sum_{n\neq 0} \overleftrightarrow{\mathbf{G}}(\boldsymbol{r}_n) e^{\mathrm{i}K_0 na} \right\} \overleftrightarrow{\boldsymbol{\alpha}} \boldsymbol{\Psi}_{\text{inc}}(\boldsymbol{r}_0) \\ \equiv& \boldsymbol{\Psi}^{(0)}(\boldsymbol{r}_0) + k^2 \overleftrightarrow{\mathbb{G}}_b \overleftrightarrow{\boldsymbol{\alpha}} \boldsymbol{\Psi}_{\text{inc}}(\boldsymbol{r}_0),\end{aligned} \tag{2.16}$$

where $\overleftrightarrow{\mathbb{G}}_b$ is the lattice 'depolarization' dyadic (or return Green function),

$$\overleftrightarrow{\mathbb{G}}_b \equiv \sum_{n\neq 0} \overleftrightarrow{\mathbf{G}}(\boldsymbol{r}_n) e^{\mathrm{i}K_0 na}. \tag{2.17}$$

$\overleftrightarrow{\mathbb{G}}_b$ tells us about the coupling strength between the resonators, and is crucial to determine all the scattering properties, as shown below. Explicit expressions of the different Green dyadics in Cartesian coordinates are given in Appendix A.

The solution of the self-consistent equation can be formally written as a function of the external plane wave:

$$\boldsymbol{\Psi}_{\text{inc}}(\boldsymbol{r}_0) = \left[\overleftrightarrow{\mathbf{I}} - k^2 \overleftrightarrow{\mathbb{G}}_b \overleftrightarrow{\boldsymbol{\alpha}} \right]^{-1} \boldsymbol{\Psi}^{(0)}(\boldsymbol{r}_0), \tag{2.18}$$

where $\overleftrightarrow{\mathbf{I}}$ is the unit (6×6) dyadic.

Once we know the self-consistent incoming field, Eq. 2.18, the field scattered by the nanorod placed at $y_n = na, z_n = 0$, is given by

$$\boldsymbol{\Psi}_{\text{scat}}(\boldsymbol{r}) \;=\; k^2 \overleftrightarrow{\mathbf{G}}(\boldsymbol{r} - \boldsymbol{r}_n) \overleftrightarrow{\boldsymbol{\alpha}}\; \boldsymbol{\Psi}_{\text{inc}}(\boldsymbol{r}_n), \tag{2.19}$$

and the total scattered field can be written as

$$\boldsymbol{\Psi}_{\text{scat-t}}(\boldsymbol{r}) = k^2 \left\{ \sum_{n=-\infty}^{\infty} \overleftrightarrow{\mathbf{G}}(\boldsymbol{r} - \boldsymbol{r}_n) e^{iK_0 an} \right\} \overleftrightarrow{\boldsymbol{\alpha}} \boldsymbol{\Psi}_{\text{inc}}(\boldsymbol{r}_0) \equiv k^2 \overleftrightarrow{\mathbb{G}}^{\pm}(\boldsymbol{r}) \overleftrightarrow{\boldsymbol{\alpha}} \boldsymbol{\Psi}_{\text{inc}}(\boldsymbol{r}_0), \tag{2.20}$$

where the tensor lattice sum $\overleftrightarrow{\mathbb{G}}^{\pm}(\boldsymbol{r})$ can be written as a sum over all diffracted spectral orders ($m = \cdots, -2, -1, 0, 1, 2 \cdots$) as:

$$\overleftrightarrow{\mathbb{G}}^{\pm}(\boldsymbol{r}) \equiv \sum_{n=-\infty}^{\infty} \overleftrightarrow{\mathbf{G}}(\boldsymbol{r} - \boldsymbol{r}_n) e^{iK_0 an} = \sum_{m=-\infty}^{\infty} \overleftrightarrow{\mathbb{G}}_m^{\pm} e^{iK_m y} e^{\pm iq_m z}, \tag{2.21}$$

where, "-" ("+") corresponds to downward scattered waves in the region $z < 0$ (upwards reflected waves in the region $z > 0$). K_m and q_m are the wavevectors of the diffracted orders, Eq. A.8. See Eq. A.13 in Appendix A for an explicit expression in Cartesian coordinates

Finally, using Eq. 2.18 in Eq. 2.20, the reflected and transmitted fields are then given by

$$\boldsymbol{\Psi}_{\mathrm{r}}(\boldsymbol{r}) = k^2 \overleftrightarrow{\mathbb{G}}^{+}(\boldsymbol{r}) \widetilde{\overleftrightarrow{\boldsymbol{\alpha}}}\, \boldsymbol{\Psi}^{(0)}(\boldsymbol{r}_0), \tag{2.22a}$$

$$\boldsymbol{\Psi}_{\mathrm{t}}(\boldsymbol{r}) = \boldsymbol{\Psi}^{(0)}(\boldsymbol{r}) + k^2 \overleftrightarrow{\mathbb{G}}^{-}(\boldsymbol{r}) \widetilde{\overleftrightarrow{\boldsymbol{\alpha}}}\, \boldsymbol{\Psi}^{(0)}(\boldsymbol{r}_0), \tag{2.22b}$$

where $\widetilde{\overleftrightarrow{\boldsymbol{\alpha}}}$ is the renormalized (dressed) polarizability,

$$\widetilde{\overleftrightarrow{\boldsymbol{\alpha}}} = \overleftrightarrow{\boldsymbol{\alpha}} \left[I - k^2 \overleftrightarrow{\mathbb{G}}_b \overleftrightarrow{\boldsymbol{\alpha}} \right]^{-1} = \left[\overleftrightarrow{\boldsymbol{\alpha}}^{-1} - k^2 \overleftrightarrow{\mathbb{G}}_b \right]^{-1}. \tag{2.23}$$

Optical Theorem

The incoming power density can be written as

$$S^{(0)} = -\frac{1}{2} \mathrm{Re} \left\{ \boldsymbol{E}^{(0)} \times \boldsymbol{H}^{(0)*} \right\} \cdot \hat{\boldsymbol{z}} = \frac{q_0}{4kZ} \left| \boldsymbol{\Psi}^{(0)} \right|^2. \tag{2.24}$$

Integrating the Poynting vector in the far field, the reflected and transmitted power densities can be shown to be given by a sum over all N_p diffracted, propagating (i.e. q_m real, Eq. A.8), beams

$$S_R = \frac{k^4}{4kZ} \boldsymbol{\Psi}^{(0)\dagger}(\boldsymbol{r}_0) \widetilde{\overleftrightarrow{\boldsymbol{\alpha}}}^{\dagger} \left(\sum_{m=0}^{N_p} q_m \overleftrightarrow{\mathbb{G}}_m^{+\dagger} \overleftrightarrow{\mathbb{G}}_m^{+} \right) \widetilde{\overleftrightarrow{\boldsymbol{\alpha}}}\, \boldsymbol{\Psi}^{(0)}(\boldsymbol{r}_0), \tag{2.25a}$$

$$\begin{aligned} S_T = &\frac{k^4}{4kZ} \boldsymbol{\Psi}^{(0)\dagger}(\boldsymbol{r}_0) \widetilde{\overleftrightarrow{\boldsymbol{\alpha}}}^{\dagger} \left(\sum_{m=0}^{N_p} q_m \overleftrightarrow{\mathbb{G}}_m^{-\dagger} \overleftrightarrow{\mathbb{G}}_m^{-} \right) \widetilde{\overleftrightarrow{\boldsymbol{\alpha}}}\, \boldsymbol{\Psi}^{(0)}(\boldsymbol{r}_0) \\ &+ \frac{q_0}{4kZ} \boldsymbol{\Psi}^{(0)\dagger}(\boldsymbol{r}_0) \left(\overleftrightarrow{\mathbf{I}} + \mathrm{i} \frac{k^2}{a q_0} \left\{ \widetilde{\overleftrightarrow{\boldsymbol{\alpha}}} - \widetilde{\overleftrightarrow{\boldsymbol{\alpha}}}^{\dagger} \right\} \right) \boldsymbol{\Psi}^{(0)}(\boldsymbol{r}_0). \end{aligned} \tag{2.25b}$$

Energy conservation (in the absence of absorption) implies that $S^{(0)} = S_R + S_T$ and, taking into account that

$$\sum_{m}^{N_p} q_m \left[\overleftrightarrow{\mathbb{G}}_m^{+\dagger} \overleftrightarrow{\mathbb{G}}_m^{+} + \overleftrightarrow{\mathbb{G}}_m^{-\dagger} \overleftrightarrow{\mathbb{G}}_m^{-} \right] = \frac{2}{a} \mathrm{Im} \left\{ \overleftrightarrow{\mathbb{G}}(\boldsymbol{r}_0) \right\}, \tag{2.26}$$

we obtain

$$2\mathrm{i} \left\{ \widetilde{\overleftrightarrow{\boldsymbol{\alpha}}} - \widetilde{\overleftrightarrow{\boldsymbol{\alpha}}}^{\dagger} \right\} = k^2 \widetilde{\overleftrightarrow{\boldsymbol{\alpha}}}^{\dagger} \mathrm{Im} \left\{ \overleftrightarrow{\mathbb{G}}(\boldsymbol{r}_0) \right\} \widetilde{\overleftrightarrow{\boldsymbol{\alpha}}}. \tag{2.27}$$

This is a general condition for the dressed polarizability tensor $\widetilde{\overleftrightarrow{\boldsymbol{\alpha}}}$ imposed by energy conservation (valid for periodic arrays of arbitrary dipolar particles) and is similar to the one obtained for

electrically small particles.[39–41] Assuming $\widetilde{\overleftrightarrow{\boldsymbol{\alpha}}}^{-1}$ exists, then we have

$$\widetilde{\overleftrightarrow{\boldsymbol{\alpha}}}^{-1} = \widetilde{\overleftrightarrow{\boldsymbol{\alpha}}}_0^{-1} - \mathrm{i}k^2 \mathrm{Im}\left\{\overleftrightarrow{\mathbb{G}}(\boldsymbol{r}_0)\right\}, \tag{2.28}$$

where, in the absence of absorption, $\widetilde{\overleftrightarrow{\boldsymbol{\alpha}}}_0^{-1}$ must be Hermitian. Taking into account Eqs. 2.11 and 2.23, it is easy to find that our grating of homogeneous isotropic cylinders

$$\widetilde{\overleftrightarrow{\boldsymbol{\alpha}}}^{-1} = \mathrm{Re}\left\{\overleftrightarrow{\boldsymbol{\alpha}}^{-1} - k^2 \overleftrightarrow{\mathbb{G}}_b\right\} - \mathrm{i}k^2 \mathrm{Im}\left\{\overleftrightarrow{\mathbb{G}}(\boldsymbol{r}_0)\right\}, \tag{2.29}$$

fulfills the general condition given by Eq. 2.27.

2.1.3 Fresnel reflection amplitudes for nanorod-based metafilms

We shall restrict our discussion to subwavelength gratings (metafilms) with period $a < \lambda$ below the onset of the first diffracted beam (this takes place at the Rayleigh condition $|2\pi/a \pm K_0| = k$). This limits the study to angles of incidence verifying Eq. 2.13, such that only the zero (specular, $m = 0$) order can propagate in the far field ($|z| \gg \lambda$) input and output regions, higher order diffracted beams being evanescent and confined in the grating region. The specular reflectance, R_0, can then be derived from Eqs. 2.24 and 2.25a for both p- and s-polarized fields

$$R_0^{(p)} = \left(\frac{k^2}{2ka\cos\theta_0}\right)^2 \left|\gamma^{(p)}\left(\widetilde{\alpha}_x^{(m)} + \widetilde{\alpha}_z^{(e)}\sin^2\theta_0 + 2k^2 G_{bzx}\widetilde{\alpha}_x^{(m)}\widetilde{\alpha}_z^{(e)}\sin\theta_0\right) - \widetilde{\alpha}_y^{(e)}\cos^2\theta_0\right|^2, \tag{2.30a}$$

$$R_0^{(s)} = \left(\frac{k^2}{2ka\cos\theta_0}\right)^2 \left|\gamma^{(s)}\left(\widetilde{\alpha}_x^{(e)} + \widetilde{\alpha}_z^{(m)}\sin^2\theta_0 + 2k^2 G_{bzx}\widetilde{\alpha}_x^{(e)}\widetilde{\alpha}_z^{(m)}\sin\theta_0\right) - \widetilde{\alpha}_y^{(m)}\cos^2\theta_0\right|^2, \tag{2.30b}$$

where

$$k^2\widetilde{\alpha}_i^{(e)} = \left(\frac{1}{k^2\alpha_i^{(e)}} - G_{bii}\right)^{-1}, \qquad k^2\widetilde{\alpha}_i^{(m)} = \left(\frac{1}{k^2\alpha_i^{(m)}} - G_{bii}\right)^{-1}, \tag{2.31}$$

and

$$\gamma^{(p)} = \frac{1}{1 - k^4 G_{bzx}^2 \widetilde{\alpha}_x^{(m)}\widetilde{\alpha}_z^{(e)}}, \qquad \gamma^{(s)} = \frac{1}{1 - k^4 G_{bzx}^2 \widetilde{\alpha}_x^{(e)}\widetilde{\alpha}_z^{(m)}}, \tag{2.32}$$

G_{bii} and G_{bzx} being the matrix elements of $\overleftrightarrow{\mathbb{G}}_b$ (see Appendix A). Since the particles are lossless, the specular transmittance, T_0, is simply given by $T_0 = 1 - R_0$. For completeness, the specular transmittance and the reflectance for any diffracted order are shown in Appendix A.

The optical theorem has been already demonstrated, but from Eq. 2.30 the energy conservation is not obvious. Nonetheless, for lossless particles and below diffraction, R_0 can be rewritten in the form $R_0 = |A/(B + \mathrm{i}A)|^2$, where A and B are real quantities.

Kerker induced Brewster's effect (KiBs)

When the cylinders form a periodic array, the response by fields along the y axis is different from fields along the z axis. Furthermore, the lattice breaks the azimuthal symmetry and evens the local density of states for electric and magnetic fields, allowing the balance between electric and magnetic multipoles. It is interesting to note that the balance is due to the cancellation of the scattering effects of the individual resonators by the array. Formally, the imaginary parts of the lattice Green functions compensate the imaginary parts of the polarizabilities, being possible to totally suppress the reflected wave at any angle of incidence. The suppression comes from the interference between the electric and the magnetic lowest multipoles, assisted by the lattice, calling this condition the Kerker induced Brewster's effect (KiBs). For example, at normal incidence the KiBs condition is easily read as

$$R_0^{(p)} = \left(\frac{k^2}{2ka}\right)^2 \left|\widetilde{\alpha}_x^{(m)} - \widetilde{\alpha}_y^{(e)}\right|^2 = 0, \quad R_0^{(s)} = \left(\frac{k^2}{2ka}\right)^2 \left|\widetilde{\alpha}_x^{(e)} - \widetilde{\alpha}_y^{(m)}\right|^2 = 0, \tag{2.33}$$

$$\Re\left[1/\alpha_x^{(m)}\right] - \Re\left[1/\alpha_{y,z}^{(e)}\right] - k^2\Re(G_{bxx} - G_{byy}) = 0 \quad \text{for} \quad p \text{ waves}, \tag{2.34a}$$

$$\Re\left[1/\alpha_x^{(e)}\right] - \Re\left[1/\alpha_{y,z}^{(m)}\right] - k^2\Re(G_{bxx} - G_{byy}) = 0 \quad \text{for} \quad s \text{ waves}. \tag{2.34b}$$

Hence, the lattice plays a crucial role, being possible to have a zero in reflexion potentially at any angle of incidence.

Until now, we have developed a coupled electric and magnetic dipole (CEMD) formulation, and general analytical expressions have been explicitly derived for the optical theorem, the Kerker conditions and the reflection and transmission of the cylinder array. The electric and magnetic polarizabilities were given by the two lowest-order Mie cylinder resonances in both polarizations, but the formulation can be applied to any geometry, where the polarizabilities can be calculated through several numerical methods. In addition, although we have derived the formalism for one particle per unit cell, it is straightforward to generalize it for an arbitrary number of particles per unit cells. In the general case, the formalism deals with $6n \times 6n$ matrices, where n is the number of particles per unit cell.

In the next section, as a case study we analyze a metasurface consisting of an array of Si nanocylinders. By unraveling the role of each dipole resonance separately, we will be able to determine the impact of the lattice on the properties. After characterizing each resonance separately, the interplay between all dipoles is fully accounted for, describing the generalized Brewster conditions and the narrow resonances that arise from the interference effects between electric and magnetic dipoles.

2.2 Reflectance and generalize Brewster's effect

Let us study the scattering properties of an array of non-absorbing dielectric cylinders with a ratio between the lattice parameter and the radius $a/R = 4$ and relative permittivity $\varepsilon = 12.25$; this is a typical semiconductor permittivity in the optical domain above the gap (e.g. crystalline Si[44]). We will first consider the role of each multipole separately and later the interplay between them; in this manner the interference among all them will become clearer. Although for semiconductor cylinders in the optical domain all multipoles somewhat overlap, recall that for very high refractive indices in the THz and microwave domain, all resonant multipoles of a single cylinder would be isolated.

2.2.1 Longitudinal electric/magnetic dipoles

Figure 2.4 shows the total reflectance for both polarizations when the cylinder array is only described by its lower-order resonant multipoles ($\widetilde{\alpha}_x^{(e)}$ and $\widetilde{\alpha}_x^{(m)}$ for s and p waves, respectively); the orientation of the equivalent, longitudinal, dipole configuration is also depicted to illustrate the discussion (recall however that, in infinitely long cylinders, a dipole along the cylinder axis is not strictly speaking meaningful, but rather a current line). The black, vertical dashed lines mark the position of the resonance of the polarizabilities. The black solid line delimits the diffractive region at which the first diffraction channel is opened.

The reflectance for the specular wave can be written as

$$R_0^{(p,s)} = \left(\frac{1}{2ka\cos\theta_0}\right)^2 \left| \left(\Re\left\{ \frac{1}{k^2 \alpha_x^{(M,E)}} - G_{bxx} \right\} - i \frac{1}{2ka\cos\theta_0} \right)^{-1} \right|^2 . \tag{2.35}$$

It is known that the scattered wave and the incident one are 180° out of phase at resonance, so that they interfere destructively in transmission: Thus the reflectance tends to unity at resonance, namely, the system behaves as a perfect mirror.[45] From Eq. 2.35 the reflectance is maximum ($R_0^{(p,s)} = 1$) if $\Re\left[1/\widetilde{\alpha}_x^{(M,E)} - k^2 G_{bxx}\right] = 0$. Therefore, the resonance of the array is shifted from the resonance of the cylinders by the action of the lattice [by G_{xx}, see Eq. 2.31]. For example, for p waves the reflectance is maximum near the resonances of the polarizability, so G_{xx} slightly modifies this condition. However, for s waves the maximum is placed at much higher energies: indeed shifted and broadened by the action of the lattice.

Furthermore, when only the longitudinal dipole is considered the system always behaves as a thin dielectric film; the scattered wave is the same both in transmission and in reflection (the scattering is symmetric and $\mathfrak{t} = 1 + \mathfrak{r}$) even if the cylinders are not thin compared to the incident wavelength. This means that the cylinder array can be described as a thin dielectric film even at wavelengths of the order of the cylinder size ($2R/\lambda > 0.1$). A retrieval of the effective parameter of the system based on the reflectance and the transmittance properties, considering a reasonable width of $2R$, leads to an unexpected non-zero magnetic susceptibility ($\mu_{\text{eff}} \neq 1$) in order to keep a symmetric scattering. Finally, note that the reflectance for p waves vanishes at low frequencies, due to its magnetic character.

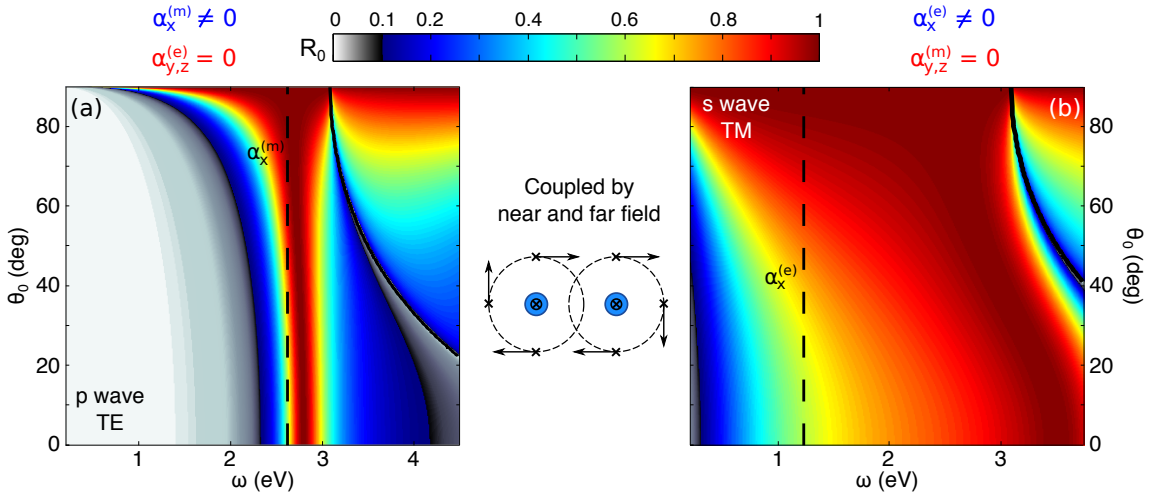

Figure 2.4: (a,b) Total reflectance calculated only considering $\widetilde{\alpha}_x^{(e)}$ and $\widetilde{\alpha}_x^{(m)}$ on Eq. 2.30 for $a/R = 4$ and $n = 3.5$ for (a) p and (b) s waves as a function of the energy ω of the incident wave and the angle of incidence θ_0. The black, vertical dashed lines mark the position of the resonance of the polarizabilities, while the black solid lines delimit the diffractive region. Middle panel: Configuration of the equivalent longitudinal dipole multipoles (bear in mind that, in infinitely long cylinders, a dipole along the axis is not strictly speaking meaningful, but rather a current line).

2.2.2 Transverse electric/magnetic dipoles

The phenomenology of the transverse dipole becomes richer because the lattice breaks the degeneracy ($G_{byy} \neq G_{bzz}$) and interference issues arise. Figure 2.5 shows the reflectance of the array for both polarizations when the lower-order resonant multipoles are neglected ($\widetilde{\alpha}_x^{(e)}$ and $\widetilde{\alpha}_x^{(m)}$ set to zero); the insets depicts dipole orientations and far-field patterns. The black vertical dashed lines, the blue dashed curves, and the black solid curves mark the resonances of the polarizabilities, the zero of reflectance, and the first diffraction condition, respectively. Although this configuration in truth only occurs for TE waves at low frequencies (or for extremely HRI materials for both polarizations), we find it very illustrative to characterize the self-interference of these dipoles alone before addressing below the more complex situation in which the two lowest-order multipoles contribute to the total response.

Close to normal incidence and near to the resonance of the cylinders (shown in black dashed lines) the reflectance goes to zero, surrounded by two high reflectivity lobes. This spectrally narrow zero comes from the destructive interference between the multipoles, sort of an electromagnetically induced transparency (EIT) window; the narrow EIT band disappears exactly at normal incidence and the reflectivity becomes large again ($R_0^{(p,s)} \sim 1$). In addition, there is a total transmission band at low frequencies for both polarizations (around $\theta_0 \sim 45°$) that corresponds to the Brewster condition achieved for p and s waves in electric and magnetic media, respectively. Also, for s waves there is another total transmission band at higher frequencies above the resonance of the polarizabilities ($\omega = 2.85$ eV). Although this band does not appear for the other polarization, the analysis of cases for different a/R ratio reveals that this characteristic depends on the spectral position of the resonance and not on the polarization (not shown here). The only difference that

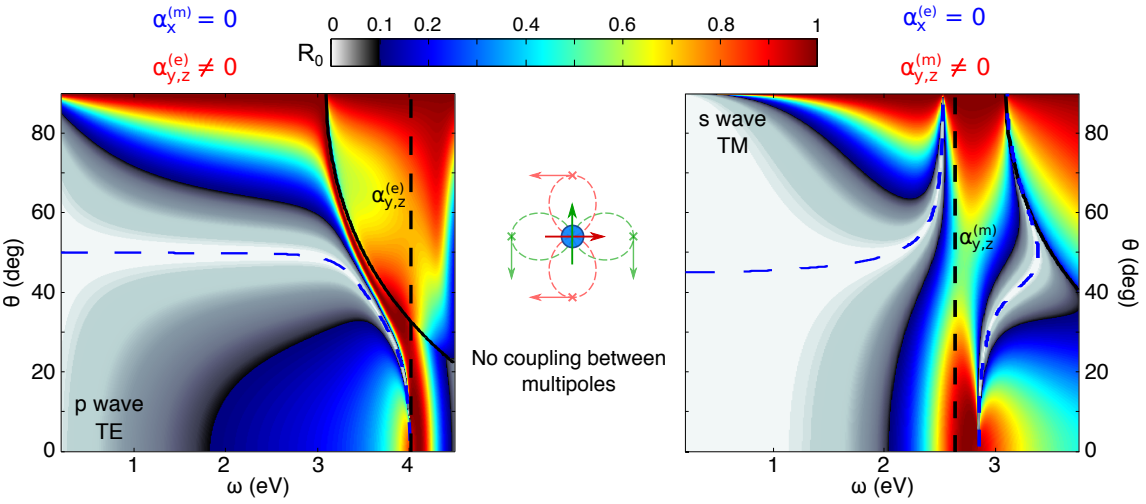

Figure 2.5: (a,b) Reflectance calculated with Eq. 2.30 setting $\widetilde{\alpha}_x^{(e)} = \widetilde{\alpha}_x^{(m)} = 0$ for $a/R = 4$ and $n = 3.5$: (a) p and (b) s waves as a function of the energy ω of the incident wave and the angle of incidence θ_0. The black, vertical dashed lines mark the position of the resonance of the polarizabilities, while the blue dashed lines show the zero reflectance (total transmission) bands. The black solid lines delimit the diffractive region. Middle panel: Configuration of the equivalent transverse dipole multipoles.

comes from the polarization itself is the extension of the reflection lobes towards lower or higher frequencies. This is explained by the different behaviour of the a_1, b_1 resonances: for p waves, a_1 goes to zero above resonance (at higher frequencies), whereas for s waves b_1 remains non-zero.

All this phenomenology can be understood from the analytic form of the reflectance. In the absence of the first multipole ($\alpha_x^{(E,M)} = 0$), Eq. 2.30 can be written as

$$R_0^{(p,s)} = \left(\frac{1}{2ka\cos\theta_0}\right)^2 \left| \sin^2\theta_0 \left(\Re\left[\frac{1}{k^2\alpha_{y,z}^{(E,M)}} - G_{bzz}\right] - i\frac{\sin^2\theta_0}{2ka\cos\theta_0}\right)^{-1} - \cos^2\theta_0 \left(\Re\left[\frac{1}{k^2\alpha_{y,z}^{(E,M)}} - G_{byy}\right] - i\frac{\cos^2\theta_0}{2ka\cos\theta_0}\right)^{-1} \right|^2, \tag{2.36}$$

which can be shown to be proportional to

$$R_0^{(p,s)} \propto \left| \Re\left[\frac{1}{k^2\alpha_{y,z}^{(E,M)}}\right] \left(\cos^2\theta_0 - \sin^2\theta_0\right) - \left(\Re\left[G_{bzz}\right]\cos^2\theta_0 - \Re\left[G_{byy}\right]\sin^2\theta_0\right) \right|^2 . \tag{2.37}$$

It is seen that the reflection must be large at resonance due to the cancellation of the incident wave in transmission. However, as the first term of Eq. 2.37 is zero at resonance, it can be compensated by the second term at some frequency, leading to a zero of reflection surrounded by a large (close to one) and broad reflectivity band. Overall, the reflectance is large, except for a specific frequency near resonance where this narrow EIT condition is met and reflectance vanishes. Furthermore, this phenomenology can be better understood if the transverse contributions are separated into the contributions along the y and z axes, namely, parallel and perpendicular to the metasurface; this is

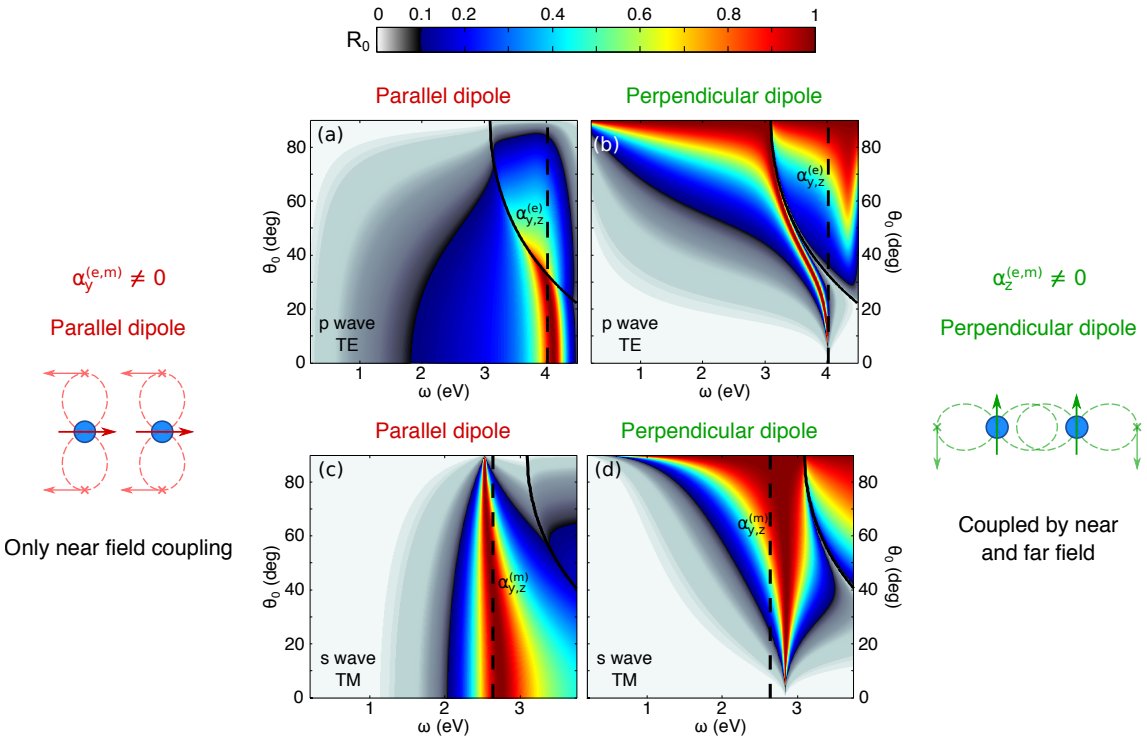

Figure 2.6: (a,b) Contribution to the p total reflectance in Fig. 2.5a from the projection of the transverse dipole multipoles along the y (a) and z axes (b). (c,d) Contribution to the s total reflectance in Fig. 2.5b from the projection of the transverse dipole multipoles along the y (c) and z axis (d). Lateral panels: Configurations of the equivalent transverse dipole multipoles.

done in Fig. 2.6a-d.

The width of each multipole is proportional to the angle of incidence

$$\Im\left[1/\widetilde{\alpha}_y^{(E,M)}\right] \propto k^2\cos^2\theta_0, \quad \Im\left[1/\widetilde{\alpha}_z^{(E,M)}\right] \propto k^2\sin^2\theta_0. \tag{2.38}$$

Thus, close to normal incidence the dipole along the z axis is extremely narrow, while the other dipole is broader. The interference of these multipoles leads to a narrow EIT window, that becomes broader as the angle of incidence increases. Interestingly, this behaviour is also observed at oblique incidence. Now the dipole along the y axis plays the role of the narrow resonance and a narrow EIT window appears close to 90°. This can be seen in Fig 2.5b for s waves, where the reflectivity goes to zero at oblique incidence. However, it is not met for p waves because the resonance falls in the diffraction region (it can be tuned by modifying the lattice parameter). The latter condition (narrow EIT window at grazing incidence with high transmission for specific frequencies) is worth mentioning since all surfaces behave as mirrors at grazing incidence.

The first term of Eq 2.37 dominates the reflectance out of resonance (recall that out of resonance $\Re\left[1/\left(k^2\alpha_{y,z}^{(E,M)}\right)\right] \gg 1$), although at the diffraction edge $\Re\left[G_{bzz}\right]$ diverges and both terms should be considered. However, the first term is always zero at $\theta_0 = 45°$. Then, at low energies there is a nearly dispersionless, total transmission band at fixed angle close to $\theta_0 = 45°$ (horizontal blue dashed curves in Fig. 2.5). This band is the zero in transmission associated with

the Brewster effect, in which a dipole cannot radiate along its axis. As the energy increases, this band becomes dispersive due to the lattice and/or to the polarizabilities, presenting different features. If there is no resonance of the polarizability in the non-diffraction region, the band bends toward smaller angles θ_0 following the frequencies at which $\Re\left[G_{bzz}\right]$ compensates the first term, up to the diffraction line at normal incidence.[46] On the other hand, if the Mie resonance lies in the spectral range of frequencies with no diffraction, the broad (Brewster-like) transmission band is connected to the lowest-energy EIT window described above, as shown in Fig. 2.5a,b. Depending on the spectral position of the resonances, the broad transmission band bends either toward normal or toward grazing incidence, for p waves or s waves, respectively. Therefore, the lattice presents a phase transition, depending of the spectral position of the resonance, that would be interesting to study. Finally, from Eq 2.37, the reflectance is always zero at $\omega = 3.3$ eV and $\theta_0 = 45°$ ($\Re\left[G_{byy} - G_{bzz}\right] = 0$) regardless of the properties of the particles. The zeros of reflections form closed bands, so this point must be included within a total transmission band. If the first narrow EIT window is located above this zero-reflection point, as for p waves, both bands appear as hybridized (see the lower-energy, blue dashed curve in Fig. 2.5a). If the narrow EIT band is otherwise placed below the zero-reflection point, as is the case for s waves, the broad transmission band exhibits a sort of splitting, as shown in Fig. 2.5b for s waves with the two blue dashed curves: interestingly, note that in this case the transmission bands behave as in a strong coupling phenomenon, where the cylinder resonance separates the broad Brewster band and the narrow EIT windows.

2.2.3 Longitudinal and transverse electric/magnetic multipoles

After studying the phenomenology of each resonance separately, we now consider all of them together. In Fig. 2.7 the reflectance of the array is shown when both dipoles (electric and magnetic) are considered. The position of the resonant frequencies are displayed in black, dashed curves, while the zeros of reflectance are shown in blue, dashed curves. In addition, all these curves are labeled. The diffraction lines are marked in black, solid lines. In this regard, it follows from Eq. 2.30 that, apart from the direct interference between the different multipoles, there is also an additional term arising from the coupling between the dipoles in the x- and z-axis. This term is zero for normal incidence ($G_{bzx} = 0$ at normal incidence) and increases toward higher angles. It is important to note that upon considering all terms, the reflectance from the exact numerical calculation (bottom half in Fig. 2.3) is in full agreement with the CEMD analytical formulation shown in Fig. 2.7, ensuring the validity of our method.

As predicted by the KiBs condition at normal incidence (Eq. 2.34) there are frequencies at which the reflectance is zero (zero back-scattering): These frequencies are at $\omega = 2.6, 4.1$ eV for p waves and at $\omega = 2.4, 4.5$ eV for s waves. Furthermore, there is another zero in reflection close to normal incidence at $\omega = 4.0$ eV for p waves and at $\omega = 2.9$ eV for s waves. For p waves the minimum mainly arises from the interference of the in-plane dipoles (EIT window) as in Fig. 2.5. Nonetheless, for s waves the zero in reflection comes from the (Fano asymmetric) interference between the longitudinal dipole and the transverse dipole in the y axis.

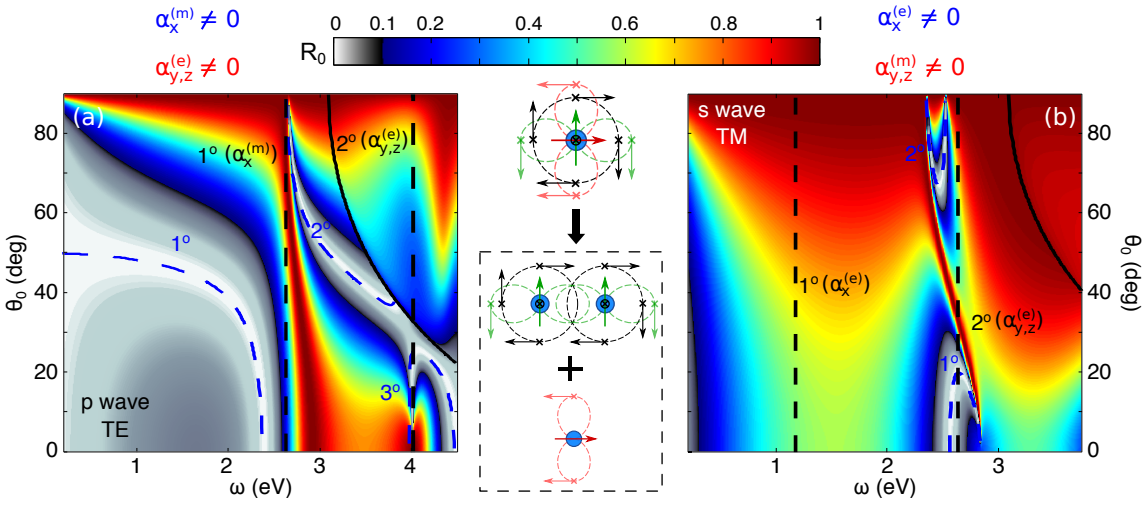

Figure 2.7: (a,b) Reflectance calculated considering all terms in Eq. 2.30 for $a/R = 4$ and $n = 3.5$: (a) p and (b) s waves as a function of the energy ω of the incident wave and the angle of incidence θ_0. The black, vertical dashed lines mark the position of the resonance of the polarizabilities, labeled for a better identification. The blue dashed lines show the zero reflectance (total transmission) bands, also labeled. The black solid line delimits the diffractive region. Middle panel: Configuration of the equivalent dipole multipoles (bear in mind that, in infinitely long cylinders, a dipole along the axis is not strictly speaking meaningful).

The interference between multipoles is easily appreciable in both cases. For p waves, the first resonance ($\alpha_x^{(m)}$) bends the first zero-reflection (Brewster-like) band that appears at $\theta_0 \sim 45°$ at low frequencies, toward the first KiBs condition ($\omega = 2.6$ eV), and a maximum of reflectance covering all angles emerges. However, above the first resonance the interference leads to a second total transmission band that starts at $\theta_0 = 90°$ and disappears when it crosses the diffraction line. The low frequency (first) band is due to the self- interference between the transverse dipoles, but the inter-resonance (second) band is induced by the coupling between the different multipoles described by $\gamma^{(p)}$ in Eqs. 2.32. This coupling would lead to a Fano interference, although both multipoles are qualitative narrow and separated in energies, so the interference is not very pronounced. Finally, there is another narrow minimum of reflectance near the resonance of $\alpha_{y,z}^{(e)}$ ($\omega = 4.0$ eV), as in Fig. 2.5. This minimum is connected to the second zero predicted by the KiBs condition ($\omega = 4.1$ eV), forming the third transmission band. In addition, the high reflectance band that covers all angles of incidences above the resonance in Fig. 2.5a disappears, as a result of the interference with the longitudinal dipole.

For s waves, the existence of electric response at low frequencies precludes the emergence of the low frequency zero-reflection band associated to the Brewster effect. In this case, multipole coupling originates a narrow high reflective band in the proximity of the second resonance that separates two regions with zero-reflection bands, the first at normal and the second at grazing incidences. However, this phenomenology changes if the resonances shift to lower frequencies (i.e, increasing the radii R): the narrow high reflective band becomes a zero-reflexion band (not shown here). The narrow band comes from the Fano interference between the multipoles connected by $\gamma^{(s)}$. For this polarization the longitudinal dipole is broad (see Fig. 2.4) and the interaction with

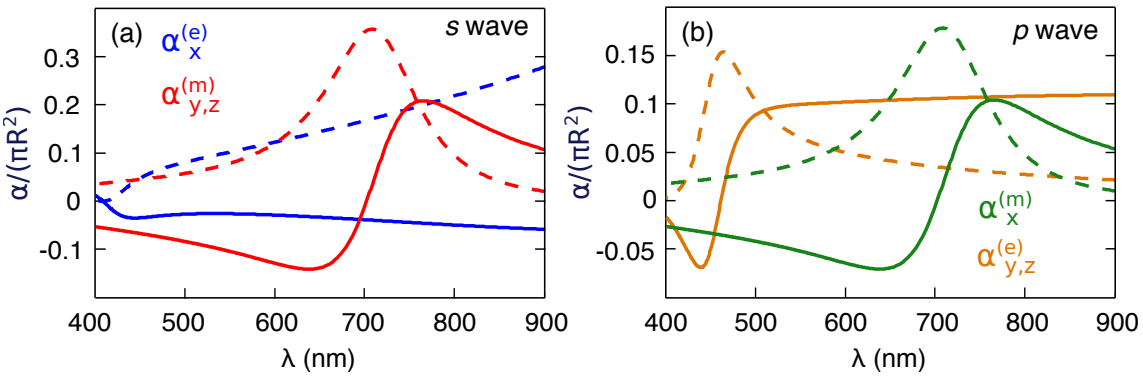

Figure 2.8: Electric and magnetic polarizibilities of a Si cylinder of radius r = 75 nm and relative permittivity $\epsilon = 12.25$, extracted from the first terms of Mie scattering theory (see text) for: s-polarized/TM waves (top) and p-polarized/TE (left). Solid (right) curves correspond to real (imaginary) parts.

the perpendicular traversal dipole leads to a strong Fano interference. Nevertheless, the normal interference with the y traverse dipole determines the background and the sign of the Fano parameter. Regarding the zero-reflection bands in Fig. 2.7b, the first one corresponds to the closed band defined by the first KiBs condition ($\omega = 2.4$ eV) and the minimum of reflectance related to the Fano interference ($\omega = 2.9$ eV). At this energy there is an EIT window for the transverse dipoles (Fig. 2.5b), but the coupling to the longitudinal dipole modifies the profile. The second zero in reflection is placed at grazing incidence, connecting the other EIT windows with a zero coming from the Fano interference, also at oblique incidence. Lastly, the second KiBs condition ($\omega = 4.5$ eV) arises at higher frequencies, forming the third band that covers all the diffraction-free region.

2.3 All-dielectric metasurface in refractive index sensing

We have seen that high-refractive index nanophotonic structures supporting strong magnetic dipole resonances in the optical domain have been proposed as a nearly lossless alternative to plasmonic nanostructures for building blocks of metamaterials and metasurfaces. However, very few works have investigated the potential of all-dielectric structures in refractive index sensing,[47–50] unlike in Plasmonics.[51–56] In the previous section we have found narrow resonances in an array of dielectric cylinders. Then, this platform seems to be suitable for refractive-index sensing and in this section its performance will be studied in detail.[38]

2.3.1 High-Q Fano resonances and electromagnetically-induced transparency

Let us study the scattering properties of an array of non-absorbing Si cylinders with the same ratio between the lattice parameter and the radius $a/R = 4$ taken in the preceding section. However, to shift the resonances to the visible, the radius is increased to $R = 75$ nm. For the sake of completeness, we show in Fig. 2.8 the polarizibilities to be used within the CEMD, which indeed stem from the corresponding Mie coefficients (Eq. 2.4). Recall that TE and TM waves are

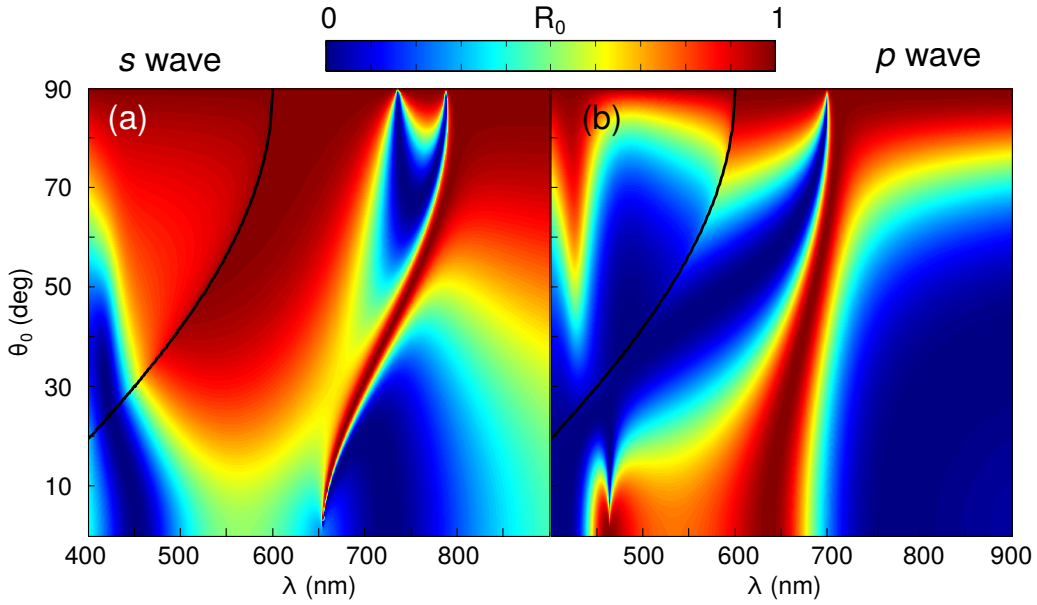

Figure 2.9: Contour maps of the specular reflectance calculated through CEMD for a Si cylinder metasurface with $R = 75$ nm, $a = 300$ nm, and relative permittivity $\epsilon = 12.25$, as a function of the incident wavelength λ and angle of incidence θ_0 for: (a) s and (b) p polarization. The diffractive region lies above the black solid curves in the upper left corners.

decoupled for incident field normal to the cylinder axis, so that each polarization can be treated independently.

From the CEMD formulation, Eqs. 2.30, the reflectance from a Si-cylinder metasurface with $a = 4R = 300$ nm in the optical domain is shown in Fig. 2.9 as a function of both wavelength λ and angle of incidence θ_0.

Zero reflection broad bands (total transmission) are evident that have been associated with Kerker-induced Brewster's (KiBs) effects similar to those discussed before. In addition, broad bands of large specular reflection (recall that Si is nearly transparent) appear also that are connected to ED and MD cylinder resonant modes. Nonetheless, we focus here on the emergence of very narrow resonances (especially those close to normal incidence), evident from Fig. 2.9, that appear despite the fact that they also stem from those broad (Mie) resonances of the isolated cylinders (cf. Fig. 2.8).

Let us study these narrow resonant modes in detail, by plotting spectral reflectances for fixed angles of incidence in Fig. 2.10. We chose near normal angles of incidence for both polarizations. All zero-reflection bands are marked, indicating their origin: broad transmission (KiBs) bands described by lattice Kerker conditions,[37] in contrast to narrow Fano/EIT resonances. Such resonances are very narrow, and for s waves are extremely asymmetric, thus exhibiting Fano line shapes similar to those discussed in connection with dielectric nanostructures and metasurfaces.[49,57–59] To

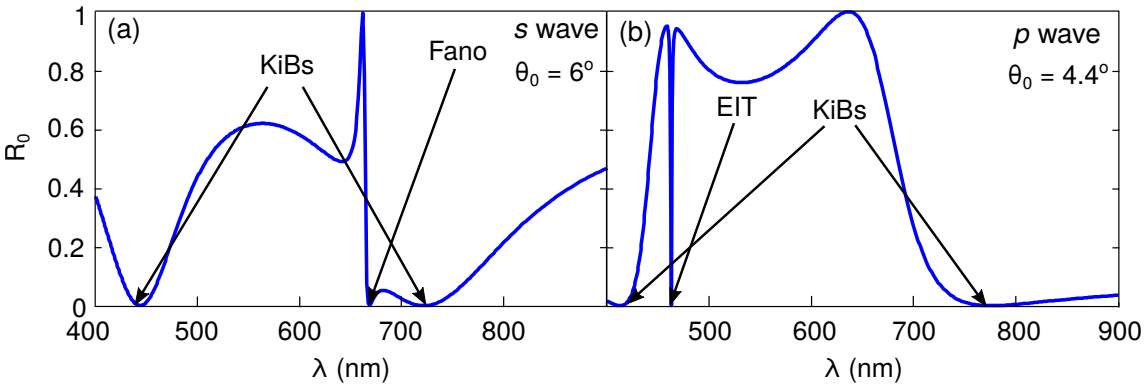

Figure 2.10: Specular reflectance spectra from Fig. 2.9 for fixed angles of incidence. (a) *s* waves at $\theta_0 = 6°$; (b) *p* waves at $\theta_0 = 4.4°$. Kerker-induced Brewster's (zero reflectance) bands are marked as KiBs; narrow Fano resonance at $\lambda \sim 655$ nm and EIT dip at $\lambda \sim 464$ nm are also highlighted.

this end, we make use of the generalized Fano formula:[60]

$$f(\varepsilon) = \sigma(\varepsilon)\frac{(\varepsilon+q)^2}{\varepsilon^2+1}, \tag{2.39a}$$

$$\varepsilon = \frac{\omega-\omega_0}{\frac{1}{2}\Gamma}, \tag{2.39b}$$

$$\sigma(\varepsilon) = \left(\frac{k^2}{2k_z a}\right)^2 \left|\widetilde{\alpha}_x - \widetilde{\alpha}_y \cos^2\theta_0\right|^2, \tag{2.39c}$$

and zoom in them in the frequency domain in Fig. 2.11. Specifically, the clearly asymmetric line shape for *s* waves appearing in Fig. 2.11a at $\lambda \sim 659$ nm ($\omega_0 = 1.89$ eV) yields a Fano parameter of $q = 1.74$ and a quality factor of $Q \equiv \dfrac{\omega_0}{\Gamma} = 420$. On the other hand, the line shape for *p* waves appearing in Fig. 2.11b at $\lambda \sim 464$ nm ($\omega_0 = 2.67$ eV) resembles a narrow electromagnetically-induced (EIT) transparency window, which can in turn be viewed as a Fano resonance for vanishing q parameter:[57] indeed it yields a $q = 0.01$ with a quality factor of $Q = 382$.

Furthermore, upon inspecting the analytical expression of the reflectance, Eqs. 2.30 and 2.39, it can be seen that the narrow Fano resonance for *s* waves stems mainly from: first, a narrow resonant mode arising from the hybridization (accounted for the lattice factor $\gamma^{(s)}$) of the transversal MD mode at $\lambda \sim 700$ nm (see Fig. 2.8), leading to a narrow surface lattice resonance; second, the latter becomes strongly asymmetric upon interfering with a much broader mode, which includes contributions from both the longitudinal ED and the above mentioned transversal MD mode (thus from both $\widetilde{\alpha}_x, \widetilde{\alpha}_z$ in Eq. 2.30). The interpretation is further confirmed by the dipole moments induced on the cylinders shown in the inset of Fig. 2.11a. The electric dipole moment p_x (longitudinal ED mode) at normal incidence is a smooth continuous function (blue dashed curve). However, at non-normal incidence p_x is hybridized with m_z (transversal MD mode) through the coupling term $\gamma^{(s)}$, leading to a Fano resonance also in the electric dipole moment (blue solid curve). The other transversal MD mode (m_y) acts as an additional background but does not play a relevant role in the asymmetry of the profile, i.e., without the longitudinal ED mode the transmittance would be

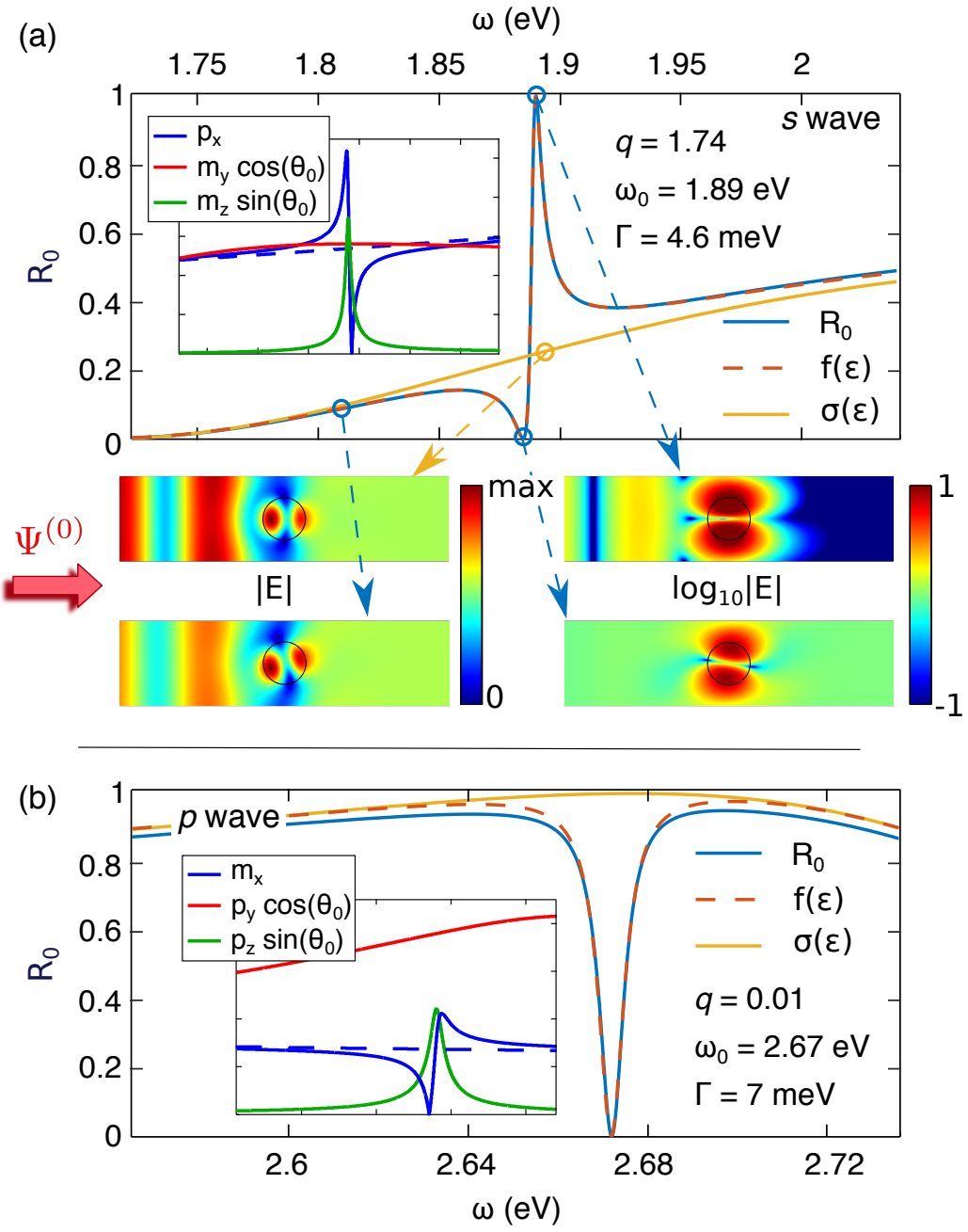

Figure 2.11: Same as Fig. 2.10 but zooming in the spectral regions of Fano and EIT resonances: (a) *s* waves at $\theta_0 = 4.4°$; (b) *p* waves at $\theta_0 = 6°$. Fits of the spectra to the Fano formula (Eq. 2.39) are also shown, with corresponding fitting parameters. The insets represent the absolute value of the dipolar moments induced on the cylinders multiplied by the value of their far field radiation patterns at the angle θ_0. In addition, near field plots at different frequencies are shown for *s* waves: in the latter, the incident plane wave propagates from left to right.

more symmetric as in Fig. 2.11b.

The near field at different frequencies is represented in the bottom part of Fig. 2.11a. Since at resonance the near field is enhanced, being more than an order of magnitude higher than that of the incoming plane wave, the field is plotted in logarithm scale. At $R_0 = 1$ it is shown that there is no transmitted wave, creating an interference in the backward direction between the incident wave and the reflected wave. Opposite, at $R_0 = 0$ the field is enhanced close to the particles but they do not radiate to the far field, so that the incoming plane wave is transmitted. In both cases, though, the near-field pattern resembles that of a MD oriented along the z axis. Thus, the transversal MD m_z mode is responsible for the high-Q resonance. In addition, the near field at normal incidence is shown in normal linear scale, together with the off-resonance field at $\theta_0 = 6°$. Both near-field patterns present similar features, given by the interference between the p_x and m_y dipole.

For *p* polarization, however, the contribution from the longitudinal MD is negligible, $\widetilde{\alpha}_x \sim 0$ in Eq. 2.39c. EIT stems entirely from the transversal ED modes at $\lambda \sim 460$ nm (see Fig. 2.8). Lattice coupling of such transversal ED modes results then in both a broad and a narrow surface lattice mode [$\widetilde{\alpha}_y$ and $\widetilde{\alpha}_z$, respectively in Eq. 2.30], the interference of which (antiphase) leads to EIT. From the induced dipole moment shown in the inset of Fig. 2.11(b), it is clear that there is also a hybridization of m_x with p_z through $\gamma^{(p)}$, but since $\widetilde{\alpha}_x$ is small, it is not manifested in the far field.

It should be mentioned that both narrow modes vanish at normal incidence with vanishing width and diverging Q-factor (see Fig. 2.9 near $\theta_0 \sim 0°$). This is a clear evidence that they become bound states in the continuum.[59,61–64] Bound states in the continuum will be studied in more detail along the next chapter.

On the other hand, as the angle of incidence increases (see Fig. 2.9), those modes behave differently. For *s* waves the Fano mode shifts to larger wavelengths due to the lattice and separates from the broad resonance of the longitudinal mode, becoming slightly broader. For even bigger angles of incidence, $\theta_0 > 45°$, the roles of the transversal modes are swapped, i.e, $\widetilde{\alpha}_y$ becomes narrower than $\widetilde{\alpha}_z$, leading to a sign flip of the Fano factor. For *p* waves, the EIT band becomes broader and the broad transversal ED mode diminishes (again, $\widetilde{\alpha}_y$ and $\widetilde{\alpha}_z$ swap their role). Close to grazing angles, the narrow transversal ED mode (now $\widetilde{\alpha}_y$) shifts toward longer wavelengths where $\widetilde{\alpha}_x$ is not negligible. Hence, the lattice couples such longitudinal MD mode with the transverse ED mode (given by $\gamma^{(p)}$) leading to an asymmetric interference.

2.3.2 Refractive index sensing

In light of the asymmetry and narrowness of the above Fano resonances, we now investigate their dependence on the refractive index of the surrounding medium n_e. We thus calculate through our CEMD the reflectance of a Si nanocylinder metasurface ($R = 75$ nm, $a = 300$ nm, and relative permittivity $\epsilon = 12.25$), in the spectral region close to the *s*-polarization Fano resonance shown in Fig. 2.11a. This is done in Fig. 2.12a for a value of n_e close to that of water, since refractive index sensors are often used in aqueous solutions. A red shift of the Fano resonance is observed as compared to Fig. 2.11a due to the higher refractive index of the surrounding medium, as expected.

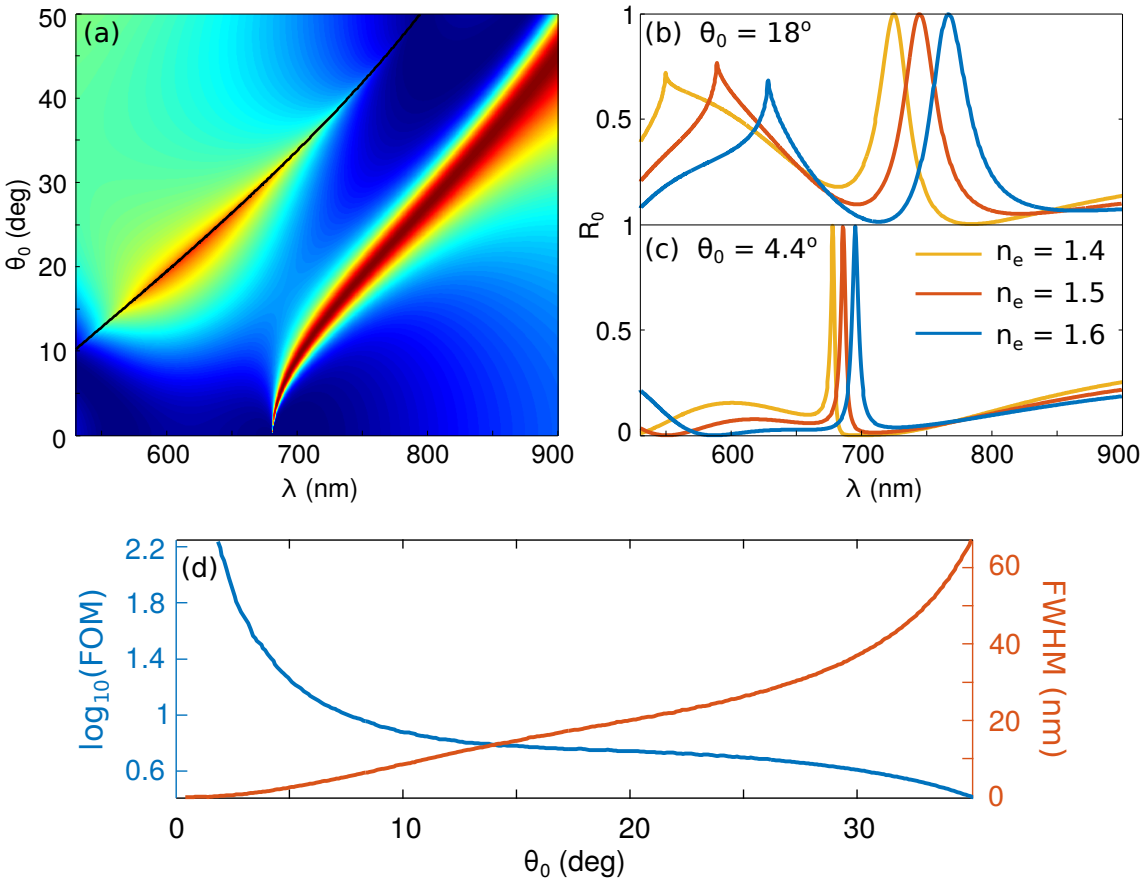

Figure 2.12: (a) Specular reflectance as in Fig. 2.9, but assuming a surrounding medium with $n_e = 1.5$ instead of vacuum, and only for *s* polarization and a narrower spectral/angular regime. (b,c) Specular reflectance spectra at fixed angles of incidence $\theta_0 = 4.4°, 18°$, as in Fig. 2.10a, but for three different values of the refractive index of the surrounding medium: $n_e = 1.4, 1.5, 1.6$. (d) FWHM and figure of merit as a function of the angle of incidence for the Fano resonance in the *s*-polarized reflectance spectra.

Indeed, this also red-shifts and smears out the broad resonance at shorter wavelengths; thus the narrow (transverse MD) surface lattice resonance originating the Fano resonance becomes less asymmetric due to the absence of broad background to interfere with. Incidentally, such reflectance map with a single narrow resonace reveals a clear bound state in the continuum with diverging Q-factor at $\lambda = 680$ nm upon approaching normal incidence, very similar to that described in Ref.[59]

Even though diverging Q-factors are ideal for sensing, we focus on angles of incidence at which the resonance, while being narrow, still yields an observable reflectance signal; recall also that specular reflectance poses experimental difficulties (not so in transmission). This is shown in Fig. 2.12b,c for two angles of incidence $\theta_0 = 4.4°, 18°$, including three different values of the refractive index of the surrounding medium to observe the sensing performance. Although the shift with varying refractive index is not very large, recall that the relevant magnitude in refractive-index sensing is however the figure of merit, f.o.m, defined as the ratio between the sensitivity S_λ and the full-width at half-maximum FWHM, namely:

$$\text{f.o.m} = S_\lambda/\text{FWHM} = (\Delta\lambda/\text{RIU})/\text{FWHM}, \tag{2.40}$$

RIU standing for refractive index unit. For the sake of clarity, we explicitly plot in Fig. 2.12d both the FWHM and the resulting figures of merit for varying angle of incidence. Note that the lattice resonance shift induced by the change of the embedding refractive index is substantially larger than that expected for the resonances of isolated HRI nanoparticles.[65,66] The extremely narrow Fano line shapes thus clearly boost f.o.m.$\sim$ 200, making these simple Si-based configurations suitable candidates for refractive-index sensing.

Chapter 3

Bound state in the continuum in metasurfaces

In the previous chapter we have studied the reflection and transmission properties of metasurfaces consisting of arrays of infinite parallel cylinders. Since there is continuum translation symmetry along one direction (the x axis in our case), the periodicity is manifested only along the other direction of the surface plane (y axis). We can refer to these systems as 1D metasurfaces. For finite particles, in general the periodicity of metasurfaces is manifested in both directions of the structured surface, opening up new degrees of freedom to deal with. In this chapter we will study these 2D metasurfaces, focusing on bound states in the continuum in two different systems: a periodic array of high reflective index disks[59] and an array of detuned dipoles.[64] We have previously derived the formalism for 1D metasurfaces and, using the same approach, it is straightforward to extend it to 2D arrays of finite particles. Although the lattice depolarization dyadic, $\overleftrightarrow{\mathbb{G}}_b$, can be evaluated in real space using convergence techniques,[67] it is convenient to convert the sum to the reciprocal space as it was done before in Eqs. A.5, A.6, A.7 and A.9. The details of the formalism are shown in Appendix B.

In this chapter, the concept of bound state in the continuum will be first introduced. Hereafter, we analyze theoretically and experimentally two different systems that support bound states in de continuum (BICs).

3.1 Introduction to bound states in the continuum

Bound states in the continuum (BICs) are ubiquitous in Physics as a general ondulatory phenomenon.[68–72] In the case of electromagnetic waves, BICs are especially relevant for their ability to confine light.[61,63,72–82] The concept of bound states in the continuum is nearly self-explanatory. A bound state is a resonant mode, identified with a wavevector k_r, that is coupled somehow to a system that has the tendency to remain localized inside. For the electromagnetic field, this means that the mode cannot radiate outside the system. A typical example of a bound state is a guided mode (as it was shown in Section 1.4.2). The field propagates along the cylinder axis but remains

confined in the radial direction. Since the propagation constant of guided modes is larger than in the surrounding media $k_z' > k_2$, due to momentum conservation they cannot couple to the external radiation modes and become localized inside the waveguide. The word "continuum" implies that there is a continuum of radiation modes characterized by some maximum accessible wavevector, say k_c. Therefore, a bound state in the continuum is a mode that lies inside the continuum of radiative modes ($k_z < k_c$) but it remains perfectly confined without radiating, coexisting with extended waves.

A BIC state is a peculiar condition because in general a mode inside the continuum of radiation is inherently coupled to radiative modes. Following the example of the guided mode, we also found solutions with $k_z' < k_2$. However, if we trace the evolution of the dispersion relation from a mode with $k_z' > k_2$ to $k_z' < k_2$, we realize that beyond $k_z' = k_2$ the wavevector irredeemably acquires an imaginary part, $k_z'' \neq 0$, accounting for radiation losses. Thus, the mode becomes leaky and is no longer bound. More details from the evolution from leaky to guided mode can be found in Section 4.1. The general convention is that a mode lying in the continuum of radiation becomes a leaky mode, and BICs are the exception to this rule. We need to find mechanisms to forbid the coupling to external modes.

However, from fundamental arguments, BICs are in general forbidden for single particle systems. Consider a compact optical structure with some material parameters ϵ_1 and μ_1 (which can be position-dependent) in a homogeneous external media characterized by ϵ_2 and μ_2. Since any electromagnetic field in an external medium follows the Helmhotz equation (Eq. 1.27), they can be expanded in spherical harmonics with wavenumber $k = k_2$. A bound state must have no radiating far field, but every term in the expansion carries energy to the far field and hence all terms must be zero., i.e., the electromagnetic field vanishes everywhere outside the optical structure. However, from the continuity of the fields, if the material parameters are neither zero nor infinite at the surface, the electromagnetic field is zero everywhere in the space.

BICs are thus forbidden in compact structures, but not in periodic systems. In finite geometries the electromagnetic field can decay in infinite multipole orders and the coupling to the continuum is always allowed. However, in periodic (infinite) systems the field can only radiate through finite diffraction orders. Thus, for some conditions it is possible to suppress the coupling to all existing channels, leading to a BIC. Nonetheless, it should be mentioned that even with basic geometries it is possible to almost suppress the external coupling. Although there are infinite channels, only few of them are the predominant and wise arrangements can support extremely long-lived states. The first BIC was proposed in a quantum mechanics system by von Neumann and Wigner.[83] They constructed a potential extending to infinity in such a way that an electronic BIC is supported. Since then, different systems that support BICs were proposed and observed in a variety of waves: electromagnetic, acoustic, elastic, water... leading to an improved understanding and to more knowledge about the mechanisms that confine waves.

In periodic system the number of radiation channels is small, as small as only one for non-diffractive arrays. Tuning the parameters of the system may suffice to completely suppress radiation into the (few) allowed channels. Generally, if radiation is characterized by N degrees of freedom, at least N parameters need to be tuned to achieve a BIC. Through the parameter tuning,

the local electromagnetic density of states is reduced to zero at the BIC conditions, but these parameters can be also perturbed to achieve arbitrarily small density of states. The perturbation from the BIC condition led to configurations with extremely high enhancement of the electromagnetic field and arbitrarily high Q-factors that can be tailored by the parameters of the system. For optical metasurfaces, they are characterized by a vanishing resonance in the reflectance spectra. The tunable properties that come from BICs have direct application in phenomena such as lasers, sensors, filters, frequency conversion and strong coupling platform, among others. In fact, the refractive index sensor investigated in Section 2.3 was based on a BIC state, in which the coupling is controled by the angle of incidence. We will discuss this and other systems later on.

In many cases the suppression of radiative channels can be attributed to two different mechanisms: a different symmetry between the available channels and the bound state (symmetry protected) and an interference effect in which two or more radiating components cancel each other (Friedrich-Wintgen[84,85]). Despite the different names, in both cases the BIC state can be associated to symmetries of the lattice.

3.1.1 Symmetry protected BIC

One mechanism for confined states is through a symmetry mismatch between the radiative states and the localized mode. A typical example of such a mode is the collective oscillation in phase of dipoles perpendicular to the surface plane. From Huygens' principle the angle at which the metasurface radiates is given by the phase difference between adjacent particles. When all particles radiate in phase the secondary wavelets form plane waves propagating perpendicular to the surface, i.e., at the direction $\theta = 0$ (see Fig. 3.1a,b). From a Brewster-like effect dipoles cannot emit energy to the far field along their own axis: thus perpendicular dipoles cannot radiate into the only allowed mode as represented in Fig. 3.1c. Remark that this argument is only valid for non-diffractive arrays (one channel, one degree of freedom).

This kind of BICs is the one observed in the previous chapter. At normal incidence, it is not possible to excite the BIC from the far field and in the reflectance spectra there is no vestige of the bound state. Once the angle of incidence is slightly changed, the coupling to perpendicular dipoles is allowed and a narrow resonance arises. The FWHM (inversely proportional to the Q-factor) as a function of the tunning parameter was shown in Fig. 2.12d, revealing the diverging character of the Q-factor. Close to normal incidence, the field is enhanced by several orders of magnitude. Nonetheless, for practical applications it is sometimes better to induce such a big enhancement at normal incidence. We observe that at normal incidence the system presents mirror symmetry, which is broken when the angle of incidence is different from zero. Therefore, the BIC is preserved by this symmetry and, in order to allow the coupling at normal incidence, we must break directly the mirror symmetry in the unit cell.

The polarizability of particles characterizes their symmetries and, in order to break the mirror symmetry of the unit cell, we can actually break the symmetry of the polarizability tensor. An easy way to do so, both theoretically and experimentally, is through disks, where the polarizability along the disk axis is in general different from that in the transversal plane. Depending on the

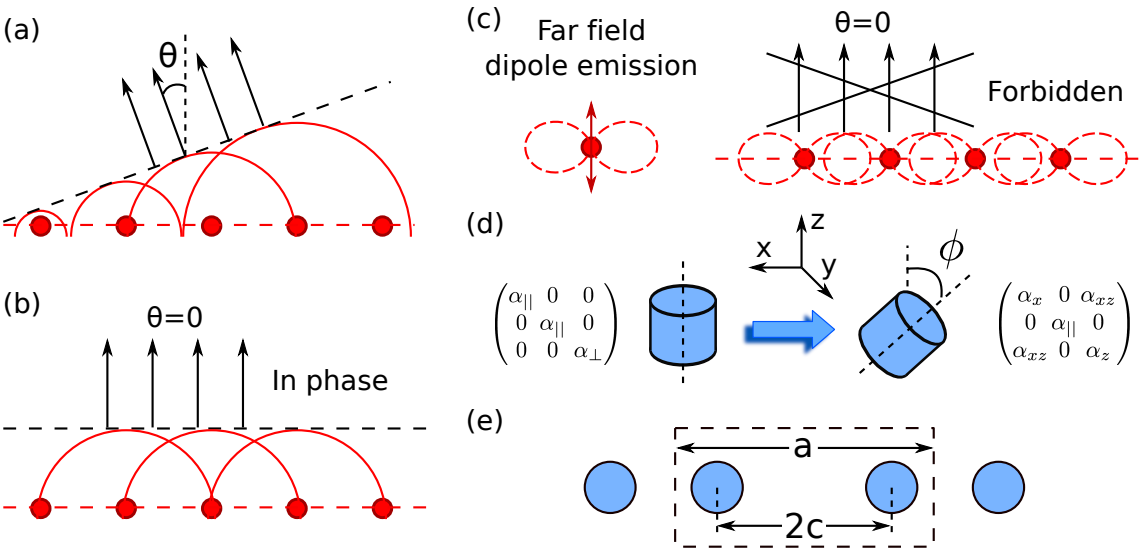

Figure 3.1: (a,b) Schematic representation of Huygens' principle. When all the sources are in phases the emitted wave is perpendicular to the surface. (c) Radiation intensity pattern of a perpendicular dipole. Since there is no emission along the dipolar axis, a collection of perpendicular dipoles oscillating in phase cannot radiate (Brewster-like effect). (d) Polarizability of a disk as a function of the titled angle ϕ. (e) Representation of an array of two parallel cylinders in the unit cell.

relative orientation of the disk with respect to the lattice (the lattice defines our coordinate system), the polarizability tensor can be diagonal or non-diagonal depending on the angle ϕ as shown in Fig. 3.1d. Note that the polarizability is always symmetric, even when it is non-diagonal, but the particle does not preserve the mirror symmetry in the plane defined by the rotation axis, $\alpha_e(\phi) \neq \alpha_e(-\phi)$. Following the sketch in Fig. 3.1d, an electric field, E_x, in the rotation plane will induce an electric field in the perpendicular direction, breaking down the BIC state. Note that the mirror symmetry is preserved for the other polarization. Now, the tilt angle ϕ can be considered the tuning parameter, so that the BIC condition is given by $\phi = 0$ and the Q-parameter can be tailored by modifying the tilt angle. In the next section we will further investigate this system.

The symmetry can be also controlled externally, very useful for practical devices. For example, the magneto-optical effect presents in some materials can be used to actively modulate the field enhancements by controlling the applied magnetic field. The application of a magnetic field in the plane of the array breaks the mirror symmetry, even for isotropic particles. From a physical perspective the effect is the same as before: an electric field in the plane induces an electric field out of plane, although in this case the associated polarizability is asymmetric. Unfortunately, materials that present magneto-optical effects are in general lossy metals and the absorption detriments their performance. In this regard, iron garnets are promising candidates for magneto-optical applications.

Until now we have considered only the electric polarizability, but the interplay between electric and magnetic dipoles can also lead to interesting effects because, although less obvious, the lattice depolarization dyadic also plays a role in the symmetries of the unit cell. Considering the 1D

metasurfaces studied before, the term G_{bzx} couples the electric (magnetic) field in the x-axis with the magnetic (electric) field in the z-axis, but at normal incidence adjacent cylinders cancel out their effects and $G_{bzx} = 0$. However, we can break the symmetry by considering a complex unit cell, with two particles per cell as in Fig.3.1e. If the separation between adjacent cylinders is different ($c \neq a/2$), the in-plane fields induce out-of-plane fields and coupling to the BIC is allowed. The different separation between adjacent cylinders breaks mirror symmetry and $a - 2c$ becomes the tuning parameter that controls the Q-factor and the field enhancement.

3.1.2 Friedrich-Wintgen BIC

Another mechanism that allows to confine waves in the continuum is the accidental destructive interference between radiative states. it is necessary that at least two different modes be coupled. The coupling between modes is given by the non-diagonal terms of the polarizability and the lattice depolarization dyadic. We will consider only diagonal polarizabilities; thus let's focus our attention on $\overleftrightarrow{\mathbb{G}}_b$, which also determines the symmetries of the unit cell. In 1D metasurfaces and incidence perpendicular to the translational symmetry axis (namely the x axis), G_{bzx} is the only non-diagonal term connecting electric dipoles to magnetic ones. This term allows the existence of a BIC that comes from to the interference between electric (magnetic) in plane dipoles and a magnetic (electric) out of plane dipoles. However, in this case the BIC is given at certain angle of incidence, i.e., there must be a phase difference between the dipole oscillation of adjacent particles. The destructive interference is similar to the Brewster-like effect shown in Fig. 3.1c, although for two (or more) dipole-modes the shape of the radiation pattern depends on the frequency and the phenomenology becomes more complex. At the moment, this kind of BIC for 1D metasurfaces has been observed only for p waves with isotropic particles and for angles close to the diffraction line,[78] but it can be observed for s waves using anisotropic particles.

In the formalism there is only one particle per unit cell, but different arrangements can lead into more complex interferences. For example, if the lattice is in the xy plane and the particles of the unit cells are placed at different positions with respect to the z axis, new interferences arise. Nonetheless, strictly speaking the interacting modes come from different particles, and these BICs are sometime called Fabry-Pérot BICs; thus it is not necessary that both modes be supported by the same particle. Moreover, the nature of the modes can be also the same, as it is discussed in the next example.

Consider two identical cylinders per unit cell equally separated that can be described only by their electric polarizability, illuminated by a normal incidence plane wave with the electric field along the x axis. We can say that there are two particles per unit cell, each one representing an array of particles. In the lattice depolarization dyadic additional terms appear that connect the dipoles in the x axis of both particles. The out-of-phase oscillation of these dipoles leads to a BIC state because both arrays of particles radiate to the far field a wave with the same amplitude but out-of-phase. Now, if the particles of the unit cell become slightly different, the 2-fold rotational symmetry (C_2) is broken, the BIC state desappears and the coupling to a narrow resonance is allowed at normal incidence. The mirror symmetry is also broken, but we will see clearly that for

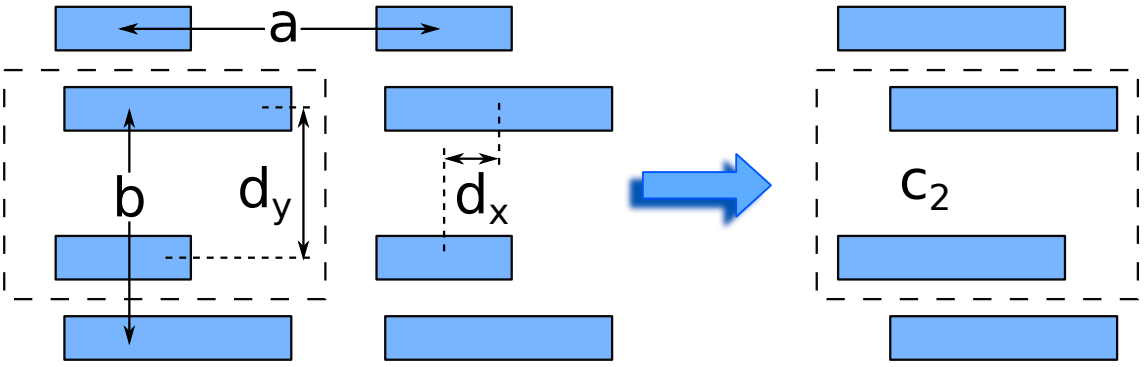

Figure 3.2: Representation of an array of detuned dipoles. When both rods are equal the unit cell presents C_2 symmetry independently of the parameters d_x, d_y, a and b.

2D metasurfaces these BICs are associated to the C_2 symmetry.

We can come back to the identical cylinder lattice shown in Fig .3.1e. Since the symmetries are preserved independently of the value of c, this BIC is robust against the distance between adjacent cylinders. However, when the magnetic response is included, the BIC state is broken because, due to the different parity of electric and magnetic dipoles, the unit cell is not mirror symmetric. Note that the mechanism that allows the coupling to radiative states is the same as that in the last example of Section 3.1.1. First, we started from a symmetry protected BIC of perpendicular dipoles oscillating in phase and by changing the inter-distance we allowed for coupling to the in-plane field. In this section the opposite was done: we have analyzed a Fabry-Pérot BIC of in-plane dipoles oscillating out of phase and coupling was allowed to the out-of-plane field. Nonetheless, it is interesting to note that in both cases the inter-distance controls coupling.

Finally, we analyze the same situation but for 2D metasurfaces. The interpretation is the same and clarifies the phenomenology. In addition, this is the case that will be analyzed in the last section of the chapter. Let's consider two different rods in a rectangular array as in Fig.3.2a, characterized by their electric polarizability. Same as for 1D metasurfaces, $\overleftrightarrow{\mathbb{G}}_b$ connects the dipoles in the x-axis of both particles. For identical rods, $b = 2a$, $d_x = 0$ and $d_y = b/2$, the array becomes square and symmetry imposes that there is a BIC given by out-of-phase oscillation of adjacent in-plane dipoles. As will be studied in detail, the BIC is robust against the relative separation, d_x and d_y, between rods and for arbitrary lattice parameters, a and b. Consequently, there is a BIC in the arrangement shown in Fig. 3.2b, but the system is not mirror symmetric. Thus these kind of BICs are associated to the C_2 symmetry. Finally, when the magnetic response becomes relevant, the mirror symmetry is broken and the BIC evolves into a leaky mode.

In the next two sections we investigate in detail two systems that support different kinds of BICs. The results of this chapter are based on the articles published by our group,[59,64] in collaboration with our colleagues of the Institut Fresnel (Marseille), the Universidad de Cantabria and the Technological University of Eindhoven. First, a symmetry protected BIC is studied in a disk array of high refractive-index particles.[59] Later, the properties of a Friedrich-Wintgen BIC is analyzed in a detuned dipole array of metallic rods.[64]

3.2 BIC in all-dielectric single magnetic resonance meta-atoms

Here we propose to exploit a Brewster-like mechanism to ensure a tunable, robust electromagnetic BIC.[59] A planar metasurface is used to impose a single outgoing channel through periodicity. In this context, the crucial idea is to combine single-channel metasurfaces (two channels in total, one for reflection and other for transmission) with a Brewster-like effect coming from a single dipole resonance, enforced by using meta-atoms that hold a single non-degenerate dipolar resonance, in turn angularly-locked through e.g. meta-atom orientation ϕ, as shown in Fig. 3.1d. Such resonance generates a lattice mode that is leaky throughout the θ-space, but for the angle at which the wavevector and meta-atom dipole moment are parallel the radiations channels are reduced. At $\theta = \phi$ the mode can only couple to one channel, that it is totally suppressed at $\theta = \phi = 0$. To this end, we propose high-refractive-index (HRI) subwavelength structures[21,23,86–90] to play the role of single-resonant meta-atoms. Such structures exhibit not only electric-dipole resonances, but also strong magnetic-dipole resonances that do not overlap with other modes. In addition, our colleagues at the Institut Fresnel have experimentally studied the system at the the microwave regime.

3.2.1 Brewster BIC concept

First, we discuss through a simple model the underlying physics. Let us consider a planar array of resonant electric or magnetic dipoles with a period and in a frequency regime such that no diffraction orders are allowed (Fig. 3.3). Such dipoles are characterized by a (electric or magnetic) polarizibility tensor $\overleftrightarrow{\alpha}_{\mathbf{0}}$ that can be described as a scalar, α_0, essentially oriented along the dipole moment (ϕ being the dipole moment locked orientation) and exhibits a resonance at a given frequency ω_0. The expression of the specular reflectivity R_0 for a given angle of incidence θ can be written as:

$$R\left(\omega,\theta\right) \propto |\left(\cos^2\phi\sin^2\theta - \cos^2\theta\sin^2\phi\right)\alpha|, \tag{3.1}$$

with α being the dressed polarizibility given by:

$$\alpha \propto \left(\frac{1}{\alpha_0} - G\right)^{-1}, \tag{3.2}$$

where G_b is the corresponding lattice depolarization Green function component projected along the dipole moment angle. Close to resonance the bare polarizibility can be written as $\alpha_0 \sim g(\phi)\omega_i/\left(\omega - \omega_0 + i\delta\omega\right)$, and it readily follows that the reflectivity, Eq. 3.1, is maximum at resonance for all angles except for those at which the incident angle coincides with the dipole orientation:

$$R\left(\omega = \omega_0, \theta = \pm\phi\right) \sim 0, \quad R\left(\omega = \omega_0, \theta \neq \pm\phi\right) \sim 1. \tag{3.3}$$

This indicates that a Brewster-like BIC appears at $(\omega_0, \pm\phi)$ due to the symmetry-protecting mechanisms: angular locking to a single scattering channel by the array periodicity, and forbidden scattering at a given angle determined by the single dipole resonance orientation. Actually, when

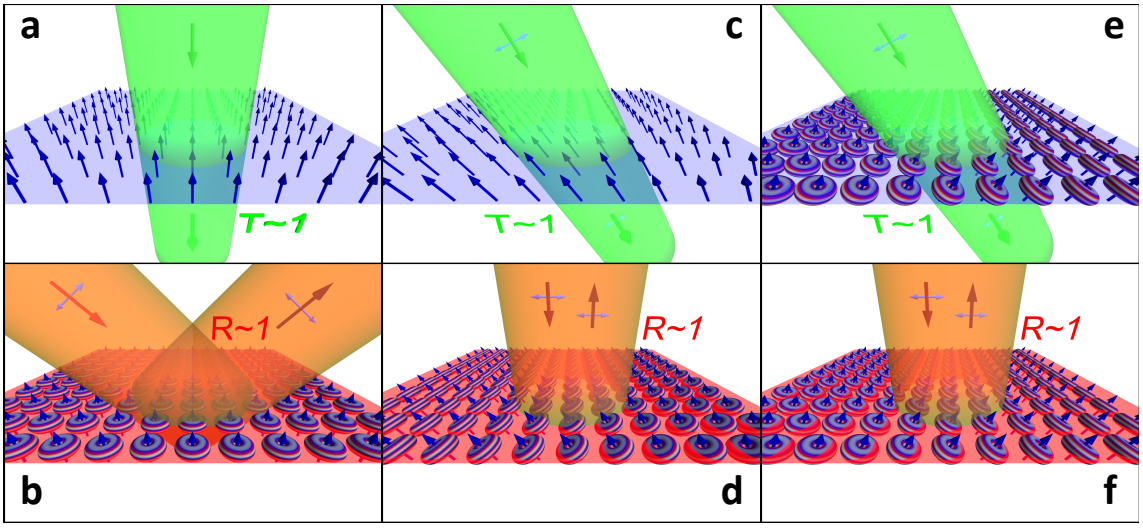

Figure 3.3: Brewster quasi-BIC concept schematic: Reflectance and transmittance through a metasurface of electric or magnetic dipolar scatterers at resonance; note that polarization vectors (blue arrows) are depicted (where needed) that refer to electric/magnetic fields depending on the electric/magnetic character of the dipoles. Dipolar emission patterns are included only when resonance excitation takes place. (a,b) Perpendicular dipole array showing a Brewster BIC at normal incidence ((a), $T \sim 1$), while exciting a resonant (leaky mode) at oblique incidence ((b), $R \sim 1$). (c,f), Oblique dipole array showing a quasi-Brewster BIC at oblique incidence with the same angle (plus or minus) such that: (c) it coincides with the direction of the dipole moments, so that coupling into dipole resonant modes is forbidden ($T \sim 1$); (e) dipole resonances are indeed excited, but reflection is (Brewster-effect) forbidden ($T \sim 1$ due to energy conservation, although dipole emission in transmission is not forbidden). (d,f) Exciting a resonant (leaky mode) at any other incidence, e.g. at normal incidence ($R \sim 1$).

$\phi = 0$ (perpendicular dipole array, see Fig. 3.3a,b), this is strictly verified and a proper BIC with diverging Q factor emerges ($T \sim 1$). However, when $\phi \neq 0$ (oblique dipole array, see Fig. 3.3c-f), there is a slight difference depending on the sign of the angle of incidence, $\theta = \pm\phi$, so that only scattering into reflection/transmission, respectively, is forbidden; reflection is identical due to reciprocity, but transmissions reveals subtle differences. When the incident wavevector coincides with resonant dipole orientation ($\theta = -\phi$, Fig. 3.3c), coupling is forbidden and all energy is specularly transmitted through ($R \sim 0$, $T \sim 1$). Conversely, if the specular reflection direction coincides with the dipole orientation ($\theta = \phi$, Fig. 3.3e), the incident wave couples into dipole resonances: however, dipole emission in reflection is forbidden ($R \sim 0$), but not in transmission, which, in spite of that, leads to total transmission ($T \sim 1$, Fig. 3.3d) thanks to incident wave cancelation. At any other angle of incidence ($\theta \neq \pm\phi$), resonant excitation and emission is allowed and the wave is totally reflected ($R \sim 1$, Fig. 3.3b,d,f). To summarize, a quasi-BIC with slightly smaller Q factors appears at oblique incidence. We will show experimentally and theoretically below that this is indeed the case.

3.2.2 Single magnetic-dipole resonance HRI disks

First of all, in order to fabricate a suitable metasurface, we search for a meta-atom that exhibits as a lowest-order Mie-like resonance a non-degenerate dipole resonance pointing only at a fixed direction. To this end, we use nearly lossless HRI disks, i.e. a cylindrical dielectric resonator with dielectric constant of $\epsilon = 78 + i0.05$ (in the GHz spectral regime of interest), and radius $R = 3$ mm and length $L = 4$ mm. Our numerical results for the scattering cross sections (Fig. 3.4) reveal that the lowest-order resonances are indeed magnetic-dipole (MD) resonances at 5.4 and 6.1 GHz, and do not overlap at all with the electric-dipole resonance, which actually lies at higher frequencies (~ 8 GHz, not shown in Fig. 3.4). Moreover, there are indeed two split MD resonances which, as shown in the scattering patterns depicted also in Fig. 3.4, result from: the nondegenerate one at 5.4 GHz with a dipole moment pointing always along the cylinder axis, whereas the other MD resonance at 6.1 GHz can actually point along any direction within the plane perpendicular to the cylinder axis (thus called doubly degenerate). Incidentally, the numerical results are also exploited to define the corresponding magnetic polarizibilities that will be used below in the coupled-electric-magnetic dipole formulations.

3.2.3 HRI Disk metasurface reflectance: Brewster BICs

Next, we investigate the collective behavior of such MD-resonant disks in a metasurface. To this end, a finite square array of 11x11 disks ($R = 3$ mm and $L = 4$ mm) with lattice constant $a = 12$ mm (as illustrated in the inset in Fig. 3.5) has been fabricated. Spectral and angular dependence of the reflectance intensity and phase are shown in Fig. 3.5a,b for TE (or S) polarization. The spectral and angular ranges ensure that there is no other diffraction order apart from the (0th-order) specular one. We show in Fig. 3.5c,d the results of a theoretical calculation, also for an infinite metasurface, based on the coupled electric/magnetic dipole (CEMD) theory developed in Section 2.1. Disks are indeed subwavelength, and can in principle be replaced by one perpendicular MD and two (degenerate) parallel MDs. An excellent agreement with the experimental results is observed, that also indicates that the finite metasurface contains enough unit cells as to reproduce the reflectance of the infinitely extended system (except for the diverging theoretical Q-factor), so a convergence study is not needed. Nevertheless, a finite CEMD (fCEMD) calculation for a finite (11x11 dipole) metasurface is identical to that in the experiment (not shown) has been carried out as well to show that the results are directly comparable to those for finite arrays.

Apart from the large reflectance at grazing incidence through most of the spectral range, two spectral features weakly dependent on the angle of incidence become evident: two total reflection bands at 5.6 GHz and 6.1 GHz. The latter one is broader at normal incidence, becoming slightly narrower at grazing angles. Conversely, the lowest-energy band is much broader at grazing incidence, narrows for decreasing angle of incidence, indeed disappearing at normal incidence. Both bands stem from the single-disk MD resonances, slightly blue-shifted due to lattice coupling (as discussed below): perpendicular/out-of-plane (respectively, parallel/in-plane) for the one at 5.6 GHz (respectively, at 6.1 GHz), referred to as $\mathrm{MD}_{\perp}$ (respectively, $\mathrm{MD}_{||}$). In addition, phase maps in Fig. 3.5b,d show an abrupt phase change along the resonant bands, with a more complex be-

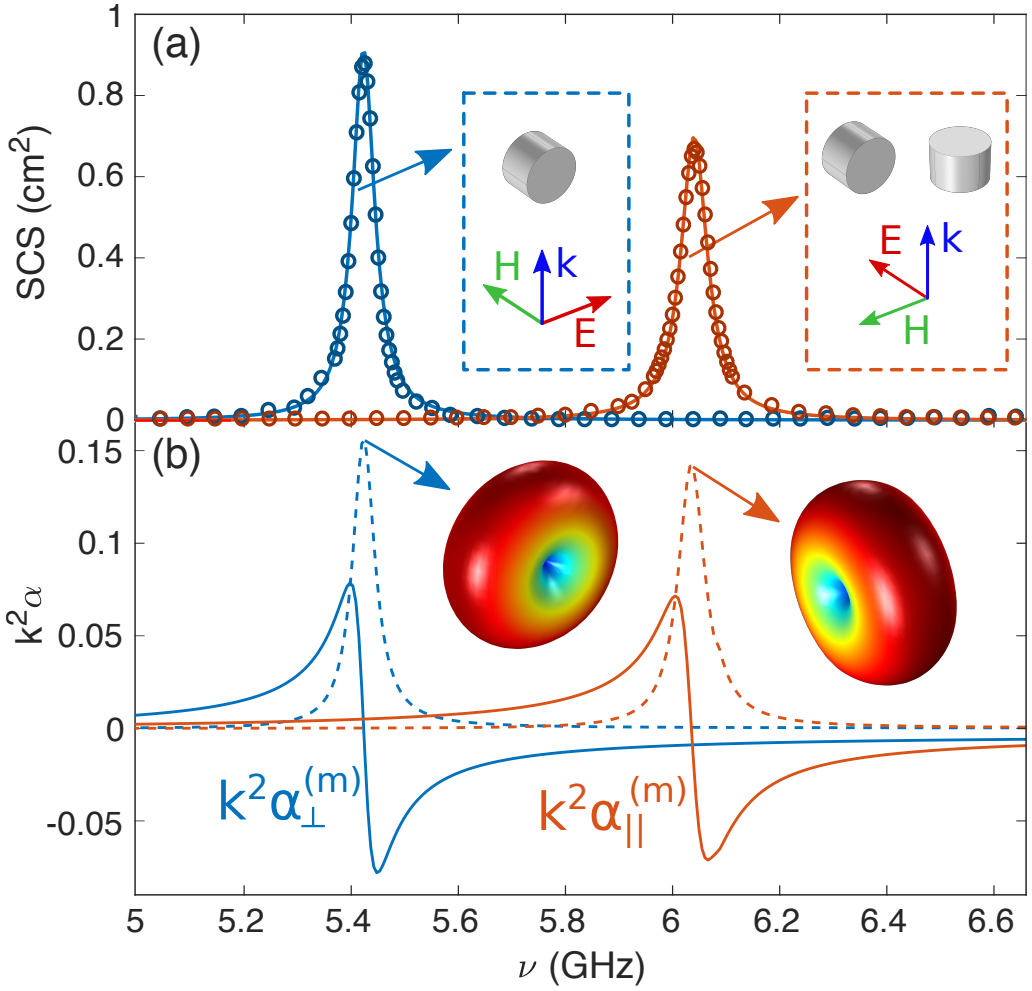

Figure 3.4: Experimental and numerical SCS of a single HRI disk reveals a non-degenerate MD resonance. (a) Scattering cross sections of a disk ($R = 3$ mm and $L = 4$ mm) with dielectric constant of $\epsilon = 78 + i0.05$ for different incident wave polarization and disk orientations: numerical results in cm^2 (solid curves) and experimental measurements in a.u. (symbols) are shown. Insets show the doughnut shape of the dipolar radiation pattern with respect to disk orientation. (b) Real and imaginary parts of the MD polarizibilities extracted from the numerical calculations that will be used below in the coupled electric/magnetic dipole formulations.

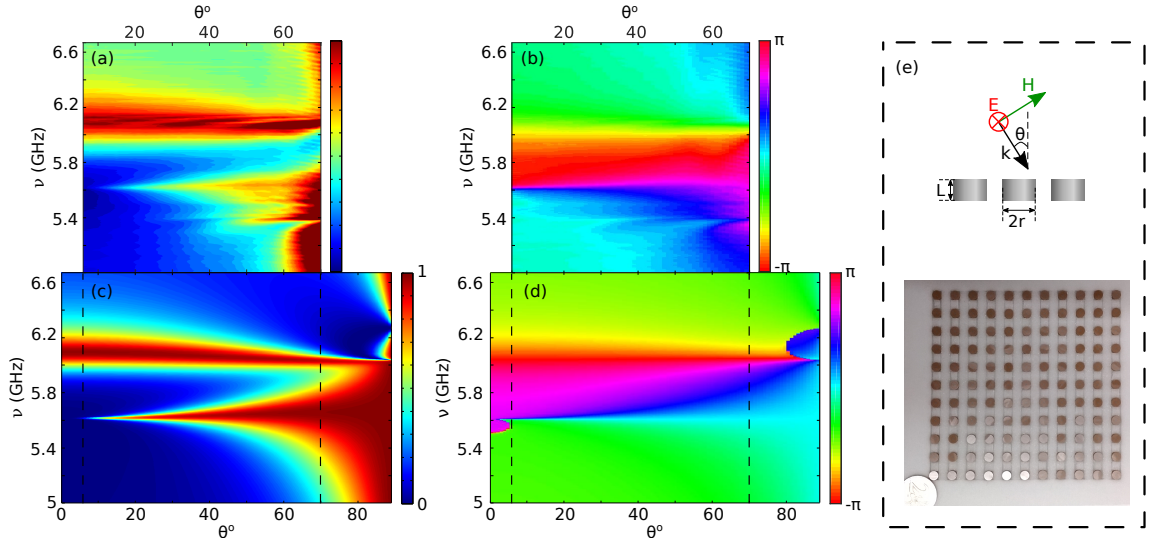

Figure 3.5: HRI disk metasurface reflectance showing Brewster BIC. Contour maps of the s-polarized reflectance $R(\nu, \theta)$ (a,b) intensity and (c,d) phase from a square array ($a = 12$mm) of dielectric resonator disks (as in Fig. 3.4) as a function of angle of incidence θ and frequency (GHz). (a,b), Experimental measurements of the specular reflection (a intensity and b phase) for a finite array of 11x11 disks. (c,d) CEMD theoretical calculations of the reflectance (c intensity and d phase) for an infinite array. (e) Schematic depicting the geometry of the plane of incidence and picture of the sample.

havior around normal incidence for the $MD_{\perp}$ band, and around grazing incidence for the $MD_{||}$ band.

Let us thus examine the $MD_{\perp}$ band around normal incidence, which exhibits clear features of a BIC: This is done in Fig. 3.6. First, we zoom in such region in Fig. 3.6a,b and explicitly show in Fig. 3.6d the experimental and theoretical Q-factors ($Q = \nu/\Delta\nu$): It is evident from them that the Q-factor increases exponentially. Indeed, it should be emphasized that the experimentally measured Q-factor is extremely large $Q \geq 300$, ideally tending to infinite as shown in the numerical calculations in the absence of losses within numerical accuracy ($Q \sim 2000$ if losses are included). To give even more evidence, the topological nature of such $MD_{\perp}$ BIC is explored by showing its associated vortex state in k-space.[78,91] Phase maps are shown in Fig. 3.6c calculated from the resulting numerical results for the reflectance electric field amplitudes as in:[91] clearly, a vortex-like feature is reproduced with an associated topological charge of 1.

Therefore, a clear BIC associated to the $MD_{\perp}$ band arises at normal incidence that is symmetry-protected through a Brewster-like effect: such perpendicular $MD_{\perp}$ resonance cannot emit along the MD direction, which is however the only (specular) direction of reflection allowed by the metasurface lattice geometry. On the other hand, there are also some features that suggest that the $MD_{||}$ band approaches a "virtual" BIC at grazing incidence (see Fig. 3.5), supported by a similar argument (even though strictly speaking there should not be such BIC right at the light line, since it would become a guided mode). In both cases, if the symmetry-protection argument holds, BICs would appear at non-zero/non-grazing angles of incidence if both MDs were rotated.

Accordingly, our colleagues at the Institut Fresnel have fabricated a metasurface with 11x11

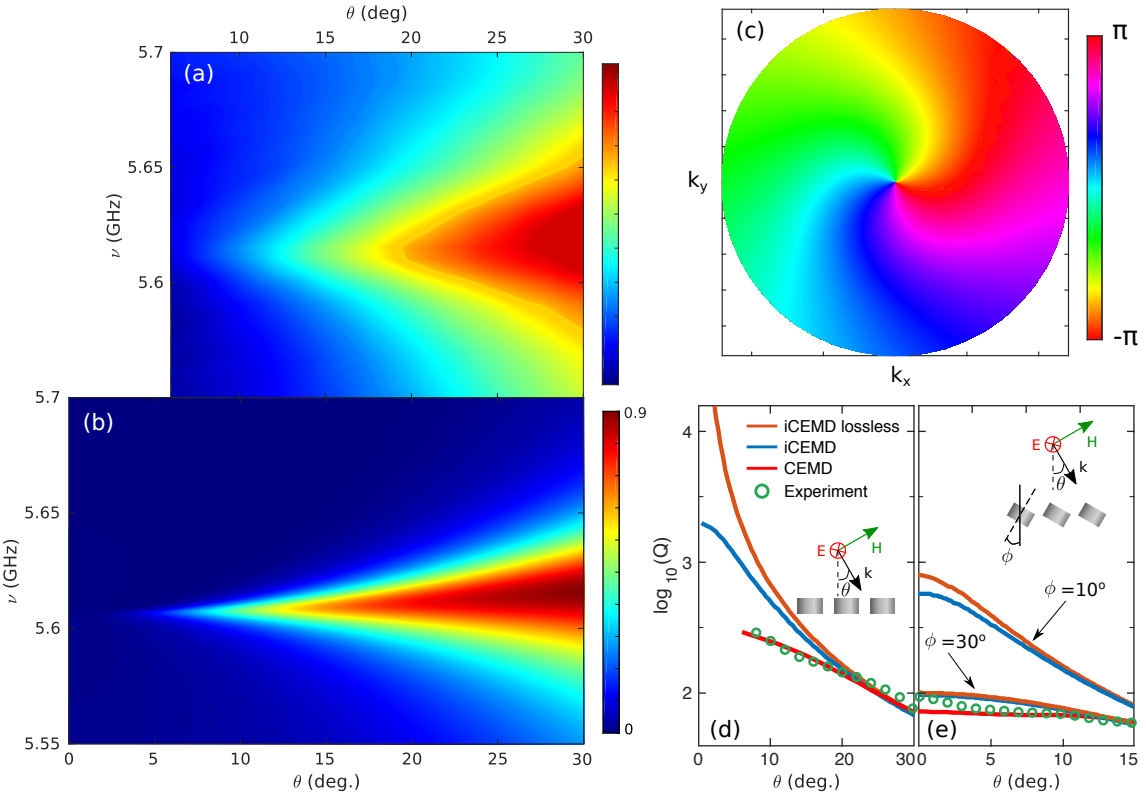

Figure 3.6: Symmetry-protected Brewster BIC characterization. (a,b) Contour maps of the s-polarized reflectance $R(\nu, \theta)$ intensity as in Fig. 3.5a,c from a square array (lattice period = 12 mm) of dielectric resonator disks (as in Fig. 3.4), zooming in the BIC region around $\nu = 5.6$ GHz and $\theta = 0°$: (a) Experimental measurements for a finite 11x11 disk array; (b) CEMD theoretical calculations for an infinite metasurface. (c) Phase map of the BIC vortex. (d) Q factors at resonance ($\nu = 5.6$ GHz) obtained from the theoretical (reflectivity) and experimental (extinction cross section) spectral full width at half maximum in (a) and (b), as a function of the angle of incidence θ. (e) Same as in (d), but for arrays of tilted disks with tilt angle $\phi = 10°$ (only theoretical CEMD) and $\phi = 30°$ (see Fig. 5). $\theta = 0°$.

disks, tilted $\phi = 30^\circ$ with respect to the plane normal, as shown in the inset in Fig. 3.7; experimental measurements are plotted in Fig. 3.7a-d. In this case, since the number of disks is even smaller than in the non-tilted disk metasurface due to sample fabrication limitations, comparisons with theoretical calculations for both finite (fCEMD, with apparent angle compensation as in the measurements) and infinite (CEMD) metasurfaces are included in Fig. 3.7e-l. Note that the agreement between measurements and finite fCEMD calculations is remarkable in all cases. Moreover, except for slightly broader resonances and minor discrepancies near grazing angles where apparent angle compensation actually enlarges noice they resemble in turn the infinite CEMD calculations. This confirms the fact that our finite samples suffice to account for the underlying physics and resulting phenomenology expected for an infinite metasurface.

In Figs. 3.7a,e,i, both measurements and theoretical calculations of reflectance intensity are shown, revealing that the $\mathrm{MD}_\perp$ (respectively, $\mathrm{MD}_{||}$) resonance bands vanish approximately at $\theta = \pm 30^\circ$ (respectively, $\theta = \pm 60^\circ$), which are the symmetry-protected (lattice-imposed) specular reflection angles at which the corresponding single-disk MDs cannot emit in reflection. Phase maps in Figs. 3.7b,f,j show a sign change at fixed frequencies, namely, those of both MD resonances. Note that Brewster bands[37,92,93] (total transmission) appear that cross the MD resonance bands at the corresponding BICs; phase jumps clearly identify the Brewster band boundaries.

Interestingly, it should be noted that the Brewster-induced suppression of reflectance does not strictly hold for transmittance, as commented above with regard to Figs. 3.3c,d. To clarify this issue, we have included in Figs. 3.7c,d the metasurface contribution into specular transmission, calculated/measured by removing the incident field amplitude from that of the total transmitted field. Brewster-induced suppression of reflectance at the $\mathrm{MD}_\perp$ resonance ($\nu \sim 5.6$ GHz) would occur strictly speaking for a symmetric angle of incidence, $\theta = 30^\circ$ (Fig. 3.3e); nonetheless, $\mathrm{MD}_\perp$ dipole excitation is allowed, so that such dipoles may contribute into specular transmission, as evidenced in Figs. 3.7c,g,k at $\theta = 30^\circ$ and $\nu \sim 5.6$ GHz, with phase sign changes in Figs. 3.7d,h,l. Energy conservation is preserved then due to the fact that dipole emission in transmission partially cancels the incident wave directly transmitted (similarly to the optical theorem argument). By contrast, incident wave coupling into the $\mathrm{MD}_\perp$ resonance is totally forbidden at $\theta = -30^\circ$ (Fig. 3.3c); there is no resonant dipole emission whatsoever (neither in reflection nor in transmission) and total transmission occurs since the incident wave is transmitted unaltered (evidenced by negligible metasurface contribution to transmission at negative $\theta = -30^\circ$ and $\nu \sim 5.6$ GHz in Figs. 3.7c,g,k, with constant phases in Figs. 3.7d,h,l). Nonetheless, reciprocity enforces that both cases yield exactly the same reflectance, as evidenced above through a symmetric reflectance for $\theta = -\theta$ in Fig. 3.7a,e,i. Likewise, the same argument holds for the $\mathrm{MD}_{||}$ resonance band at $\nu \sim 6.1$ GHz for angles of incidence $\theta = \pm 60^\circ$, with an obvious sign change in the angle of incidence due to the fact that disk tilting by $\phi = 30^\circ$ leads to a $\mathrm{MD}_{||}$ orientation change of $\phi = -60^\circ$.

Therefore, symmetry-protected MD-induced Brewster BICs emerge in HRI disk metasurfaces at different angles of incidence, which can be selectively tuned by tilting the disk with respect to the metasurface plane. We term this scenario as Brewster quasi-BICs: basically, such BICs cannot couple into outgoing channels but Brewster argument by itself does not suffice, and resulting modes show non-diverging Q-factors slightly smaller than those obtained at normal incidence (see

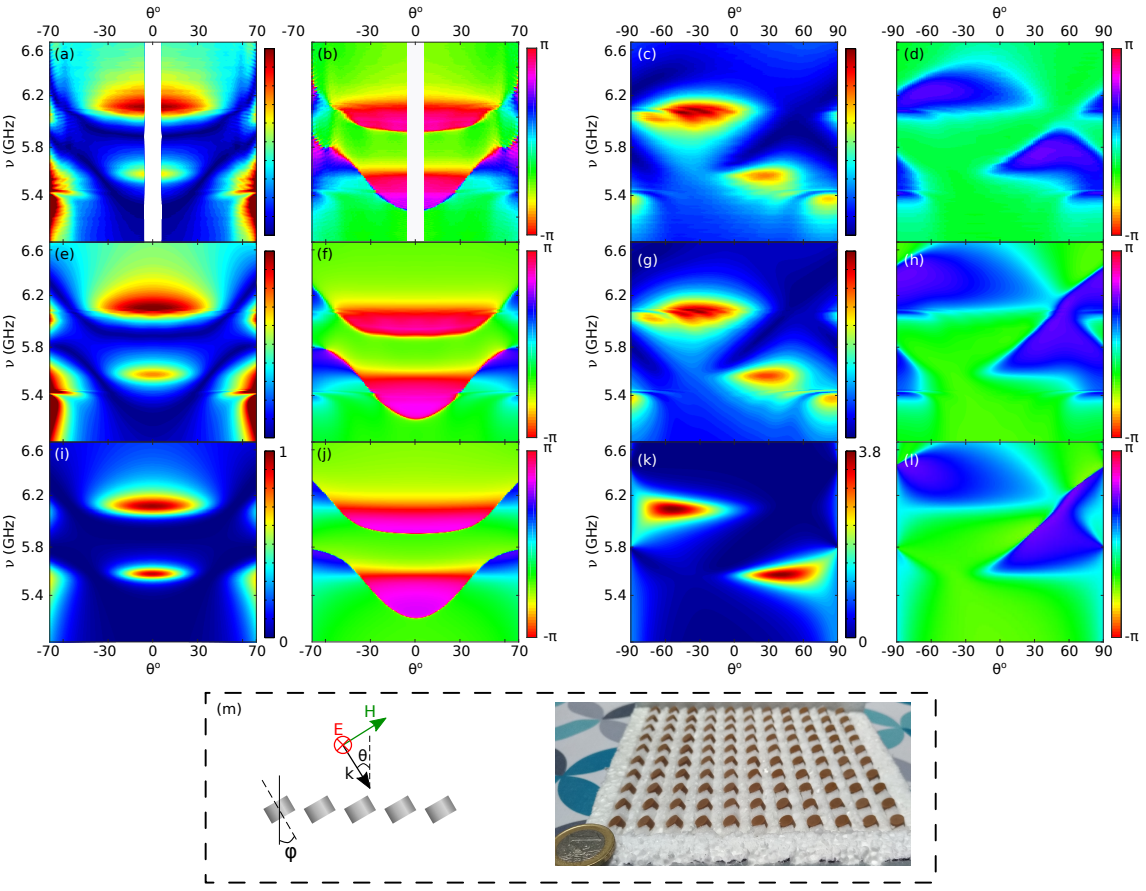

Figure 3.7: Angularly-tuned Brewster quasi-BICs in HRI tilted-disk metasurface. Contour maps of the s-polarized reflectance $R(\nu, \theta)$ intensity and phase from a square array (lattice period=12 mm) of dielectric resonator disks (as in Fig. 3.4), tilted $\phi = 30^\circ$ with respect to the plane normal, as a function of angle of incidence θ and frequency (GHz). (a-d) Experimental measurements of intensity and phase for a finite 11x11 array of disks: (a,b) reflection (excluding the non-accessible backscattering region); (c,d) zero-order contribution into transmission, obtained by (complex) substrating of the field trnasmitted without the disk array from the total transmitted field. (e-h) same as in (a-d), but for fCEMD theoretical calculations. (i-l) same as in (a-d), but for the CEMD theoretical calculations for an infinite array. (m) Schematic depicting the geometry of the plane of incidence and picture of the sample.

Fig. 3.6c). Despite being non-diverging, the possibility of exploiting such quasi-BICs to enhance yet strong resonant modes with a tunable single (or none) outgoing channel makes them especially attractive for a variety of enhanced optical processes, as is the case of a recent demonstration of a (different) quasi-BIC-based directional lasing.[79]

To shed light on the physics underlying such quasi-BICs, we now make use of our CEMD theory for infinite arrays mentioned above.[37] Contour maps of the reflectance (intensity and phase) as a function of frequency and angle of incidence are shown in Fig. 3.8, including both MD contributions separately, for 3 angles of incidence (columns): $\phi = 0°, 10°, 30°$. Contour maps of the transmittance (intensity and phase, third and fourth rows) are also included; absorption losses (not shown) are nearly negligible except for a very narrow band close to the MD resonances near BICs.

Upon inspecting the MD contributions at $\phi = 0°, 10°, 30°$, it becomes evident that symmetry-protected Brewster BICs appear for the $MD_{\perp}$ (respectively, $MD_{||}$) resonances at $\theta = 0°, 10°, 30°$ (respectively, at $\theta = 90°, 80°, 60°$). A broadening near the Brewster BIC condition is observed for both $MD_{\perp}$ and $MD_{||}$ resonances as the tilt angle increases, becoming as discussed above quasi-BICs. Phase maps (note that they differ from vortex maps) actually reveal Brewster BICs through a cross pattern with two abrupt phase jumps (sign change) delimited by: a horizontal line at resonance (already mentioned) and a vertical line at fixed Brewster angle. Our results also account for the lattice-induced shift of the single-disk MD resonances to 5.6 GHz and 6.1 GHz.

When all contributions are accounted for, the tails of each MD have a slight impact on the positions of the other MD-BIC, slightly shifting them to a different angle, as was indeed observed in the experimental and theoretical results shown above (Figs. 3.5 and 3.7). In addition, it is evident from the phase maps shown also in Figs. 3.5 and 3.7 that the vertical Brewster-induced phase jump bends as a result of the interaction between both MD resonances, as expected, whereas the horizontal jumps related to resonance positions remain unaltered.

Finally, as yet another evidence of the existence of the proposed Brewster quasi-BICs, we make use of our CEMD to calculate the eigenmodes with associated Q factors (Figs. 3.9a). This was done in Figs. 3.6d,e for non-tilted and tilted disk metasurfaces. In both cases, eigenmode dispersion relation entirely coincides with the reflectance bands shown in Figs. 3.8. For the non-tilted disk case, a canonical BIC is observed with diverging Q factor; however, as expected, a large (but finite) Q-factor is retrieved for the tilted disk metasurface. To further confirm their nature, numerical simulations have been carried out to reveal local electromagnetic fields for finite (though large) metasurfaces using on- and off-resonance excitation, see Figs. 3.9b-d. A vertical MD is placed inside the central disk, plotting the electric field intensity distribution on a horizontal plane parallel and very close to the metasurface. Off-resonance, the MD field is rapidly emitted, so that the near-field only concentrates in the excited disk. On-resonance, the MD field excites the true BIC (non-tilted disk) and the quasi-BICs (tilted disks), extending all of them over a large number of neighboring disks, as expected. Notably, both exhibit a similar decay away from the center, revealing that the quasi-BIC finite Q factor is large enough so that the finiteness of the samples has a larger impact on leakage, although its Q-factor is larger the closer is the tilt angle to the vertical direction, as shown also in Fig. 3.9d,e.

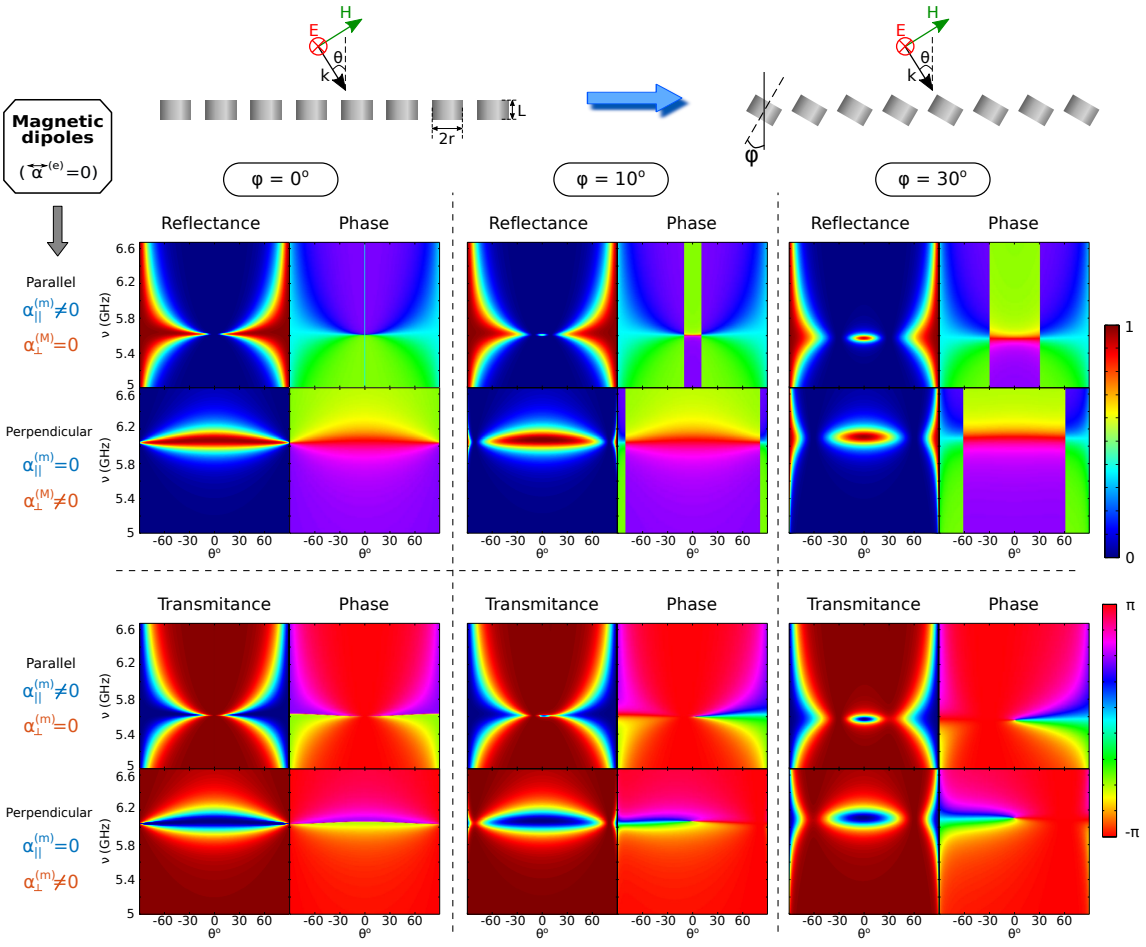

Figure 3.8: Brewster quasi-BIC theoretical model based on coupled electric and magnetic dipole array. Contour maps of the s-polarized reflectance (first and second rows) and transmittance (third and fourth rows) intensities/phases from an infinite square array (lattice period = 12 mm) of dielectric resonator disks (as in Fig. 3.4), tilted $\phi = 0°, 10°, 30°$ (first to third groups of columns, respectively) with respect to the plane normal, as a function of angle of incidence θ and frequency (GHz), calculated through the coupled electric and magnetic dipole array (third row), including separately the contributions from each MD polaribilities: out-of-plane (first and third rows) and in-plane (second and fourth rows).

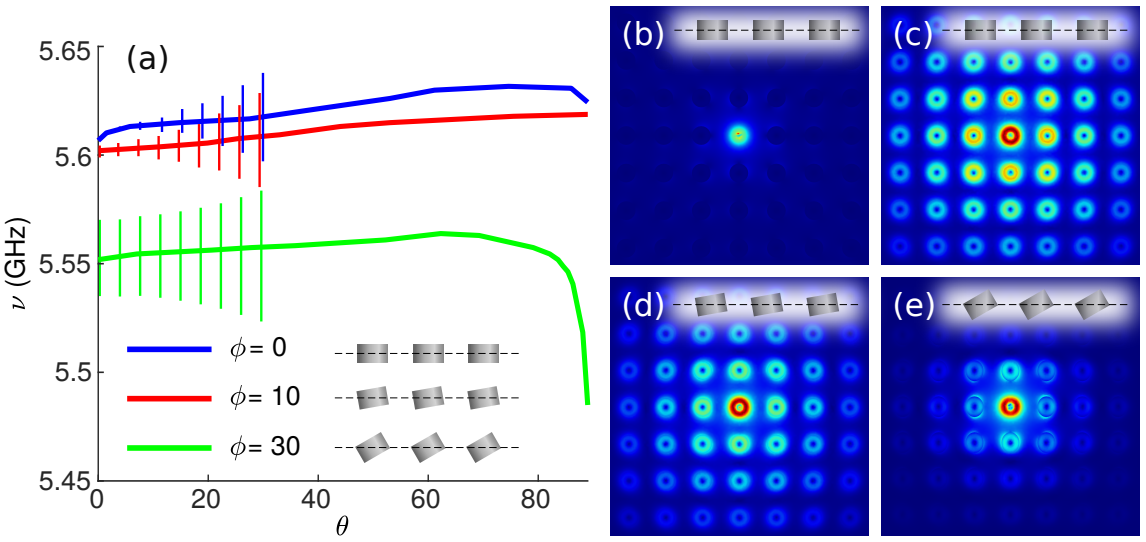

Figure 3.9: Brewster quasi-BIC theoretical analysis of eigenmodes. (a) CEMD calculations of eigenmode dispersion relation (solid curves) and half-width (error bars, up to 30°). (b-d) Numerically calculated (COMSOL) contour maps of near-electric field intensities on a horizontal plane crossing the disks through the center ($z = 0$) for a 11x11 finite square array (lattice period = 12 mm) of dielectric resonator disks, upon excitation with a MD located at the center of the central disk as follows (only shown the central 7x7 disk area): (b,c) vertical MD at (b) off-resonance ($\nu =$ 5 GHz) and (c) at resonance ($\nu = 5.605$ GHz) for non-tilted disks; (d,e) tilted MD at resonance for equally tilted disks by an angle (d) 10° ($\nu = 5.605$ GHz) and e 30°($\nu = 5.555$ GHz) .

3.3 BIC in a detuned dipole array

An elegant system that we propose to study Friedrich-Wintgen BICs is a lattice of gold rod resonators.[64] Sub-wavelength metallic rods are shown to have dipolar-like $\lambda/2$-resonances, leading to a variety of resonant phenomena such as surface plasmon lattice resonances in the optical domain[94–100] and electromagnetically-induced transparency at optical and THz frequencies.[101–108] With the aid of our colleagues of the group of Jaime Gómez Rivas, at the Technological University of Eindhoven, we experimentally demonstrate that metasurfaces consisting of sub-wavelength gold rod dimers exhibit strong and narrow Fano resonances in the THz transmission spectra. Such Fano resonances become narrower as the dimensions of the dimer rods approach each other, disappearing when rods are identical as a clear signature of BICs. Apart from full numerical calculations in agreement with the experimental results, a simple model for arrays of detuned-resonant-dipole dimers is developed. Hereby, we show analytically that such arrays hybridize both dipolar resonances in the form of broad and narrow lattice resonances, whose interference leads to asymmetric Fano resonances in the zero-order transmittance. This dark Fano resonance is shown in the parameter space of dipole-detuning to get infinitely narrow, becoming an infinite-Q BIC for zero detuning. These calculations fully explain the experimental results in this wider theoretical context of detuned-dipole arrays.

3.3.1 Experiments

Using optical lithography, metal deposition, and lift-off, samples containing 2D periodic lattices of gold rods on top of a 1.5 mm thick amorphous quartz substrate have been fabricated at the Technological University of Eindhoven. These samples were clamped against another 1.5 mm substrate with index matching liquid in between to suppress unwanted reflections, making the total sample thickness 3 mm. Before the thermal evaporation of the 100 nm gold layer, a 3 nm Ti adhesion layer was deposited. All the samples consist of 2D periodic lattices of two gold rods per unit cell. The lattice has a square symmetry with a pitch of $a = b = 300$ μm. One of the rods has a fixed dimension of 200 μm $\times$ 40 μm, while the dimension of the other rod is different for each sample that is investigated. The long dimension of the rods is aligned with the y-axis, and the rods inside the unit cell are separated by a distance d_x along the x-axis. Both rods support $\lambda/2$-resonances in the THz range, given by their length. The resonance frequency is controlled by the long axis of the rods, so we classify each lattice by the length of the second rod, L_2, covering the range $L_2 = 125 - 250$ μm in steps of 25 μm while keeping $L_1 = 200$ μm constant.

Two different sets of samples have been measured, with separation between rods fixed at d_x = 120 and 150 μm. THz transmittance spectra of these samples have been measured at normal incidence using a 4-f far-field THz time domain spectrometer (Menlo TeraK15). The transmittance of the lattices for different L_2 is shown in Fig. 3.10a. Numerical simulations calculated through SCUFF[109,110] (open-source software package for analysis of electromagnetic scattering problems using the method of moments) are shown in Fig. 3.10b, corresponding to transmittance spectra at normal incidence for the same geometrical parameters, but considering gold rods as planar perfectly conducting rectangles embedded in a uniform medium with $n = 1.55$ (the average of those of air and the supporting quartz substrate[111]). There is a shift between the Fano resonances simulated and the measurements, which can be corrected by slightly adjusting this refractive index. Good qualitative, and nearly quantitative, agreement is observed between the measurements and the simulations.

The more relevant feature in Fig. 3.10 is that for $L_2 \neq 200$ μm all spectra present a strong Fano resonance with a narrow asymmetric line shape. The resonance moves toward smaller frequencies as L_2 is increased, and disappears for $L_2 = 200$ μm. In addition, as the rods become more similar in size, the resonance becomes narrower; it should be mentioned, though, that the resonance narrowing is not clearly visible in the measurements for $L = 175, 225$ μm due to the limited frequency resolution in the measurements. The Fano resonance can be understood in terms of the lattice resonances that the array supports: a bright, broad symmetric mode and a dark, narrow antisymmetric mode.[106] Incidentally, by lattice resonances we mean the resonances resulting from the lattice-induced modification of meta-atom resonances,[37] rather than those emerging near Rayleigh anomalies.[95] The symmetry of these modes is preserved in the lattice and they interfere either destructively or constructively, producing a characteristic dip/peak pair in the spectra. Moreover, the dark mode becomes inaccessible at $L_2 = 200$ μm and the interference disappears; as we will show below, the width of the resonance thus tends to zero, leading to a BIC that cannot be detected in the far field.

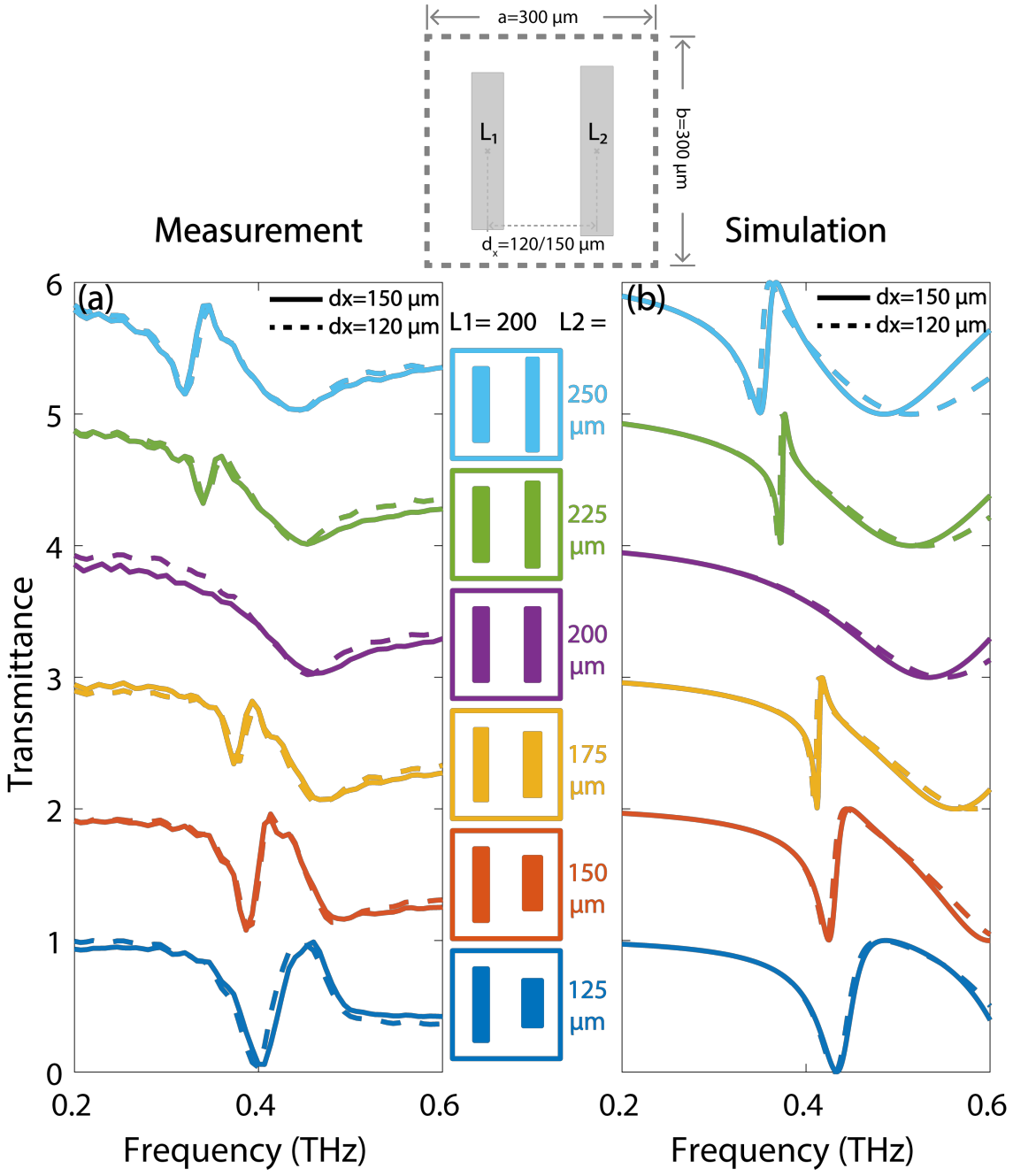

Figure 3.10: (a) Measured transmittance spectra for square lattices ($a = 300\ \mu$m) of two gold rods per unit cell, deposited on a quartz substrate, with two different rod separations: $d_x = a/2$ (solid curves) and $d_x = 2a/5$ (dashed curves). One of the rods has fixed dimensions of $L_1 = 200\,\mu$m and $w_1 = 40\,\mu$m, while the other varies as shown in the center insets, with $L_2(\mu\text{m}) = 125, 150, 175, 200, 225, 250$, while keeping the surface area fixed: $L_2 w_2 = L_1 w_1$. All rod thicknesses are $t = 0.1\,\mu$m. (b) Transmittance spectra numerically calculated through SCUFF[109,110] for the same geometrical parameters, but considering gold rods as planar perfectly conducting rectangles embedded in a uniform medium (see text). Curves are offset by 1 for each different L_2.

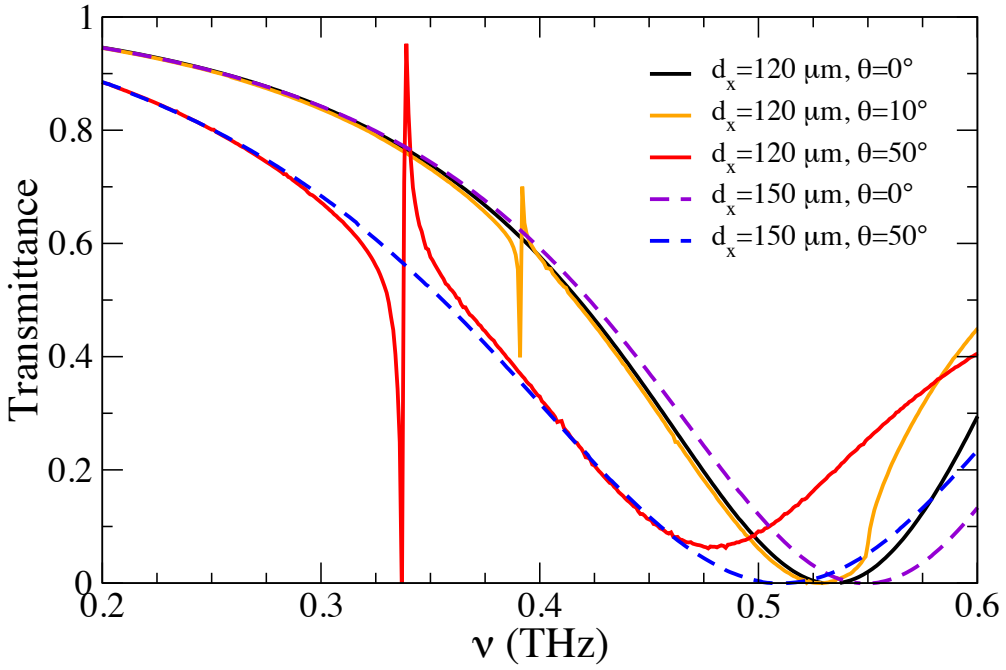

Figure 3.11: Transmittance spectra numerically calculated through SCUFF for a plane wave incident at $\theta = 0°, 50°$ on a square lattice ($a = 300$ μm) of two planar gold rods per unit cell embedded in a uniform medium with $n = 1.55$, with two different rod separations: $d_x = a/2$ (dashed curves) and $d_x = 2a/5$ (solid curves), in the latter case, $\theta = 10°$ is also considered to further illustrate the emergence of a Fano resonance. Gold rods are identical and have dimensions $L_1 = L_2 = 200\,\mu$m and $w_1 = w_2 = 40\,\mu$m.

It should be noted that, when $d_x = 150\,\mu$m, the BIC state is connected to the guided mode that the lattice supports. Indeed, for $L_2 = 200$ μm both rods are identical, so that the array becomes a single rod lattice with lattice constant halved along the x-axis. We call this condition as the "half-period lattice". The Brillouin zone is doubled when $d_x = a/2$; thus, if one artificially assumes that the actual lattice constant is a, part of the lowest guided mode band (always below the light line of the true Brillouin zone) will be bent back into the propagating region (above the light line) of the artificially reduced Brillouin zone, indeed leading to an artificial BIC (stemming from a guided mode rather than from a leaky mode) at the Γ point. Furthermore, the number of resonances that the lattice supports can be associated to the number of particles per unit cell. For the identical symmetric lattice, i.e. one particle per unit cell, there is only a bright (symmetric) mode. Therefore, for the symmetric lattice it is difficult to relate the BIC with a real state.

Nonetheless, for a lattice with $d_x = 120\,\mu$m, where the symmetric lattice is not recovered at $L_2 = 200\,\mu$m for equal rods, the BIC is no longer directly connected to any guided mode, so that the system has two well defined lattice modes and a true BIC emerges. This is further verified through numerical calculations at oblique incidence Fig. (3.11), which reveal a Fano resonance emerging for equal rods only in the case of the asymmetric lattice ($d_x = 2a/5$); yet another evidence of the true BIC behavior.

3.3.2 Theoretical model

To shed light onto this rich phenomenology, we developed a simple coupled dipole-dimer model of an infinite array embedded in a homogeneous environment developed by myself.[37] Dipoles are fully characterized by their electric polarizabilities along the y-axis, namely, $\alpha_y^{(1)}$ and $\alpha_y^{(2)}$, where (1) and (2) account for each dimer dipole in the unit cell. The array is excited by an external plane wave, ψ_0 being its electric field polarization along the y-axis. Upon imposing Bloch's theorem, the local field at the position of the dipoles, $\psi_{loc}^{(i)}$, with $i = 1, 2$, can be found through a self-consistent field equation

$$\begin{bmatrix} \psi_{loc}^{(1)} \\ \psi_{loc}^{(2)} \end{bmatrix} = \left[\overleftrightarrow{I} - k^2 \overleftrightarrow{G}_b \overleftrightarrow{\alpha} \right]^{-1} \begin{bmatrix} \psi_0^{(1)} \\ \psi_0^{(2)} \end{bmatrix}, \tag{3.4}$$

where $\psi_0^{(i)}$ is the incident field on dipole $i = 1, 2$, $\overleftrightarrow{I}$ is the identity matrix, $\overleftrightarrow{\alpha}$ is the polarizability tensor and $\overleftrightarrow{G}_b$ is the lattice "depolarization" dyadic (or return Green function)

$$\overleftrightarrow{\alpha} = \begin{bmatrix} \alpha_y^{(1)} & 0 \\ 0 & \alpha_y^{(2)} \end{bmatrix}, \quad \overleftrightarrow{G}_b = \begin{bmatrix} G_{byy} & G_{yy}^{(1-2)} \\ G_{yy}^{(2-1)} & G_{byy} \end{bmatrix}. \tag{3.5}$$

G_{byy} describes the self-interaction of each dipole array; $G_{yy}^{(1-2)}$ and $G_{yy}^{(2-1)}$ are the interaction of the dipole array labeled as (1) over (2) and vice versa. Due to symmetry, at normal incidence $G_{yy}^{(1-2)} = G_{yy}^{(2-1)}$.

Surface lattice resonances are the solutions of Eq. 3.4 in the absence of the external plane wave. To solve it, we diagonalize the system and find the condition at which the eigenvalues, Λ, are equal to zero. Recall that the imaginary components of $\overleftrightarrow{G}_b$ and $\overleftrightarrow{\alpha}$ (for lossless particles) are well defined and satisfy the following condition

$$\Im\left[\left(\frac{1}{\alpha_y} - G_{byy}\right) + G_{yy}^{(1-2)}\right] = 0, \tag{3.6}$$

where we define the magnitudes

$$\frac{2}{\alpha_y} = \frac{1}{k^2}\left(\frac{1}{\alpha_y^{(1)}} + \frac{1}{\alpha_y^{(2)}}\right), \quad \Delta\alpha_y = \frac{1}{k^2}\left(\frac{1}{\alpha_y^{(1)}} - \frac{1}{\alpha_y^{(2)}}\right). \tag{3.7}$$

For more details about the detuned dipole formulation see Appendix C. At a small detuning, $\Delta\alpha_y \ll 2G_{yy}^{(1-2)}$, the imaginary components of the eigenvalues can be approximated by

$$\Im\left[\Lambda^+\right] = \Im\left[\frac{(\Delta\alpha_y)^2}{8G_{yy}^{(1-2)}}\right], \tag{3.8a}$$

$$\Im\left[\Lambda^-\right] = \Im\left[2\left(\frac{1}{\alpha_y} - G_{byy}\right) - \frac{(\Delta\alpha_y)^2}{8G_{yy}^{(1-2)}}\right]. \tag{3.8b}$$

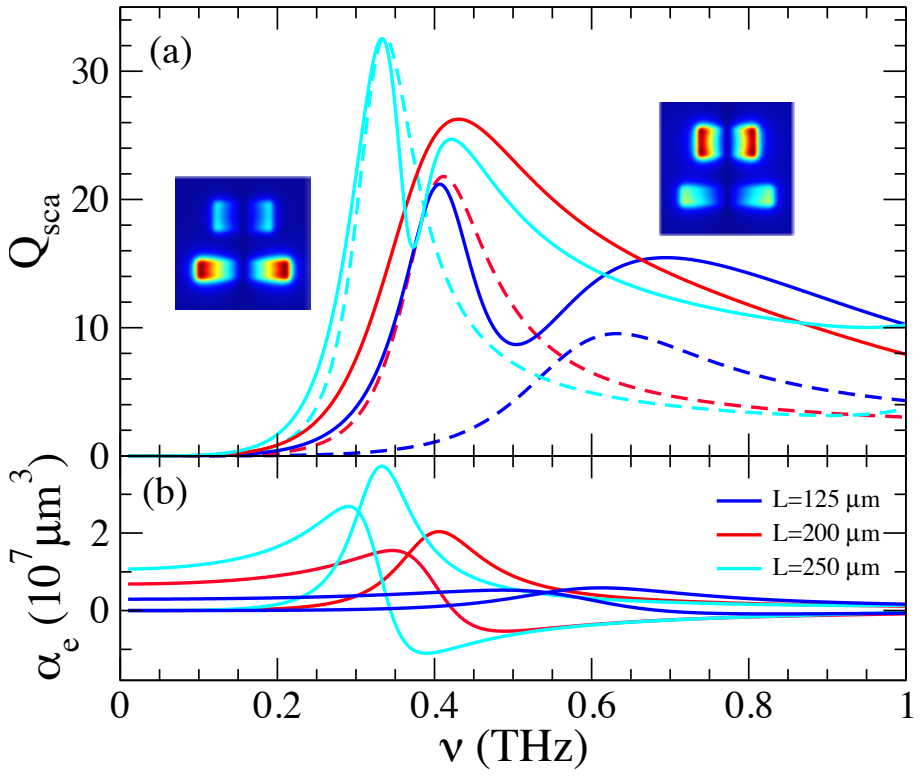

Figure 3.12: (a) Scattering efficiencies (solid curves) numerically calculated through SCUFF for perfectly conducting planar dimer rods (separated by $d = 120$ μm) with lengths $L_1 = 200$ μm and: $L_2 = 125, 200$ and 250 μm (widths satisfy $w(\mu\text{m}) = 8000/L$). Corresponding efficiencies for single isolated rods with $L = L_2$ are also included (dashed curves). Insets show the near-field maps (magnetic field perpendicular to the dimer plane) for the dimer with $L_2 = 125\mu$m at the two resonances. (b) Real and imaginary parts of the polarizibilities of the single rods extracted from (a).

Finally, the corresponding eigenvectors are given by

$$\Lambda^{\pm} = 0 \rightarrow \nu^{\pm} = \begin{bmatrix} \psi_{loc}^{(1)} \\ \psi_{loc}^{(2)} \end{bmatrix} = \begin{bmatrix} 1 \\ \mp 1 \end{bmatrix}. \tag{3.9}$$

The lattice resonances are associated to two modes in which the rods are out-of-/in-phase (anti-symmetric/symmetric). From Eq. 3.8, it follows that the out of phase mode Λ^+ is very narrow and becomes a BIC at zero detuning, whereas the in-phase mode Λ^- is broad. Therefore, for $L_1 \neq L_2$ ($\alpha_y^{(1)} \neq \alpha_y^{(2)}$) we have a broad mode that interferes with a very narrow mode, leading to a Fano resonance. For $L_1 = L_2$, the narrow mode converges into a BIC state.

Interestingly, if there is also an additional displacement along the y-axis, given by d_y, Eq. 3.6 still holds. Moreover, this identity is also valid for non-square lattices where $a \neq b$. This is evidenced in the detailed formulation in Appendix C, where the expressions of the imaginary parts of all three terms in Eq. 3.6 are shown to cancel out in the absence of diffraction orders despite the fact that both $G_{yy}^{(1-2)}$ and G_{byy} depend on lattice parameters. Hence, Eq. 3.6 is universal, as long as there is no coupling involving higher multipoles, and holds for: (i) any set of lattice

constant parameters, a and b; and (ii) any relative displacement between dipoles inside the unit cell. *Therefore, a major conclusion is that the BIC state is symmetry-protected and robust against changes in the specific lattice parameters: a, b, d_x and d_y.* In this regard, bear in mind that this statement is purely theoretical (no experimental evidence is provided). Indeed, it is thus restricted to the domain of applicability of our coupled detuned-dipole formulation, namely: dimer meta-atoms accounted for by parallel detuned dipoles, with couplings among them fully reproduced by dipole-dipole interactions, and within the spectral regime where no diffraction orders are allowed other than the specular ones.

Let us now analyze the Fano-BIC transition using our coupled dipole-dimer model. The polarizability of the rods is calculated through SCUFF,[109,110] considering the rods as perfect electric conductors. The scattering efficiency for perfectly conducting planar dimer rods (separated by $d = 120$ μm) with lengths $L_1 = 200$ μm and $L_2 = 125, 200$ and 250 μm are shown in Fig 3.12a. Significant interference between rods is observed in the dimer spectra, which do not correspond to simply a linear combination of the isolated spectra of each rod. Rather, rod interference leads to a stronger/weaker impact of the higher/lower frequency rod resonance (apart from their opposite phases, not shown), as expected.[102] In Fig 3.12b the polarizability along the long axis is shown for the same parameters used before. In order to avoid numerical problems related to unphysical absorption, we consider in our coupled dipole model that dipoles are lossless so that the imaginary parts of the polarizabilities are fixed to $\Im\left[1/\alpha_y^{(i)}\right] = -k^3/(6\pi)$ to fulfill the optical theorem, taking for the real parts the values calculated numerically.

We plot in Fig. 3.13a,c the spectra of the transmission coefficient ($T = 1 - R_0$) intensity and phase, for a square lattice with two dipoles per unit cell, separated by a distance of $d_x = 120$ μm for varying L_2; cuts for fixed lengths are shown in Fig. 3.13b,d. Figure 3.13 shows that the coupled dipole-dimer model reproduces all the features exhibited in Fig. 3.10, fully extending the characterization of the BIC into the L_2-parameter space. Remarkably, the contour map in Fig. 3.13a reveals the classical narrowing of the leaky resonance (Q-factor tending to infinity) towards a BIC state, with the distinct feature that the resonant state [surface lattice dipole resonance with an abrupt π-phase jump shown in the contour map in Fig. 3.13c] manifests itself as a narrow Fano resonance instead. Transmittance spectra (intensity and phases) are shown in Fig. 3.13c,d for given L_2 illustrating this Fano-like behavior that disappears at $L_2 = L_1$ as a signature of the BIC.

Furthermore, we show in Fig. 3.13e,f the field amplitudes ($\psi_{loc}^{(1)}, \psi_{loc}^{(2)}$) and phases ($\phi_{loc}^{(1)}, \phi_{loc}^{(2)}$, where $\Delta\phi = \phi_{loc}^{(1)} - \phi_{loc}^{(2)}$) of the local fields over the dipoles, for the dipole dimer corresponding to $L_2 = 150$ μm. At low frequencies, both dipoles are driven in phase. At $\nu = 0.38$ THz, coinciding with the zero of $\psi_{loc}^{(1)}$, $\Delta\phi$ presents a discontinuity and becomes maximum (rods out of phase, with a high dispersion in both). The field amplitudes are enhanced and, indeed, exhibit a resonant lineshape, corresponding to the dark lattice resonance, where the Fano asymmetric lineshape emerges in the far field. Then at $\nu = 0.48$ THz, upper-frequency end of the Fano resonance, $\Delta\phi$ presents another discontinuity exactly at the zero of $\psi_{loc}^{(2)}$; for higher frequencies the phase difference vanishes and the dipoles are in phase again. Thus, at given frequencies at the lower/upper band of the Fano resonance, the fields at the long/short rods are strictly zero, manifesting the strong interaction that exist between the different rods near resonance. In addition,

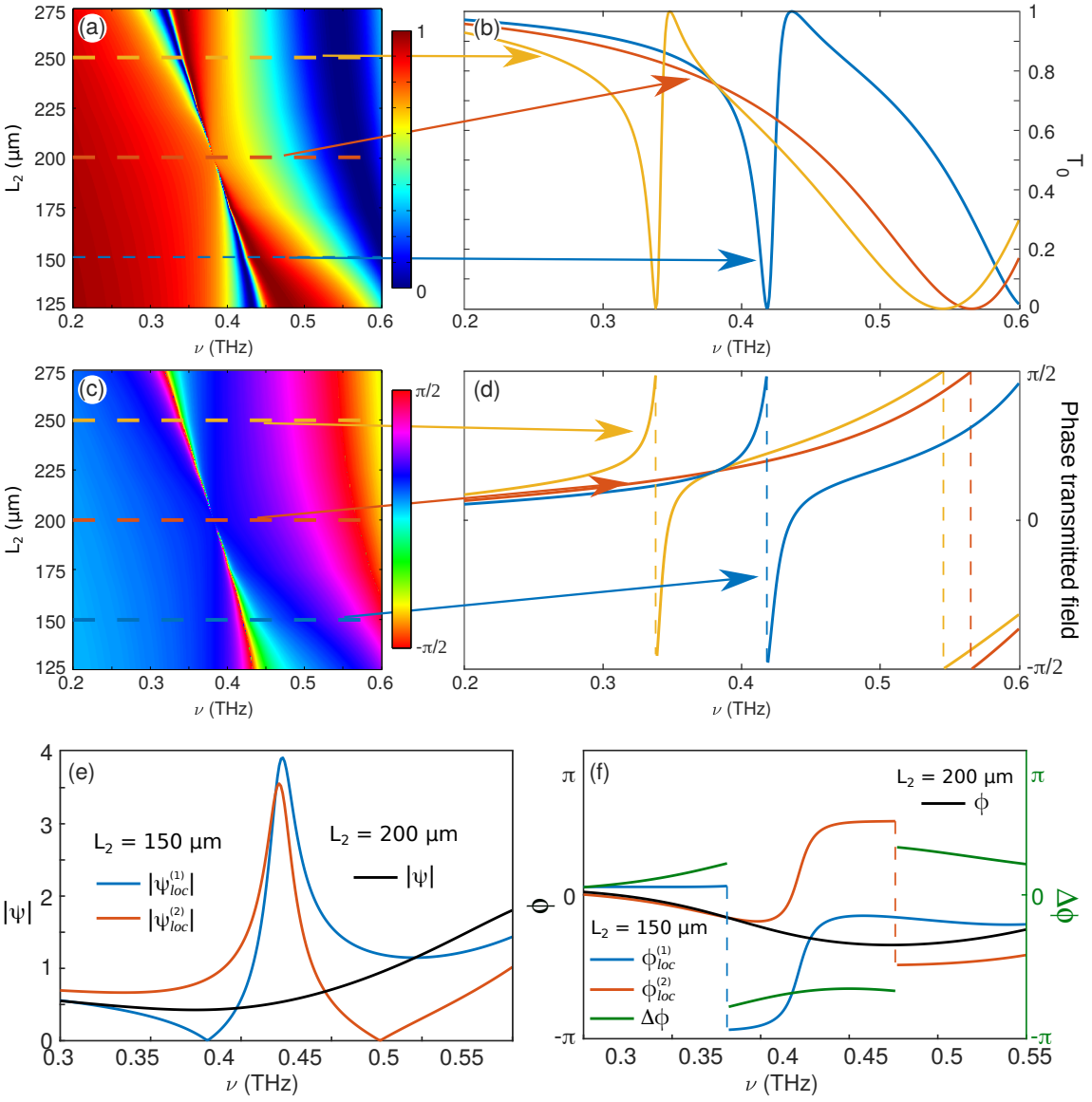

Figure 3.13: (a-d) Theoretical transmittance spectra calculated through coupled dipole theory for a square lattice ($a = 300$ μm) as in Fig. 3.10, but consisting of two detuned dipoles per unit cell, separated by $d_x = 2a/5$: (a,b) Transmittance; (c,d) phase. Dipole polarizibilities are extracted from the numerically calculated scattering cross sections shown in Fig. 3.12: One is fixed and corresponds to a rod with dimensions L_1 =200 μm and w_1 =40 μm, while the other one L_2 (with identical areas $L_2 w_2 = L_1 w_1$) varies continuously in the contour maps in (a,b), whereas those cases corresponding to three of the experimental dimers, $L_2(\mu\text{m}) = 150, 200, 250$, are shown in (b,d).

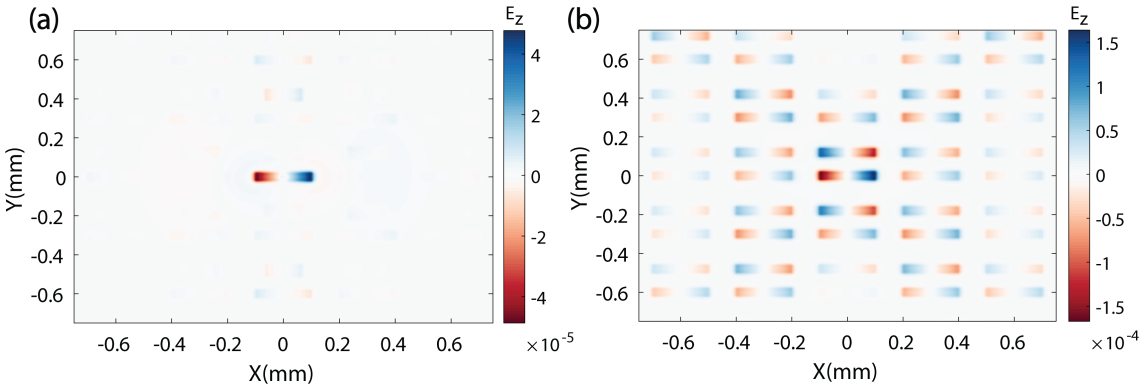

Figure 3.14: Near field map showing the electric field component along the z-direction, numerically calculated through Lumerical, for a dipole source (located at the image center) inside a square lattice ($a = 300\ \mu$m) of Au rod dimers deposited on a quartz substrate, with rod separation $d_x = 2a/5$. One of the rods has fixed dimensions of $L_1 = 200\,\mu$m and $w_1 = 40\,\mu$m, while the other is (a) $L_2 = 125\ \mu$m (i.e. detuned dipoles) and (b) $L_2 = 200\ \mu$m (i.e. equal dipoles), while keeping the surface area fixed: $L_2 w_2 = L_1 w_1$. The dipole source emits near the BIC frequency at $\nu = 0.357$ THz.

the local field is enhanced by more than a factor of three in both rods. At $L_2 = L_1$, the anti-phase behavior is not allowed, so that the field at both rods is identical [cf. Figs. 3.13e,f], with no evidence whatsoever of a Fano resonance, thus becoming a BIC [as shown in Fig. 3.13a,b].

To reveal even more neatly the BIC behavior, we show a near-field map in Fig. 3.14, numerically calculated through FDTD simulations (Lumerical), for a dipole source (located at the center of the image) inside a dimer rod array ($d_x = 120\ \mu$m) with identical dimensions ($L_2 = L_1 = 200\ \mu$m) lying on a quartz substrate, at the BIC frequency $\nu = 0.357$ THz [Fig. 3.14b]; another case with different rods $L_2 = 125\ \mu$m is also shown for comparison [Fig. 3.14a]. In Fig. 3.14a the excitation with a point dipole is radiated to the far field immediately, without propagation to the neighboring rods. The near field map reveals that only the rod dimer adjacent to the dipole is excited; in particular, the resonant rod with $L_1 = 200\ \mu$m, as expected. By contrast, the near field for equal rod dimers is effectively trapped in the BIC mode as shown in Fig. 3.14b: many dimers in the lattice are resonantly excited, with the expected opposite phase for each rod within the (dimer) unit cell that protects the BIC and precludes out-of-plane radiation losses.

Chapter 4

Scattering properties of finite semiconductor nanowires

Semiconductor nanowires are attracting an increasing interest in recent years due to the advance in synthesis and their unique optical properties.[112] As discussed in the Introduction, they possess strong optical resonances and/or guided modes that can be richly tuned by their geometrical and/or material properties.[113,114] These features make them specially suitable to selectively enhance light scattering, absorption, and photoluminescence at the nanoscale.[112,115–120] The resulting realm of phenomenology, some in turn in connection with ad-hoc electronic and/or quantum properties, holds promise for potential: single-photon sources and nanolasers,[121–124] solar light absorbers and photodetectors in Photovoltaics,[44,115–117,125–129] antireflection coatings,[130] metamaterials,[89] etc. Nonetheless, fundamental properties of dielectric nanowires are still unexplored.

Along this chapter we focus on the absorption and scattering properties of dielectric cylinders. In the first section, we study the conection between Mie resonances and leaky/guided modes in infinitely long cylinders, and we determine the role of guided modes in the absorption in finite nanowires.[113] Later, it is shown that finite nanowires act as Fabry-Perot cavities whose modes interfere with Mie resonances, leading to strong Fano resonances.[49] The work presented in this chapter was done in collaboration with Ramón Paniagua-Domínguez during its period at the Instituto de Estructura de la Materia (Madrid)[113] and with Miguel A. G. Mandujano and Eugenio R. Méndez,[49] colleagues at the Centro de Investigación Científica y de Educación Superior de Ensenada.

4.1 Unraveling the Janus Role of Mie Resonances and Leaky/Guided Modes in Semiconductor Nanowire Absorption

The phenomenon of light absorption in semiconducting nanowires (NWs) has been mostly described theoretically in two manners. On the one hand, it has been addressed in the context of light-coupling into leaky/guided modes,[118,131–136] well known in Electrodynamics for infinitely long NWs.[6,137,138] On the other hand, Mie light scattering from infinitely long cylinders[5] al-

lows to interpret absorption and scattering properties of semiconducting NWs through Mie resonances.[139–143] Nonetheless, no clear connection between them has been formally established.

In this section we discuss the optical properties of infinitely long nanowires described in Section 1.4, indeed directly revealing the connection between Mie resonances and leaky modes in the corresponding equations, formally equivalent.[113] Furthermore, we unify both theoretical pictures by subtly including Mie extinction cross sections at normal and oblique incidences onto the waveguide mode dispersion relation. This analysis allows to determine the appropriate nanowire dimensions and spectral regime for the ad-hoc coupling to (or excitation of) desired modes/resonances alike. On this basis, the unified theoretical picture is exploited also in connection with Mie absorption cross sections, in order to shed light onto designing semiconducting nanowires for enhanced light absorption, showing numerical results for specific, finite-length nanowire configurations that allow also for guided mode excitation at grazing incidence.

4.1.1 Infinite cylinders: Leaky/guided modes versus Mie resonances

First of all, we study the optical properties of infinitely long semiconducting nanowires through a scheme that accounts jointly for leaky/guided modes and Mie resonances. Let us focus on an InP nanowire in vacuum at a wavelength in the visible, i.e. $\lambda = 532$ nm. As a first approach, for the sake of simplicity that will allow a better understanding, the InP refractive index[144] is assumed to be real: $n_c = n_{\mathrm{InP}} = 3.7$ (absorption is neglected). The dispersion relation is calculated from Eq. 1.42 in terms of $\omega R/c$ vs $k_z' R$ (recall that $k_z = k_z' + \imath k_z''$ is complex). This means that, strictly speaking, the nanowire radius R is the independent variable, whereas $\omega = 2\pi/\lambda$ remains fixed; alternatively, as long as the refractive index remains constant, the resulting dispersion relation can also be applied to a proper spectral dependence for fixed nanowire radius R. In this manner, we do not incorporate in the discussion the spectral dependence of the semiconductor refractive index (nor that of the absorption), which will be dealt with in connection with light absorption spectra later on.

By solving the dispersion relation given by Eq. 1.42, the results are shown in Fig. 4.1: the light line $\omega/c = k_z$ separates the guided modes $k_z' \geq \omega/c$ from the leaky modes $k_z' < \omega/c$. The latter modes thus leak out of the NW due to the non-negligible wavevector component in the plane perpendicular to the NW axis, unlike guided modes. Leaky modes are continued outside the light cone into guided modes as long as their symmetry is preserved (same notation in Fig. 4.1), and will be discussed below.

In the case of $m = 0$ in Eq. 1.42, transverse electric (TE_{0m}) and magnetic (TM_{0m}) modes are decoupled. The lowest ($m = 1$) electromagnetic (EM) mode is referred to as HE_{11}, exhibiting no cutoff in the low energy limit $\omega = 0$. Conversely, for fixed ω, this no-cutoff mode HE_{11} is present also no matter how thin the NW might be. Nonetheless, in such $\omega R \to 0$ limit, this hybrid mode becomes very weakly guided, its electromagnetic field being mainly localized into the surrounding medium,[120] with no significant impact on absorption.

On the other hand, Mie resonances are determined by calculating the extinction Q_{ext}, scattering Q_{sca}, and absorption Q_{abs} efficiencies from the following expressions for TE and TM polar-

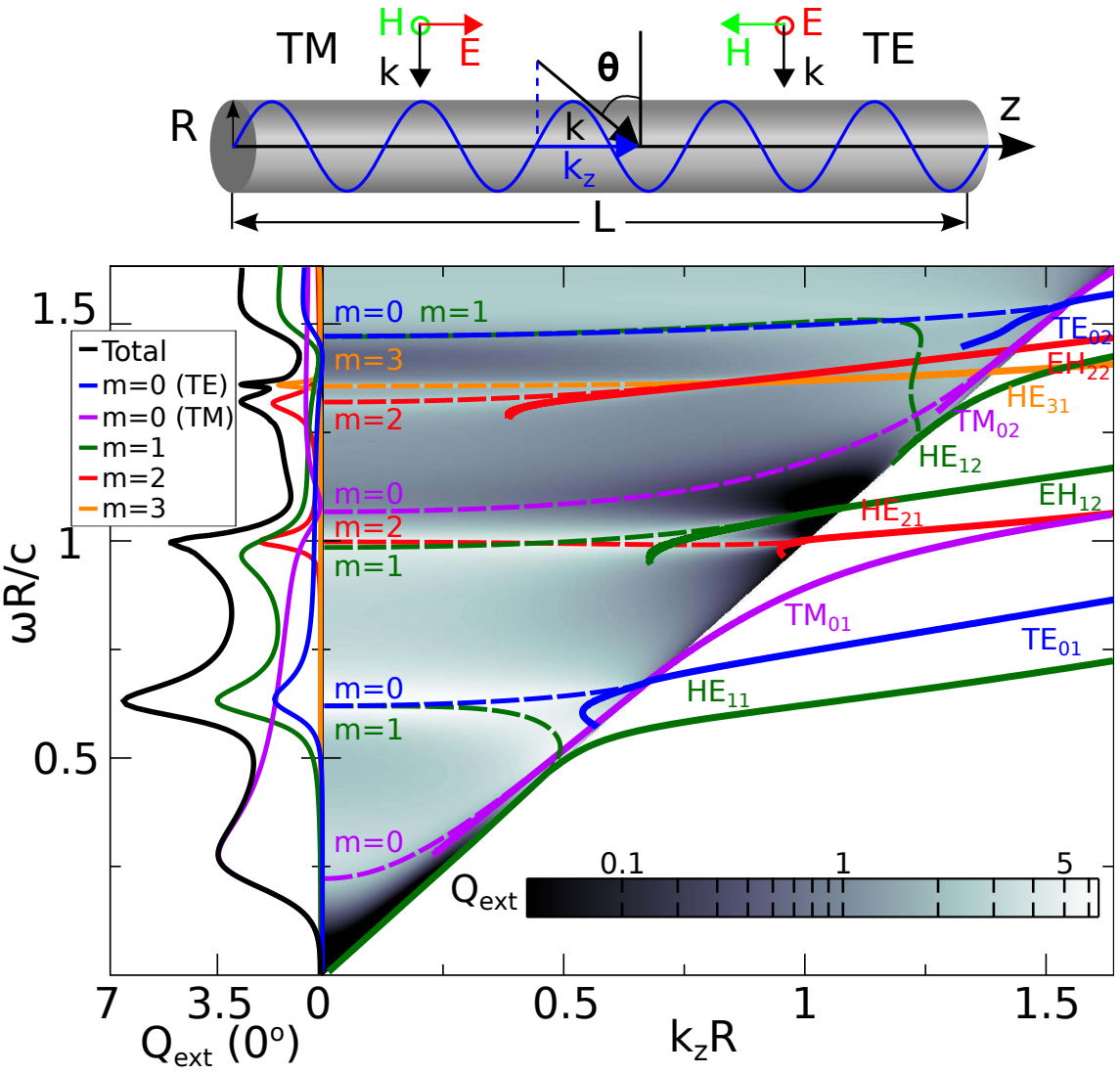

Figure 4.1: Top panel: Schematic of the Mie scattering configuration, including also the convention for the leaky/guided mode wavevectors used for their dispersion relations. Lower (center) graph: Dispersion relation $\omega R/c$ vs $k_z R$ from Eq. 1.42 (solid curves) of the first leaky/guided modes of InP nanowires with varying radius R at $\lambda = 532$ nm (refractive index $n_c = n_{\rm InP} = 3.7$). The spectral dependence of the extinction efficiency $Q_{\rm ext} \equiv Q_{\rm sca}$ is superimposed as a contour map within the light cone, calculated through Mie scattering (TE and TM polarization, eqs 4.1) for varying angle of incidence θ such that $k_z = (\omega/c)\sin\theta$ ($\theta = 90°$ coincides with the light line). The complex (Mie-like, see text) $\omega(k_z)$ solutions of Eq. 4.2 for real $ck_z/\omega = ck_z'/\omega$ are also included (dashed curves). Left graph: $Q_{\rm ext}$ at $\theta = 0°$, including the lowest-order (up to $m = 3$) contributions (for $m = 0$, TE and TM polarizations are shown separately).

ization:[5]

$$Q_{\text{ext}}^{(\text{TE})} = \frac{2}{kR}\Re\left[a_{0\text{II}} + 2\sum_{m=1}^{\infty} a_{m\text{II}}\right], \tag{4.1a}$$

$$Q_{\text{ext}}^{(\text{TM})} = \frac{2}{kR}\Re\left[b_{0\text{I}} + 2\sum_{m=1}^{\infty} b_{m\text{I}}\right], \tag{4.1b}$$

$$Q_{\text{sca}}^{(\text{TE})} = \frac{2}{kR}\left[|a_{0\text{II}}|^2 + 2\sum_{m=1}^{\infty}\left(|a_{m\text{II}}|^2 + |b_{m\text{II}}|^2\right)\right], \tag{4.1c}$$

$$Q_{\text{sca}}^{(\text{TM})} = \frac{2}{kR}\left[|b_{0\text{I}}|^2 + 2\sum_{m=1}^{\infty}\left(|b_{m\text{I}}|^2 + |a_{m\text{I}}|^2\right)\right], \tag{4.1d}$$

$$Q_{\text{abs}} = Q_{\text{ext}} - Q_{\text{sca}}, \tag{4.1e}$$

where $a_{m\text{I}}, b_{m\text{I}}, a_{m\text{II}}, b_{m\text{II}}$ are the corresponding Mie scattering coefficients (introduced in the Section 1.4.1), for a plane wave impinging on the infinite nanowire (see top panel in Fig. 4.1), polarized either parallel (TM) or perpendicular (TE) to the plane defined by the NW axis and the incident wavevector at the oblique angle of incidence θ.

Let us discuss whether a connection can be established between a leaky/guided mode and a Mie resonance. This connection has been pointed out and being unequivocally shown for a particular (TM_{01}) leaky mode and (lowest-order, TM polarized) Mie resonance.[118,143] However, a proper formal expression has not been derived yet. Mie resonances are obtained from the zeros of the denominators of the Mie scattering coefficients $a_{m\text{I}}, b_{m\text{I}}, a_{m\text{II}}, b_{m\text{II}}$. It turns out that all coefficients share the same denominator,[5] so that the Mie resonance condition can be written as:

$$\begin{aligned}&\imath\xi^2\left[\xi J_m'(\eta)H_m(\xi) - \eta J_m(\eta)H_m'(\xi)\right]\left[n_c^2\xi J_m'(\eta)H_m(\xi) - \eta J_m(\eta)H_m'(\xi)\right]\\ &-\imath\left[m\eta\sin\theta J_m(\eta)H_m(\xi)\left(\tfrac{\xi^2}{\eta^2}-1\right)\right]^2 = 0,\end{aligned} \tag{4.2}$$

where $\xi = (\omega R/c)\cos\theta$ and $\eta = (\omega R/c)(\epsilon_c - \sin^2\theta)^{1/2}$. If we identify the incident wavevector component along the cylinder axis as $k_z = (\omega/c)\sin\theta$, it follows that $\xi = v$ and $\eta = u$, (recall $u = k_1 R, v = k_2 R$). Then, after some algebraic manipulation, the latter equation can be rewriten as:

$$\begin{aligned}\imath\left[uv^2 J_m(u)H_m(v)\right]^2 \times \quad &\left\{\left[\frac{\mu_c}{u}\frac{J_m'(u)}{J_m(u)} - \frac{\mu}{v}\frac{H_m'(v)}{H_m(v)}\right]\left[\frac{\epsilon_c}{u}\frac{J_m'(u)}{J_m(u)} - \frac{\epsilon}{v}\frac{H_m'(v)}{H_m(v)}\right]\right.\\ &\left.-m^2\frac{(k_z R)^2}{(\omega R/c)^2}\left(\frac{1}{v^2}-\frac{1}{u^2}\right)^2\right\} = 0;\end{aligned} \tag{4.3}$$

upon imposing that the term in braces is equal to zero, we retrieve a condition formally identical to Eq. 1.42, which is in fact the dispersion relation of leaky/guided mods discussed above.

To illustrate our procedure, we focus again on an InP nanowire in vacuum ($n = 1$) at $\lambda = 532$ nm, as in Fig. 4.1, including the analysis of Mie resonances in the same graph in the following manner. The unpolarized extinction (or scattering, since absorption is neglected thus far) efficiency, $Q_{\text{ext}} = (Q_{\text{ext}}^{(\text{TE})} + Q_{\text{ext}}^{(\text{TM})})/2$, for the same nanowire parameters, is plotted for an incident

plane wave (TE and TM polarization) as a color map, by assuming that k_z is connected to the wavevector component along the nanowire axis $k_z = (\omega/c)\sin\theta$ (see Fig. 4.1 inset). To make it more evident, we have solved Eq. 1.42 for complex $\omega(k_z)$ solutions for real $ck_z/\omega = \sin\theta$ in the non-radiative region; these Mie resonances are superimposed in Fig. 4.1 (dashed curves), lying alongside the maxima of the Mie extinction efficiencies throughout the light cone, and connecting with corresponding leaky modes for large k_z, thus confirming a formal equivalence that resembles the two faces of "Janus bifrons". The resulting scheme enables us to understand the complex interplay between leaky modes and Mie resonances in a relatively simple manner. [Incidentally, it should be noted that the Mie resonances are red-shifted with regard to the extinction maxima in Fig. 4.1; this is connected with the asymmetric (Fano-like) line shape of Mie resonances in cylinders.[145]]

Nonetheless, note that the correspondence between them is subtle. This stems from the fact that leaky modes are complex $k_z(\omega)$ zeros, at real ω, of the above Eq. 1.43; whereas Mie resonances arise as complex $\omega(k_z)$ zeros, at real $ck_z/\omega = \sin\theta$. The imaginary part of the leaky mode yields the mode decay rate due to leakage (and absorption if present) along propagation. By contrast, the imaginary part of the Mie resonance frequency yields the resonance width due to scattering (and absorption if present). Therefore, such correspondence manifests as a direct overlap in the $k_z - \omega$ plane only when the leaky modes posses very small k_z'' (large decay lengths, or low radiation losses) and the Mie resonance has a small width ω''. This predominantly occurs when the leaky mode dispersion curve yields large k_z', actually close to the light line at ω/c; in turn overlapping with Mie resonances at large, oblique angle of incidence θ. For small angles of incidence θ, $k_z = (\omega/c)\sin\theta \to 0$, the existing leaky modes exhibit large k_z'' (not shown in Fig. 4.1), and no direct overlap with its corresponding Mie resonance is observed in the $k_z - \omega$ plane. In general, leaky modes should play a leading role in point dipole excitations,[146] whereas Mie resonances properly account for plane wave scattering[143] (at least over a wide angular range), as is the case of NW absorption studied herein.

To shed more light on this argument, let us plot the EM field patterns associated with the lower $m = 0, 1$ leaky/guided modes, which in turn determine their symmetry, as shown in Fig. 4.2. First, we focus on the leaky modes exhibiting the lowest-order TM_{01} and TE_{01} symmetries (see Figs. 4.2a,c and 4.2e,g); the EM field patterns associated to the $m = 0$ Mie resonance obtained by illuminating the same nanowires with either TM or TE polarized plane wave at $\theta = 0°$ are shown in Figs. 4.2b,d and 4.2f,h, respectively, revealing a strong resemblance with their associated leaky modes, as expected. With regard to the lowest $m = 1$ Mie resonance, note that no associated leaky mode exists; in fact, it redshifts for large angles and approaches the light line along with the no cut-off HE_{11} guided mode, which remains (weakly) guided in the low energy limit (overlapping with the light line). Thus, we show instead the EM field pattern of the HE_{11} guided mode in Figs. 4.2i,k, which strongly resembles the symmetry of such lowest $m = 1$ Mie resonance (Figs. 4.2j,l), revealing their connection. Note that, despite the unambiguous resemblance in all cases, the plane wave illumination associated to the Mie scattering results introduces certain asymmetry with respect to their corresponding (highly symmetric) leaky/guided mode patterns.

Moreover, from the dispersion relation shown in Fig. 4.1, guided modes in the non-radiative

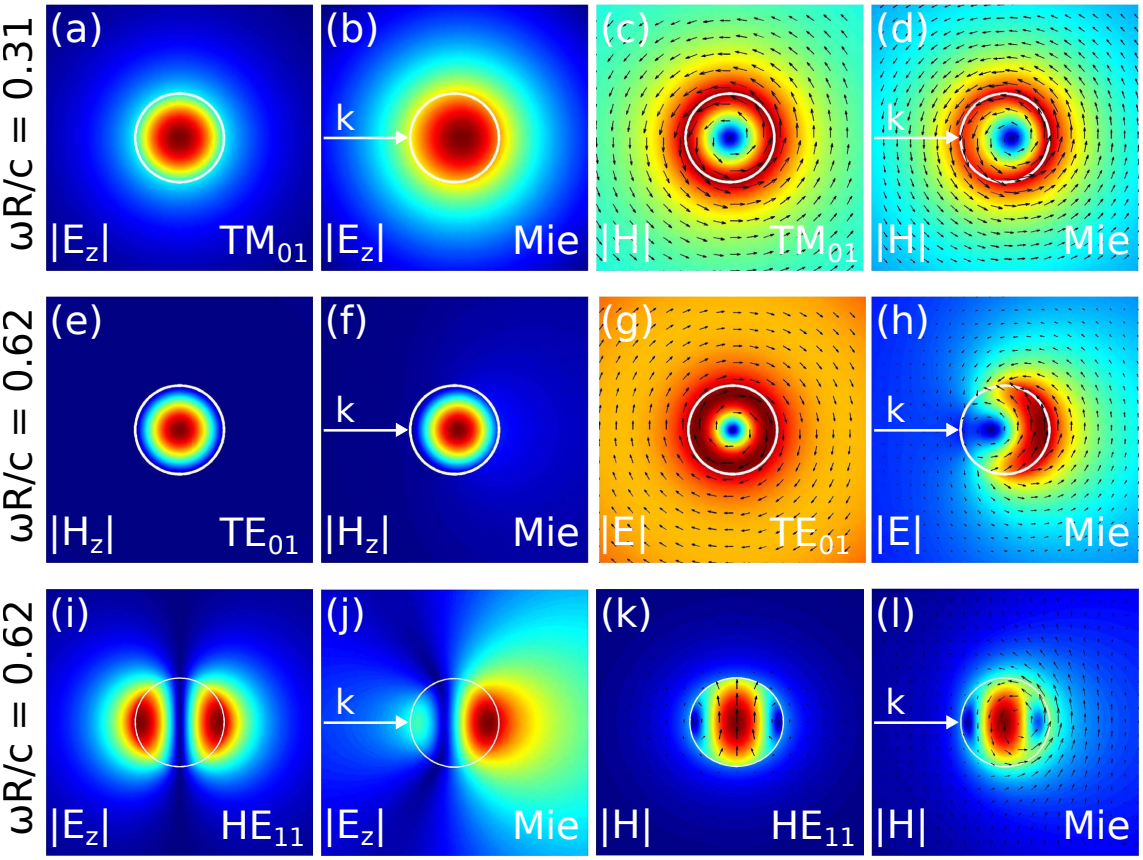

Figure 4.2: (a,c,e,g,i,k) Contour maps of the intensity of the relevant EM field components of the two lowest-order leaky modes of an infinite InP cylinder at $\lambda = 532$ nm (refractive index $n_{\mathrm{InP}} = 3.7$): (a,c) TM_{01} mode for radius $R = 26.25$ nm, which corresponds to $\omega R/c = 0.31$ in Fig. 4.1. (e,g) TE_{01} mode for radius $R = 52.5$ nm, which corresponds to $\omega R/c = 0.62$ in Fig. 4.1. (i,k) HE_{11} guided mode for radius $R = 52.5$ nm, which corresponds to $\omega R/c = 0.62$ in Fig. 4.1. (b,d,f,h,j,l) Correspondingly, contour maps of the intensity of the total EM field components resulting from the plane wave scattering by the same InP cylinders (the white arrow indicates the in-plane incident wavevector, with $\theta = 0°$, out-of-plane component $k_z = 0$), for the frequencies/radii exciting the three lowest order Mie resonances: (b,d) TM-polarized ($m = 0$) Mie resonance for radius $R = 26.25$ nm, which corresponds to $\omega R/c = 0.31$ in Fig. 4.1. (g,h) TE-polarized ($m = 0$) Mie resonance for radius $R = 52.5$ nm, which corresponds to $\omega R/c = 0.62$ in Fig. 4.1. (j,l) HE ($m = 1$) Mie resonance (excited with TM-polarized light) for radius $R = 52.5$ nm, which corresponds to $\omega R/c = 0.62$ in Fig 4.1. The small black arrows in (c,d,g,h,k,l) indicate directions of the in-plane electric or magnetic field vectors.

region are related to leaky modes across the light line,[146] and in turn to their corresponding Mie resonances, even if strongly shifted in $\omega R/c$. This is supported by the EM field patterns, which manifest their analogue symmetries, as shown above.

4.1.2 Finite NWs: Mie resonances and leaky modes

In order to address light absorption by finite NWs, Mie resonances (and, correspondingly, leaky modes) of the infinite NW ought to be studied first. This can be done as in Fig. 4.1, but properly taking into account the dispersive behavior of the semiconductor in the spectral regime of interest, including of course absorption. This is shown in Fig. 4.3 for an InP cylinder of radius $R = 20$ nm for vacuum wavelengths covering the visible and NIR domains up to $\lambda = 0.8\,\mu$m (shown also in eV for the sake of convention in this field). Within this spectral regime, such InP cylinder supports only the lowest-order leaky mode TM_{01}, and the very weakly guided (no cutoff) HE_{11} mode: the radius of the NW ($R = 20$ nm) is chosen so that coupling into the TM_{01} leaky mode predominates in the visible (high absorption). The corresponding $m = 0$ Mie resonance is clearly observed as a bright band in the extinction/absorption efficiencies, in turn associated to such leaky mode.

To distinguish the impact of spectral dispersion from that of absorption, we have plotted in Fig. 4.3a the leaky mode dispersion relation and Mie extinction efficiency neglecting absorptive losses $\mathrm{Im}(n_{InP}(\omega)) = 0$. Dispersion of $\mathrm{Re}(n_{InP}(\omega))$ indeed induces a bending of the lowest-order ($m = 0$) Mie resonance about $E \gtrsim 3$ eV; recall that this Mie resonance exhibits the symmetry of the TM_{01} mode. Upon introducing absorption (see Fig. 4.3b), the Mie resonance is substantially broadened, mainly at frequencies beyond $E \geq 2.5$ eV ($\lambda \leq 500$ nm) where InP exhibits large absorption coefficients. Consequently, larger absorption efficiencies are thus expected in such spectral domain, in turn coinciding for this NW radius with Mie resonances and leaky modes. To distinguish the polarization dependence of the absorption bands, we plot in Fig. 4.3c,d each contribution separately. As expected the TM-polarized Mie resonance at near-normal incidence is only excited with TM-polarized incident light.

Moreover, the angular span of the absorption bands can also be predicted from Fig. 4.3b, as inferred from the $k_z = (\omega/c)\sin\theta$ dependence of the absorption efficiencies (shown in Fig. 4.3c,d). In fact, broad angle absorption is observed in Fig. 4.3d for the $m = 0$ Mie resonance with a broad maximum at $\theta \sim 50°$, associated with the overlap with the TM_{01} leaky mode excitation; recalling that the extinction maximum without absorption (Fig. 4.3a) occurs at $\theta = 0°$ coinciding with the $m = 0$ TM mode, this indicates that absorption is somewhat enhanced at large angles through leaky mode coupling.

We now investigate the spectral/angular dependence of the absorption efficiency for finite NWs through numerical calculations, exploiting the physical insight provided above with regard to Mie resonances and leaky modes. We show in Fig. 4.4 the absorption efficiency Q_{abs} for a finite InP NW of radius $R = 20$ nm and length $L = 3$ μm, presented as in Fig. 4.3b. It should be noted that numerical absorption cross sections have been normalized to match Mie absorption efficiencies as $Q_{\mathrm{abs}} = C_{\mathrm{abs}}/(2RL)$. In fact, Q_{abs} closely resembles that of an infinite NW obtained through Mie

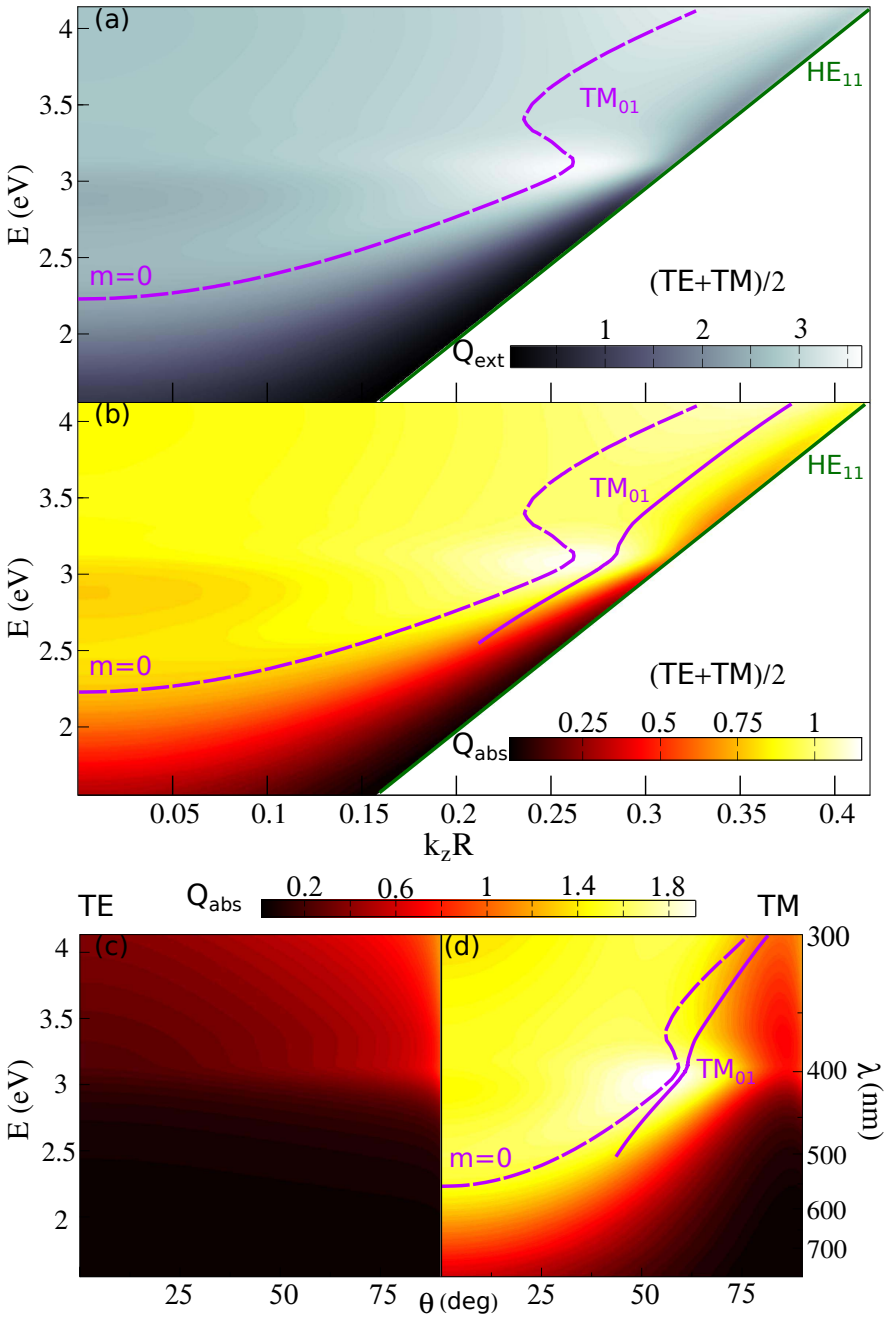

Figure 4.3: (a,b) The spectral dependence of the corresponding unpolarized Mie efficiency Q within the light cone as a contour map, calculated through Mie scattering (TE and TM polarization) for varying angle of incidence θ such that $k_z = (\omega/c)\sin\theta$, for InP nanowires of radius $R = 20$ nm, fully taking into account the complex, frequency-dependent InP refractive index $n_{InP}(\omega)$. (a) Absorptive losses are neglected $\mathrm{Im}(n_{InP}(\omega)) = 0$ and the extinction efficiency Q_{ext} is plotted; (b) Absorptive losses are fully accounted for and the absorption efficiency Q_{abs} is shown instead. (c,d) Same as in (b), but for TE (c) and TM (d) polarization separately as a function of the angle of incidence θ. In all cases, the dispersion relation $E = \hbar\omega$ (eV) vs $k_z R$ of leaky/guided modes from Eq. 1.42 is superimposed (solid curves), along with the complex (Mie-like, see text) $\omega(k_z)$ resonances (dashed curves), both for $\mathrm{Im}(n_{InP}(\omega)) = 0$.

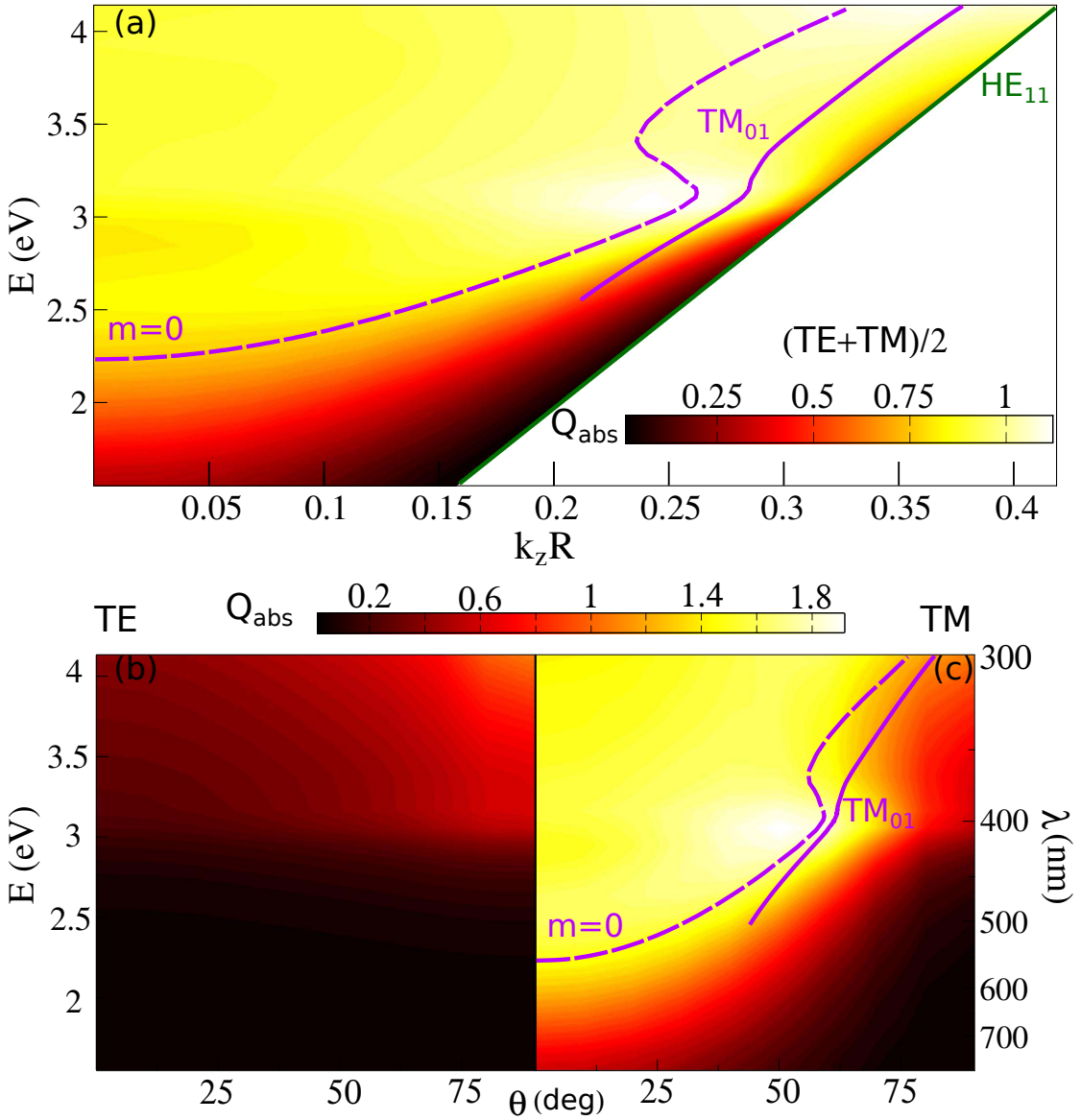

Figure 4.4: Contour map of the spectral dependence of the absorption cross section Q_{abs} for a finite InP nanowire of radius $R = 20$ nm and $L = 3$ μm, numerically calculated for varying angle of incidence θ such that $k_z = (\omega/c)\sin\theta$: (a) Unpolarized; (b) TE and (c) TM polarization, separately. The dispersion relation $\omega R/c$ vs $k_z R$ of leaky/guided modes from Eq. 1.42 for an infinite InP nanowire of the same radius is superimposed (solid curves), along with the complex Mie $\omega(k_z)$ resonances (dashed curves), both for $\text{Im}(n_{InP}(\omega)) = 0$.

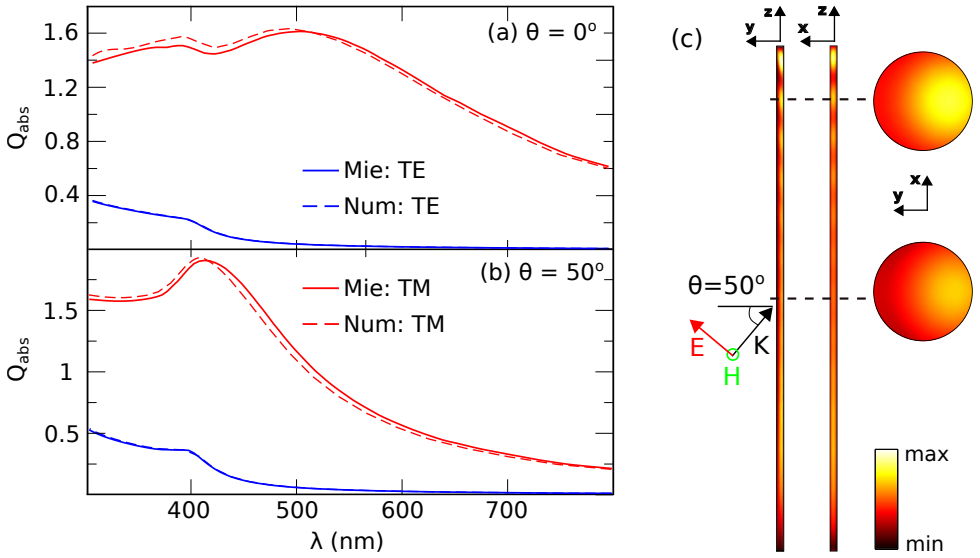

Figure 4.5: (a,b) Spectral dependence of the absorption efficiencies $Q_{\rm abs}(\lambda)$ for an InP nanowire of radius $R = 20$ nm, obtained from Fig. 4.3c,d (Mie calculation for an infinite NW, solid curves) and from Fig. 4.4b,c (numerical calculations for a finite NW of length $L = 3\,\mu$m, dashed curves), for the angles of incidence $\theta = 0°, 50°$. (c) Corresponding near-field images of the total absorbed power inside the NW at $\lambda = 400$ nm for $\theta = 50°$, for two planes along the NW and for two transverse cross sections, as depicted.

theory.

Next, we plot in Fig. 4.5a,b the spectral dependence of the absorption efficiencies at $\theta = 0°, 50°$ incidence, compared to that obtained for an infinite InP NW through Mie calculations. At normal incidence, the broad absorption band due to the lowest (TM, $m = 0$) Mie resonance is observed with two nearby local maxima ($\lambda = 400, 500$ nm) due to the InP absorption dispersion, the numerical calculation for the finite NW being nearly identical to that of infinite-NW Mie absorption. Also, the absorption efficiency at $\theta = 50°$ incidence numerically calculated for a finite NW closely resembles the Mie efficiency for an infinite NW, exhibiting a maximum exactly at the position of the Mie resonance at $\lambda = 400$ nm. This correspondence is somewhat expected for a wide angular range perpendicular to the NW axis. At parallel incidence one could expect the impact of the NW finiteness to become stronger, since coupling to guided modes (forbidden in the infinite case) is allowed. However, only the $\rm HE_{11}$ (no cutoff) guided-mode is present for such a thin NW, and turns out to be very weakly guided in this spectral regime: most of the EM energy in the mode is localized outside the NW (i.e., the mode area is very large), so that absorption is not efficiently enhanced. Therefore, for thin (and sufficiently long) NWs in the absence of other (higher-order) guided modes, absorption is fully described by Mie theory for infinitely long NWs, its maximum stemming from the lowest (TM, $m = 0$) Mie resonance (nearly indistinguishable from the contribution from its leaky-mode counterpart). For thicker NWs supporting strongly-coupled guided modes, the general principle holds, as expected, and the absorption efficiency for the finite NW might differ from the Mie $Q_{\rm abs}$, as will be described below.

Let us further explore the physical mechanisms underlying the strong absorption enhancements

observed. Recall that, close to parallel incidence, Mie resonances nearly coincide with their leaky modes of analogous symmetry close to the light line, due to the fact that their widths (in the $\omega-$ and k_z-space, respectively) are very small, as mentioned above. Light impinging obliquely onto the NW couples into leaky modes and is absorbed more efficiently than at normal incidence (regardless of the NW finiteness). To illustrate this effect, contour maps of the absorbed power $\langle P_{\rm abs}\rangle = (\pi c/\lambda){\rm Im}(\varepsilon_c)|E|^2$ are shown in Fig. 4.5c for the absorption maximum: large absorption is observed throughout the NW, which no doubt results from the $m = 0$ TM Mie resonance, correlated with the $\rm TM_{01}$ leaky mode excitation, as confirmed by the transverse patterns (see Fig. 4.2a,b). However, unlike for an infinite NW, the absorbed power is not uniform along the NW, but exhibits some oscillations, especially near the NW end opposite to the incident light, resulting from diffraction effects. Upon averaging along the NW, though, the absorbed power is nearly identical to that of a segment of length L of an infinite NW, so that $C_{\rm abs} = 2RLQ_{\rm abs}^{Mie}$.

4.1.3 Finite NWs: role of guided modes

In the previous section, the InP NW radius was such that no absorption stemming from guided modes might take place in the visible (spectral region with higher absorption for InP). Since coupling to guided modes, though forbidden for infinitely long cylinders, is plausible at finite NWs due to the light scattering at the NW end-facets,[143] we now consider a thicker InP NW that supports at least a guided mode in the visible. Again, we investigate first the Mie resonances (and, correspondingly, leaky modes) of the infinite NW, properly taking into account the dispersive behavior of the semiconductor in the spectral regime of interest as in Fig. 4.3. This is shown in Fig. 4.6 for an InP cylinder of radius $R = 40$ nm for vacuum wavelengths covering the visible and NIR domains: Within this spectral regime, such InP NWs support various lowest-order leaky/guided modes $\rm TE_{01}$, $\rm TM_{01}$, and $\rm HE_{11}$.

Bright bands in the extinction/absorption efficiencies are clearly observed at normal incidence that extend over most of the angular range due to the Mie resonances and associated leaky modes. As in Fig. 4.3a, we have plotted in Fig. 4.6a the dispersion relations of Mie resonances (dashed curves) and leaky/guided modes (solid curves), along with the Mie extinction efficiency, neglecting in all cases absorptive losses ${\rm Im}(n_{InP}(\omega)) = 0$: Note that InP dispersion now induces significant splittings in various modes. Among them, the $m = 0$ TE Mie resonance is remarkably split into three flat branches, all of them with the symmetry of the $\rm TE_{01}$ mode (not shown here). The $m = 1$ Mie resonance (with a hybrid TM and TE character analogous to the $\rm HE_{11}$ mode) exhibits two branches, the upper-one indeed bending over itself. The impact of dispersion on the lowest-order $m = 0$ TM Mie resonance is smaller: its lower branch, lying below 2.7 eV, barely changes; nonetheless, an upper branch emerges very close to the light line in the region 3.2–4 eV. At large angles, the corresponding $\rm TE_{01}$ and $\rm TM_{01}$ leaky modes appear, also exhibiting complicated band structures: the two curved branches of the leaky $\rm TE_{01}$ leading to three corresponding guided bands outside the light cone (strictly speaking, there are only two, since the lower two bands are bent/connected at higher k_z); and the alternating leaky/guided character of the $\rm TM_{01}$ mode, with a small guided band within 2.7–3.2 eV. As expected for the sake of symmetry, the

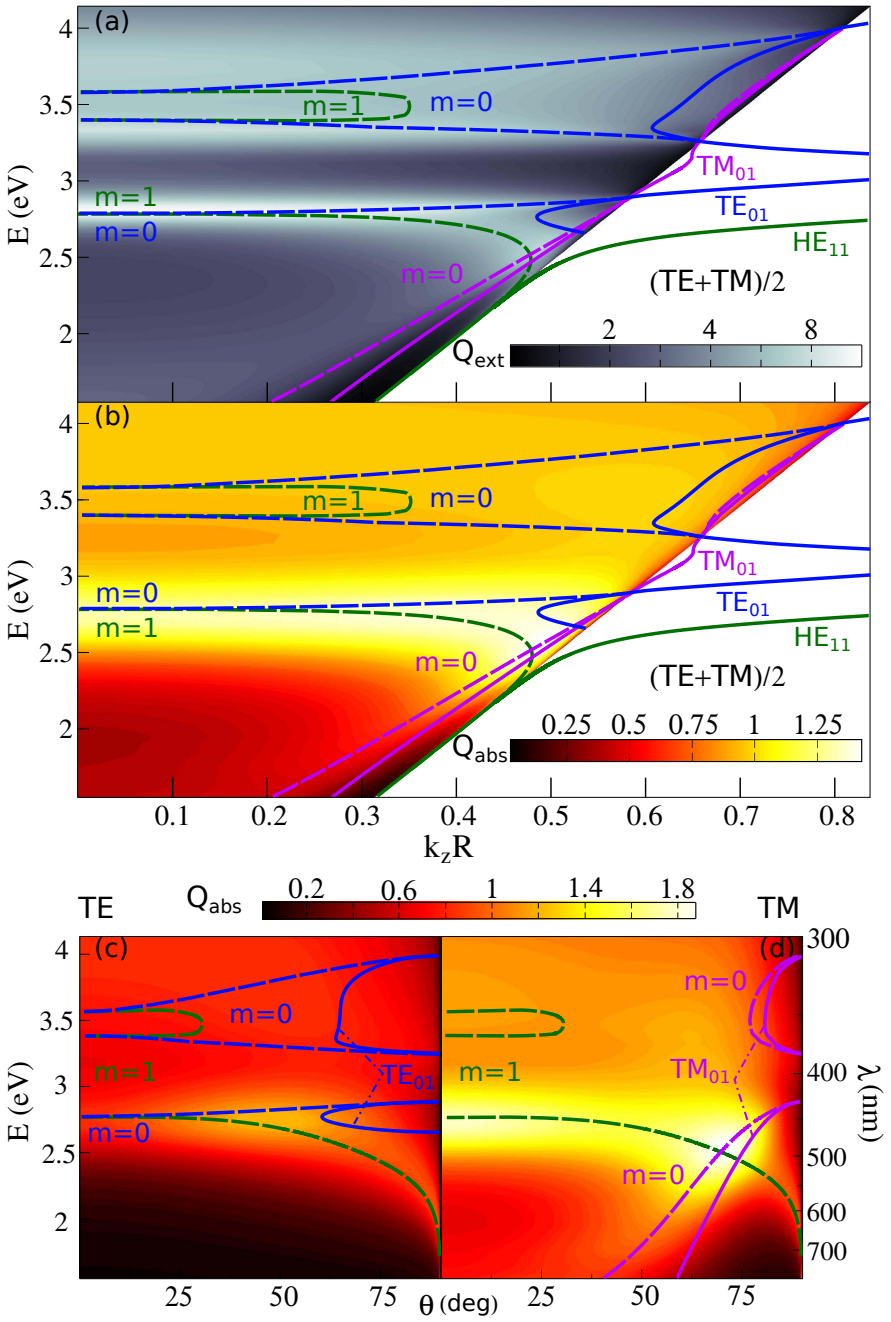

Figure 4.6: (a,b) The spectral dependence of the corresponding unpolarized Mie efficiency Q within the light cone as a contour map, calculated through Mie scattering (TE and TM polarization) for varying angle of incidence θ such that $k_z = (\omega/c)\sin\theta$, for InP nanowires of radius $R = 40$ nm, fully taking into account the complex, frequency-dependent InP refractive index $n_{InP}(\omega)$. (a) Absorptive losses are neglected $\mathrm{Im}(n_{InP}(\omega)) = 0$ and the extinction efficiency Q_{ext} is plotted; (b) Absorptive losses are fully accounted for and the absorption efficiency Q_{abs} is shown instead. (c,d) Same as in (b), but for TE (c) and TM (d) polarization separately as a function of the angle of incidence θ. In all cases, the dispersion relation $E = \hbar\omega$ (eV) vs $k_z R$ of leaky/guided modes from Eq. 1.42 is superimposed (solid curves), along with the complex Mie $\omega(k_z)$ resonances (dashed curves), both for $\mathrm{Im}(n_{InP}(\omega)) = 0$.

TE_{01} and TM_{01} modes cross the light line in all cases at the same frequency. On the other hand, note that the lowest guided HE_{11} mode remains largely unaltered and connects with the lowest $m = 1$ Mie band along the light line towards the low energy limit. However, the guided band also bends in the highly dispersive region around 3 eV, not shown since it lies beyond the $k_z R$ scale covered in Fig. 4.6a.

Upon introducing absorption (see Fig. 4.6b), Mie resonances are substantially broadened and/or even smeared out, as expected; for the sake of clarity, Fig. 4.6c,d shows the absorption efficiencies and mode dispersion for TE and TM polarization separately as a function of the angle of incidence θ. In fact, broad band and broad angle absorption is expected for the lowest $m = 1$ Mie resonances (HE_{11} mode) shown therein, indeed occurring for both TM- and TE-polarized light (see Fig. 4.6c,d), being stronger at normal incidence for TM polarization.[136] In addition, Fig. 4.6d reveals that the TM_{01} leaky mode band lies, as mentioned in the preceding section, close to the $m = 0$ TM Mie resonance at large oblique angles, which yields a large absorption area at ~ 2.5 eV (500 nm) near $\theta \simeq 70°$, as a result in turn of the overlap with the $m = 1$ Mie band. In the low energy region below 2.5 eV, this $m = 0$ TM Mie resonance continues, as mentioned above, as a weak absorption band for smaller angles of incidence. The lowest $m = 0$ TE Mie branch yields a weaker absorption maximum in Fig. 4.6c for $\theta \simeq 50°$ at ∼450 nm. In the blue part of the spectrum and into the UV, InP absorptive losses increase, so that the above mentioned upper branches of the $m = 0$ TE and and $m = 1$ TM Mie resonances result in (spectrally and angularly) broaden bands of moderate absorption.

We now calculate numerically the absorption cross section in the case of a finite NW, as shown in Fig. 4.7 for $L = 3$ μm. $Q_{\rm abs}(\omega, \theta)$ closely resembles from a qualitative standpoint that of an infinite NW obtained through Mie theory (see Fig. 4.6b,d) at normal incidence, confirming: (i) the $m = 0, 1$ Mie resonances at $\lambda \sim 450$ nm; (ii) a broad absorption region in the UV part of the spectra ($E > 3$ eV, $\lambda < 400$ nm), where the (split) branches of the $m = 0$ (TE) and $m = 1$ (hybrid HE_{11}) Mie resonances are smeared out due to the strong InP absorption. Nevertheless, a significantly brighter (more absorptive) area near 2.5 eV ($\lambda = 500$ nm) appears at grazing $\theta = 90°$ incidence in Fig. 4.7a, which differs from all the other bands lying nearby for an infinite NW ($m = 0, 1$ Mie resonances and the two $m = 0$, TE and TM leaky bands, see Fig. 4.6b,d): it is clearly a polarization-independent, grazing-angle excitation (see Fig. 4.7b,c) occurring only for a finite NW. In addition to this bright band, higher absorption is observed in the finite NW at grazing incidence into the UV region, presumably owing to the interplay with the complex upper branches of the $m = 0$ (TE and TM) leaky/guided modes.

To make clear the differences, we also plot in Figs. 4.8 and 4.9 the spectral dependence of the absorption efficiencies $Q_{\rm abs}$ at parallel and perpendicular incidence, compared to that obtained for an infinite InP NW through Mie calculations. At incidence perpendicular to the NW axis (see Fig. 4.8a), the absorption efficiency numerically calculated for a finite NW closely resembles the Mie efficiency for an infinite NW, exhibiting maxima exactly at the frequency of both Mie resonances (which coincide). Incidentally, the contour maps showing the absorbed power in Fig. 4.8b,c nicely manifest the interplay of those two modes: TE polarization seems to predominantly couple to the $m = 0$ (TE) Mie resonance (compare Fig. 4.8c to the mode patterns in Fig. 4.2g,h);

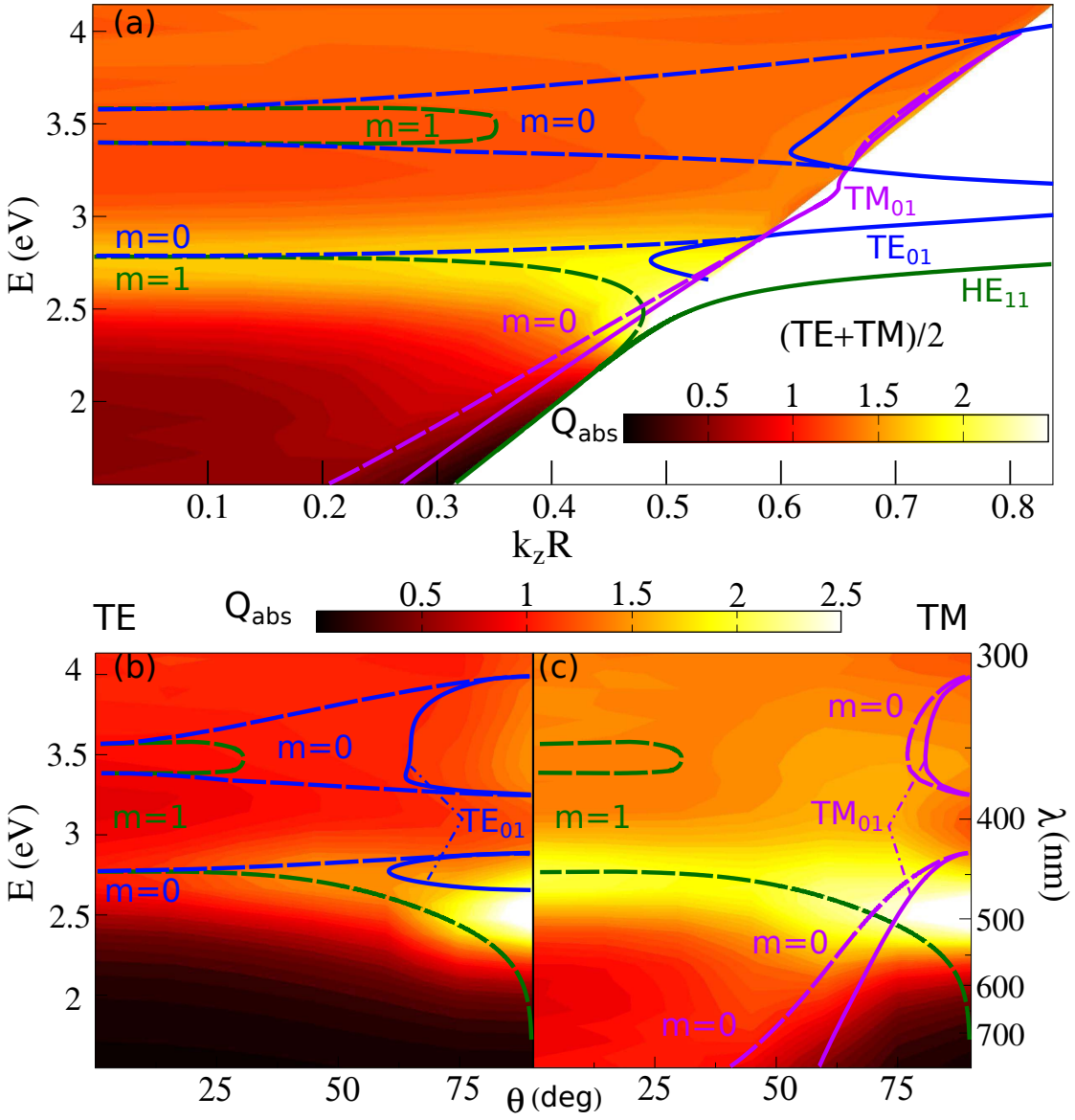

Figure 4.7: Contour map of the spectral dependence of the absorption cross section Q_{abs} (both TE and TM polarization) for a finite InP nanowire of radius $R = 40$ nm and $L = 3$ μm, numerically calculated for varying angle of incidence θ such that $k_z = (\omega/c)\sin\theta$. (a) Unpolarized; (b) TE and (c) TM polarization, separately. The dispersion relation $\omega R/c$ vs $k_z R$ of leaky/guided modes from Eq. 1.42 for an infinite InP nanowire of the same radius is superimposed (solid curves), along with the Mie $\omega(k_z)$ resonances (dashed curves), both for $\text{Im}(n_{InP}(\omega)) = 0$.

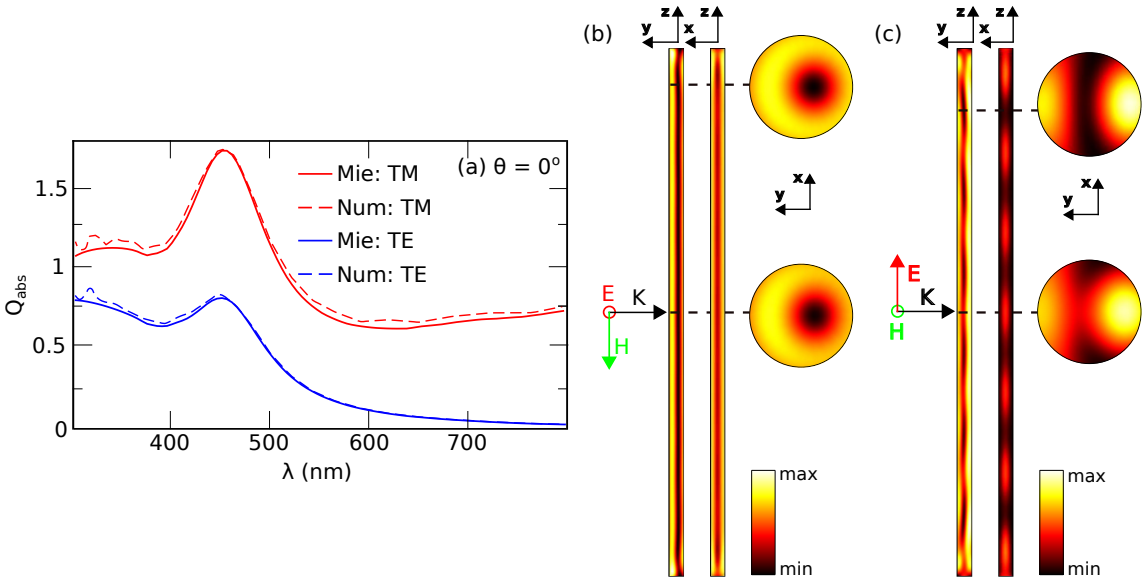

Figure 4.8: (a) Spectral dependence of the absorption efficiencies $Q_{\rm abs}(\lambda)$ for an InP nanowire of radius $R = 40$ nm, obtained from Fig. 4.6c,d (Mie calculation for an infinite NW) and Fig. 4.7b,c (numerical calculations for a finite NW of length $L = 3\,\mu$m), for the angle of incidence $\theta = 0°$. (b-c) Corresponding near-field images of the total absorbed power inside the NW at $\lambda = 450$ nm for (b) TE and (c) TM polarization for two planes along the NW, including also a transverse cross section, as depicted.

whereas TM polarization (Fig. 4.8c) can only couple into the $m = 1$ (HE_{11}) hybrid resonance (see Fig. 4.2i,j). It should be recalled that this hybrid mode becomes predominantly TM near normal incidence, as pointed out also in Ref.,[136] thus being weakly excited by TE light (as mentioned above). In any case, Mie calculations for an infinite NW reproduce very accurately the absorption efficiencies for finite NWs (see Fig. 4.8a), and fairly well the EM fields inside the NW, except for some weak oscillations associated to finite size diffraction (as commented in the preceding section). These similarities extend over a wide angular range up to grazing incidence.

At parallel incidence, however, the impact of the NW finiteness becomes stronger and the absorption efficiency for the finite NW differs both qualitatively and quantitatively from the Mie $Q_{\rm abs}$ (see Fig. 4.9a). The absorption maximum is slightly blue-shifted, and more importantly, remarkably larger for the finite NW throughout the UV. In fact, this larger, blue-shifted maximum does not correspond to the (TM, $m = 0$) Mie resonance; rather, it is due to the (NW-finiteness-induced) excitation of the lowest-order HE_{11} guided mode, as demonstrated below.

Recently, a very similar configuration has been experimentally described,[143] theoretically demonstrating that guided modes come into play at such NW radii, since light scattering at the finite NW end-facets provides the extra momentum (phase matching) to allow coupling. In this particular range, it is the HE_{11} guided mode the one responsible for such coupling and the associated enhanced absorption. Recall that, unlike for the $R = 20$ nm NW, the HE_{11} guided mode becomes for this thicker NW radius ($R = 40$ nm) a properly guided mode with significant electric field intensity inside the NW at the spectral regime where absorption is relevant. Transverse and longitudinal contour maps of the power $\langle P_{\rm abs}\rangle$ absorbed along the NW, shown in Fig. 4.9b for the

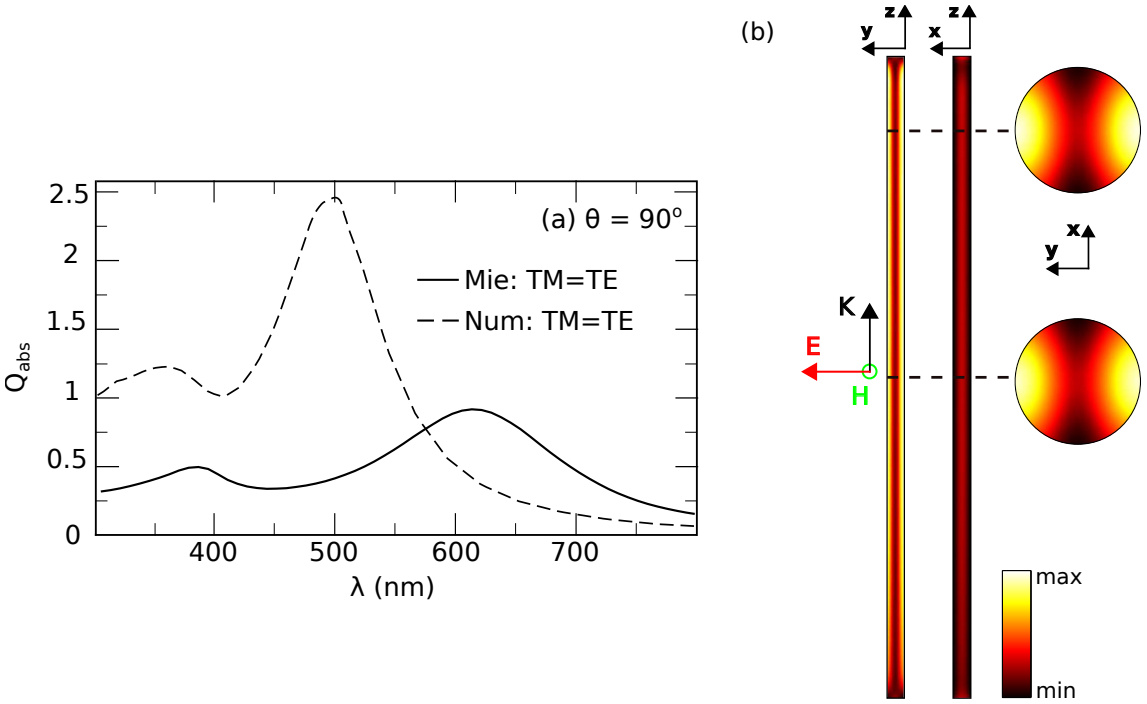

Figure 4.9: (a) Same as in Fig. 4.8 but for $\theta = 90°$. (b) Corresponding near-field images of the total absorbed power inside the NW at $\lambda = 500$ nm for $\theta = 90°$, for two planes along the NW, including also a transverse cross section, as depicted.

absorption maximum at grazing incidence, support this reasoning: large absorption is observed throughout the NW with the HE_{11} guided-mode symmetry (see also Fig. 4.2i-l).

Therefore, although Mie scattering theory provides useful insight into the absorption efficiency of finite NWs associated to Mie resonance and leaky-mode excitation for a broad angular range, it largely underestimates absorption at incidence nearly parallel to the NW axis, leading to enhanced guided mode coupling (forbidden in infinite NWs), which in turn provide strong absorption cross sections. A contour map of $C_{\rm abs} = 2RLQ_{\rm abs}$ properly accounting for the finite NW length, such as those depicted in Figs. 4.4 and 4.7, is needed to properly tune and enhance absorption, carefully accounting for the dispersive behavior of the semiconductor material in the spectral region of interest (large absorption).

For light incident near normal to the NW axis, Mie scattering faithfully predicts absorption. Thus the NW dimensions can be correspondingly tuned to match a large, Mie-resonant absorption band (or bands), in turn continued as a leaky mode for very large angles of incidence, which can conveniently be split into two (or more) bands (for broad band absorption) due to the InP (and other semiconductor) refractive index dispersion. Near grazing incidence, guided modes should also be tuned to remarkably boost absorption for finite NWs due to light scattering at the NW end-facets. Furthermore, if broad angle incidence is experimentally feasible, our theoretical analysis reveals that both kinds of absorption mechanisms can coincide in a broad spectral region, thus leading to remarkably large absorption efficiencies. Thicker NWs can also be considered supporting several guided modes,[133] very likely enhancing absorption cross sections at the expense of diminishing

efficiencies.

4.2 High-Contrast Fano Resonances in Single Dielectric Nanorods

Next, we explore the optical resonances in much shorter semiconductor nanowires (namely, nanorods), where Fabry-Perot resonances appear with a variety of (even asymmmetric, i.e. Fano) line shapes. In this regard, the emergence of distinct Fano resonances in all-dielectric nanostructures was largely unexplored. Only very recently some attention has been paid to Fano resonances in all-dielectric nanoparticles, nonetheless requiring either nanosphere dimers, oligomers, nanobelts, nanocrosses, or more complex arrangements.[147–153] Recall that, in general, very complex metal nanostructures are required to obtain remarkable Fano resonances;[154,155] whilst those found in simple geometries such as single metallic nanorods[54,156–159] or nanostars[160] are relatively faint.

In this section we study single semiconductor nanoparticles with simple finite cylindrical geometry as a platform to support strong and narrow Fano resonances.[49] Note that semiconductor nanobelts and nanorods a few hundred nanometers long, to be distinguished from $> 1\mu$m nanowires, have been investigated to address some interesting scattering properties, in connection with their shape dependence[44,161,162] or with the transition of Mie resonances from a nanosphere to a short nanocylinder,[163] nonetheless revealing no Fano line shapes; except for a low-contrast measured for nanobelts.[148] We first study the scattering efficiencies of semiconductor nanorods with diameter below ~ 200 nm, thus supporting a few guided modes while exhibiting lowest Mie resonances in the optical domain. It is shown that nanorod lengths of about half-micron ensure that low-order (narrow and intense) Fabry-Perot resonances of the supported guided modes overlap with the Mie resonances, leading to either strongly or weakly asymmetric (Fano) line shapes with a large contrast over the background. The corresponding higher or lower degree of interference is then explained through a theoretical model as a result of the far-field overlap of broad Mie modes with narrow Fabry-Perot resonances, leading to an heuristic quasi-analytical expression for the Fano line shapes that fully reproduces the numerical scattering cross sections, in agreement also with a generalized Fano formula.

4.2.1 Scattering cross sections of semiconductor nanorods

First, we present in Fig. 4.10 numerical calculations of the scattering efficiency spectra $Q_{\rm sca}$ of semiconductor nanorods with varying length L and fixed radius $R = 80$ nm, carried out through SCUFF;[109,110] the scattering geometry is depicted therein. The refractive index is fixed at $n = 3.5$ corresponding to GaP at $\lambda = 400$ nm;[144] recall that, without absorptive losses, the extinction efficiency is identical to the scattering one $Q_{\rm ext} = Q_{\rm sca}$. For simplicity we have neglected the (slight) dispersion of the real part of the refractive index in the spectral range $\lambda = 400 - 1000$ nm to neatly determine the impact of nanorod dimensions on the spectral properties of all resonances; however, as long as absorption is negligible,[164] our results could be applicable throughout the visible and near-infrared and to any other semiconductor with similar refractive index, such as

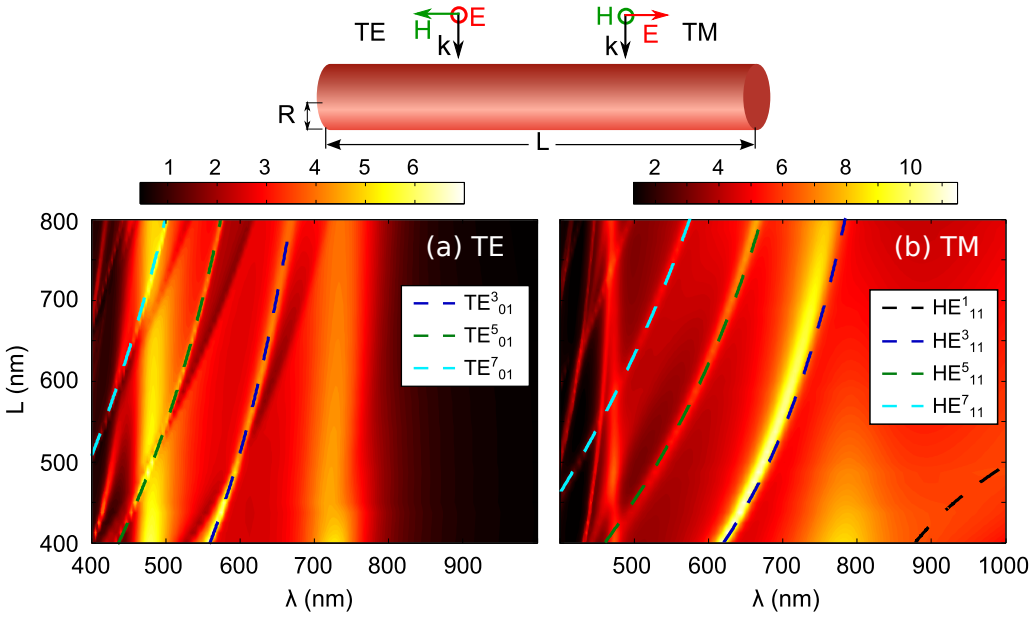

Figure 4.10: Color maps of the spectral dependence of the scattering efficiency Q_{sca} for a finite semiconductor ($n = 3.5$) nanowire of radius $R = 80$ nm and normal incidence, numerically calculated (SCUFF) for varying length L: (a) TE and (b) TM polarization, separately. The condition for Fabry-Perot resonances of the corresponding guided modes from Eq. 4.4 is superimposed (colored curves). The schematic reveals the scattering geometry.

cristalline Si[32,34,44] or i.e. GaAs, InP, etc., upon scaling wavelength and nanorod dimensions accordingly if needed. The nanorod radius is fixed at $R = 80$ nm (shown above to be in the range of interest for coupling to few lowest-order guided modes), whereas the length is varied between $L = 400 - 1000$ nm. Indeed, since the refractive index is fixed, variations of the nanorod radius can be easily inferred from Fig. 4.10, considering the corresponding Q_{sca} for nanorod length L such that the aspect ratio L/R is preserved, with wavelength accordingly scaled. Larger aspect ratios lead to denser spectra with overlapping resonances.

Basically, leaving aside broad dispersionless (L-independent) resonances (to be associated to lowest-order Mie resonances of the infinite cylinder), a few narrow resonances appear for both polarizations that redshift for increasing nanorod length crossing in different ways the broader resonances. Essentially, we assign them to Fabry-Perot resonances occurring at multiples of half-wavelength of the guided modes supported by the semiconductor nanorod, identical to those involved in nanowire photoluminescence.[114] The resonance condition is thus described by:

$$k_z(\omega)L^* = \pi l, l = 1, 2, 3, ..., \tag{4.4}$$

k_z being the guided mode complex wavevector along the cylinder axis, $\omega/c = 2\pi/\lambda$ (λ is the wavelength in vacuum), and L^* an effective wavelength very close to L that depends on the guided mode involved,[114] as explained below. $k_z(\omega)$ itself is frequency dependent, and obeys the dispersion relation given by Eq. 1.42. For our purpose, only guided modes with $k_z > \omega/c$ will be considered, propagating along the nanorod, and bouncing back and forth so that Fabry-Perot res-

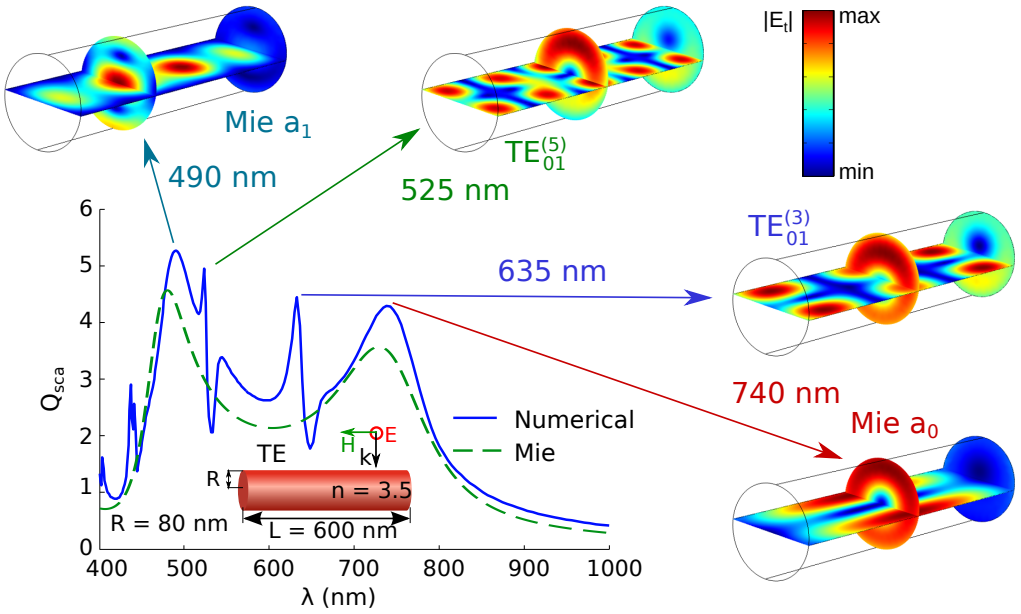

Figure 4.11: Spectral dependence of the scattering efficiency $Q_{\rm sca}$ (blue solid curve) at normal incidence (TE polarization) for a finite semiconductor ($n = 3.5$) nanorod of radius $R = 80$ nm and fixed length $L = 600$ nm, numerically calculated (SCUFF). Mie calculation for an infinite cylinder with the same radius is also included (green dashed curve). Contour color maps are also included at various fixed wavelengths corresponding to Mie and FP resonances, showing the transverse electric field amplitude $|E_t| = (|E_r|^2 + |E_\phi|^2)^{1/2}$ on the longitudinal and (two) transverse cross sections of the nanorod.

onances occur. Only the three lowest-order guided modes play a role for the nanorod dimensions and spectral region shown above: the no cutoff, lowest order hybrid HE_{11} mode, and the pure transverse TM_{01} and TE_{01} modes.

The corresponding FP resonances, from Eqs. 4.4 and 1.42, are tagged in Fig. 4.10 through a superscript indicating the l-th FP-order in Eq. 4.4. Note that no FP resonances associated to the TM_{01} are indicated. Indeed, the frequency above which this mode becomes guided is the same as that of the TE_{01} mode, but it is weakly guided with a small wavevector $k_z \gtrsim \omega/c$ (large wavelength) so that no significant FP are excited within the ω, L domain in Fig. 4.10b. For TE polarization, most FP resonances stem from the TE_{01} mode, as expected due to symmetry. This mode has a complex reflection coefficient, which we account for by assuming that the effective length in Eq. 4.4 is slightly different from the nanorod length $L^* = 1.05L$.[114] The agreement of the FP condition for $\mathrm{TE}_{01}^{(l)}$ ($l = 1, 3, 5, 7, ...$) with the resonances in Fig. 4.10a is excellent (recall no even resonances are present at normal incidence in Fig. 4.11). Likewise, very good agreement is found in TM polarization for FP resonances $\mathrm{HE}_{11}^{(l)}$ ($l = 1, 3, 5, 7, ...$), for which the reflection coefficient is real,[114] so that $L^* = L$. Low-order FP resonances associated to higher-energy guided modes appear in the high-frequency regime too.

In addition to those narrow FP resonances, a background pattern with various broad resonances nearly dispersionless is observed in Fig. 4.10. To properly characterize them, we present the numerical calculations of $Q_{\rm sca}$ for a fixed nanorod length L in Figs. 4.11 and 4.12; the Mie-like

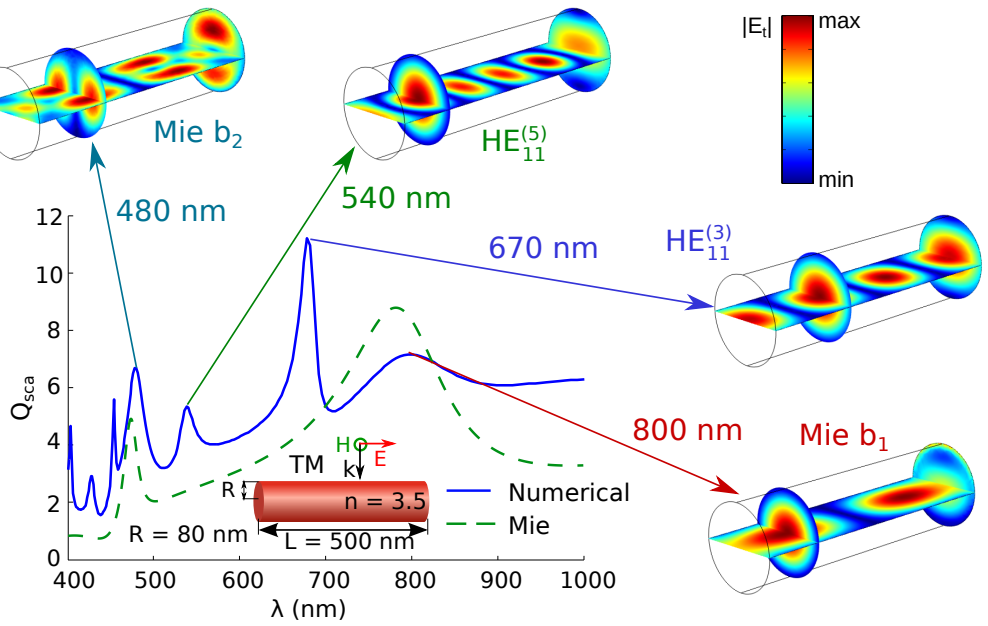

Figure 4.12: Spectral dependence of the scattering efficiency Q_{sca} (blue solid curve) at normal incidence and TM polarization for a finite semiconductor ($n = 3.5$) nanorod of radius $R = 80$ nm and fixed length $L = 500$ nm, numerically calculated (SCUFF). Mie calculation for an infinite cylinder with the same radius is also included (green dashed curve). Contour color maps are also included at various fixed wavelengths corresponding to Mie and FP resonances, showing the transverse electric field amplitude $|E_t| = (|E_r|^2 + |E_\phi|^2)^{1/2}$ on the longitudinal and (two) transverse cross sections of the nanorod.

scattering efficiencies Q_{Mie} are also included for normal incidence with respect to the nanorod axis. From Eq. 4.1, the scattering efficiencies at normal incidence obey the following expressions[5]

$$Q_{\text{Mie}}^{(TE)} = \frac{2}{kR}\left[|a_0|^2 + 2\sum_{m=1}^{\infty}|a_m|^2\right], \tag{4.5a}$$

$$Q_{\text{Mie}}^{(TM)} = \frac{2}{kR}\left[|b_0|^2 + 2\sum_{m=1}^{\infty}|b_m|^2\right], \tag{4.5b}$$

where a_0, a_m, b_0, b_m are the corresponding Mie scattering coefficients for a plane wave impinging perpendicular to the infinite nanocylinder, polarized either perpendicular (TE) or parallel (TM) to its axis (see Section 1.4.1).

For TE polarization (see Fig. 4.11), three narrow resonances are clearly identified, two of them at least revealing a strong asymmetric lineshape, standing over broader resonances. Those two broad resonances centered at $\lambda = 740$ and 490 nm, also observed in the Q_{Mie}, obviously correspond to the two lowest-order Mie resonances stemming from Mie coefficients a_0 and a_1; a_0 can be considered an effective longitudinal magnetic dipole (eMD), and a_1 is the transverse electric dipole (ED) contribution. This is in turn confirmed by the transverse electric field patterns inside the nanorod numerically calculated at $\lambda = 740, 490$ nm through FEM simulations (COMSOL),

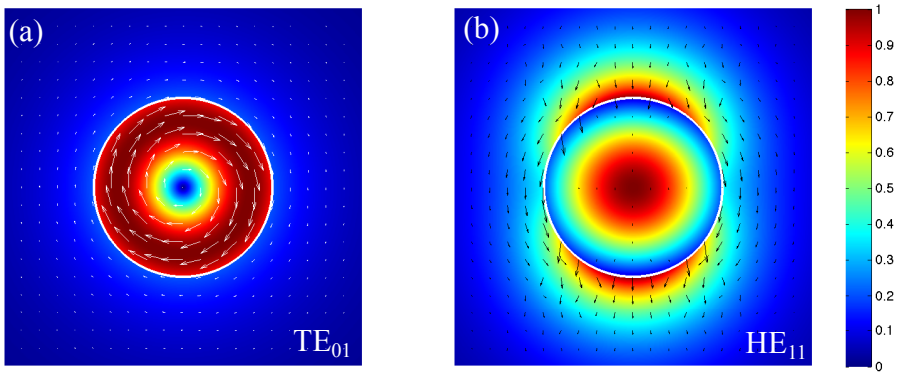

Figure 4.13: Color maps of the electric field norm of guided modes supported by an infinite semiconductor ($n = 3.5$) cylinder of radius $R = 80$ nm at the following wavelengths: (a) TE_{01} mode at $\lambda = 635$ nm, and (b) HE_{11} mode at $\lambda = 670$ nm. The arrows represent the direction of the in-plane components of the electric field, with size proportional to the norm.

also included in Fig. 4.11. Near-field maps inside the nanorod are also shown at the narrow Fano resonances for $\lambda = 635$ nm and 525 nm to guide their assignment: both of them correspond to the TE_{01} guided mode predicted by the FP condition (Eq. 4.4) with $l = 1, 3$, as confirmed through the following arguments. The transverse electric field maps exhibit a ring shape with mostly azimuthal polarization; the transverse magnetic field, not shown, is dominated by its axial component. Both features can be unequivocally associated to the TE_{01} guided mode of the infinitely long cylinder,[114] as confirmed by the ring-shaped, in-plane electric field pattern with rotating polarization depicted in Fig. 4.13a for TE_{01} guided mode at $\lambda = 635$ nm (the one at $\lambda = 525$ nm, nearly identical, is not shown). On the other hand, the number of nodes observed in the near-field maps along the nanorod length agrees well with the expected FP order: $l = 3, 5$, respectively, for the Fano resonances at $\lambda = 635$ and 525 nm.

Before describing in detail the asymmetry of such strong Fano lineshapes, let us now discuss the TM polarization in Fig. 4.12. Note that similar narrow resonances are identified over the broad Mie-like resonances. In this case, broad Mie resonances stem from b_0, b_1, b_2 coefficients with, respectively, effective longitudinal electric dipole (eED), and transverse magnetic dipole (MD) and quadrupole character; the lowest-order b_0 term being extremely broad and lying at lower frequencies not shown in Fig. 4.12 (incidentally, it can be observed in Fig. 4.10b at $\lambda \gtrsim 1\,\mu$m). Narrow resonances at $\lambda = 670$ nm and 540 nm stem both from the $l = 3, 5$ FP orders of the HE_{11} guided mode, as determined by the FP condition Eq. 4.4. Indeed, the electric field maps inside the nanorod (transverse centered lobe with hybrid polarization), also included, agree very well with the expected in-plane electric field pattern of the HE_{11} guided mode at $\lambda = 670$ nm for an infinite cylinder (see Fig. 4.13b).

However, such narrow resonances exhibit a weakly asymmetric line shapes, much unlike the highly asymmetric Fano resonances in TE polarization described above, even though some of the modes involved in both kind of resonances have identical FP orders; recall that FP order has been associated to the parity order used to describe Fano/Lorentz line shapes in metallic nanorods.[159] Therefore, further investigation is needed to account for this richer phenomenology found for

semiconductor, rather than metal, nanorods supporting a wide variety of both broad and narrow (high-contrast) resonances.

4.2.2 Interplay of Fabry-Perot resonances and Mie modes

Therefore, to fully understand the emergence of Fano resonant modes for semiconductor nanorods, we propose a simple model combining (transverse) Mie scattering resonances (playing the role of the broad continuum) and (longitudinal) FP resonances (dark modes). Near-field coupling between modes within a single nanorod is rather complex. This was shown in the case of metal nanorods,[54] where the near-field pattern of the narrow resonant mode predominates within the spectral region of the Fano line shape; likewise, the near-field patterns at resonances in Figs. 4.11 and 4.12 are dominated by the FP resonances. Hence, we assume that the interference is more clearly manifested in the far field, expressing the scattering cross section in the following manner:

$$\mathrm{SCS}(\omega) = \int d\Omega \frac{\Re\left\{\mathbf{E}_\Omega(\mathbf{r},\omega) \times \mathbf{H}^*{}_\Omega(\mathbf{r},\omega)\right\}}{2|E_0|^2}, \tag{4.6}$$

where the angular- and frequency-dependent far-field pattern $\mathbf{E}_\Omega(\mathbf{r},\omega)$ has two contributions:

$$\mathbf{E}_\Omega(\mathbf{r},\omega) = \mathbf{E}^{(\mathrm{Mie})}(\mathbf{r},\omega) + \mathbf{E}^{(\mathrm{FP})}(\mathbf{r},\omega), \tag{4.7}$$

stemming from transverse Mie-like scattering $\mathbf{E}^{(\mathrm{Mie})}$ and the longitudinal Fabry-Perot resonances $\mathbf{E}^{(\mathrm{FP})}$.

At this point, the crucial issue is what exactly governs the higher/lower degree of interference in Eqs. 4.6 and 4.7: basically, the far-field integral over solid angles in Eq. 4.6 which both electric field amplitudes in Eq. 4.7 contribute to. To shed light on it, we now plot the far-field pattern associated with all (Mie and FP) resonances. Mie-like far-field patterns are calculated numerically (SCUFF) to properly account for the finiteness of the NW. They resemble over a long interval of polar angles the Mie theory calculation for an infinite cylinder (Eqs. 4.5), being nearly identical at a far-field plane perpendicular to the nanorod axis, while expectedly breaking the translational invariance along the nanorod axis so that the angular pattern vanishes at its poles. These Mie-like patterns (shown in Figs. 4.14a, 4.14d and 4.15a) are calculated within the corresponding broad Mie resonances, but at a fixed wavelength chosen so that no overlap occurs with the narrow FP resonances.

Far-fields of Fabry-Perot resonances cannot be extracted from the numerical calculations, due to the fact that the resulting patterns are dominated by the profiles of the background Mie resonance. To infer the far-field profile of such (isolated) FP resonances, we extrapolate the expression for the far-field emitted/scattered by a 1D line current.[113,114] For transverse electric or magnetic modes with (magnetic or electric, respectively) polarization along the nanorod axis, the electric far

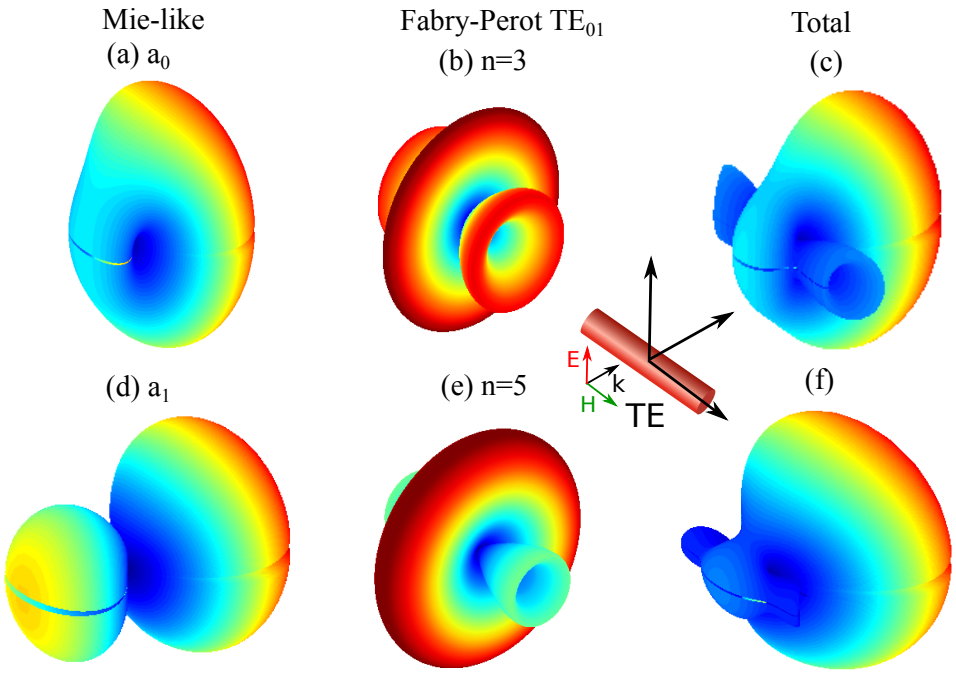

Figure 4.14: Far-field angular scattering patterns at normal incidence for TE polarization for a finite semiconductor ($n = 3.5$) nanorod of radius $R = 80$ nm and fixed length $L = 600$ nm, calculated through: (a,c,d,f) SCUFF numerical calculations at the following wavelengths: (a) $\lambda = 740$ nm (isolated a_0 mode) and (d) $\lambda = 490$ nm (isolated a_1 mode); (c) $\lambda = 635$ nm and (f) $\lambda = 525$ nm at Fano resonance maxima. (b,e) 1D line current model (Eqs. 4.8 and 4.10) for the following odd FP resonances (see Eq. 4.4): $TE_{01}^{(3)}$ at $\lambda = 635$ nm, (e) $TE_{01}^{(5)}$ at $\lambda = 525$ nm. The inset depicts the scattering geometry.

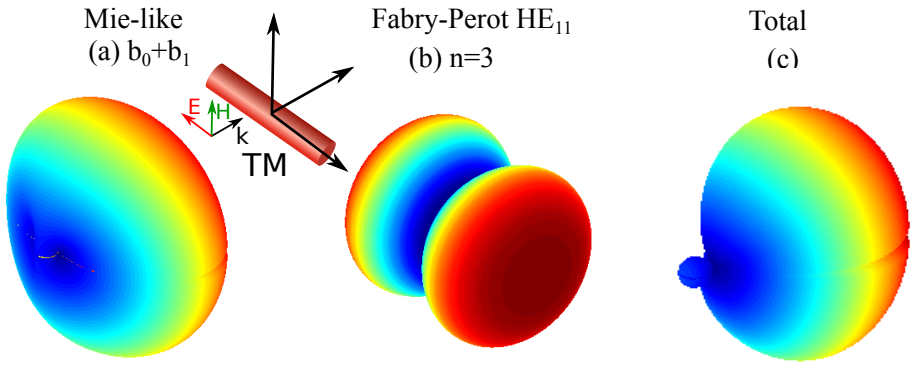

Figure 4.15: Far-field angular scattering patterns at normal incidence for TM polarization for a finite semiconductor ($n = 3.5$) nanorod of radius $R = 80$ nm and fixed length $L = 500$ nm, calculated through: (a,c) SCUFF numerical calculations at the following wavelengths: (a) $\lambda = 800$ nm (isolated b_1 mode) and (c) $\lambda = 670$ nm at a Lorentz resonance. (b) 1D line current model (Eqs. 4.9 and 4.10) for the odd FP resonances (see Eq. 4.4) $HE_{11}^{(3)}$ at $\lambda = 670$ nm. The inset depicts the scattering geometry.

field exhibits axial symmetry, so its only component is the polar one:

$$E_\theta^{(\mathrm{FP})} = \frac{\imath k_0 \eta_0 S_{xy}}{4\pi} \sin\theta \int_{-L/2}^{L/2} J(z) e^{-\imath k_0 z \cos\theta} dz, \tag{4.8}$$

where η_0 stands for the vacuum impedance and $S_{xy} = \pi R^2$ is the geometrical cross section of the nanorod. For hybrid guided modes with non-transverse polarization, such as the HE_{11} mode, the far-field pattern can be written as follows:

$$E_\theta^{(\mathrm{FP})} = \frac{\imath k_0 \eta_0 S_{xy}}{4\pi} \cos\theta \sin\phi \int_{-L/2}^{L/2} J(z) e^{-\imath k_0 z \cos\theta} dz, \tag{4.9a}$$

$$E_\phi^{(\mathrm{FP})} = \frac{\imath k_0 \eta_0 S_{xy}}{4\pi} \cos\phi \int_{-L/2}^{L/2} J(z) e^{-\imath k_0 z \cos\theta} dz. \tag{4.9b}$$

The 1D current density of the FP resonances at normal incidence is expressed in the following manner:

$$J(z) = J_\gamma \frac{\cos k_z^{(\gamma)}(\omega) z}{\cos k_z^{(\gamma)}(\omega) L^*/2}, \tag{4.10}$$

where γ denotes the guided mode involved, J_γ being an unknown constant depending on each mode. The above expression has been deduced from the 1D current used for metallic nanorods at normal incidence,[159] so that only odd FP resonant modes (see Eq. 4.4 for $l = 1, 3, ...$) are accounted for, which suffices for our purpose.

We can now qualitatively determine the emergence of Fano line shapes at the corresponding FP resonances. The highly asymmetric Fano resonance for TE polarization at $\lambda \approx 635$ nm in Fig. 4.11 results from the $TE_{01}^{(3)}$ FP mode and lies within the broad a_0 Mie resonance. Both exhibit far-field patterns that strongly overlap (see Figs. 4.14a and 4.14b), specially the large central ring

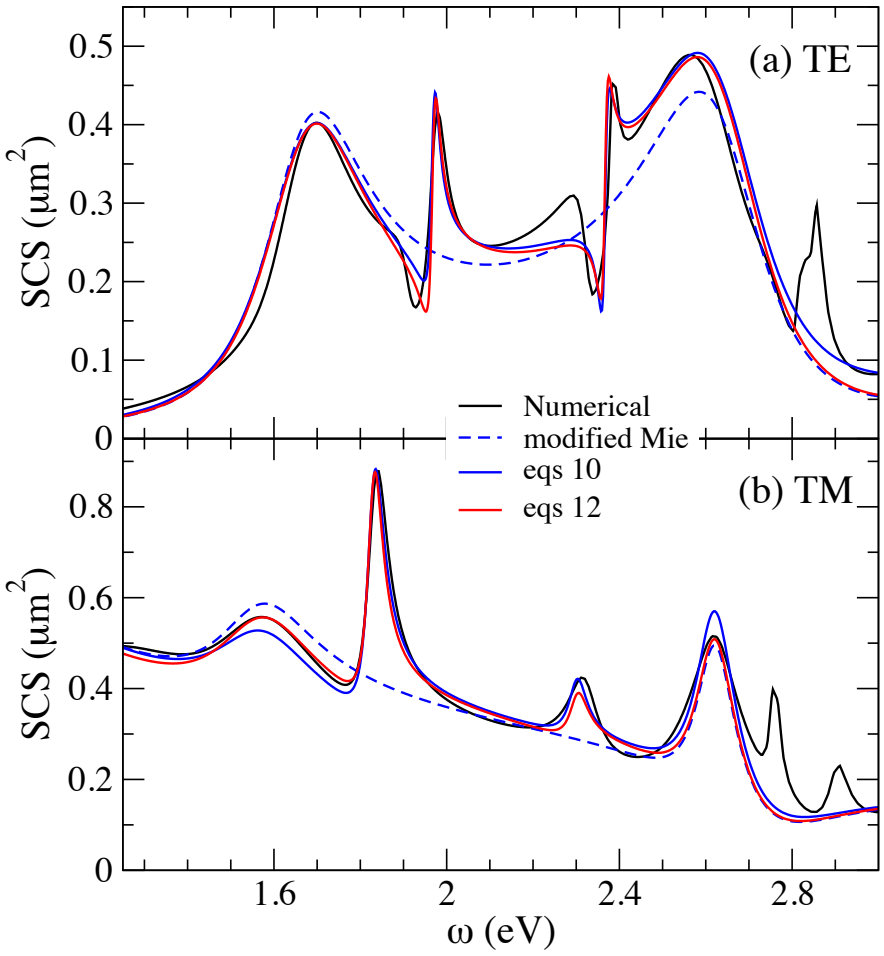

Figure 4.16: Spectral dependence of the scattering cross section $Q_{\rm sca}$ at normal incidence for a finite semiconductor ($n = 3.5$) nanorod of radius $R = 80$ nm and fixed length L, calculated through Eqs. 4.11 (blue curves) and generalized Fano formula (Eqs. 4.13, red curves), both in turn including the Mie coefficients from Eq. 4.5, modified to properly account for the finite nanorod background (dashed blue curves) as described in the text. The exact (SCUFF) numerical calculation is also included for comparison (black curves). (a) TE polarization, $L = 600$ nm. (b) TM polarization, $L = 500$ nm.

of the FP pattern with the elliptical lobe of the Mie-like a_0 (eMD) at similar scattering angles, and indeed with analogous polarization (electric field perpendicular to the nanorod axis, rotating around it), which therefore interfere very strongly. Likewise, the other strong Fano resonance in Fig. 4.11 at $\lambda \approx 525$ nm is due to the strong interference of the $\mathrm{TE}_{01}^{(5)}$ FP mode with the broad a_1 Mie resonance, both with overlapping far-field patterns: see Figs. 4.14d and 4.14e, in particular the FP central ring with the dipole-like pattern with two lobes of the ED Mie resonance.

Conversely, the weakly asymmetric resonances for TM polarization at $\lambda \approx 640$ nm in Fig. 4.12 results from the narrow $\mathrm{HE}_{11}^{(3)}$ FP mode at $\lambda \approx 670$ nm, overlying on a broad background with contributions from both b_0 and b_1 Mie resonances. Weak interference is expected since the corresponding far-field pattern of the FP mode, with two polar (yo-yo-like) lobes, barely overlaps with the center lobe of the b_0, b_1 Mie-like far-field pattern (see Figs. 4.15a and 4.15b). The same

argument explains the nearly Lorentzian lineshape of the narrow $\mathrm{HE}_{11}^{(5)}$ FP mode at $\lambda \approx 500$ nm, whose far field overlaps even less than the former FP mode with that of the background, stemming from the broad b_1 and (only slightly) b_2 Mie resonances (not shown here).

4.2.3 Fano line shapes

Based on the above physical arguments, we next propose a phenomenological expression of the spectral dependence of the SCS that accounts for the Fano interference as follows:

$$\mathrm{SCS}^{\mathrm{TE}}(\omega) = \frac{4L}{k}\left\{\alpha_0\left|a_0(\omega)\left[1+\sum_{i=1}^{\mathrm{FP}_m}\frac{\phi_{0i}}{\nu_i+\imath}\right]\right|^2 + 2\sum_{m=1}^{\infty}\alpha_m\left|a_m(\omega)\left[1+\sum_{i=1}^{\mathrm{FP}_m}\frac{\phi_{mi}}{\nu_i+\imath}\right]\right|^2\right\}; \tag{4.11a}$$

$$\mathrm{SCS}^{\mathrm{TM}}(\omega) = \frac{4L}{k}\left\{\beta_0\left|b_0(\omega)\left[1+\sum_{i=1}^{\mathrm{FP}_m}\frac{\phi_{0i}}{\nu_i+\imath}\right]\right|^2 + 2\sum_{m=1}^{\infty}\beta_m\left|b_m(\omega)\left\{1+\sum_{i=1}^{\mathrm{FP}_m}\frac{\phi_{mi}}{\nu_i+\imath}\right\}\right|^2\right]. \tag{4.11b}$$

The above SCS is nothing but the Mie scattering efficiencies in Eqs. 4.5, converted to scattering cross sections by multiplying by a geometrical factor $2RL$, allowing also for a constant factor α_m, β_m independent for each Mie contribution, to match the background of the numerical calculation (for the sake of completeness); FP resonances are included through complex Lorentzians, where ν_i is their reduced frequency

$$\nu_i = (\omega - \omega_i)/\Gamma_i, \tag{4.12}$$

with frequency ω_i and halfwidth Γ_i. Every FP resonance is allowed to interfere with the m-th Mie contribution according to their ϕ_{mi} factor, which can indeed be complex.

On the other hand, we will also fit the resulting line shapes to a canonical Fano formula.[154] However, the fact that the role of the continuum is played in Plasmonics by a broad resonance modifies the canonical Fano line shape in a peculiar manner, as pointed out with different approaches.[165,166] In our case, a few broad Mie resonances contribute to the background, rather than a single broad dipolar (plasmon) resonance. Therefore, we introduce a heuristic expression to account for the complex background scattered by semiconductor nanorods,[166] as follows

$$\mathrm{SCS}^{\mathrm{TE}}(\omega) = \frac{4L}{k}\left[\alpha_0\left|a_0(\omega)\right|^2 + 2\sum_{m=1}^{\infty}\alpha_m\left|a_m(\omega)\right|^2\right]\prod_{i=1}^{\mathrm{FP}}\frac{(\nu_i+q_i)^2+\delta_i}{\nu_i^2+1}, \tag{4.13a}$$

$$\mathrm{SCS}^{\mathrm{TM}}(\omega) = \frac{4L}{k}\left[\beta_0\left|b_0(\omega)\right|^2 + 2\sum_{m=1}^{\infty}\beta_m\left|b_m(\omega)\right|^2\right]\prod_{i=1}^{\mathrm{FP}}\frac{(\nu_i+q_i)^2+\delta_i}{\nu_i^2+1}, \tag{4.13b}$$

where q_i, δ_i are generalized Fano factors determining, respectively, the degree of asymmetry (as in the canonical Fano formula) and the contrast, the latter in turn related to intrinsic losses.[166]

The resulting SCSs from our heuristic expression (Eqs. 4.11) and the generalized Fano formula (Eqs. 4.13), are shown in Fig. 4.16 in the same cases as shown in Figs. 4.11 and 4.12, but in the frequency domain to clearly reveal the asymmetric line shapes. The lowest-order Mie contributions considered in the calculation have been corrected in Fig. 4.16 with the following factors

$$\alpha_0 = 1.25, \quad \alpha_1 = 1.03, \quad \beta_0 = 1.65, \quad \beta_1 = 0.44, \quad \beta_2 = 1.3. \tag{4.14}$$

As expected, the impact of the finiteness of the nanorod (with regard to the infinite nanocylinder described by Mie theory) is much larger in TM polarization, since the electric field in the latter case is polarized along the nanorod axis. The total SCSs including FP resonances from either Eqs. 4.11 or Eqs. 4.13 exhibit a good agreement with the numerical simulations previously shown. The corresponding parameters in Eqs. 4.11 are:

$$\phi_{01}^{(\mathrm{TE})} = 0.2 - 1.14\imath, \ \phi_{02}^{(\mathrm{TE})} = 0.5 + 0.1\imath, \ \phi_{1i}^{(\mathrm{TE})} = \phi_{0i}^{(\mathrm{TE})} e^{-\imath\pi/4}, \ i = 1, 2; \tag{4.15a}$$

$$\phi_{m1}^{(\mathrm{TM})} = 1.7 + 0.6\imath, \quad \phi_{m2}^{(\mathrm{TM})} = 0.3 + 0.8\imath, \quad m = 0, 1. \tag{4.15b}$$

And the generalized Fano factors used in Eqs. 4.13 are given by

$$q_1^{(\mathrm{TE})} = 0.53, \quad \delta_1^{(\mathrm{TE})} = 1.2, \quad q_2^{(\mathrm{TE})} = 0.44, \quad \delta_1^{(\mathrm{TE})} = 0.85, \tag{4.16a}$$

$$q_1^{(\mathrm{TM})} = 0.3, \quad \delta_1^{(\mathrm{TM})} = 1.95, \quad q_2^{(\mathrm{TM})} = 0.08, \quad \delta_1^{(\mathrm{TM})} = 1.3. \tag{4.16b}$$

All four FP Fano resonances are qualitatively (and nearly quantitatively) reproduced regardless of their degree of asymmetry. Particularly, the high asymmetry and contrast of the line shapes in TE polarization are accounted for through the fitting parameters in the following manner: large $\phi^{(\mathrm{TE})}$ factors (either nearly real or imaginary) in Eqs. 4.11; and large $q^{(\mathrm{TE})}$ and relatively small $\delta^{(\mathrm{TE})}$ factors, though non-negligible (for $\delta = 0$ the resonance minimum would be zero), in Eqs. 4.13. On the other hand, the weaker interference of the FP resonances in TM polarization is also manifested through: comparable real and imaginary parts in $\phi^{(\mathrm{TM})}$ in Eqs. 4.11 (weaker interference); much larger $|\phi^{(\mathrm{TM})}|$ for the stronger, lower frequency FP resonance. And correspondingly, small Fano factors $q^{(\mathrm{TM})}$ and large $\delta^{(\mathrm{TM})}$ in Eqs. 4.13 that make the line shape slightly asymmetric and relatively large. Overall, this remarkable agreement firmly supports our physical interpretation relying on Eqs. 4.7, included heuristically in the scattered amplitude in Eqs. 4.11, and in the scattered intensity through the generalized Fano formula in Eqs. 4.13.

Chapter 5

Angular momentum and strong coupling in semiconductor waveguides

After studying the scattering and absorption in dielectric NWs, in the last chapter we continue to investigate other fundamental properties. First, the spin and orbital angular momentum of light is theoretically studied in semiconductor waveguides[167] Finally, in collaboration with our colleagues at the Universidad Autónoma de Madrid, Johhannes Feist and Francisco J. García Vidal, and Jaime Gómez-Rivas at the Technological University of Eindhoven, we inspect the condition to achieve strong coupling in a system consisting of a semiconductor nanowire embedded in an excitonic medium.[168]

5.1 Spin and orbital angular momentum in semiconductor waveguides

To place this work in the proper context, let me remind you that in 1964 Lipkin discovered new conservation laws for the electromagnetic field.[169] He found ten conserved extensive quantities (expressed in a tensor of rank three) that collectively called "zilch" of the electromagnetic fields, due to the lack of satisfactory physical interpretation. In the following years, the physical meaning of these quantities was obtained,[170–172] relating the zilches to the angular momentum of light. However, it was also shown that zilches are members of an infinite hierarchy of conserved quantities which exist for any self-adjoint linear system of equations and it was conjectured that some of them possess no physical significance.[170,173,174] These conserved quantities are consequence of the momentum (helicity) conservation. In addition, the continuous dual-symmetry of Maxwell's equations with respect to the electric-magnetic rotation also implies conservation of helicity,[175] but some of the conservation theorems derived until our dates do not preserve the dual-symmetry of the electromagnetic field.

Thus, although the new conservation laws were found back in 1964, it was not until the begginning of the decade when the relation of the helicity conservation law, spin and Lipkin's Zinches was examined in detail,[174,176,177] finding the correct dual-symmetric expressions and interpreta-

tion for the conserved quantities. Hence, during the last years the angular momentum properties of a variety of wave fields have been investigated in terms of its decomposition into spin and orbital parts (SAM and OAM, respectively),[178–183] showing the lack of knowledge over fundamental properties of light.

Recall that propagating waves in the paraxial limit can carry longitudinal orbital angular momentum (OAM) given by its wave vector, and also longitudinal spin angular momentum (SAM) arising from its intrinsic helicity due to circular polarization; they can be associated to, respectively, spatial and polarization degrees of freedom that can be straightforwardly separated. Nonetheless, recent work carried out on SAM and OAM in a variety of optical fields beyond paraxial fields[178–180,182–184] reveals a wealth of spin-orbit interactions (SOI) of light that are attracting a great deal of attention nowadays.[181,185–187]

In this regard, non-paraxial, subwavelength-structured wavefields appear naturally in Nano-Optics. Therein the vector nature of electromagnetic waves has to be fully accounted for, so that spatial and polarization properties can no longer be decoupled, leading to a variety of novel phenomenology and functionalities at the nanoscale where spin-orbit interactions play a crucial role.[181] Particularly relevant and widespread in nano-optics is the emergence of transverse SAM, theoretically described in connection with evanescent waves: such polarization-independent, transverse spin component stems from the spatially decaying field of the evanescent wave away from the interface, and carries in turn a longitudinal (Belinfante's) SAM.[188] Transverse SAM has been later on studied in several geometries involving well known evanescent waves[178,180,189–196] such as plasmons, total internal reflection, etc. In this regard, it is worth mentioning that the following experimental works have exploited spin-orbit interaction also in waveguides,[197–201] in most cases enforcing through the spin-orbit locking the coupling of a circularly polarized exciting field (spin locked in the evanescent tail) into propagating guided waves with ad-hoc directionality (orbit thus driven).

Nonetheless, the peculiar structured wavefield arising *inside* waveguides has not been addressed in detail up to now. Recall that cylindrical waveguides support a wealth of transverse and hybrid leaky/guided modes as shown in Section 1.4.2. Nanowires and fibers are no doubt extremely interesting optical platforms that hold potential of novel nanophotonic devices, wherein SOI and locking inside could be exploited to manipulate i.e. quantum well and dot emission and photoluminescence. Subwavelength waveguides in lower-frequency regimes are amenable to SOI phenomena; moreover, optical forces and torques in the IR to GHz domain could be manipulated inside i.e. water-filled waveguides.[202]

In this section, we study theoretically the spin and orbital angular momenta of confined light inside waveguides. First, we show analytically that guided modes carry transverse spin density and longitudinal (so-called) Belinfante's spin momentum inside the waveguide, connecting them to relevant magnitudes stemming from light confinement such as energy density and transverse wave vector components. This is done not only for an infinite cylinder (NW) geometry which supports, as mentioned above, not only pure transverse modes, but also hybrid modes with intrinsic helicity. For the sake of simplicity, a planar waveguide geometry with only transverse electric/magnetic modes is studied before cylindrical waveguides. The analytical formulation is

exploited to explore spin-orbit interactions through the resulting SAM and OAM in nanophotonic waveguide geometries (semiconductor nanoslabs and nanowires), and water-filled waveguides are considered to illustrate optical forces and torques in the microwave regime.

5.1.1 Planar waveguides

Transverse guided modes in planar waveguides

Let us consider a planar waveguide (see inset in Fig.5.1a) consisting of a dielectric slab (core, medium 1) of thickness $2d$ surrounded by another dielectric material (cladding, medium 2) that has a lower refractive index, $n_1 = c\sqrt{\epsilon_1\mu_1} = \sqrt{\epsilon_{r1}\mu_{r1}} > n_2$, where $c = 1/\sqrt{\epsilon_0\mu_0}$ is the speed of light in vacuum. Unlike in preceding sections, we define both relative and absolute dielectric permittivities and magnetic permeabilities (ϵ_r, μ_r and ϵ, μ, respectively). In what follows, only non-dispersive and lossless dielectric waveguides are considered. We assume propagation along the z direction and translational invariance along the y direction. Transverse electric (TE) and magnetic (TM) modes stand for modes with only electric/magnetic field component along the y axis, propagating along the z axis with propagation constant k_z and transversal wavevector k_t. For TE modes, the corresponding fields (omitting the time harmonic factor $e^{-\imath\omega t}$) are:[203]

$$\mathbf{E} = \hat{y}\sqrt{\mu_i}A_i f(k_t x)e^{\imath k_z z}, \tag{5.1a}$$

$$\mathbf{H} = A_i \frac{1}{\omega\sqrt{\mu_i}}[k_z f(k_t x)\hat{x} + \imath k_t f'(k_t x)\hat{z}]e^{\imath k_z z}, \tag{5.1b}$$

with $i = 1, 2$ and

$$= e^{-\alpha x}, x > d, \tag{5.2a}$$

$$f(k_t x) = \left\{ \begin{matrix} \sin(k_x x) \\ \cos(k_x x) \end{matrix} \right\}, |x| < d, \tag{5.2b}$$

$$= \mp e^{\alpha x}, x < -d. \tag{5.2c}$$

the terms in braces denoting antisymmetric (top) and symmetric (bottom) modes, respectively; its derivative with respect to its argument $f^{'}(k_t x)$. The electromagnetic fields for TM modes can be straightforwardly obtained from the above Eqs. 5.1 by replacing $\mathbf{E}, \mathbf{H} \Rightarrow \mathbf{H}, -\mathbf{E}$ and $\mu \Rightarrow \epsilon$. Field amplitudes A_i outside/inside the waveguide are connected through corresponding boundary conditions. The wavevector $\mathbf{k}$ components in Cartesian coordinates of such fields are given by $\mathbf{k} = (k_t, 0, k_z)$, with $k_t = \pm i\alpha$ ($|x| > d$) and $k_t = k_x$ ($|x| < d$). For waves confined inside the waveguide, the sign of k_x and k_z must be the same for the sake of consistence. Herein we have used the same notation for the transversal component of the wavevector inside and outside the waveguide, bearing in mind that outside is complex, its sign depending on the considered

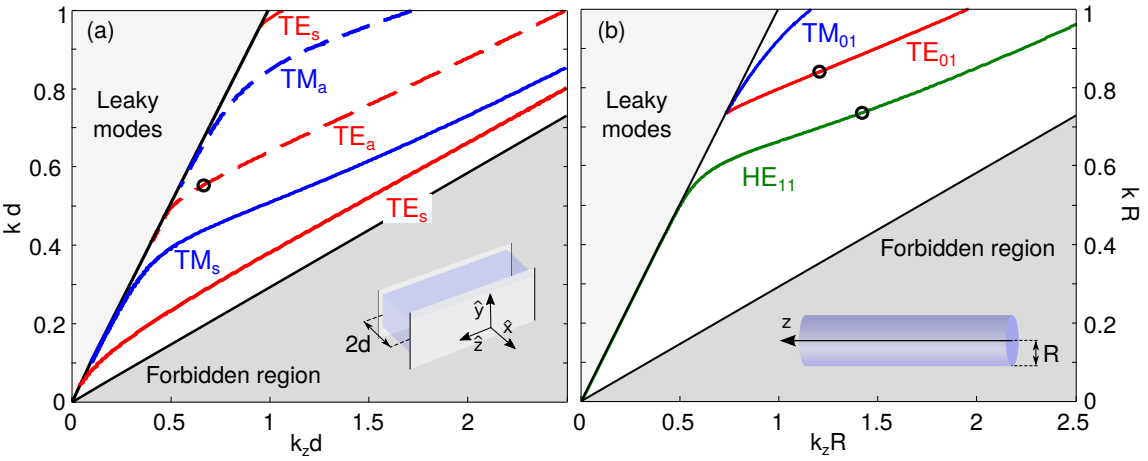

Figure 5.1: Dispersion relations for the lowest-order guided modes inside waveguides with refractive index $n = 3.43$ (vacuum outside): (a) (anti-)symmetric transverse electric and magnetic (TE and TM) guided modes (slab); (b) TE, TM, and hybrid (HE) guided modes (cylinder). Circles indicate the specific modes and corresponding wavevectors considered below. Insets: Schematic of the dielectric waveguides considered hereafter: (a) slab of width $2d$ and (b) cylinder of radius R.

semi-region. The wavevector components are related by:

$$k_z^2 + k_t^2 = \epsilon_{r1}\mu_{r1}\left(\frac{\omega}{c}\right)^2 = \left(n_1\frac{\omega}{c}\right)^2, |x| > d, \tag{5.3a}$$

$$k_z^2 - \alpha^2 = \epsilon_{r2}\mu_{r2}\left(\frac{\omega}{c}\right)^2 = \left(n_2\frac{\omega}{c}\right)^2, |x| < d; \tag{5.3b}$$

where ω is the angular frequency. Since the dielectric waveguide is intended to guide the light, the propagation constant k_z has to be in the range $n_2/n_1 < ck_z/\omega < n_1$ and will also depend on mode number and polarization. Indeed, upon imposing boundary conditions, we can obtain the corresponding dispersion relation,[203] that determines the wavevectors of symmetric and antisymmetric, transverse electric and magnetic (TE and TM) guided modes (see Fig. 5.1a).

Next we define all electromagnetic quantities for non-dispersive and lossless media; otherwise, the expressions must be modified accordingly, see e.g.[204] The energy density,

$$W = \frac{\epsilon}{4}|\mathbf{E}|^2 + \frac{\mu}{4}|\mathbf{H}|^2, \tag{5.4}$$

is given for both TE and TM modes by:

$$W = |A_2|^2\frac{k_z^2}{2\omega^2}|f(x)|^2, |x| > d, \tag{5.5a}$$

$$= |A_1|^2\frac{1}{2\omega^2}\left[k_z^2|f(x)|^2 + \frac{k_x^2}{2}\right], |x| < d. \tag{5.5b}$$

Next, the momentum density given by the Poynting vector,

$$\mathbf{P} = \frac{1}{2c^2}\Re\left[\mathbf{E}^* \times \mathbf{H}\right] = \frac{1}{2c^2}\Re\left[\mathbf{E} \times \mathbf{H}^*\right], \tag{5.6}$$

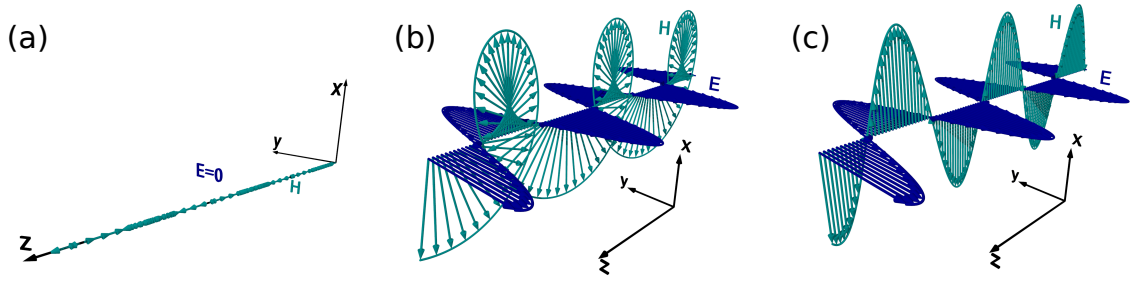

Figure 5.2: An asymmetric TE mode is considered at transverse positions inside the waveguide satisfying: (a) $k_x x = 0$, (b) $k_x x = \pi/4$, and (c) $k_x x = \pi/2$. TM modes will be identical upon replacing $\mathbf{E}, \mathbf{H} \Rightarrow \mathbf{H}, -\mathbf{E}$. It follows that, as will be shown below, for TE (respectively, TM) modes, the spin inside the waveguide is $S_e \equiv 0$ (respectively, $S_m \equiv 0$) everywhere, and $S_m \neq 0$ (respectively, $S_e \neq 0$) [as in (b)] except for specific x-points where (a) or (c) is satisfied.

yields:

$$\mathbf{P} = \hat{z}|A|^2 \frac{k_z}{2c^2\omega}|f(x)|^2, \tag{5.7}$$

for both TE and TM modes.

Let us plot the expected electric and magnetic fields along the waveguide for a typical guided mode (asymmetric TE) at given positions inside the waveguide yielding relevant phenomenology. In Fig. 5.2a (center of the waveguide for the asymmetric mode), the electric field does vanish, and the magnetic field has only a nonzero longitudinal component, the fields thus appearing as a longitudinal wave. In Fig. 5.2b (corresponding approx. to the center of the lobe of maximum electric field of the lowest-order asymmetric TE mode), both the electric and magnetic fields have large contributions: the electric one is perfectly transverse, while the magnetic has a strong longitudinal (out of phase) component, apart from its transverse component. This is no doubt expected to yield a strong spin. Finally, a case is shown in Fig. 5.2c where the wave appears purely transverse (no spin expected). All such varied behavior will certainly give rise to a rich spin phenomenology, as we will now show.

Spin and momentum density in planar waveguides

Following the convention in Ref[188] (although using the SI units), the spin angular momentum (SAM) density is defined as:

$$\mathbf{S} = \frac{\epsilon_0 \mu_r^{-1}}{4\omega} \Im \left[\mathbf{E}^* \times \mathbf{E}\right] + \frac{\mu_0 \epsilon_r^{-1}}{4\omega} \Im \left[\mathbf{H}^* \times \mathbf{H}\right] = \mathbf{S}_e + \mathbf{S}_m, \tag{5.8}$$

also referred to as spin density for the sake of simplicity. Recall that the helicity,

$$h = -\frac{\sqrt{\epsilon_0 \mu_0}}{2\omega} \Im[\mathbf{E}^* \cdot \mathbf{H}], \tag{5.9}$$

of all guided modes in this planar waveguide is $h = 0$. The spin density is proportional to the local ellipticity of the field polarization, and can have both longitudinal and transverse components in structured fields (with both electric- and magnetic-field contributions). On the other hand, the optical helicity density (also referred to as optical chirality) is related to the so-called dual symmetry between the electric and magnetic field.[182]

From the electric and magnetic field components it follows that $S_e = 0$ (S_m = 0) for TE (respectively, TM) guided modes. The only nonzero components of the spin densities are $\mathbf{S_m} = \hat{\mathbf{y}} S_m$ for TE modes and $\mathbf{S_m} = \hat{\mathbf{y}} S_m$ for TM modes. Upon introducing them into Eq. 5.8, we end up with the resulting total spin density, which can be written in a compact form as follows:

$$\mathbf{S} = \hat{y}|A_2|^2 \frac{k_z k_t}{4\omega^3 n_2^2} \frac{d}{d(k_t x)} |f(k_t x)|^2. \tag{5.10}$$

Three features should be emphasized at this point regarding the spin density above: (i) unlike that of the evanescent field, it can be locally positive or negative inside the waveguide; (ii) it is either purely magnetic ($S_e = 0$) or electric ($S_m = 0$) for, respectively, TE or TM guided modes, and (iii) it is proportional to the transverse component of the wavevector k_t. Incidentally, recall that guided modes in planar waveguides can be described as the combination of two plane waves bouncing on the two waveguide walls. Thus, an alternative explanation of the emergence of transverse spin density can be given in terms of a two-wave interference.[179]

We now turn to calculate the (Belinfante's) spin momentum density, obeying:

$$\mathbf{P}^S = \frac{1}{2} \nabla \times \mathbf{S}. \tag{5.11}$$

Since the spin density has only a nonzero component along the y axis [cf. Eq. 5.10], which in turn does not depend on the propagation direction z, the spin momentum has only a nonzero component along z, namely:

$$\mathbf{P}^S = \hat{z}|A|^2 \frac{k_z k_t^2}{8\omega^3 n^2} \frac{d^2}{d(k_t x)^2} |f(k_t x)|^2, \tag{5.12}$$

for both TE and TM modes. As the spin density, the spin momentum is either purely magnetic (TE modes) or electric (TM modes).

Finally, the canonical (orbital) part $\mathbf{P}^O$ of the momentum density can be simply obtained from:

$$\mathbf{P} = \mathbf{P}^O + \mathbf{P}^S. \tag{5.13}$$

Thus, from Eqs. 5.7 and 5.12, it follows that:

$$\mathbf{P}^O = \hat{z}|A_2|^2 \frac{k_z^3}{2n_2^2\omega^3} e^{\mp 2\alpha x}, \quad |x| > d, \tag{5.14a}$$

$$= \hat{z}|A_1|^2 \frac{k_z}{2n_2^2\omega^3} \left[k_z^2 |f(x)|^2 + \frac{k_x^2}{2} \right], |x| < d, \tag{5.14b}$$

for both TE and TM modes. Incidentally, we have verified that the same $\mathbf{P}^O$ is obtained if directly calculated from its canonical expression.[182] Nonetheless, the orbital momentum presents both contributions, electric and magnetic. It follows from the latter equations that the orbital momentum in both polarizations is proportional to the wavevector along the propagation direction in the expected manner:

$$\frac{P_z^O}{W} = \frac{k_z}{\omega n^2}. \tag{5.15}$$

In addition, it can be shown that the spin momentum can be expressed as:

$$\frac{P_z^S}{W} = \frac{k_t^2}{\omega n^2 k_z}[1 - \tilde{P}_{NP}(\mathbf{r})], \tag{5.16}$$

where $\tilde{P}_{NP}(\mathbf{r})$ is a non-paraxial term (which vanishes for paraxial waves),

$$\begin{aligned}\tilde{P}_{NP}(\mathbf{r}) = \frac{1}{8k_t^2}\{&(\mathbf{k}\cdot\mathbf{E})(\mathbf{k}\cdot\mathbf{E}^*)\epsilon + (\mathbf{k}\cdot\mathbf{H})(\mathbf{k}\cdot\mathbf{H}^*)\mu \\ &+ [\mathbf{k}\times\mathbf{E} - \mu\omega\mathbf{H}]\,[\mathbf{k}\times\mathbf{E}^* - \mu\omega\mathbf{H}^*]\,\epsilon \\ &+ [\mathbf{k}\times\mathbf{H} + \epsilon\omega\mathbf{E}]\,[\mathbf{k}\times\mathbf{H}^* + \epsilon\omega\mathbf{E}^*]\,\mu\}\,.\end{aligned} \tag{5.17}$$

Therefore, it is evident from Eqs. 5.10 and 5.12, the main results of this subsection, that a transverse SAM arises inside planar waveguides, which in turn yields an extraordinary longitudinal spin momentum, both proportional to the guided mode transverse wavevector component. The contribution from the longitudinal spin momentum, which, unlike in the evanescent region, can be positive or negative inside the waveguide (as we will show below), is indeed crucial to retrieve the proper dependence of the canonical momentum on mode wavevector, Eq. 5.15. Finally, the orbital angular momentum (OAM) density is encoded in the orbital part of the momentum density through the relation $l = \mathbf{r}\times\mathbf{P}^O$. Before discussing in detail these terms, we will show next that similar transverse SAM arise in a more complex waveguide geometry in order to assess the universal character in connection to guided light.

5.1.2 Cylindrical waveguides

Transverse and hybrid guided modes in cylindrical waveguides

Let us now study cylindrical waveguides, which support a wealth of guided modes (thoroughly described in preceding sections on NWs) that will be shown to exhibit a rich spin phenomenology. Incidentally, although we consider cylindrical waveguides, all general statements can be likely applied to strip waveguides, no doubt an interesting platform in terms of practical applications.[205–207] The fields of the waveguide can be expressed in cylindrical coordinates [see Fig. 5.1b] and exhibit transverse spatial dependence given by the appropriate Bessel function that matches the boundary conditions $Z_m(k_t r)$, and by its derivative with respect to the argument $Z_m'(k_t r)$ (see Eqs. (1.41), where k_z and k_t are again the longitudinal and transverse components of the wavevector, respectively, and $k = |\mathbf{k}|$ is the modulus of the wavevector. Recall that k_t is imaginary outside the waveguide. We show in Fig. **??**b the dispersion relation (solutions to Eq. 1.42) of the lowest-order

modes: TM_{01}, TE_{01}, and the hybrid HE_{11} (no cutoff, lowest-order mode), which are the guided modes we will considered explicitly below.

The generic expressions for the energy density, Poynting vector, and helicity, from Eqs. 5.4, 5.6, and 5.9, for arbitrary guided modes in a cylindrical lossless waveguide with corresponding electromagnetic fields are explicitly shown in the Appendix D. In addition, we also show therein the generic expressions for all spin-related magnitudes, namely: spin density and momentum, Eqs. 5.8 and 5.11, and resulting orbital momentum, Eq. 5.14. Interestingly, we should emphasize that the orbital momentum P_z^O satisfies the expected dependence on longitudinal wavevector k_z [Eq. 5.15]. Let us now discuss all these relevant magnitudes for given lowest-order guided modes with most relevant symmetries.

Transverse guided modes: Confinement-induced SAM

In the case of transverse guided modes ($m = 0$), it is evident from their field components that the helicity vanishes ($h = 0$). Thus the spin density should vanish except for the evanescent component of the EM fields outside the waveguide. However, it follows from the Appendix D.2 for the specific case of TE modes, that the spin density vanishes neither outside (as expected) nor inside the waveguide:

$$S_r = S_z = 0, \tag{5.18a}$$

$$S_\theta = \frac{\mu k_z}{2n^2\omega k_t} |b_0|^2 \, Z_0^* \left(k_t r\right) Z_0^{'} \left(k_t r\right); \tag{5.18b}$$

which leads to an extraordinary spin momentum with a longitudinal component, as follows:

$$P_z^S = \frac{\mu k_z}{4n^2\omega} |b_0|^2 \left[\frac{k_t^2}{|k_t|^2} \left| Z_0^{'} \left(k_t r\right) \right|^2 - \left| Z_0 \left(k_t r\right) \right|^2 \right]. \tag{5.19}$$

The electromagnetic properties for the TM modes follow the same expressions as for TE waves after replacing $|b_0|^2\mu \rightarrow |a_0|^2\epsilon$. Importantly, the contribution to the SAM density and spin momentum for TE (TM) waves is fully magnetic (electric). Actually, if we revisit the electromagnetic fields for TE guided modes shown in Fig. 1.41, we realize that, at given transverse positions within the cylindrical waveguide, the electric and magnetic fields exhibit a behavior analogue to that shown in Fig. 5.2 for planar waveguides, with an imaginary longitudinal component of **H** leading to the magnetic spin density (for TM modes, it is the complex **E** which yields the electric spin density). In this regard, in a similar manner to the alternative explanation given above for planar waveguides, the field for cylindrical guided modes could also be seen as the combination of an entire angular spectrum of plane waves, their complex wave interference thereby leading to a non-zero transverse spin density.[179]

Moreover, after rewriting the energy density for pure transverse modes as:

$$W = \frac{\mu}{4} |b_0|^2 \left[\frac{k_z^2 + k^2}{|k_t|^2} \left| Z_0^{'} \left(k_t r\right) \right|^2 + \left| Z_0 \left(k_t r\right) \right|^2 \right], \tag{5.20}$$

we realize that, remarkably, the orbital and spin momentum satisfies the same expression as for planar waveguides [Eqs. 5.15 and 5.16], with the non-paraxial term $\tilde{P}_{NP}$ given by Eqs. 5.17. Recall that, for weakly guided waveguides, the electromagnetic field inside becomes paraxial;[203] this confirms the crucial role of confinement in the emergence of large spin density and momentum inside waveguides.

Therefore, the transverse spin density and longitudinal spin momentum inside both planar and cylindrical waveguides do not vanish (despite not being evanescent) and depend on the transverse momentum k_t; whereas the orbital momentum has been shown above to depend as expected on the guided mode wavevector along the propagation direction k_z. Incidentally, transverse momentum has been associated to an effective mass $k_t \sim m$ if we rewrite Eq. 5.3 as $\omega = \sqrt{k_t^2 + k_z^2} \propto \sqrt{m^2 + p^2}$, which thus formally underlies the emergence of extraordinary SAM for guided modes.[208,209]

Hybrid guided modes: Intrinsic-helicity-induced spin

We now turn to study the spin angular momentum of the HE_{11} hybrid guided mode, which in fact exhibits strong intrinsic helicity. This is done in detail in the Appendix D.3. From the resulting formula, it is evident that: (i) the transverse spin density S_θ includes both electric and magnetic contributions (first term) along with a new hybrid contribution (second term); (ii) the spin density yields a longitudinal contribution S_z stemming from intrinsic helicity. The corresponding expressions for the orbital and spin momenta (P_z^O, P_θ^O, P_z^S and P_θ^S) are given also in the Appendix D.3. Interestingly, the longitudinal components of the orbital and the spin angular momentum can be related to the energy as in the case of pure transverse modes shown above. Therefore, Eqs. 5.15 and 5.16 are generic for planar and cylindrical waveguides.

Due to the quantum nature of photons, the helicity for any electromagnetic wave is bound to the maximum value $|h_{max}| = W/(\omega n)$. This value is reached when all photons are left- or right-hand polarized. For the HE_{ml} hybrid guided mode, it can be shown that the helicity is related to the energy as follows:

$$h = sign(m)\frac{W}{\omega n} - \frac{1}{4\omega n}\tilde{F}_{asy}(\mathbf{r})\left[|a_m|\sqrt{\epsilon} - |b_m|\sqrt{\mu}\right]^2, \tag{5.21}$$

where $\tilde{F}_{asy}(\mathbf{r})$ is a function that only depends on the distance $\mathbf{r}$ and is defined in the Appendix D.3. The second term in Eq. 5.21 is proportional to the factor $\left[|a_m|\sqrt{\epsilon} - |b_m|\sqrt{\mu}\right]$, which measures the electric-magnetic field asymmetry of the mode. As an example, for evanescent (and propagating) plane waves, the sum of the Stokes parameters $\tau^2 + \chi^2$ yields the field asymmetry. If the sum is zero, then the electromagnetic field asymmetry is also zero. Therefore, the energy is equally distributed in the electric and magnetic fields, $\sigma^2 = 1$, and the helicity takes the maximum value h_{max}.[188] By contrast, for guided modes, although the total energy stored in the electric and magnetic fields is the same, they are different locally (as a function of $\mathbf{r}$) . In fact, the difference between the electric and magnetic field components for all the magnitudes studied ($W^e - W^m$, $S_z^e - S_z^m$, $S_\theta^e - S_\theta^m$, and so on) is proportional to the same term ($\left[|a_m|\sqrt{\epsilon} - |b_m|\sqrt{\mu}\right]$). Going back

to the helicity, $\tilde{F}_{asy}(\mathbf{r})$ is a positive definite function (see the Appendix D.3) in agreement with the condition $|h| \leq W/(\omega n)$. Interestingly, when we study confined waves the non-paraxiality of the field and the field asymmetry become relevant.

5.1.3 Spin-orbit interactions inside nanophotonic waveguides

To shed light onto the emergence of confinement-induced spin angular momentum, let us plot all relevant magnitudes for planar and cylindrical waveguides with $\epsilon_r = 11.76$. Incidentally, as mentioned above, this choice of refractive index makes our results applicable throughout the visible and near-infrared to many semiconductors with similar refractive index,[32,49,113,114,210] such as crystalline Si, GaP, GaAs, InP, etc.; indeed, it corresponds approximately to the photoluminescence band of InP at $\lambda \approx 870$ nm, which could be illustrative of SOI in emission processes inside InP nanostructures, such as slabs or nanowires,[210] especially if circularly polarized (or even more complex) dipole sources could be engineered.[195] In fact, circularly polarized luminescence has been recently reported e.g. from coupled InGaN/GaN quantum well and quantum dots structure,[211] from perovskite nanocrystals suitable to deploy flexible devices,[212] and also from colloidal CdS quantum dots.[213,214] The latter colloidal quantum dots could be exploited in micron-sized, liquid-filled waveguides, in which the liquid itself might play the role of the denser optical medium (its refractive index does not have to be very high). On the other hand, recall that magnetic dipole emission is also available through lanthanide-doped nanostructures and nanoparticles.[215,216]

SAM in semiconductor nanoslabs

First, we show in Fig. 5.3 the simplest case: a semiconductor nanoslab supporting the first-order anti-symmetric TE mode (see the mode dispersion relation in Fig. 5.1). The transverse energy density W is plotted for the sake of comparison in Fig. 5.3b (transverse color map) and Fig. 5.3d; in the latter the orbital momentum is also included to explicitly show that the expected direct proportionality $P_z^O/W = k_z/(\omega n^2)$ is satisfied [Eq. 5.15, note that the factor n is different inside/outside]. Transverse spin momentum, Eq. 5.10, arises inside the waveguide with a rich phenomenology depending on the mode symmetry, rotating differently on each half waveguide (evident from the sign of S_y in Fig. 5.3c,e and depicted also by loops). In turn, it results in a corresponding longitudinal spin momentum [Eq. 5.12] which can point along (or opposite) to the guided mode propagation direction, and thus to the orbital momentum (evident from the sign of P_z^s, depicted by arrows). Moreover, it is simultaneously parallel and antiparallel on each half waveguide. In fact, the latter behavior can be understood in light of the complex electric and magnetic fields plotted in Fig. 5.2. The spin density maxima occur at symmetric positions inside the waveguide where electric and magnetic fields rotate as in Fig. 5.2b. At the waveguide center, the spin density vanishes as a result of the vanishing of the electric field (see Fig. 5.2b); the spin density also vanishes near the waveguide boundaries, at positions where the electric and magnetic fields are locally paraxial as in Fig. 5.2c.

Finally, note that outside the waveguide, the transverse spin density, Eq. 5.10, stems from the evanescent character of the guided modes outside, as expected from the case of pure evanescent

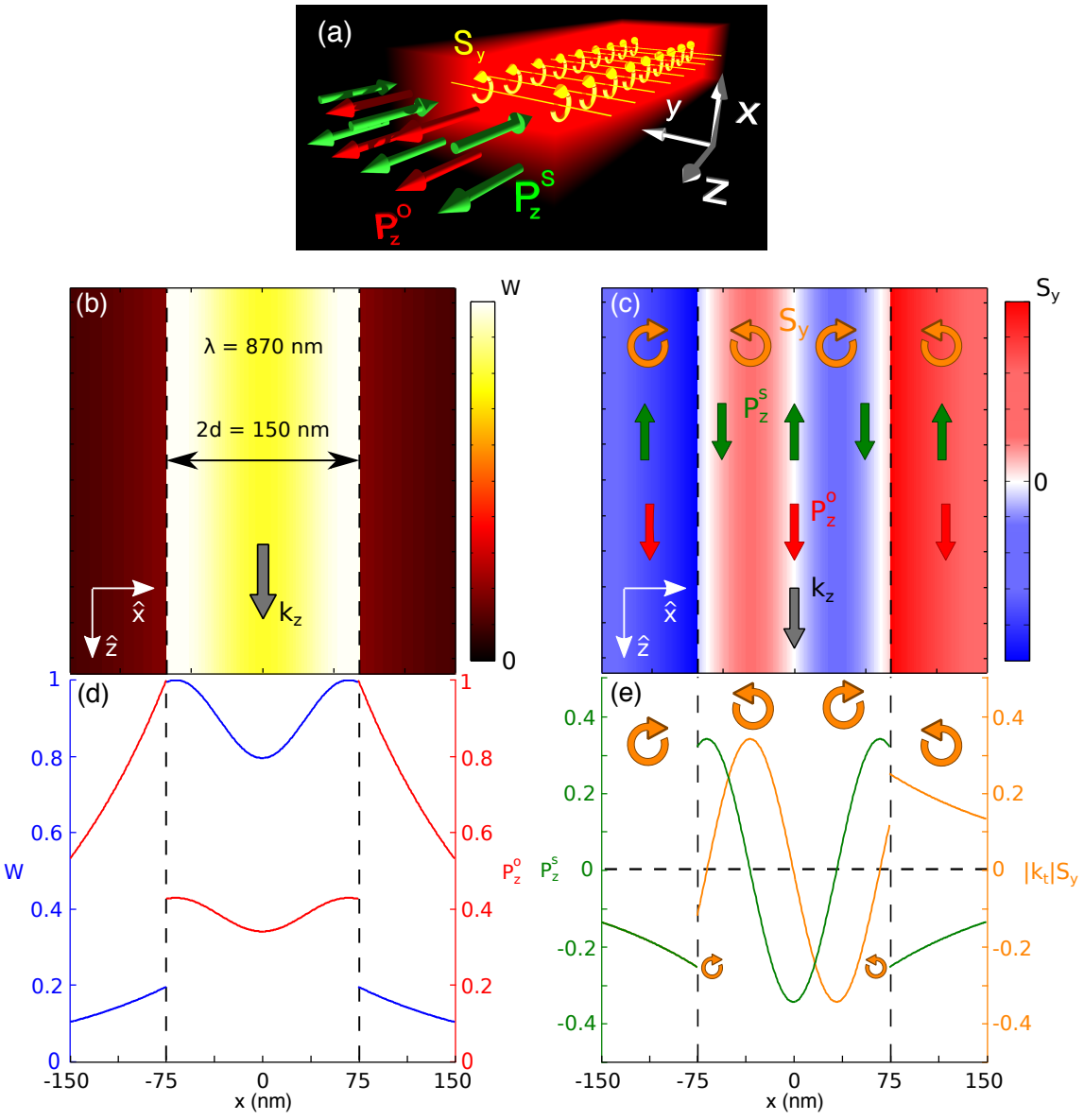

Figure 5.3: (a) Schematic depicting the orientation of orbital $\mathbf{P}^O$ (red arrows) and spin $\mathbf{P}^S$ (green arrows) momenta, inside the planar waveguides, with loops inside illustrating the confinement-induced SAM density $\mathbf{S}$. (b-e) The anti-symmetric lowest-order TE mode is considered for a planar waveguide of width $2d$ and $\epsilon_r = 11.76$ for normalized half-width $\omega d/c$ = 0.54 (which corresponds to an InP nanoslab with thickness $2d = 150$ nm at $\lambda = 870$ nm). (b, d) Contour map and radial dependence of the energy density W, the latter including also the orbital P_z^O momentum. (c, e) Contour map and radial dependence of the only non-zero component of the spin density S_y, the latter (e) multiplied by the transverse wavevector component and including also the only non-zero component of the spin momentum P_z^S (normalized by P_z^O).

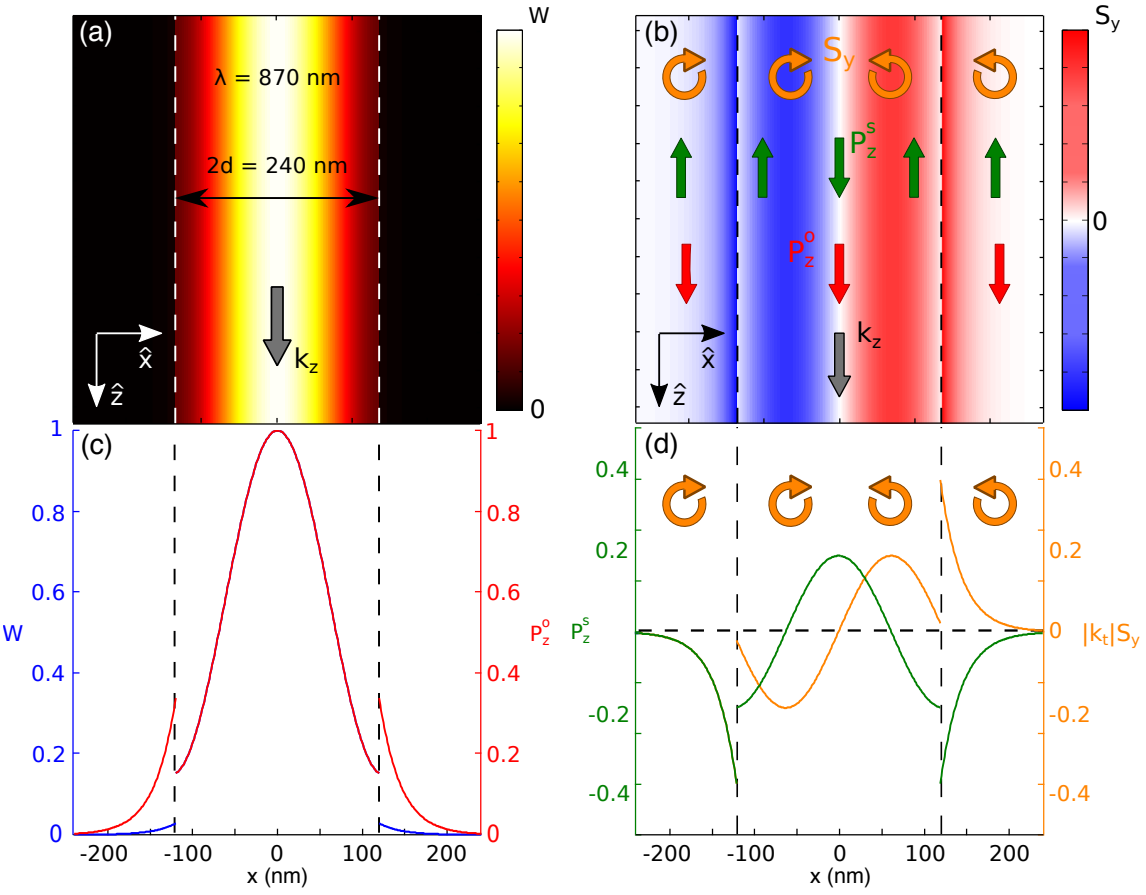

Figure 5.4: (a-d) The symmetric lowest-order TM mode is considered for a planar waveguide of width $2d$ and $\epsilon_r = 11.76$ for normalized half-width $\omega d/c$ = 0.87 (which corresponds to an InP nanoslab with thickness $2d = 240$ nm at $\lambda = 870$ nm). (a, c) Contour map and radial dependence of the energy density W, the latter including also the orbital P_z^O momentum. (b, d) Contour map and radial dependence of the only non-zero component of the spin density S_y, the latter including also the only non-zero component of the spin momentum P_z^S.

waves;[188] however, its associated longitudinal spin momentum [Eq. 5.12] outside the waveguide (unlike inside) always points opposite to the orbital momentum direction. Analogous results for TM modes are included in Fig. 5.4 that confirm the emergence of transverse spin density with extraordinary longitudinal momentum; as expected, since the TM mode shown in Fig. 5.4 is more confined than the TE mode shown in Fig. 5.3, the evanescent SAM reaches larger values but decays more abruptly away from the waveguide. The behavior for symmetric modes (not shown here) is very similar, except for the fact that spin density/momentum is symmetric/antisymmetric instead. Finally, higher-order guided modes do preserve the symmetry and polarization of the spin-related magnitudes discussed above, introducing additional number of alternating-sign layers.

SAM in semiconductor nanowires: transverse modes

Next, let us plot all spin-related magnitudes for the lowest-order TE guided mode (zero helicity) in a cross section of the cylindrical waveguide with $\epsilon_r = 11.76$ in Fig. 5.5. First of all,

a 3D schematic illustrating the orientation of the corresponding spin (loops) and momenta (arrows) is depicted in Fig. 5.5a, clearly revealing its transverse character with axial symmetry. The energy density W is included for the sake of completeness in Fig. 5.5b, revealing the strong confinement of this guided mode for the choice of parameters. Its radial dependence is explicitly plotted in Fig. 5.5d, along with the orbital momentum, to confirm again its linear dependence $P_z^O/W = k_z/(\omega n^2)$, Eq. 5.15. The emergence of the transverse confinement-induced SAM becomes evident in the right column. First, a strong contribution within the cylinder to the azimuthal spin density [magnetic/electric for TE/TM modes, cf. Eq. 5.18], is observed in the color map in Fig. 5.5c, which rotates about the cylinder axis. Its radial dependence is shown explicitly in Fig. 5.5e: note that it is zero in the center and close to the boundary, achieving its maximum within a ring inside the cylinder. Such behavior can be fully understood in light of the complex electric and magnetic fields represented in Fig. 5.2, also discussed in connection to Fig. 5.3, bearing in mind that the translational invariance along the transverse direction in the planar waveguide is replaced by the axial symmetry of this cylindrical waveguide. The corresponding extraordinary longitudinal spin momentum [Eq. 5.19] is also strong inside the waveguide, concentrated at the center and pointing along the cylinder axis (see Fig. 5.5e), opposite to the guided mode propagation direction, except for a thin corona near the exterior boundary where it is parallel. A weaker transverse spin density is also observed outside the cylinder in Figs. 5.5c and 5.5e, which stems from the evanescent character of the guided modes outside. Indeed, the spin rotation and momentum direction outside (antiparallel with respect to orbital momentum), unlike those inside, is also fixed, similarly to what was observed in planar waveguides (see Fig. 5.3).

Slight differences arise depending on whether the guided modes is weakly or strongly confined. What can we expect for the transverse spin from Eq. 5.18? Actually, it depends linearly on the transverse component k_t of the wavevector inside. Recall that this component is smaller the weaker the confinement is. Nonetheless, the energy density W, which increases inside the waveguide with increasing confinement, compensates such decrease in a non trivial manner, so that a compromise between transverse wavevector and energy confinement yields the optimum transverse spin; as an example, we show in Fig. 5.6 the same results as in Fig. 5.5 but for a TE_{01} guided mode that is weakly confined. Transverse spin density inside the waveguide in Fig. 5.4 is indeed comparable to that in Fig. 5.5; differences are in turn more obvious in the transverse spin in the evanescent region, wherein the expected behavior is observed:[188] more spread outside the cylinder in the latter case (Fig. 5.4), but larger close to the waveguide boundary in the former (strongly confined case, see Fig. 5.5). For the sake of completeness, a TM_{01} guided mode is also shown in Fig. 5.7; apart from the (relevant) fact that the spin density is entirely electric ($\mathbf{S} = \mathbf{S_e}$), the qualitative behavior is very similar to that of the TE_{01} guided mode shown in Fig. 5.5.

Higher-order transverse modes (not explicitly shown here), as for planar guided modes, essentially preserve the (in this case, rotational) symmetry and polarization of the spin-related magnitudes, introducing additional lobes in the radial dependence in accordance with the radial mode order l. Nonetheless, this could lead to various rings alternating spin rotation inside the cylindrical waveguide, preserving for all the modes the continuity across the cylinder boundary of the outermost ring (even if very thin) with respect to the evanescent-region spin, which remains unaltered.

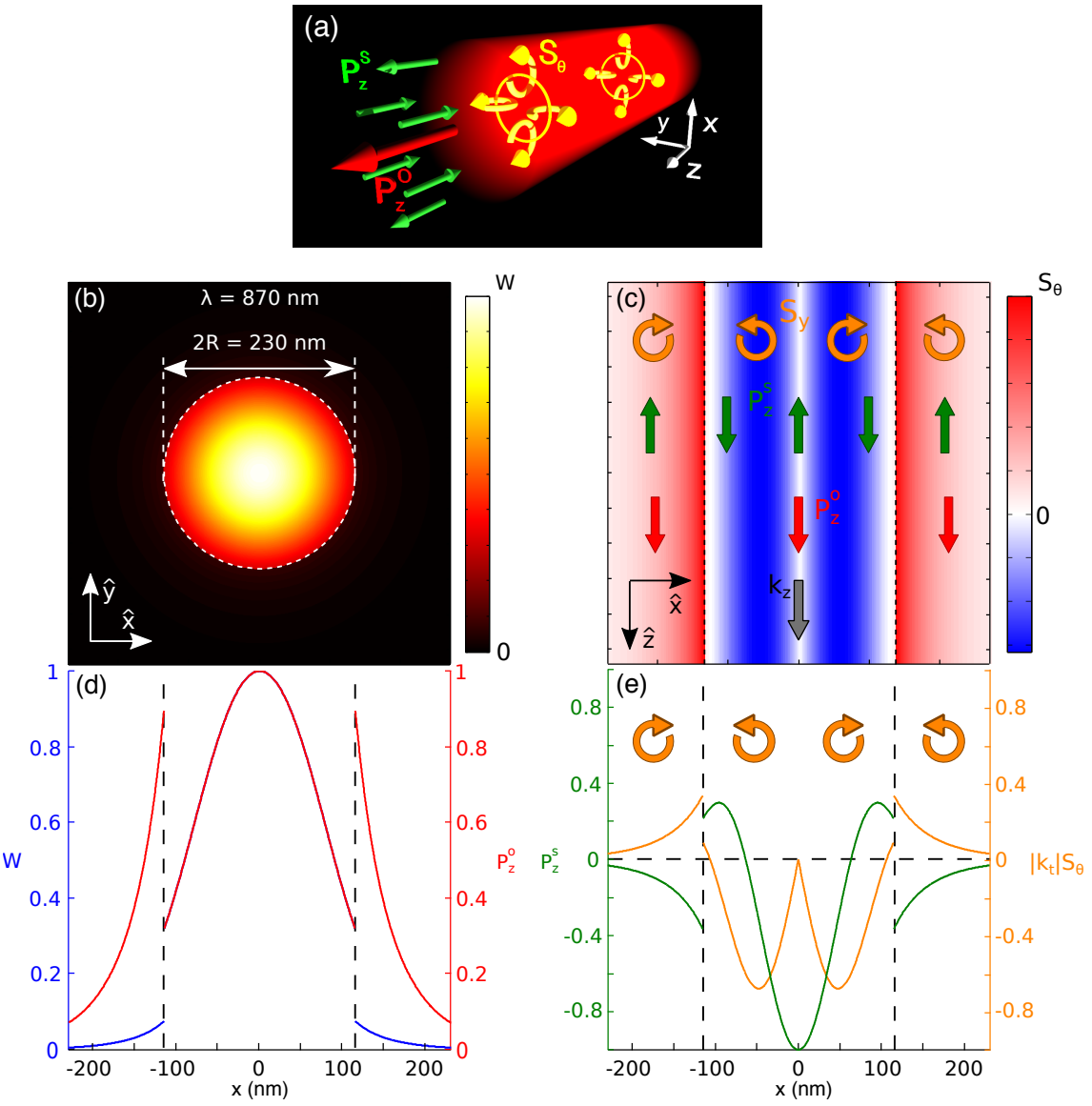

Figure 5.5: (a) Schematic depicting the orientation of orbital (red arrows) and spin (green arrows) momenta, along with spin density (loops) inside the cylindrical waveguides; as in Fig.5.3. (b-e) The lowest-order TE_{01} guided mode for a cylindrical waveguide of radius R and $\epsilon_r = 11.76$ is considered for a normalized radius $\omega R/c = 0.83$ (which corresponds to an InP nanowire with $2R = 230$ nm at $\lambda = 870$ nm): (b, d) Contour map and radial dependence of the energy density W, the latter including also the orbital P_z^O momentum. (c, e) Contour map and radial dependence of the only non-zero component of the spin density S_θ, the latter (e) multiplied by the transverse wavevector component and including also the only non-zero component of the spin momentum P_z^S (normalized by P_z^O).

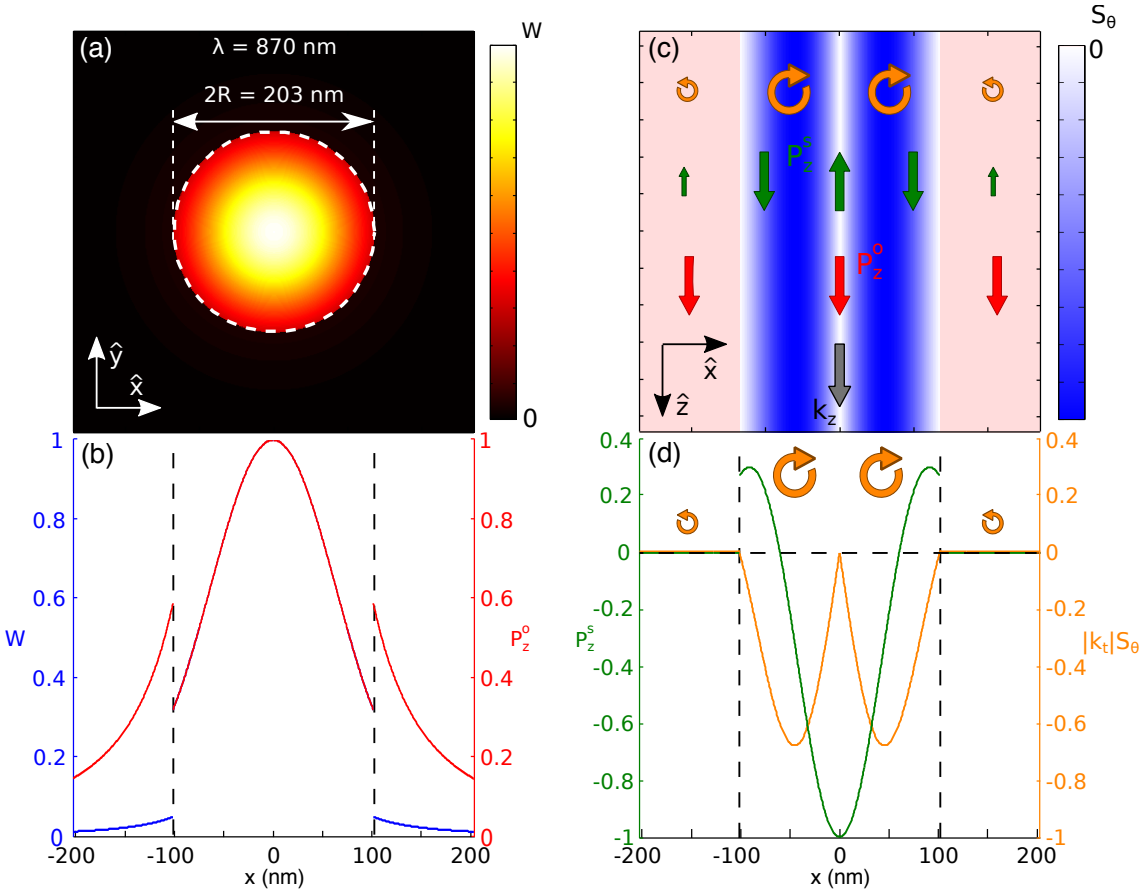

Figure 5.6: (a-d) The lowest-order TE_{01} guided mode for a cylindrical waveguide of radius R and $\epsilon_r = 11.76$ is considered for a normalized radius $\omega R/c = 0.73$ (which corresponds to an InP nanowire with $2R = 203$ nm at $\lambda = 870$ nm, near by the cutoff frequency): (a, c) Contour map and radial dependence of the energy density W, the latter including also the orbital P_z^O momentum. (b, d) Contour map and radial dependence of the only non-zero component of the spin density S_θ, the latter including also the only non-zero component of the spin momentum P_z^S.

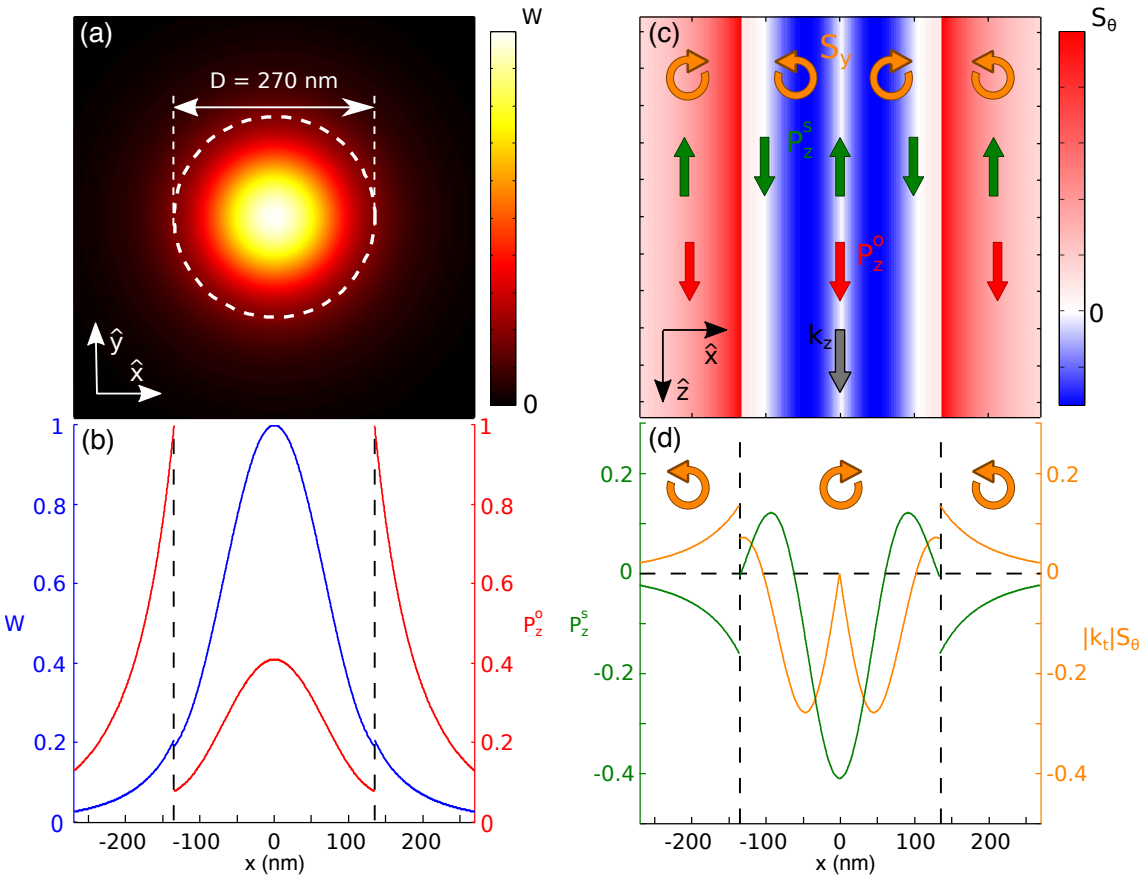

Figure 5.7: (a-d) The lowest-order TM_{01} guided mode for a cylindrical waveguide of radius R and $\epsilon_r = 11.76$ is considered for a normalized radius $\omega R/\lambda = 0.97$ (which corresponds to an InP nanowire with $2R = 270$ nm at $\lambda = 870$ nm): (a, c) Contour map and radial dependence of the energy density W, the latter including also the orbital P_z^O momentum. (b ,d) Contour map and radial dependence of the only non-zero component of the spin density S_θ, the latter including also the only non-zero component of the spin momentum P_z^S.

SAM in semiconductor nanowires: hybrid modes

In order to shed light on the different contributions to the spin density and angular momentum for hybrid modes, we now plot them making special emphasis on separating intrinsic-helicity terms from transverse confinement effects. We show all of them in Figs. 5.8 and 5.9 for a HE_{11} guided mode in a cross section of the cylindrical waveguide with $\epsilon_r = 11.76$, along with 3D schematics illustrating the orientation of the corresponding vectors; the transverse confinement-induced spin (loops) and related longitudinal momenta (green arrows) are shown in Fig. 5.8c,e, whereas the longitudinal helicity-induced spin and transverse momenta are shown in Fig. 5.9b,d. A color map of the energy density *W* revealing mode confinement is included in Fig. 5.8b, with its radial dependence and that of the longitudinal momentum explicitly shown in Fig. 5.8d; the corresponding intrinsic helicity *h* is included in a contour map in Fig. 5.9c for the sake of comparison, showing also explicitly its radial dependence in Fig. 5.9a, along with that of the helicity-induced transverse orbital momentum P_θ^O.

First, a strong transverse (respectively, longitudinal) contribution to the spin density (respectively, extraordinary longitudinal momentum) is observed inside, which stems from the transverse confinement (k_t-related) as above. Note that the corresponding SAM inside is also concentrated inside an inner ring; however, unlike for transverse modes, it rotates similarly to the evanescent-region SAM, and its longitudinal spin momentum points towards the orbital momentum inside (being opposite outside, as expected for evanescent waves). This behavior reveals a richer phenomenology for the confinement-induced transverse SAM governed by guided mode symmetry. Second, it is clear that the intrinsic helicity governs the emergence of a strong longitudinal SAM, which leads to an azimuthal spin momentum density, both resembling the spatial pattern of the helicity density (see Fig. 5.9c). Its behavior does not differ much from the helicity-induced spin exhibited by circularly polarized plane and/or evanescent waves, although again guided mode symmetry renders its phenomenology much richer. Higher-order hybrid guided modes (HE_{ml}) make the analysis more complex. The rotational symmetry of all the spin-related magnitudes (not shown here) is preserved, introducing however alternating spin-sign rings in the radial dependence when the radial index is $l > 1$, similarly to higher-order transverse modes mentioned above. The azimuthal index m is directly connected to the helicity, as expected; in addition, for $m \geq 2$ the dependence on Bessel functions of the electromagnetic fields inside imposes $W = 0$ at the waveguide center.

5.1.4 Spin-momentum locking in semiconductor nanowires

The complex spin density structure inside waveguides can lead to spin-orbit locking: the emission of circular polarized dipoles inside the waveguide excite the propagation of guided modes in one preferential direction. Alternatively, circularly polarized sources can probe the spin density distribution of a field by measuring the asymmetry in the coupling to different directions. To analyze this effect, we have carried out numerical simulations showing the emission in a cylindrical waveguide of a transverse circularly polarized electric dipole as a function of the position of the source, Δx. To avoid coupling to modes different from the HE_{11} guided mode, the same system as

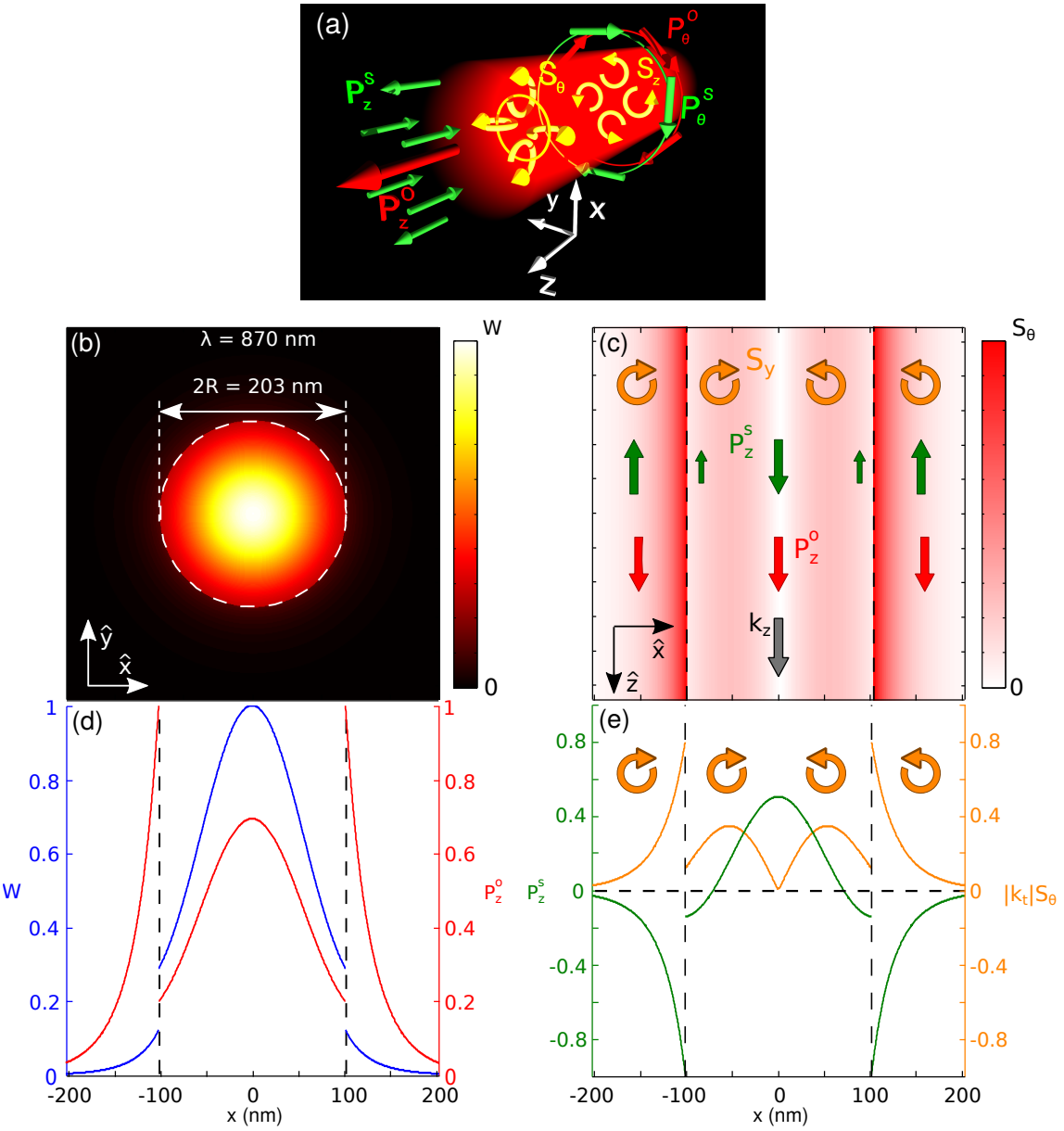

Figure 5.8: (a) Schematic depicting the orientation of orbital momenta, spin momenta and spin densities induced inside the waveguide by the confined nature and by the helicity of the hybrid guided modes. The lowest-order hybrid HE_{11} guided mode is considered for $\epsilon_r = 11.76$ and a normalized radius $\omega R/c = 0.73$ (which corresponds to $2R = 230$ nm at $\lambda = 870$ nm): (b, d) Contour map and radial dependence of the energy density W, the latter including also the orbital P_z^O momentum. (c, e) Contour map and radial dependence of the transverse component of the spin density S_θ, the latter (e) multiplied by the transverse wavevector component and including also the longitudinal component of the spin angular momentum P_z^S (normalized by P_z^O).

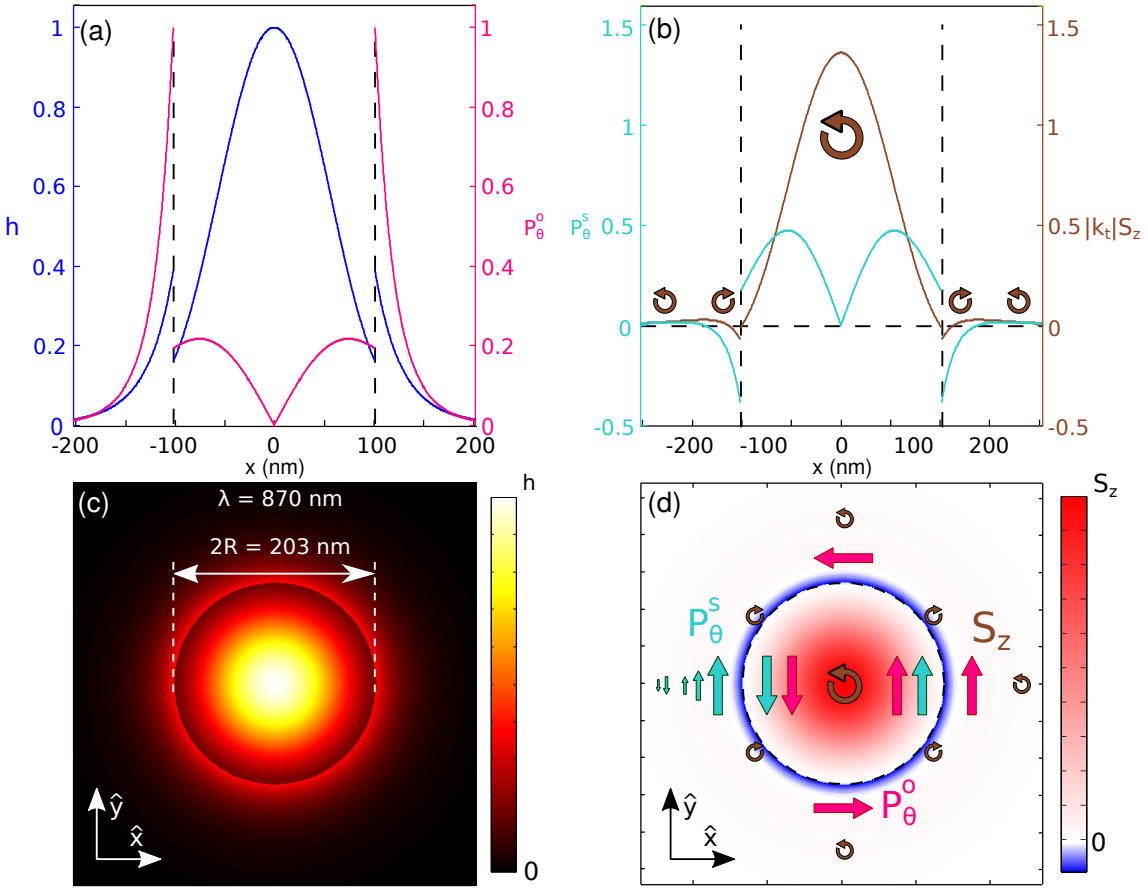

Figure 5.9: The lowest-order hybrid HE_{11} guided mode is considered for $\epsilon_r = 11.76$ and a normalized radius $\omega R/c = 0.73$ (which corresponds to $2R = 230$ nm at $\lambda = 870$ nm): (a, c) Radial dependence and contour map and of the helicity density h, including also in (a) the helicity-induced transverse orbital momentum P^O_θ. (b, d) Radial dependence and contour map in the transverse plane of the helicity-induced longitudinal spin density S_z, the former (b) multiplied by the transverse wavevector component, and including also the related transverse spin angular momentum P^S_θ (normalized by P^O_θ); dark loops and cyan/magenta arrows indicate spin rotation and transverse spin/orbital momenta.

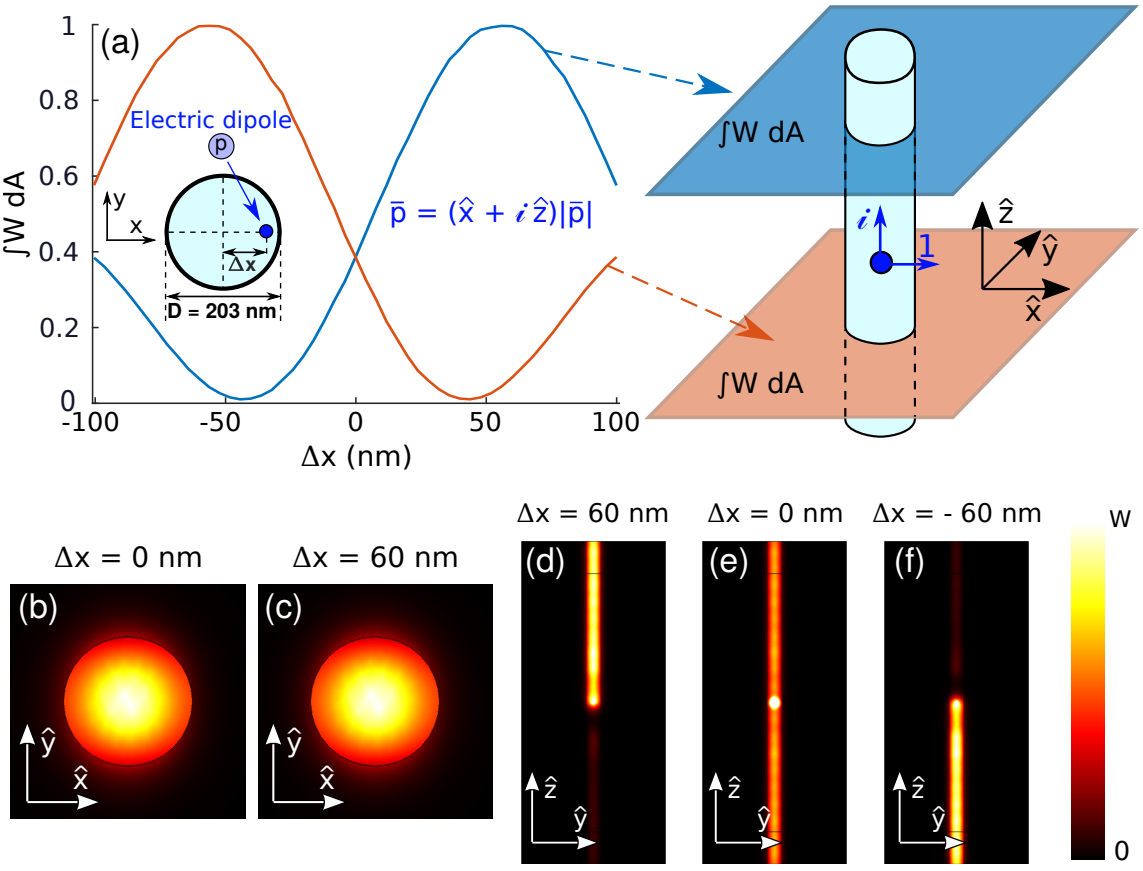

Figure 5.10: Results for the numerical simulation of a circularly polarized electric dipole emitting inside a cylindrical waveguide of radius R and $\epsilon_r = 11.76$ at a normalized radius $\omega R/c = 0.73$ (which corresponds to an InP nanowire with $2R = 203$ nm at $\lambda = 870$ nm). (a) Integration of the energy density W (normalized to its maximum) at two planes, above and below, equidistant to the dipole source ($z = \pm 2\lambda$, where $z = 0$ is the position of the dipole) as a function of the lateral position of the dipole, Δx. Contour map of the energy density W (b-c) in the xy plane at $z = 2\lambda$ and (d-f) in the yz plane for different values of Δx.

in Fig. 5.8 is considered. As shown in Fig. 5.10a, a circular (transverse) electric dipole is placed at the plane $z = 0$ and the total energy density is measured as a function of the lateral displacement Δx at two equidistant planes (above and below, at $z = z_p^{\pm} = \pm 2\lambda$).

To confirm that the emitter couples to the same mode we plot in Fig. 5.10b,c the energy density at the plane $z = z_p^{+}$ for different lateral displacements, being unequivocally assigned to the HE_{11} hybrid guided mode. Moreover, it has been checked that the results shown in (a-c) are practically independent of the value of $z_p^{\pm}$ (if sufficiently far away from the dipole source).

Most importantly, our results reveal that a circularly polarized source couples to the HE_{11} guided mode propagating along different directions depending on its position in the transverse plane. This routing is unequivocally demonstrated through the energy density along the waveguide (in the plane x = 0) for different values of Δx shown in Fig. 5.10d-f, where the spin-orbit locking is clearly verified through the distinct guided mode directionality depending on the dipole position on either side of the cylinder (in the plane perpendicular to the cylinder axis), bearing in mind that its fixed circular polarization matches a different azimuthal component of the spin density of the guided mode at $\pm\Delta x$ (see Fig. 5.8). Such configuration could be realized in practice by e.g. embedding spin-polarized QDs in waveguides, as done for asymmetric waveguides.[217]

5.1.5 Optical radiation forces and torques in water-filled waveguides

Finally, let us briefly explore the impact on optical forces of the transverse SAM inside waveguides shown above. As an example, we consider water-filled planar channels (inside e.g. metal plates) in the GHz domain; recall that water in this regime exhibits a large refractive index with relatively low absorption, which makes it suitable for tunable high-index-dielectric metamaterials.[202] Actually, this scenario could also be realized for higher frequencies up to the near-IR regime, which is in turn suitable for optical trapping and manipulation of microscopic particles through optical tweezers.[218–220] The lower-refractive index of water (or other liquids) in this electromagnetic regime comes only at the expense of requiring thicker waveguides.

By way of example, we consider a planar metallic waveguide filled with water ($n = \sqrt{80}$ at 1 GHz): particularly, we focus on the asymmetric TE_2 and TM_2 guided modes in planar waveguides with $2d = 3.4$ cm in Fig. 5.11. Assuming that the metallic boundaries behave as a perfect electric conductor, the dispersion relation reduces to (upon imposing that the transverse electric field at the interfaces vanishes):

$$k_x d = (2m+1)\frac{\pi}{2} \quad \text{or} \quad k_x d = m\pi \quad (m = 0, 1, 2\ldots). \tag{5.22}$$

We would like to stress the fact that, as pointed out above, qualitatively (and nearly quantitatively) similar results would be obtained for a metallic, water-filled waveguide with widths of the order of a micron operating in the IR ($\lambda \sim 1.55\mu$m). Along with energy and spin densities, radiation forces and torques felt by electric (p) and magnetic (m) dipole particles stemming from, respectively, longitudinal momenta and transverse SAM, are explicitly revealed through arrows and loops.

The rich phenomenology inside with alternating layers/rings with opposite torques is evident in Fig. 5.11b,d. Moreover, recall that the SAM may stem from either the electric (S_e, Fig. 5.11d)

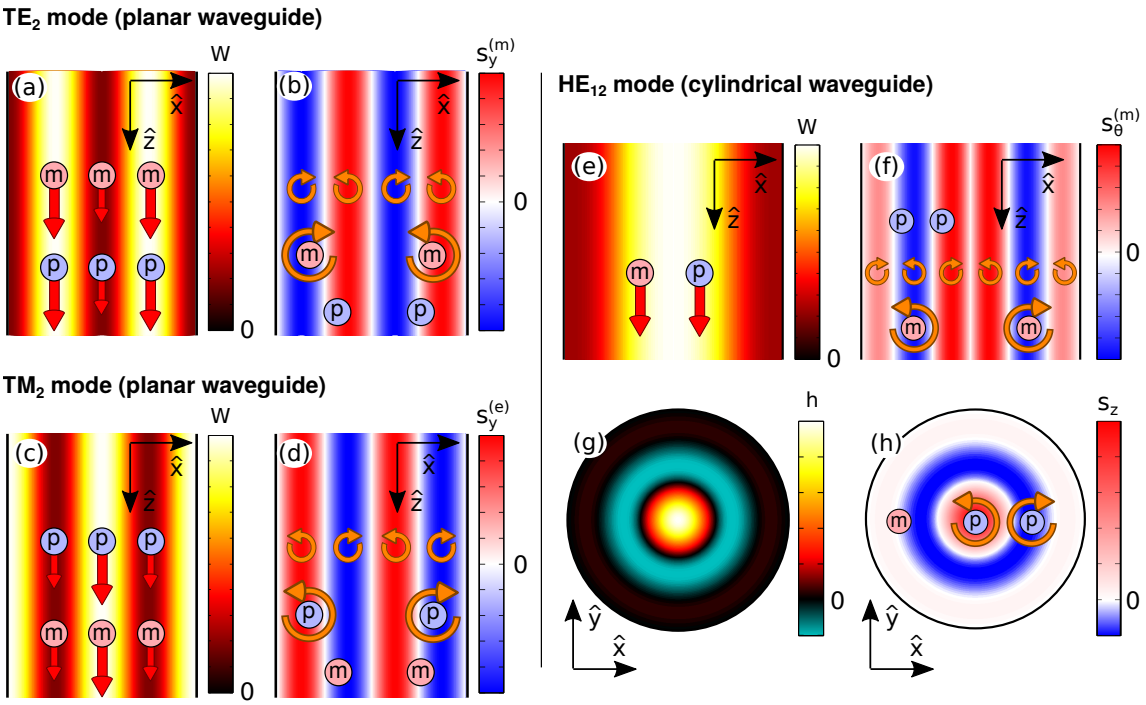

Figure 5.11: (a, c) Energy densities and (b, d) spin densities for anti-symmetric TE_2 (top) and TM_2 (bottom) modes in a planar waveguide of width $2d$ and $\epsilon_r = 80$ for normalized half-width $\omega d/c = 0.36$ (which corresponds to water-filled slabs with thicknesses $2d = 3.4$ cm at $\nu = \omega/(2\pi) = 1$ GHz). (e, g) Energy and helicity densities W and (f, h) spin densities for the hybrid HE_{12} guided mode in a cylindrical waveguide of radius R and $\epsilon_r = 80$ is considered for a normalized radius $R/\lambda = 0.097$ (which corresponds to a water-filled cylinder with thickness $2R = 5.8$ cm at $\nu = 1$ GHz). Arrows in (a, c, e) indicate the radiation pressure force felt by electric (p) and magnetic (m) dipole particles due to longitudinal momenta, whereas loops in (b, d, f, h) reveal the corresponding torque induced inside the waveguides by transverse confinement-induced spin densities.

or magnetic (S_m, Fig. 5.11b) contribution depending on the nature of the transverse mode (TM and TE, respectively). This implies that p and m dipoles will respond differently to such SAM, exhibiting non-negligible torques only if matching character:[194,219] Thus TE (respectively, TM) guided modes exert torque only to magnetic (respectively, electric) dipolar particles, see Fig. 5.11b (respectively, Fig. 5.11d). On the other hand, both electric/magnetic dipolar particles would suffer a radiation force along the guided mode propagation direction, being locally higher at layers with larger energy density (see Fig. 5.11a,c). Such radiation force $F \sim P^O$ can be anomalously large (respectively, small), as compared to the Poynting vector ($\mathbf{P} = \mathbf{P^O} + \mathbf{P^S}$), in alternating layers within the waveguide where the resulting spin momentum P^S points opposite, $P^O = P + P^S$, (respectively, along, $P^O = P - P^S$), as observed in Fig. 5.11a,c.

Lastly, we analyze the role of the optical forces on hybrid modes that carry intrinsic helicity. We focus on the HE_{12} hybrid mode of a cylindrical metallic waveguide, again, filled by water. In cylindrical waveguides with perfectly conducting walls, guided modes dispersion relation reduces to the values of $k_t R$ for which the corresponding Bessel functions vanish.[203] In particular, the HE_{12} hybrid mode exhibits a varied phenomenology. First, radiation forces are shown as

expected for both probe particles in Fig. 5.11e; as above, recall that radiation forces might be anomalously larger/shorter than those expected from the Poynting vector density for longitudinal spin momentum opposite/along the canonical momentum. Next, the transverse spin density is plotted in Fig. 5.11f, revealing three rings with alternating spin sign inside with vanishing spin density at the center. Nonetheless, despite being hybrid, such mode becomes transverse electric so that the spin density contribution is purely magnetic ($S_\theta^{(e)} \equiv 0$), leading to radiation torque acting only on the magnetic dipole particle m. Finally, the helicity density and related spin density are shown in Fig. 5.11g,h, exhibiting three rings alternating sign. It should be mentioned that such helicity-dependent spin density has both electric and magnetic contributions; however, the electric contribution is much larger $S_z^{(e)} \gg S_z^{(m)}$, and is thus indicated in Fig. 5.11h with torque only exerted on the p probe particle. Interestingly, this implies that an electric (respectively, magnetic) dipole particle would undergo in such a waveguide a longitudinal (respectively, transverse) torque. Incidentally, we have omitted in Fig. 5.11 the transverse force induced by the longitudinal spin momentum, which actually exerts no radiation force in the dipole approximation, but does produce a helicity-dependent transverse force in multipolar interactions with larger particles.[188]

It should be emphasized that sub-wavelength particles with high-refractive index have been shown to yield strong magnetic dipole resonances,[23] as experimentally demonstrated in the optical and lower-frequency domains,[86,87] leading to a wealth of phenomenology associated to the high-refractive-index dielectric resonant nanostructures[21] and sub-wavelength structures in lower frequency regimes in general,[86] where very large refractive indices are indeed ubiquitous. Recall also that, apart from its impact on induced torques, it has been recently demonstrated that such electric/magnetic spin contributions can be experimentally discerned through high-dielectric-index nanoparticles exhibiting both electric and magnetic dipole resonances.[196] Therefore, multi-resonant sub-wavelength particles would feel electric or magnetic torque depending on the resonant wavelength and guided mode involved (the latter influencing also the spatial dependence of such torque), which overall allows for a rich phenomenology. Finally, recall also a related spin-orbit locking is evidently expected if suitable electric or magnetic dipole sources are located inside, which could be exploited all along the electromagnetic spectrum.

5.2 Strong coupling in semiconductor waveguides

Tailoring light-matter interaction at the nanoscale is the foundation to improve, beyond unpredictable limits, the efficiency of previous devices and to develop novel applications.[221] Among others, much effort has been undertaken to engineer the emission properties between electronic energy states of system such as quantum dots, wells, and dye molecules, through the coupling to optical systems such as cavities, photonic crystals, metallic interfaces and semiconductor NWs.[222–226] Depending on the strength of the coupling between the systems two distinct regimes, weak and strong, can be established. In the weak regime, the spontaneous emission rate is strongly affected by the electromagnetic local densities of states and can be completely suppressed or enhanced by several orders of magnitude,[227–230] but the natural frequency of the transition remains unaltered. Otherwise, the strong regime is characterized by a coherent exchange of energy between modes

inducing new hybrid states with fascinating properties that can be very different from those of the initial systems.[104,231–233]

Metallic nanostructures, through localized surface plasmons (LSP) and surface plasmon polaritons (SPP), can effectively couple to electronic transition states due to their optical near-field enhancement and confinement.[234–240] However, the presence of losses limits their employment in transport applications. In this regard, semiconductor NWs overcome this issue and allow for a long-range coupling through propagating guided modes, being in turn a suitable platform to manage the electromagnetic environment at optical frequencies at the nanoscale.[112] Nevertheless, they have been mainly studied as optical cavities,[241–244] in which quantum dots or wells are placed inside the NW during the growth process, constricting light propagation inside. In fact, to the best of our knowledge, coupling NW propagating modes to external excitonic media has not been studied yet; this will presumably have a strong impact on exciton transport applications.[245–248]

In this connection, as yet another fascinating optical property of dielectric cylinders, we finally study theoretically the appearance of strong coupling regimes in a system consisting of a semiconductor NW embedded in an excitonic medium, by means of the interplay between guided modes and excitonic states. Upon exploiting the evanescent tail of various weakly guided modes outside the semiconductor NW, analyzed in detail through classical electrodynamics, coupling to excitonic modes of an organic dye surrounding the NW is plausible. A quantum model is developed to properly determine the polaritonic modes revealed through an avoided crossing with expectedly large enough Rabi splittings, showing that a strong coupling regime can be accomplished. The distribution of the energy is also affected by the coupling, going from pure photonic to excitonic states, revealing the hybrid nature of the modes. These entangled modes can be relevant for exciton transport purpose, for which the half-life and propagation length must be optimized.

5.2.1 Weakly guided semiconductor NW modes

We study the dispersion relation of polaritons arising from the coupling between guided modes in semiconductor NW and excitons in a surrounding molecular medium, through both classical and quantum models. We first discuss the classical electromagnetism approach, which is based on solving Maxwell's equations to obtain guided modes in the system. Here, the molecular medium surrounding the nanowire is modelled through its dielectric function, with excitons manifesting as resonances leading to broad absorption bands. In a second step, we discuss a quantum model in which the guided photonic modes of the semiconductor NW are quantized explicitly and coupled to dye molecules modelled as point dipole emitters,[238] with a level structure and molecular density that reproduce the classical dielectric function in the (linear) low-excitation limit.

For both procedures, the dispersion relation of the nanowire modes must be solved within classical electromagnetism through Eqs. 1.42. We first consider the "bare" modes of the nanowire embedded in a host material without organic molecules. We consider high-refractive-index, lossless semiconductor nanowires; without loss of generality, a refractive index of $n = \sqrt{\epsilon_1} = 4.2$ (close to those of GaAs, GaP, AlSb in the visible spectrum) is used for the nanowire, while the background dielectric constant is set to $\epsilon_2 = \epsilon_h = 2.4$ (typical for polymers such as PMMA or

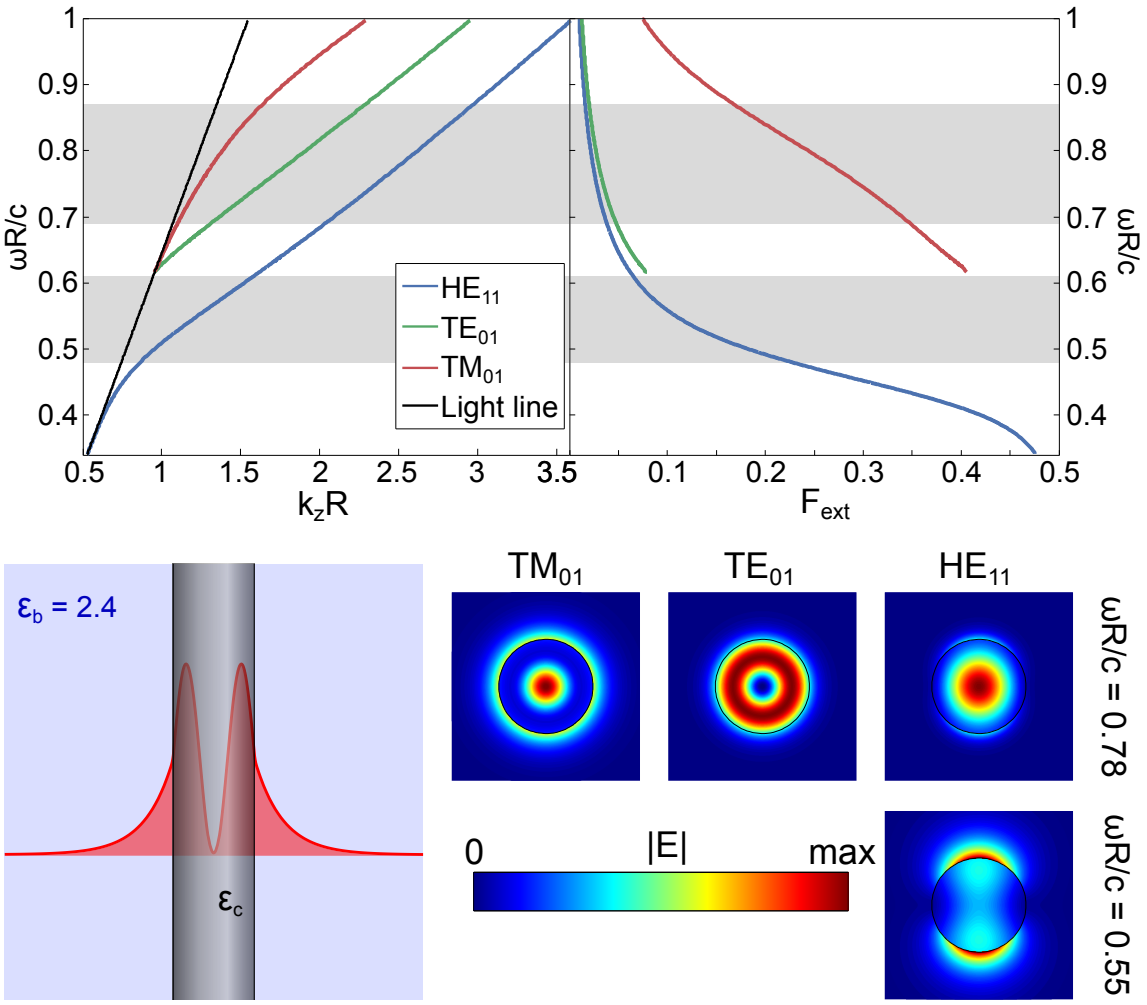

Figure 5.12: Bare system. Top left: Dispersion relation $\omega R/c$ vs $k_z R$ for the first three guided modes for $\epsilon_2 = \epsilon_h 2.4$ and $\epsilon_1 = 4.2^2$. Top right: fraction of mode energy store in the electric field outside the nanowire. The grey-shadow areas mark the spectral regions that will be studied later. Bottom: Schematic of the waveguide system and norm of the electric field profile of each mode at $\omega R/c = 0.55$ and $\omega R/c = 0.78$.

PVAc). The top left panel of Fig. 5.12 shows the dispersion relations ($k_z R$ vs. $\omega R/c$) of the first three guided modes (HE_{11}, TE_{01}, TM_{01}). In order to optimize the coupling of these modes to molecules that will be placed in the medium surrounding the nanowire, the mode should carry as much energy as possible outside the wire. This implies that the maximum coupling can be achieved with weakly guided modes close to the light line, since their field profiles possess large evanescent tails outside the wire. To quantify this, the top right panel of Fig. 5.12 shows F_{ext}, defined as the fraction of mode energy stored in the electric field outside the nanowire. As the excitonic transitions of dye molecules correspond, to a very good approximation, to electric dipole transitions, only the energy density from the electric field is taken into account. This implies that $F_{\text{ext}} \leq 0.5$, since for guided propagating modes the energy is equally divided between electric and magnetic fields. As can be seen, the cutoff-free HE_{11} mode at lower frequencies and the (predominant) transverse magnetic modes (for dielectric waveguides) close to their cut-off frequencies

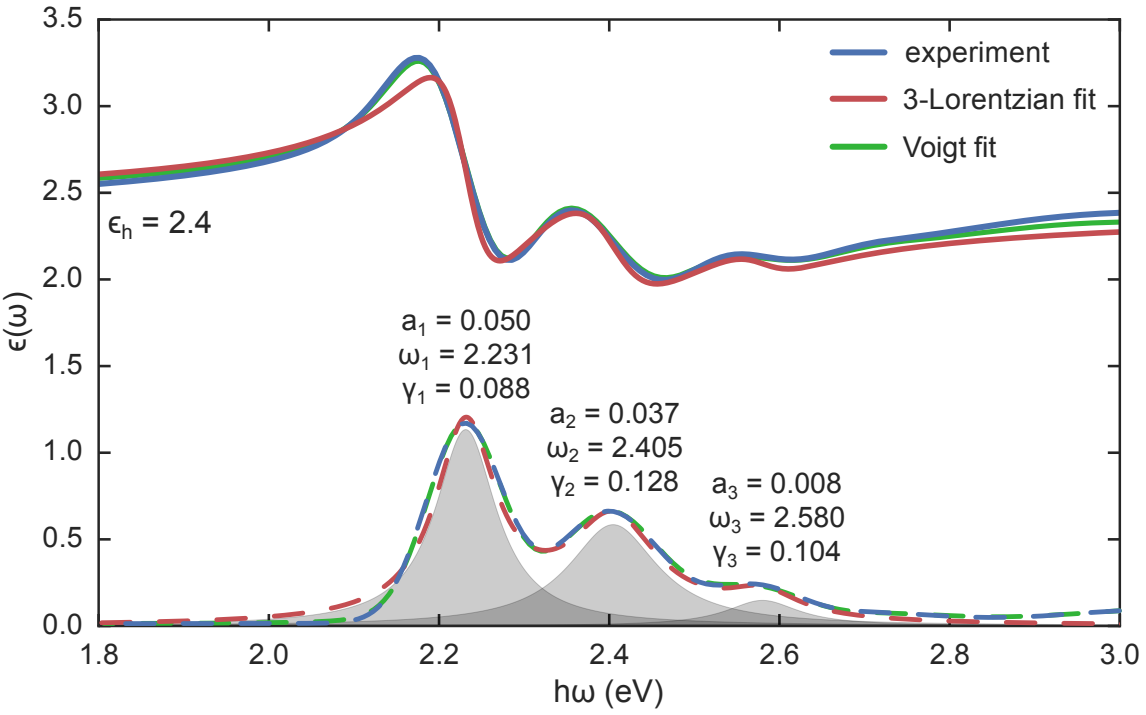

Figure 5.13: Experimental value, fit to three Lorentzians and Voigt fit of the dye dielectric function, both real parts (solid curves) and imaginary parts (dashed curves). The shaded areas show the contribution to the imaginary part of each Lorentzian peak. Note that the Lorentzian fit overestimates losses at the low frequency tail of the first resonance.

are both candidates to exhibit strong coupling phenomenology, F_{ext} coming close to its maximum value of 0.5, and both modes become more bounded as the normalized frequency $\omega R/c$ increases. For transverse electric modes, the continuity of all field components across the boundaries causes a flatter dispersion relation and a larger confinement of the field inside the nanowire. As we will see later, strong coupling can still be achieved for TE modes, albeit with smaller Rabi splittings. The bottom of Fig. 5.12 shows the electric field intensity profiles for each mode at normalized frequencies $\omega R/c = 0.55$ (where only the HE_{11} mode exists) and $\omega R/c = 0.78$, as well a pictorial representation of the system. The field profiles confirm the information for F_{ext}, showing large electromagnetic fields outside the nanowire for the HE_{11} and TM_{01} modes. We note that in the upper panels of Fig. 5.12, the shaded areas mark the spectral regions where the excitonic states are located for nanowire diameters $D = 2R = 90$ nm (bottom shaded area) and $D = 120$ and 130 nm (top shaded area), as will be studied below.

After identifying the suitable bare photonic modes of the system, we now include the effect of an organic dye within the host medium, first staying within a classical description. Without loss of generality, we choose a rylene dye [N, N'-Bis(2,6-diisopropylphenyl)-1,7- and -1,6-bis (2,6-diisopropylphenoxy)-perylene-3,4:9,10-tetracarboximide] as the dye molecule. This molecule has been used in experiments achieving strong coupling as it shows little biexciton annihilation even at high densities, and is well-characterized.[249,250] Its measured electric permittivity (both real and imaginary part) is shown in Fig. 5.13 (blue lines), together with a fit to a model dielectric function

containing three Lorentzian resonances to represent dye excitations (red lines):

$$\epsilon(\omega) = \epsilon_h + \sum_{k=1}^{3} \frac{a_k}{\omega_k - i\gamma_k/2 - \omega}, \tag{5.23}$$

where ϵ_h is the background permittivity of the host medium and ω_k, γ_k and a_k are the frequency, decay rate, and amplitude of each resonance, respectively. The fit parameter values are given in Fig. 5.13 next to each peak. While the fit with Lorentzian resonances is reasonably accurate, we note here that a nearly perfect fit to the dielectric function can be achieved by using Voigt profiles instead of Lorentzian ones. These correspond to the convolution of Lorentzians with Gaussians and can represent both homogeneous and inhomogeneous broadenings, while only homogeneous broadening (i.e., losses and dephasing) is accounted for through Lorentzian profiles.

Since the physical results do not change significantly (we have compared both approaches), for simplicity we use the Lorentzian fit to calculate the dispersion relations. However, since Lorentzians have much longer tails than seen in the experimental absorption spectrum, this approximation significantly overestimates the losses at frequencies below about 2.1 eV. As we will see later, using the experimental dielectric function (or equivalently, the fit to Voigt profiles) leads to significantly longer lifetimes and propagation lengths when strong coupling "pushes" the polaritonic states away from the molecular resonances.

The dispersion relation of the nanowires surrounded by molecules, as calculated within a classical approach by solving Eq. 1.42, is shown in Fig. 5.14 for the first three modes (solid curves) and for three different NW diameters $D = 90, 120, 130$ nm, in order to analyze the coupling to different modes. Here, the dot-dashed curves represent the dispersion relations for the bare system and the (horizontal) dotted lines represent the resonance frequencies of the excitons. In contrast to the bare-wire case, the lossy nature of the dye resonances implies that the wave vector k_z acquires an imaginary part representing the propagation losses of the polariton modes. The dispersion relations show significant energy shifts close to the resonances of the molecule excitons, and also feature a back-bending that can indicate a mode hybridization, i.e., strong coupling or polariton formation, in the classical calculations. As expected, the observed splitting is more pronounced for bare photonic modes that are only weakly confined within the nanowire, as well as for dye resonances with larger associated transition dipole moments (i.e., larger absorption amplitude a_n). However, it should be noted that even the more strongly confined TE_{01} mode displays back-bending at the first excitonic resonance.

5.2.2 Quantum model: Rabi splittings

The classical analysis shows bending bands in the dispersion relation, which are an indicative signature of a strongly coupled system in which avoided crossings arise at resonances. Nonetheless, such behavior could be just the result of the lossy medium itself.[251] In addition, the real coupling is difficult to quantify without a representative quantity such as the Rabi splitting, which has a direct meaning in a quantum description, but does not show up explicitly in the classical calculation.

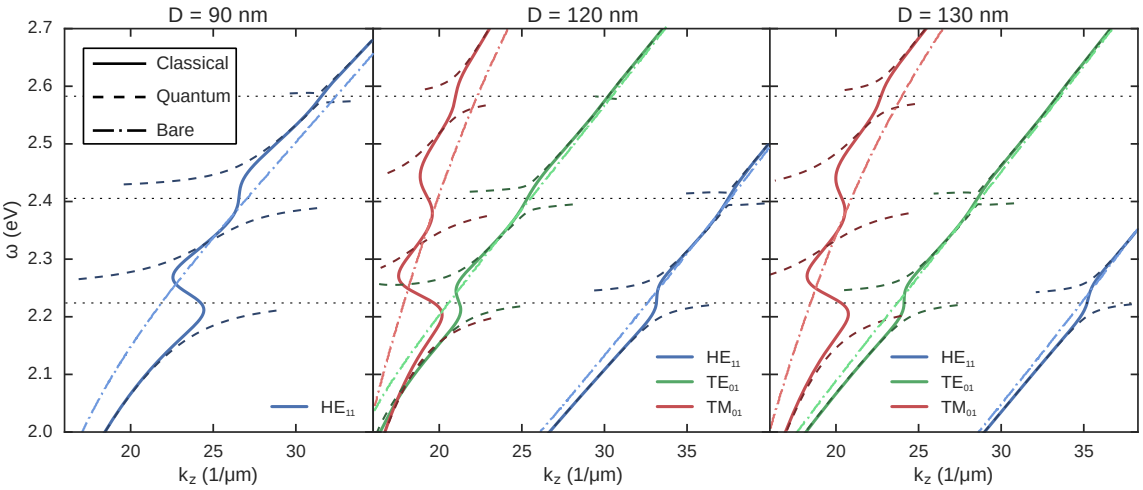

Figure 5.14: Comparison between the classical electromagnetics calculation of mode dispersions (solid curves) from Eq. 1.42 with $\epsilon_1 = 4.2^2$ and ϵ_1 from the fit to Eq. 5.23 shown in Fig. 5.13, and the quantum model (dashed curves), Eq. 5.34, for three nanowire diameters $D = 90$, 120, 130 nm. For clarity, only quantum modes with a significant photon fraction are shown (the parts not shown are basically straight lines at the bare emitter frequencies, marked by dotted horizontal lines). For comparison, the bare dispersion relations are shown as dot-dashed curves [Eq. 1.42 with $\epsilon_1 = 4.2^2$ and $\epsilon_2 = 2.4$].

To construct a quantum model, we start by quantizing the guided bare-nanowire modes by placing the system within a box of length L along the wire axis and imposing periodic boundary conditions in this direction.[238] This restricts the allowed values of the parallel momentum to $k_z = \frac{2\pi n}{L}$, with $n \in \mathbb{Z}$. Since the bare nanowire modes are lossless and confined in the transverse direction, this also allows for their straightforward quantization by imposing that the integrated energy density is equal to the photon energy.[248] Defining the quantized field profile $\vec{\mathcal{E}}(\vec{r}) = C\vec{E}(r)e^{ik_z z + im\phi}$ in cylindrical coordinates r, ϕ, z, where $\vec{E}(r)$ is the electric field profile of the mode with arbitrary normalization, gives

$$C = \sqrt{\frac{\hbar\omega}{2\pi L U_{\mathrm{rad}}}}, \tag{5.24}$$

where U_{rad} is an integral over the electromagnetic energy density of the mode, given by

$$U_{\mathrm{rad}} = 2\int \epsilon(r)|\vec{E}(r)|^2 \mathrm{d}r. \tag{5.25}$$

Here, the factor 2 accounts for the fact that equal energy is stored in the magnetic field and in the electric field. Note that we are only treating guided waveguide modes, for which U_{rad} is well-defined as k_b is purely imaginary and the mode profile decays exponentially far away from the NW. In addition, there is a continuum of freely propagating modes inside the light cone, which we neglect as they do not play a large role in the situations we study here (although they can have important effects in specific cases[252]). The Hamiltonian of the system within the rotating-wave

approximation is then given by

$$H = \sum_{n,m} \omega_{c,nm} \hat{a}^\dagger_{nm} \hat{a}_{nm} + \sum_j H_{\mathrm{mol},j} + \sum_{n,m,j} \vec{\mathcal{E}}_{nm}(\vec{r}_j) \cdot \vec{d}_j \, (\hat{\mu}^-_j \hat{a}^\dagger_{nm} + \hat{\mu}^+_j \hat{a}_{nm}), \tag{5.26}$$

where $\hat{a}_{nm}$ is the bosonic annihilation operator corresponding to the mth mode with parallel momentum $k_z = \frac{2\pi n}{L}$, while $H_{\mathrm{mol},j}$ and $\hat{\mu}_j = \hat{\mu}^+_j + \hat{\mu}^-_j$ are the bare Hamiltonian and dipole operator of molecule j, respectively, and $\vec{d}_j$ is a unit vector describing the orientation of the molecule. We have here neglected an extra term (proportional to A^2 or $\hat{\mu}^2$, depending on the gauge) in the light-matter interaction, which becomes only important in the limit of ultrastrong coupling, i.e., when coupling strengths become comparable to the bare transition frequencies.[253–256] The dye molecules are represented as few-level emitters with parameters chosen to reproduce the macroscopic dielectric function. In particular, we treat the molecules as four-level systems, with one ground and three excited states,

$$H_{\mathrm{mol},j} = \begin{pmatrix} 0 & 0 & 0 & 0 \\ 0 & \omega_1 - i\frac{\gamma_1}{2} & 0 & 0 \\ 0 & 0 & \omega_2 - i\frac{\gamma_2}{2} & 0 \\ 0 & 0 & 0 & \omega_3 - i\frac{\gamma_3}{2} \end{pmatrix}, \tag{5.27}$$

$$\hat{\mu}_j = \begin{pmatrix} 0 & a_1 & a_2 & a_3 \\ a_1 & 0 & 0 & 0 \\ a_2 & 0 & 0 & 0 \\ a_3 & 0 & 0 & 0 \end{pmatrix}, \tag{5.28}$$

where the parameters ω_k, γ_k, and a_k are taken from the fit in Eq. 5.23. Note that we also neglect direct dipole-dipole interactions between the molecules, as their (averaged) effect is already included in the transition frequencies ω_k extracted from the dielectric function. We note for completeness that an alternative (but much costlier) approach would be to extract the molecular parameters from a fit to the bare-molecule polarizability (obtained from the dielectric function using the Clausius-Mossotti relation), and then explicitly include dipole-dipole interactions between the molecules.

We treat the experimentally relevant limit that the host material contains many randomly oriented organic dye molecules, distributed evenly in the region around the nanowire with number density $\rho_{\mathrm{mol}} = 1/V_{\mathrm{mol}}$, where V_{mol} is the average volume occupied by each molecule. Considering the random distribution of the molecules along the NW, translational symmetry is approximately conserved,[238] and, consequently, superpositions of molecular states can be formed with a well-defined wavevector k_z. The Hamiltonian thus becomes (approximately) diagonal as a function of the parallel wavevector index n, significantly simplifying its diagonalization.

In addition, for the case where more than a single guided mode exists at a given k_z (as is the case for $D = 120\,\mathrm{nm}$ and $D = 130\,\mathrm{nm}$), we can also assume that, since the nanowire modes are orthogonal, they couple to independent Dicke states (superpositions of molecular excitations). This implies that the coupling between different NW modes and molecular excitations is independent. The collective coupling strength between the ith mode with parallel momentum k_n and the

molecular Dicke state corresponding to the kth excitation is then given by

$$g_{nmk}^2 = \sum_j |\vec{\mathcal{E}}_{nm}(\vec{r}_j) \cdot \vec{d}_j a_k|^2. \tag{5.29}$$

Considering the cylindrical symmetry of the system, and that the molecules are randomly oriented and fill all of the space outside the NW evenly, the coupling strength can be approximated by

$$g_{nmk}^2 \approx \frac{4\pi L}{3} \frac{a_k^2}{V_{\text{mol}}} \int_R^\infty r|\vec{\mathcal{E}}_{nm}(r)|^2 \mathrm{d}r. \tag{5.30}$$

Using Eq. 5.24 and Eq. 5.25, the coupling strength can be written as

$$g_{nmk}^2 = \frac{2\hbar\omega_{c,nm}}{3\pi\epsilon_h} \frac{a_k^2}{V_{\text{mol}}} \frac{U_{\text{ext},nm}^{el}}{U_{\text{rad},nm}}, \tag{5.31}$$

where U_{ext}^{el} is the part of the mode energy stored in the electric field outside the NW

$$U_{ext}^{el} = \int_{r>R} \epsilon_h |\vec{\mathcal{E}}(\vec{r})|^2 \mathrm{d}\vec{r}. \tag{5.32}$$

This can be expressed through $F_{\text{ext}} = U_{\text{ext}}^{el}/U_{\text{rad}}$ and the molecular density ρ_{mol} as

$$g_{nmk} = a_k \sqrt{\frac{2\hbar\rho_{\text{mol}}}{3\pi\epsilon_h} \omega_{c,nm} F_{\text{ext},nm}}. \tag{5.33}$$

It is interesting to note that the coupling strength does not depend on whether the guided nanowire mode has a small mode volume (strong localization of the field). The only information about the NW mode entering the final expression is its frequency and the fraction of the mode energy that is outside the NW. Note that this assumes that space is completely filled with molecules, so that a less confined mode effectively interacts with more molecules to give the same (or even larger) collective coupling as a confined mode. The localization of the mode is compensated by the field strength and in that sense, well-confined (out of the NW) modes are advantageous only in terms of needing less space and not in terms of reaching strong coupling.

We can now take the limit $L \to \infty$, such that $k_z = 2\pi n/L$ becomes a continuous variable, and proceed to construct an effective 4×4 model Hamiltonian for each k_z and each nanowire mode independently:

$$H_i(k_z) = \begin{pmatrix} \omega_{c,m}(k_z) & g_{m1}(k_z) & g_{m2}(k_z) & g_{m3}(k_z) \\ g_{m1}(k_z) & \omega_1 - i\frac{\gamma_1}{2} & 0 & 0 \\ g_{m2}(k_z) & 0 & \omega_2 - i\frac{\gamma_2}{2} & 0 \\ g_{m3}(k_z) & 0 & 0 & \omega_3 - i\frac{\gamma_3}{2} \end{pmatrix}, \tag{5.34}$$

where m labels the nanowire mode, and $g_{mk}(k_z)$ is given by Eq. 5.33.

In Fig. 5.14, the dispersion relations calculated by the eigenvalues of Eq. 5.34 are shown (dashed colored curves) with proper avoided crossings appearing near excitonic frequencies man-

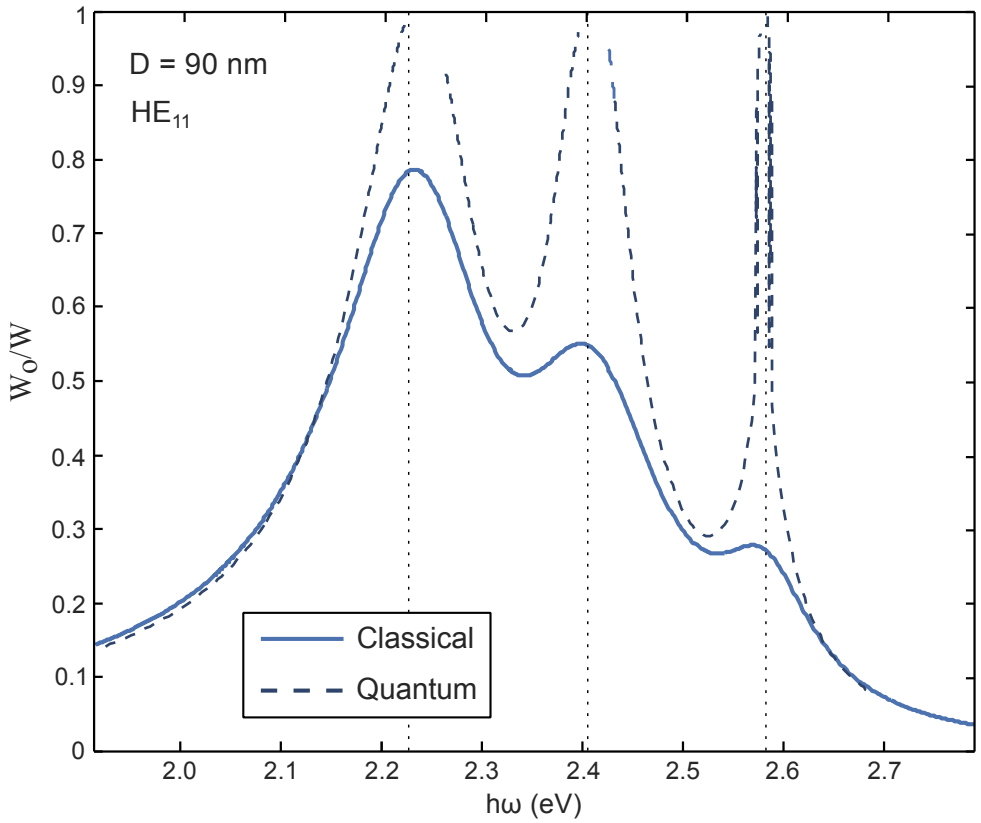

Figure 5.15: Fraction of the energy stored in the excitons calculated by the classical (solid curve) and quantum approach (dashed curve) for the HE_{11} mode at a nanowire diameter of $D = 90$ nm. The material properties are the same as in Fig. 5.14. The resonant frequencies of the excitons are marked by dotted vertical lines.

ifesting the strong coupling leading to polaritonic modes. Out of resonance, as expected, the dispersion relations are practically the same as those of the classical bare photonic modes. It should be pointed out that the classical electromagnetic calculations work at real energies ω, but allow complex momenta k_z (describing propagation loss). On the other hand, the quantum model works at real k_z, but allows complex energies (describing temporal loss). These two pictures represent the same physics, but are not completely equivalent. These differences are the reason for the different behavior close to the regions of largest absorption where the classical modes bend backwards (stationary electromagnetic field solutions), while the quantum modes are actually split (time dynamic driving process). We also note that the good agreement between quantum and classical calculations in Fig. 5.14, without any fit parameters, cannot be reproduced by the often-used strategy of constructing an approximate model with k_z-independent couplings g_{mk} (corresponding to approximating $\omega_c F_{\text{ext}}$ as constant).

Furthermore, we emphasize that the quantum model here clearly shows that strong coupling is reached for these conditions. The Rabi splitting Ω_R is estimated from the splitting of the eigenenergies of Eq. 5.34 at resonance. For example, the cleanest system is given by the nanowire with diameter $D = 90\,\text{nm}$, for which only the HE_{11} mode is guided. This system supports strong coupling with significant Rabi splittings $\Omega_R > 100\,\text{meV}$ for both the first and second molecular

excitations. Moreover, nanowires with larger diameters support multiple polaritons (also with significant Rabi splitting) at the same frequency, which might be interesting for possible applications.

5.2.3 Energy distribution: photonic and excitonic modes

An important characteristic of strong coupling is coherent energy exchange between different physical systems, inducing hybrid states that no longer can be seen or described as individual systems. The distribution of the energy into photonic and excitonic parts is important to characterize the new states.

From a classical perspective, the electromagnetic energy for lossy media the can be calculated as a perturbation from the lossless case. However, the strong dispersion and the high losses of the permittivity invalidate the usual expressions for the electromagnetic energy stored in the system. In addition, there is no clear distinction between the energy stored in the medium and that stored in the electromagnetic field. For this purpose, we follow the approach taken by Loudon[257] for the energy of a medium with a single resonant frequency, and its extension to multiple resonances,[258,259] considering each excitonic state as an independent resonance.

The energy of an absorbing dielectric medium described by resonances is

$$W = W_o + W_f, \tag{5.35a}$$

$$W_o = \frac{1}{4}\int_R^\infty r\epsilon_0 |\vec{E}(\vec{r})|^2 \mathrm{d}r \sum_n \frac{2a_n\omega\left(\omega_n^2+\omega^2\right)}{\left(\omega_n^2-\omega^2\right)^2+\omega^2\gamma_n^2}, \tag{5.35b}$$

$$W_f = \frac{1}{4}\int_0^\infty r\left[\epsilon_0\epsilon_r|\vec{E}(\vec{r})|^2 + \mu_0\mu_r|\vec{H}(\vec{r})|^2\right]\mathrm{d}r, \tag{5.35c}$$

where

$$\epsilon_r = \begin{cases} \epsilon_c, & r<R \\ \epsilon_h, & r>R \end{cases} \qquad \mu_r = \begin{cases} \mu_c, & r<R \\ \mu_b, & r>R \end{cases}. \tag{5.36}$$

The first term of Eq. 5.35a, W_o, is the energy stored in the excited oscillators (excitons) and it goes to zero out of the resonances. The second term, W_f, is the energy carried by the electromagnetic field.

Within the quantum model, the excitonic energy is calculated as the (real part of the) expectation value of the molecular exciton Hamiltonian H_{mol} in each state, relative to the total energy of the eigenstate.

As we have previously seen that each nanowire mode is independent from the point of view of the coupling with the excitonic media, we now focus only on the case $D = 90$ nm (results for other modes are analogous). The ratio between the energy stored in the oscillators and the total energy of the system, $W = W_o + W_f$, characterizes the nature of the mode (photonic/excitonic). Figure. 5.15 shows the percentage of the energy stored in the excitons obtained by the classical (solid curve) and quantum approaches (dashed curve) for the HE_{11} mode at $D = 90$ nm. The agreement between both approaches is extremely good at the frequencies where both dispersion relations coincide (see Fig. 5.14). Far from resonance, the energy stored in the oscillators goes to zero, thus there

is no interaction with the excitons and the mode is practically photonic. In the spectral region of the resonance bands, the fraction of the energy in the excitons increases, as the mode becomes polaritonic. Close to resonance, as expected from the differences in the dispersion relation, the approaches differ: whereas the energy fraction within the classical model yields smooth maximal values (below 100%) at the excitonic frequencies (corresponding to the regions in which the mode dispersion relation bends backwards in Fig. 5.14), the quantum approach asymptotically tends to 1, namely, to 100% of energy stored as excitons (flat dispersion relation in Fig. 5.14).

It is interesting to note that a high enough fraction of excitonic energy is required for this system to be a suitable platform for excitonic applications; however, at the same time, it is desirable to minimize losses, which is achieved for high photon components. A good compromise can be achieved at intermediate energy fractions below the onset of losses in the dielectric function ($h\omega \approx 2.1$ eV, at which $W_o/W \approx 0.3$), as we will show below.

5.2.4 Half-life, propagation length and energy velocity

While up to now, we have focused on the real part of the quantities (wave vectors and/or energies), the losses of the system are also a very important part necessary to obtain a complete characterization. In particular, they determine dynamic properties such as the mode propagation length that are crucial for practical applications. Thus far, we have studied the properties of the system using a Lorentzian fit for the dielectric function, rather than the experimentally measured one, since this allows more direct comparison with a simple quantum model, and gives almost identical results for the dispersion relation and allows us to determine the existence of strong coupling. However, the Lorentzian fit severely overestimates losses away from the resonances, and much more reliable results are obtained when using the actual experimental values in order to calculate properties such as the half-life τ and the propagation length L_p (linked through the group velocity v_g).

The propagation length, L_p, is the distance after which the energy of the wave is reduced to $1/e$ of its initial value. For the classical approach, the propagation length of a guided mode is given by $L_p = 1/2k_z''$, inversely proportional to the imaginary part of the propagation constant, $k_z = k_z' + ik_z''$, that accounts for the attenuation of the mode. In Fig. 5.16 the propagation length of the HE_{11} mode for $D = 90$ nm (as in Fig. 5.15) is plotted in logarithmic scale as a function of the frequency, using both the experimental value of the dielectric function and the Lorentzian fit from Eq. 5.23 shown in Fig. 5.13.

At frequencies below the first resonance, L_p, using the experimental dielectric function gives values that are typically one order of magnitude larger than with the Lorentzian fit, and gives propagation lengths that are one to two orders of magnitude larger than the wavelength of the mode.

We also note that the difference between dielectric functions is much smaller for the TE_{01} and TM_{01} modes at very low frequencies (not shown here). This is due to the fact that, as the modes become leaky, the radiation processes begin to dominate losses and the imaginary part of the permittivity is no longer determinant. On the other hand, as expected, both methods give

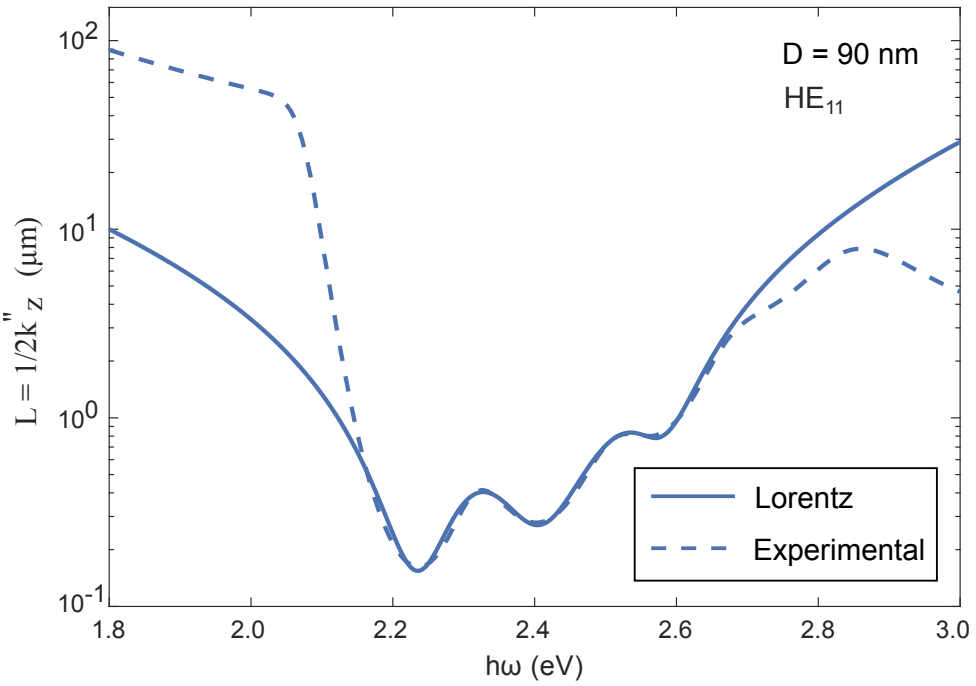

Figure 5.16: Classical calculations of the propagation length L_p (in logarithmic scale) as a function of frequency for the HE_{11} mode ($D = 90$ nm). Solid curve: the dielectric function is fitted to a Lorentzian model, Fig. 5.13. Dashed curves: the experimental value of the dielectric function is used.

similar results at frequencies close to resonance (2.2-2.6 eV), where the Lorentzian fits accurately reproduce the dielectric function. Finally, the Lorentzian fit leads to higher (unphysical) values of L_p at high frequencies since another resonance appears that was not included in the fit therein.

For current and future applications that rely on exciton transport,[245–247,260] large propagation lengths are desired while simultaneously keeping a considerable amount of energy in the excitons (excited oscillators). To achieve better coupling, the mode energy must be outside the NW, although the localization of the energy in the excitonic medium would imply higher losses. These two issues must be balanced in order to optimize the propagation length. An important effect to take into account here is that the propagation length is determined by the dielectric losses at the frequency of the polariton mode. This implies that strong coupling can be used to push the exciton peak away from the exciton losses through polariton formation, allowing us to create states with high exciton character that do not suffer from the large excitonic losses. This is a particular strength of the semiconductor nanowire systems studied here, where the bare photonic modes are essentially lossless. For example, focusing on the HE_{11} mode and demanding that 30% of the energy be in the excitons, the maximum propagation length is reached at a diameter $D = 70$ nm, with $L_p = 48$ μm at $h\omega = 2.02$ eV (at the lower part of the first resonant frequency). The propagation wavelength of the mode at that frequency is 367 nm, 130 times smaller than the propagation length. As a general consideration, the propagation length is optimal (related to the energy stored in the excitonic media) close to frequencies at which losses start to substantially increase due to inhomogeneous broadening.

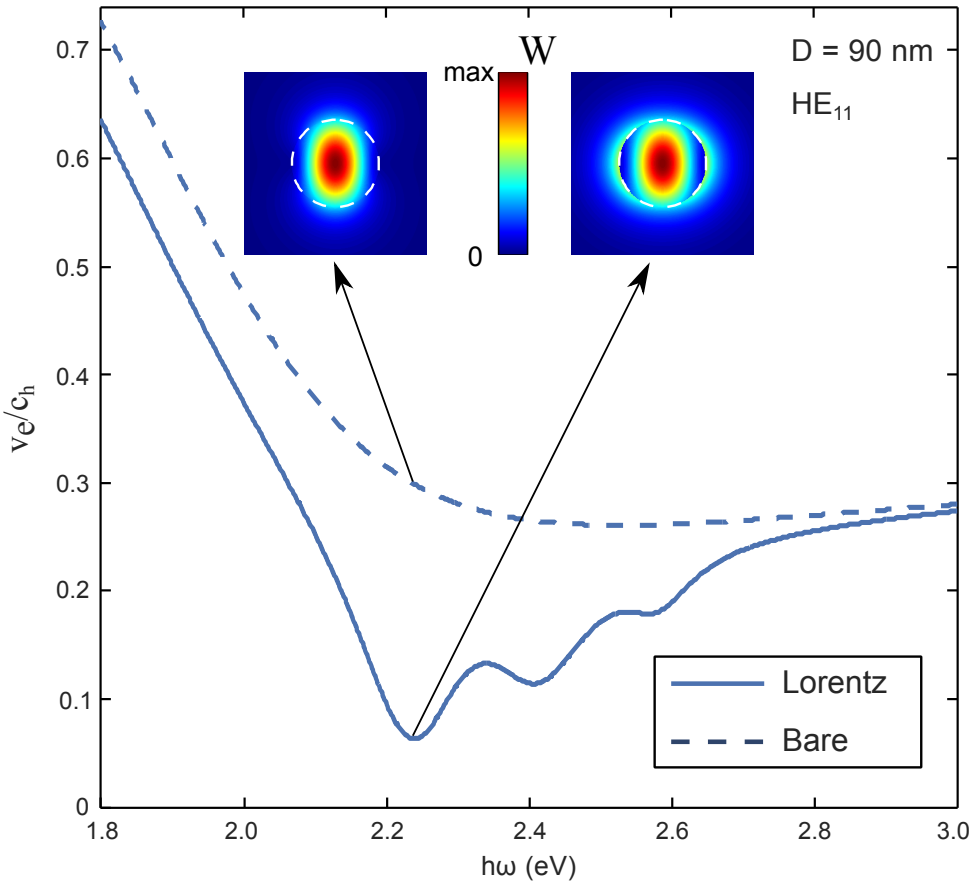

Figure 5.17: Classical calculations of the energy velocity v_e divided by the speed of light in the host medium, c_h, as a function of frequency for the HE_{11} mode ($D = 90$ nm): Solid curve: dielectric function fitted to a Lorentzian model; dashed curve: bare system ($\epsilon_2 = 2.4$). The insets show the energy distribution at the first resonant frequency $\omega = 2.23$ eV for both cases.

The velocity at which energy is transported by a propagating mode is normally given by the group velocity, v_g, defined as

$$v_g = \frac{\mathrm{d}\omega}{\mathrm{d}k}. \tag{5.37}$$

However, the velocity at which the energy is transported must always be lower than the speed of light, which is not fulfilled by this definition; for example, in the region where the photonic bands bend backward, the group velocity goes to infinity. Therefore, as for the energy, an alternative definition is needed in lossy media. Following the works of Loudon and Brillouin,[257,261] we define the energy velocity, v_e, as the ratio between the flow of energy, given by the Poynting vector, and the total energy stored in the system

$$v_e = \frac{S_z}{W} = \frac{\int_0^\infty r S_z(\vec{r}) dr}{W}. \tag{5.38}$$

For the bare photonic states calculated before (lossless case), the results given by Eq. 5.37 and Eq. 5.38 are identical (not shown here).

In Fig. 5.17 the energy velocity (divided by the speed of light in the host medium, c_h) of the HE_{11} mode is shown for $D = 90$ nm. In addition, the result for the bare system is also included (dashed line). The energy velocity presents dips at resonant frequencies. Strong coupling manifests as a reduction in the energy velocity, since the coherent exchange of energy slows down the light flow. At resonant frequencies, the electric permittivity of the excitonic media matches the value of the background ϵ_h. Despite the non-zero imaginary part, the field profiles for both cases (with and without resonances) are very similar, and so are the value of the Poynting vector and the energy inside the NW. However, the energy outside the NW presents an additional contribution W_o due to the excitons (see inset in Fig. 5.17), slowing the propagation of the energy down.

Chapter 6

Conclusiones

En esta sección se exponen los avances más importantes incluidos en esta Tesis. El trabajo desarrollado en cada capítulo puede resumirse como:

- Capítulo 2: Presentación analítica de la formulación (CEMD) para describir las propiedades electromagnéticas de metasuperficies basado en un modelo de dipolos acoplados en el que las respuestas dipolares eléctricas y magnéticas están incluidas. La formulación se ha utilizado para analizar la reflexión y transmisión de metasuperficies dieléctricas formadas por cilindros de alto índice de refracción, mostrando un acuerdo excelente en el régimen dipolar con simulaciones numéricas.

- Capítulo 3: Estudio de los estados ligados en el continuo (BICs) en configuraciones periódicas de partículas dipolares con diferente simetría. Las propiedades teóricas de los BICs, calculados con la formulación CEMD, se han usado para entender y predecir las medidas experimentales.

- Capítulo 4: Estudio teórico de la absorción y dispersión de nanohilos (NWs) infinitos y finitos, mostrando la conexión entre las resonancias de Mie y los modos guiados, la amplificación de la absorción debido al acoplo a modos guiados y la presencia de resonancias Fano estrechas e intensas en cilindros dieléctricos.

- Capítulo 5: Análisis de la distribución del momento angular orbital y de spin de luz guiada en guías planas y cilíndricas, así como su impacto en fuerzas ópticas. Además, se ha desarrollado un modelo teórico para estudiar las condiciones necesarias para alcanzar el régimen de acoplamiento fuerte en un sistema formado por un NW semiconductor embebido en un medio excitónico, así como para investigar sus propiedades.

Por lo tanto, las conclusiones seguirán el mismo esquema.

Empezaremos revisando las contribuciones más significantes en relación con el Capítulo 2 sobre metasuperficies:

- En la Sección 2.1 se ha desarrollado una formulación de dipolos eléctricos y magnéticos acoplados para una cadena unidimensional de cilindros basada en las polarizabilidades dipolares de las partículas constituyentes. Se han derivado explicitamente expresiones analíticas generales para la reflexión y transmisión, el teorema óptico y las condiciones de Kerker para la red de cilindros. A partir de las expresiones analíticas se ha encontrado que los dipolos perpendiculares a la superficie y aquellos a lo largo del eje de los cilindros están acoplados, dando lugar a resonancias intensas y asimétricas en los espectros de reflectancia y transmitancia. Las condiciones de Brewster se han obtenido para ambas polarizaciones a incidencia normal, predichas analíticamente por las condiciones de red the Kerker; considerando que las condiciones de Kerker están prohibidas en cilindros aislados. Este efecto puede ser generalizado, siendo posible tener cero de reflexión potencialmente a cualquier ángulo de incidencia.

- Como caso de estudio, se han analizado en la Sección 2.2 las propiedades de una red periódica de nanocilindros de silicio. Desentrañando el papel de cada dipolo por separado (paralelos y perpendiculares), se ha determinado el efecto total de la red en todos los casos, considerando después la interacción entre todos ellos y determinando las características de cada dipolo en el espectro de reflectancia. A pesar de ser transparente, se ha observado que en resonancia la reflectancia es total, encontrándose resonancias Fano intensas y asimétricas. También, se han encontrado bandas de transmisión total de Brewster en ambas polarizaciones, mostrando que esta simple estructura tiene una fenomenología compleja. Por último, los resultados analíticos han sido comparados con simulaciones numéricas, mostrando total concordancia tanto cualitativamente como cuantitativamente.

- En la Sección 2.3 se ha mostrado especial interés en la emergencia de resonancias Fano (y en transparecía electromagnéticamente inducida, EIT por sus siglas en ingles) en el espectro de reflectancia, relacionado con los estados ligados en el continuo. Se ha demostrado analíticamente que la interferencia intensa entre modos se evidencia a través de una variada fenomenología, incluyendo resonancias Fano extremadamente estrechas con factores de calidad mayores de 10^3. Analizando la dependencia de estas resonancias estrechas con el medio externo, se ha explorado la eficiencia de esta metasuperficie dieléctrica como sensor de índice de refracción, prediciendo figuras de mérito f.o.m. $\geq 10^2$. De este modo, se has descrito las resonancias Fano con alto factor de calidad en esta geometría simple, mostrando su uso potencial como nanodispositivos para medir el índice de refracción.

A continuación se muestra un resumen sobre las principales contribuciones relacionadas con el tema de estados ligados en el continuo presentado en el Capítulo 3:

- En la Sección 3.2 las características de un BIC en una red cuadrada bidimensional de discos de alto índice de refracción ($\epsilon \sim 78$) han sido estudiadas teoréticamente y experimentalmente. Los BICs se originan por la oscilación coherente de los dipolos orientados a lo largo del eje del disco. Los experimentos se han realizado en el Institut Fresnel en Marsella. En particular los resultados más relevantes son:

  - El concepto de Brewster quasi-BICs ha sido introducido al combinar la restricción angular a un solo canal especular impuesto por la periodicidad de la metasperficie con el comportamiento resonante de los discos (meta-átomos), que presentan una única resonancia que irradia en todos los ángulos, excepto en el de su dipolo inducido (efecto Brewster).
  - Se ha demostrado teóricamente que tales quasi-BICs de tipo Brewster emergen de un BIC inducido por la oscilación coherente de dipolos magnéticos en discos de alto índice de refracción sin inclinar, estando el BIC protegido por simetría en la metasuperficie. A medida que aumenta el ángulo de inclinación del dipolo magnético, se convierten en quasi-BIC, sin embargo, son inaccesibles en diferentes ángulos de incidencia (onda plana), que pueden ajustarse selectivamente inclinando los ejes del disco con respecto al plano de la metasuperficie, en total acuerdo con resultados experimentales.
  - Se han observado elevados factores de calidad a incidencia normal, mientras que disminuyen para la metasuperficie de discos inclinados, debido a la relajación de las condiciones de Brewster.

- Por otro lado, en la Sección 3.3 se ha analizado un BIC originado por la oscilación fuera de fase de dipolos paralelos a la matasuperficie. Los experimentos se han realizado en la Technological University de Eindhoven. Los principales resultados de esta colaboración son:

  - Se ha mostrado teoréticamente que las metasuperficies con dos particulas (dipolares) por celda unidad presentan BICs cuando las partículas son idénticas; tales BICs surgen de resonancias Fano que se estrechan a medida que las partículas de la celda unidad se vuelven idénticas. Cabe destacar que se ha demostrado analíticamente que esta condición de BIC es independiente de la posición relativa entre los dipolos de la celda unidad y de los parámetros de red (mientras que no haya ningún orden de difración accesible).
  - El modelo teórico ha sido verificado experimentalmente a través de medidas de transmisión en el rango de los THz en metasuperficies formadas por redes de barras de oro.
  - Por lo tanto, estas propiedades hacen de esta red de dipolos desiguales un escenario general para diseñar metasuperficies robustas y versátiles que presenten estados ligados en el continuo a lo largo del espectro electromagnético.

Las principales resultados sobre las propiedades teóricas de NWs semiconductores estudiados en el Capítulo 4 se presentan ahora.

- En la Sección 4.1 se ha investigado teoréticamente y numéricamente la absorción de luz en NWs semiconductores finitos. Los resultados principales de este trabajo de este trabajo se pueden resumir como:

  - Partiendo de la relación de dispersión de los modos de una guía cilíndrica y de la teoría de dispersión de Mie, se ha demostrado que existe una estrecha relación entre los modos guiados y las resonancias de Mie, donde ambos fenómenos están descritos formalmente por la misma ecuación, como las dos caras de Janus. Esta imagen unificada ha sido explotada teniendo como propósito el diseño de NWs con propiedades ópticas ad-hoc.
  - Se ha mostrado que para NWs finos, en los que solo hay modos *leaky* espectralmente disponibles, la absorción es prácticamente idéntica a la absorción teórica dada por un NW infinitamente largo. Este hecho refuerza la conexión entre las resonancias de Mie y los modos guiados.
  - Por contraste, el ángulo de incidencia es crítico para NWs anchos: la absorción esta gobernada por las resonancias de Mie a incidencias perpendiculares (y oblicuas) al eje del NW, coincidiendo con la absorción del NW infinito. Sin embargo, la excitación de modos guiados gobierna y amplifica la absorción a incidencias cercanas al eje del NW.
  - Además, se obtiene una mayor sección eficaz de absorción (sustancialmente más elevada que aquella predicha por la teoría de Mie en cilindros infinitos) a incidencias paralelas al eje del NW, a las cuales el acoplo a modos guiados (prohibidos en NW infinitos) juega un papel crucial en la amplificación de la absorción.
  - Sobre el conocimiento de las dependencias angulares y espectrales de las resonancias de Mie (semejantes a los modos *leaky*) se han investigado las condiciones para obtener bandas anchas espectral y angularmente, así como para amplificar la absorción. También, se ha encontrado que para el caso del InP (y otros semiconductores con propiedades similares) la dispersión del índice de refracción induce escisiones en la relación de dispersión de las resonancias de Mie, ensanchando y amplificando la sección eficaz de absorción a lo largo de un amplio intervalo angular.

- La dispersión de luz de NWs semiconductores finitos se estudia teoréticamente y numéricamente en la Sección 4.2. Las conclusiones principales se presentan a continuación:

  - Cuando el radio de los NWs es del orden de cientos de nanómetros y la longitud es del orden de media micra, las resonancias de Mie de orden más bajo coexisten con las resonancias Fabry-Perot de orden más bajo de los modos guiados. Su interferencia mutua produce intensas resonancias Fano en el espectro de dispersión.
  - Para polarización TE, el espectro de dispersión presenta líneas intensas y asimétricas con forma Fano con más contraste e intensidad que aquellas encontradas con anterioridad en nanovarillas metálicas. En polarización TM se encuentran líneas menos asimétricas, pero aun así de gran intensidad.
  - Se ha dado interpretación física a dichas líneas Fano en términos de interferencia entre el patrón angular del campo lejano de las resonancias anchas de Mie y de los modos estrechos FP, calculados con un modelo de corriente unidimensional. En este sentido,

se ha dado una expresión simple para determinar de forma casi analítica las secciones eficaces de dispersión, en excelente acuerdo con las simulaciones numéricas. También se presentó una fórmula generalizada de Fano extendida para dar cuenta de un amplio espectro multiresonante. Ambos producen factores de asimetría consistentes con nuestra interpretación física.

Por último, en el Capítulo 5 profundizamos en las propiedades fundamentales de los NWs semiconductores.

- En la Sección 5.1 los momentos angulares orbitales y de spin (OAM y SAM) de la luz se han investigado analíticamente en guías de onda planas y cilíndricas que soportan los modos transversal eléctrico/magnético e híbrido (solo en cilindros). Dejando a un lado el conocido spin transversal asociado con la componente evanescente de los modos guiados fuera de las guías de onda, se ha puesto énfasis en el impacto del confinamiento del modo en el interior. A continuación, se presentan las principales aportaciones extraídas de este análisis.

  - Se ha mostrado que todos los modos (transversales e híbridos), a pesar de no ser evanescentes dentro de la guía de onda, exhiben SAM transversal $S_t \propto (W/k_z\omega)\, k_t$ proporcional al momento transversal k_t en guías de ondas planas y cilíndricas. Además se muestra que tal densidad transversal de spin lleva el denominado momento (de Belinfante) longitudinal de spin, paralelo o anti-paralelo al propio momento angular orbital, gobernado por la dependencia transversal del modo impuesta por su orden y polarización.
  - Se ha demostrado analíticamente que el momento de spin $\mathbf{P^S}$ es crucial a través de la relación $\mathbf{P} = \mathbf{P^O} + \mathbf{P^S}$ (estando $\mathbf{P}$ relacionado con la densidad de momento dado por el vector de Poynting) para recuperar la dependecia del momento orbital con el vector de propagación $P_z^O \propto k_z$.
  - Además del spin transversal anterior, se muestra que los modos híbridos en las guías de onda cilíndricas llevan spin longitudinal que surge de su helicidad intrínseca; dichos SAM longitudinales se concentran especialmente en el interior (confinamiento fuerte) de la guía de onda cilíndrica.
  - También se incluyó una discusión sobre el impacto de tales SAM trasversales dentro de las guías de onda sobre las fuerzas en las partículas dipolares, por ejemplo, guías de onda llenas de agua en los regímenes de infrarrojos y microondas. Toda esta fenomenología se ha discutido para los modos guiados de orden inferior en guías de onda planas y cilíndricas simples para mayor claridad, pero se puede extrapolar directamente a otras geometrías conservando el confinamiento del modo guiado.

- En la Sección 5.2 se ha mostrado que se puede conseguir acoplamiento fuerte entre los modos débilmente guiados de un NW con un medio externo excitónico, exhibiendo separaciones de Rabi de mas de $\Omega_R > 100$ meV para un colorante orgánico. Como puntos destacables:

- La cola evanescente de los modos débilmente guiados permite alcanzar el régimen de acoplamiento fuerte de los modos del NW con los excitones de las moléculas de un colorante orgánico externo. El mecanismo físico subyacente es similar a los polaritones de plasmón de superficie en nanovarillas metálicas, pero con la ventaja de que las longitudes de propagación son mucho más grandes debido a la casi total ausencia de absorción dentro del NW semiconductor.
- Se ha presentado un modelo cuántico (desarrollado en colaboración con Johannes Feist en la Universidad Autónoma de Madrid) que proporciona una expresión analítica directa para la separación de Rabi y muestra que la cantidad relevante no es la concentración de campo sino la fracción de campo que interactúa con los excitones. El modelo cuántico también revela que el intercambio coherente de energía juega un papel importante en el sistema: las relaciones de dispersión presenta bandas que se evitan con claras separaciones de Rabi, como se espera en el régimen de acoplamiento fuerte.
- Los modos de polaritón en estos sistemas pueden lograr longitudes de propagación significativas de hasta dos órdenes de magnitud más grandes que las longitudes de onda del modo simple, mientras se mantiene un carácter excitónico significativo. Esto sucede porque el acoplamiento fuerte puede mover los modos excitónicos a regiones de frecuencia donde las pérdidas de material son mucho más pequeñas que alrededor de las resonancias excitónicas.

Chapter 7

Conclusions

In the present section an overview of the most significant advances included in this Thesis is detailed. The work developed in each chapter can be summarized as follows:

- Chapter 2: Presentation of an analytical (CEMD) formulation to describe the electromagnetic properties of metasurfaces based on a coupled dipole model in which both electric and magnetic dipole responses have been included. The formulation has been used to analyze the reflection and transmission of all-dielectric metasurfaces consisting of HRI cylinders, showing an excellent agreement in the dipolar regime with full numerical simulations.

- Chapter 3: Study of bound states in the continuum (BICs) with different symmetries in an array of dipolar particles. The theoretical properties of BICs, calculated with the CEMD formulation, have been used to understand and predict the experimental results.

- Chapter 4: Theoretical study of absorption and scattering from infinite and finite nanowires (NWs), revealing the connection between Mie and leaky/guided mode resonances, the enhancement of absorption due to the coupling to guided modes, and the emergence of strong narrow Fano resonances in dielectric cylinders.

- Chapter 5: Analysis of the spin and orbital angular momentum distributions of guided light in planar and cylindrical waveguides and its impact on optical forces. Also, a theoretical model has been developed to study the necessary conditions to achieve strong-coupling regimes in a system consisting of a semiconductor nanowire embedded in an excitonic medium, as well as their properties.

Hence, the conclusions will follow the same structure.

Let us start reviewing the most significant contributions regarding Chapter 2 about metasurfaces:

- In Section 2.1 I have developed a coupled electric and magnetic dipole formulation for a one dimensional cylinder array based on the dipolar polarizabilities of the constituent particles. General analytical expressions were explicitly derived for reflection and transmission,

the optical theorems and the Kerker conditions of the cylinder array. From the analytical expressions it was found that dipoles perpendicular to the surface and along the cylinder axis are coupled so that the reflectance (and transmittance) can exhibit strong asymmetric features. In addition, Brewster conditions are obtained in both polarizations at normal incidence, predicted analytically through lattice Kerker conditions; recall that Kerker conditions are forbidden for isolated cylinders. The effect can be generalized, making it possible to have a zero in reflection potentially at any angle of incidence.

- As a case study, a metasurface consisting of an array of Si nanocylinders has been analyzed in Section 2.2. By unraveling the role of each dipole resonance separately, the impact of the lattice has been determined in all cases; then the interplay between them is fully accounted for, identifying the feature of each dipole in the reflectance spectra. Despite being transparent, total reflection from the dielectric cylinder array was observed on resonance. Also, Brewster bands of total transmitance were found for both polarizations, showing that such a simple system possesses a complex phenomenology. Finally, the analytical results were compared with numerical simulations, in agreement not only qualitatively but also quantitatively.

- In Section 2.3 special interest has been paid to the emergence of Fano resonances (and electromagnetic-induced transparency, EIT) in the reflectance spectra, closely related to bound states in the continuum. It has been demonstrated analytically that strong interference between modes is evidenced though a varied phenomenology, including extremely narrow EIT-like and Fano resonances with Q-factors exceeding 10^3. By looking into the dependence of those narrow asymmetric resonances on the surrounding medium, the performance of those Si nanocylinder metasurfaces has been explored as refractive-index sensors; figures of merit f.o.m. $\geq 10^2$ were predicted. In this manner, the appearance of high-Q Fano resonances has been described in such simple-geometry, Si-based metasurfaces, showing that they hold potential, in turn, for refractive-index sensing devices at the nanoscale.

A summary of the main contributions related to the topic of bound states in the continuum presented in Chapter 3 is given now:

- In Section 3.2 the features of a BIC in a two dimensional square array of extremely HRI disks ($\epsilon \sim 78$) have been studied theoretically and experimentally. BICs come from a coherent oscillation of dipoles along the disk axis. The experiments have been carried out in the Institut Fresnel in Marseille. In particular the more significant results are:

  - The concept of Brewster quasi-BICs has been introduced by combining the angular constraint to a single specular channel imposed by metasurface periodicity with the resonant behavior of single dipole, non-degenerate meta-atoms that radiate at all angles except for that of their induced dipole-moment orientation (Brewster effect).
  - Such Brewster quasi-BICs have been theoretically shown to emerge from a symmetry-protected magnetic dipole (MD)-induced BIC in HRI non-tilted disk metasurfaces. As

the MD tilt-angle is increased, they become quasi-BICs, however being inaccessible at different angles of (plane-wave) incidence, which can be selectively tuned by tilting the disk axes with respect to the metasurface plane, in full agreement with experimental results.

  - Huge Q-factors were evidenced at normal incidence for perpendicular dipoles, while slightly smaller ones were obtained at oblique angles with opposite signs (reciprocal scenarios), i.e. for quasi-BICs, due to the relaxation of the Brewster condition either in reflectance or transmittance.

- On the other hand, in Section 3.3 a BIC originated by the out-of phase oscillation of dipoles parallel to the surface array has been analyzed. The experiments have been carried out in the Technological University of Eindhoven. The main results of this collaboration are:

  - It has been shown theoretically that metasurfaces consisting of two (dipolar) particles per unit cell support BICs when the particles are identical; such BICs emerge from strong Fano resonances that become narrower as the dipole detuning vanishes. Remarkably, such BIC condition was shown to be independent of both the relative position between dipoles/rods inside the unit cells and the lattice constants (provided that no diffractive orders come into play).
  - The theoretical model has been verified experimentally through the THz transmission spectra of metasurfaces consisting of sub-wavelength gold-rod dimers.
  - Hence, these properties make an array of detuned dipoles a general scenario to engineer robust and versatile metasurfaces supporting bound states in the continuum throughout the electromagnetic spectrum.

The main results on theoretical properties of semiconductor NWs studied in Chapter 4 are now presented.

- In section 4.1 the light absorption in finite semiconducting NWs has been investigated theoretically and numerically. The main contributions of this work can be summarized as:

  - From the leaky mode dispersion relation and Mie scattering theory it has been shown that a close relation exists between leaky/guided modes and Mie resonances, which stems from a formally equivalent equation, as the two faces of Janus bifrons. This unified picture has been then exploited for the purpose of designing nanowires with ad-hoc optical properties.
  - It was shown that for thin NWs, in which only leaky modes are spectrally available, the absorption is practically identical to the theoretical absorption for infinitely long NW. This fact reinforces the connection between Mie resonances and leaky modes.
  - Opposite, the angle of incidence becomes critical in thick NWs: absorption is dominated by Mie resonances at incident angles perpendicular (and oblique) to the nanowire

axis; by contrast, guided mode excitation governs and enhances absorption at grazing incidence.

  - Moreover, the largest absorption cross sections (substantially larger than those predicted by Mie theory for infinite cylinders) are obtained for light incidence parallel to the NW axis, at which guided mode coupling (forbidden for infinite NWs) plays a crucial role in boosting absorption.

  - Conditions for broad-band, broad-angle, enhanced absorption efficiencies were investigated on the basis of the spectral and angular dependence of Mie resonance (likewise, leaky mode) excitation. Incidentally, it has been found that, in the case of InP (and of many other similar semiconductors), the dispersion of the (real part of the) refractive index typically induces a split of the Mie resonances (leaky modes) involved, broadening the spectral region over which Mie-resonant absorption is enhanced for light incident over a broad angular range perpendicular and oblique to the NW axis.

- Light scattering from finite semiconducting NWs is theoretically and numerically studied in Section 4.2. The main conclusions of the research are listed below:

  - When NW radii are on the order of a hundred nanometers and lengths are of about half a micrometer, the lowest-order Mie resonances coexist with Fabry-Perot (FP) resonances of the lowest-order guided modes. Their mutual interference leads to strong Fano resonances in the scattering spectra.

  - Highly asymmetric Fano line shapes are found in TE polarization, with far more contrast and intensity than those previously reported for metallic nanorods. Less asymmetric, but also very strong, Fano resonances are found in TM polarization.

  - A physical interpretation has been given in terms of the interference of far-field angular patterns of broad Mie resonances with narrow FP modes, accounted for with a 1D line current model. In this regard also, a simple expression has been obtained to quasi-analytically determine the scattering cross sections, in excellent agreement with the numerical simulations. A generalized Fano formula extended to account for a broad multiresonant continuum has also been presented. Both yield asymmetry factors consistent with our physical interpretation.

Finally, Chapter 5 deepens into the fundamental properties of semiconductor NWs.

- In Section 5.1 the spin and orbital angular momenta (SAM and OAM) of light have been analytically investigated in planar and cylindrical waveguides supporting transverse electric/magnetic and hybrid (only in cylinders) modes. Leaving aside the well known transverse spin associated to the evanescent component of the guided modes outside the waveguides, the emphasis has been put on the impact of mode confinement inside. The main contributions extracted from this analysis are presented.

  - It has been shown that all (transverse and hybrid) modes, despite not being evanescent inside, exhibit a transverse SAM $S_t \propto (W/k_z\omega)\, k_t$ proportional to the transverse momentum k_t for planar and cylindrical waveguides. Such transverse spin density is shown to carry so called (Belinfante's) longitudinal spin momentum, parallel or anti-parallel to the proper orbital angular momentum, governed by the mode (spatial) transverse dependence imposed by its order and polarization.
  - It is demonstrated analytically that the spin momentum $\mathbf{P^S}$ is crucial through this relationship $\mathbf{P} = \mathbf{P^O} + \mathbf{P^S}$ ($\mathbf{P}$ being related to the Poynting vector momentum density) to retrieve the proper dependence of orbital momentum on propagation wavevector $P_z^O \propto k_z$.
  - Apart from the former transverse spin, hybrid modes in cylindrical waveguides are shown to carry longitudinal spin arising from its intrinsic helicity; such longitudinal SAM concentrates especially inside (strong confinement) the cylindrical waveguide.
  - A discussion is also included on the impact of such transverse SAM inside waveguides on forces on dipolar particles inside e.g. water-filled waveguides in the IR and microwave regimes. All this phenomenology has been discussed for lowest-order guided modes in simple planar and cylindrical waveguides for the sake of clarity, but can be straightforwardly extrapolated to other geometries preserving guided mode confinement.

- In Section 5.2 it has been shown that strong coupling between weakly guided modes of a semiconductor nanowire and a surrounding excitonic medium can be achieved, exhibiting Rabi splittings of more than $\Omega_R > 100$ meV for an organic dye. As remarkable points:

  - The evanescent tail of weakly guided modes allows for strong coupling of the nanowire modes with the excitons in external dye molecules. The underlying physical mechanism is similar to surface plasmon polaritons in metallic nanorods, but with the advantage of much larger propagating lengths due to the nearly total absence of absorption inside the semiconductor nanowire.
  - A quantum model has been presented (developed in collaboration with Johannes Feist at the Universidad Autónoma de Madrid) that provides a straightforward analytical expression for the Rabi splitting and reveals that the relevant quantity is not the field concentration but the fraction of the field interacting with the emitters. The quantum model also reveals that coherent energy exchange plays an important role in the coupled system: the dispersion relations reveal avoided crossings with clear Rabi splittings, as expected from strong coupling.
  - The polariton modes in these systems can achieve significant propagation lengths up to two orders of magnitude larger than the bare mode wavelengths while still maintaining a significant excitonic character. This happens because strong coupling can shift exciton modes to frequency regions where material losses are much smaller than around the exciton resonances.

Appendix A

Details of the CEMD formulation

A.1 Green tensors of a single cylinder

The scalar Green function in 2D, $g(\boldsymbol{r}-\boldsymbol{r}_n)$, is the solution of the 2D Helmholtz equation with a point source located at $\boldsymbol{r}=\boldsymbol{r}_n$: $\nabla^2 g + k^2 g = -\delta(\boldsymbol{r}-\boldsymbol{r}_n)$,

$$g(\boldsymbol{r}-\boldsymbol{r}_n) = \frac{\mathrm{i}}{4}H_0(k|\boldsymbol{r}-\boldsymbol{r}_n|) = \int_{-\infty}^{+\infty}\frac{dK}{2\pi}e^{\mathrm{i}K(y-y_n)}\left\{\frac{\mathrm{i}}{2q}e^{\mathrm{i}q|z-z_n|}\right\}, \qquad q=\sqrt{k^2-K^2}. \tag{A.1}$$

We then have:

$$\begin{aligned}\mathbf{G}(\boldsymbol{r},\boldsymbol{r}_n) &= \left\{\mathbf{I}+\frac{\boldsymbol{\nabla}\boldsymbol{\nabla}}{k^2}\right\}g(\boldsymbol{r}-\boldsymbol{r}_n)\\ &= \begin{pmatrix}G_{xx}&0&0\\0&G_{yy}&G_{yz}\\0&G_{yz}&G_{zz}\end{pmatrix} = \frac{1}{k^2}\begin{pmatrix}k^2&0&0\\0&k^2+\partial^2/\partial y^2&\partial^2/\partial y\partial z\\0&\partial^2/\partial y\partial z&k^2+\partial^2/\partial z^2\end{pmatrix}g(\boldsymbol{r}-\boldsymbol{r}_n),\end{aligned} \tag{A.2}$$

$$\begin{aligned}\mathbf{G}_{EM}(\boldsymbol{r},\boldsymbol{r}_n) &= \mathrm{i}\frac{\boldsymbol{\nabla}}{k}\times\left(g(\boldsymbol{r}-\boldsymbol{r}_n)\,\mathbf{I}\right)\\ &= \begin{pmatrix}0&G_{xy}^{(EM)}&G_{xz}^{(EM)}\\-G_{xy}^{(EM)}&0&0\\-G_{xz}^{(EM)}&0&0\end{pmatrix} = \frac{\mathrm{i}}{k}\begin{pmatrix}0&-\partial/\partial z&\partial/\partial y\\\partial/\partial z&0&0\\-\partial/\partial y&0&0\end{pmatrix}g(\boldsymbol{r}-\boldsymbol{r}_n).\end{aligned} \tag{A.3}$$

A.2 Lattice depolarization dyadic

The lattice depolarization function can be written as:

$$\overleftrightarrow{\mathbb{G}}_b \equiv \sum_{n\neq 0}\overleftrightarrow{\mathbf{G}}(-\boldsymbol{r}_n)e^{\mathrm{i}K_0 na} = \lim_{\boldsymbol{r}\to\boldsymbol{r}_0}\left\{\overleftrightarrow{\mathbb{G}}(\boldsymbol{r})-\overleftrightarrow{\mathbf{G}}(\boldsymbol{r})\right\} = \begin{pmatrix}\mathbb{G}_b&\mathbb{G}_b^{(EM)}\\-\mathbb{G}_b^{(EM)}&\mathbb{G}_b\end{pmatrix}, \tag{A.4}$$

where $\mathbb{G}_b$ is a matrix whose elements can be written as:

$$G_{bxx} \equiv (\mathbb{G}_b)_{xx} = \mathrm{i}\left[\frac{1}{2q_0 a} - \frac{1}{4}\right] + \frac{1}{2a}\sum_{m=1}^{\infty}\left(\frac{\mathrm{i}}{q_m} + \frac{\mathrm{i}}{q_{-m}} - \frac{2}{k_m}\right) + \frac{1}{2\pi}\left[\ln\frac{ka}{4\pi} + \gamma_e\right], \tag{A.5}$$

$$G_{byy} \equiv (\mathbb{G}_b)_{yy} = \frac{\mathrm{i}}{4}\left[\frac{2q_0}{k^2 a} - \frac{1}{2}\right] + \frac{1}{2k^2 a}\sum_{m=1}^{\infty}\left(\mathrm{i}q_m + \mathrm{i}q_{-m} + 2k_m - \frac{k^2}{k_m}\right) + \frac{1}{4\pi}\left[\ln\frac{ka}{4\pi} + \gamma_e - \frac{1}{2}\right] - \frac{q_0^2}{4k^2\pi} + \frac{1}{6}\frac{\pi}{k^2 a^2}, \tag{A.6}$$

$$G_{bzz} \equiv (\mathbb{G}_b)_{zz} = \frac{\mathrm{i}}{4}\left[\frac{2K_0^2}{k^2 q_0 a} - \frac{1}{2}\right] + \frac{1}{2k^2 a}\sum_{m=1}^{\infty}\left(i\frac{K_m^2}{q_m} + \mathrm{i}\frac{K_{-m}^2}{q_{-m}} - 2k_m - \frac{k^2}{k_m}\right) + \frac{1}{4\pi}\left[\ln\frac{ka}{4\pi} + \gamma_e - \frac{1}{2}\right] - \frac{K_0^2}{4k^2\pi} - \frac{1}{6}\frac{\pi}{k^2 a^2}, \tag{A.7}$$

where

$$k_m = \frac{2m\pi}{a}, \qquad K_m \equiv K_0 - k_m, \qquad q_m = \sqrt{k^2 - K_m^2}, \tag{A.8}$$

and γ_e is the Euler-Mascheroni constant. In addition, $G_{bxx} = G_{byy} + G_{bzz}$.

The non-vanishing components of $\mathbb{G}_b^{(EM)}$ are given by:

$$\begin{aligned} G_{bzx} &\equiv \left(\mathbb{G}_b^{(EM)}\right)_{zx} = -\left(\mathbb{G}_b^{(EM)}\right)_{xz} \\ &= \mathrm{i}\frac{K_0}{2kq_0 a} + \frac{\mathrm{i}}{2ka}\sum_{m=1}^{\infty}\left(\frac{K_m}{q_m} + \frac{K_{-m}}{q_{-m}}\right) - \frac{1}{2\pi}\frac{K_0}{k}. \end{aligned} \tag{A.9}$$

A.3 Lattice Green dyadic

Combining the Poisson summation formula:

$$\frac{2\pi}{a}\sum_{m=-\infty}^{+\infty}\delta\left(K - \frac{2\pi m}{a}\right) = \sum_{n=-\infty}^{+\infty} e^{\mathrm{i}Kan}, \tag{A.10}$$

with the Weyl expansion of the Green function, Eq. A.1, and for $\boldsymbol{r}_n = (y_n = na, z_n = 0)$, we have:

$$\begin{aligned}\sum_{n=-\infty}^{\infty} e^{iK_0 an} g(\boldsymbol{r}-\boldsymbol{r}_n) &= \int_{-\infty}^{+\infty} \frac{dK}{2\pi} \left\{ \sum_{n=-\infty}^{\infty} e^{i(K_0-K)an} \right\} e^{\mathrm{i}Ky} \left\{ \frac{\mathrm{i}}{2q} e^{\pm \mathrm{i}qz} \right\} \\ &= \sum_{m=-\infty}^{\infty} e^{\mathrm{i}K_m y} e^{\pm \mathrm{i}q_m z} \frac{\mathrm{i}}{2aq_m}. \end{aligned} \tag{A.11}$$

The lattice Green dyadic can then be easily written as:

$$\begin{aligned}\overleftrightarrow{\mathbb{G}}(\boldsymbol{r}) \equiv \sum_{n=-\infty}^{\infty} e^{iK_0 an} \overleftrightarrow{\mathbf{G}}(\boldsymbol{r}-\boldsymbol{r}_n) &= \sum_{n=-\infty}^{\infty} e^{iK_0 an} \begin{pmatrix} \mathbf{G}(\boldsymbol{r}-\boldsymbol{r}_n) & \mathbf{G}_{EM}(\boldsymbol{r}-\boldsymbol{r}_n) \\ -\mathbf{G}_{EM}(\boldsymbol{r}-\boldsymbol{r}_n) & \mathbf{G}(\boldsymbol{r}-\boldsymbol{r}_n) \end{pmatrix} \\ = \sum_{m=-\infty}^{\infty} e^{iK_m y} e^{\pm iq_m z} \overleftrightarrow{\mathbb{G}}{}_m^{\pm} &= \sum_{m=-\infty}^{\infty} e^{iK_m y} e^{\pm iq_m z} \begin{pmatrix} \mathbb{G}_m^{\pm} & \mathbb{G}_{EMm}^{\pm} \\ -\mathbb{G}_{EMm}^{\pm} & \mathbb{G}_m^{\pm} \end{pmatrix}, \end{aligned} \tag{A.12}$$

where

$$\mathbb{G}_m^{\pm} = \frac{i}{2q_m a} \frac{1}{k^2} \begin{pmatrix} k^2 & 0 & 0 \\ 0 & k^2 - K_m^2 & \mp q_m K_m \\ 0 & \mp q_m K_m & k^2 - q_m^2 \end{pmatrix}, \quad \mathbb{G}_{EMm}^{\pm} = \frac{i}{2q_m a} \frac{1}{k} \begin{pmatrix} 0 & \pm q_m & -K_m \\ \mp q_m & 0 & 0 \\ K_m & 0 & 0 \end{pmatrix}. \tag{A.13}$$

For a subwavelength grating, the far-field ($|z| \to \infty$) Green dyadic is simply given by:

$$\overleftrightarrow{\mathbb{G}}(\boldsymbol{r}) \sim e^{iK_0 y} e^{\pm iq_0 z} \begin{pmatrix} \mathbb{G}_0^{\pm} & \mathbb{G}_{EM0}^{\pm} \\ -\mathbb{G}_{EM0}^{\pm} & \mathbb{G}_0^{\pm} \end{pmatrix}, \tag{A.14}$$

where

$$\mathbb{G}_0^{\pm} = \frac{i}{2q_0 a} \frac{1}{k^2} \begin{pmatrix} k^2 & 0 & 0 \\ 0 & q_0^2 & \mp q_0 K_0 \\ 0 & \mp q_0 K_0 & K_0^2 \end{pmatrix}, \quad \mathbb{G}_{EM0}^{\pm} = \frac{i}{2q_0 a} \frac{1}{k} \begin{pmatrix} 0 & \pm q_0 & -K_0 \\ \mp q_0 & 0 & 0 \\ K_0 & 0 & 0 \end{pmatrix}. \tag{A.15}$$

A.4 Imaginary part of the lattice Green dyadic

$$\begin{aligned}\mathrm{Im}\left[\overleftrightarrow{\mathbb{G}}(0)\right] \equiv& \frac{1}{2}\mathrm{Im}\left[\overleftrightarrow{\mathbb{G}}{}^{+}(0) + \overleftrightarrow{\mathbb{G}}{}^{-}(0)\right] \\ =& \mathrm{Im}\left[\begin{pmatrix} \mathbb{G}_0 & \mathbb{G}_{EM0} \\ -\mathbb{G}_{EM0} & \mathbb{G}_0 \end{pmatrix} + \sum_{m\neq 0}^{\text{diffracted}} \begin{pmatrix} \mathbb{G}_m & \mathbb{G}_{EMm} \\ -\mathbb{G}_{EMm} & \mathbb{G}_m \end{pmatrix}\right], \end{aligned} \tag{A.16}$$

where the sum runs over the propagating diffracted waves (with q_m 'real'). For a subwavelength

grating:

$$\mathrm{Im}\left[\mathbb{G}_0\right] = \frac{1}{2q_0 a}\frac{1}{k^2}\begin{pmatrix} k^2 & 0 & 0 \\ 0 & q_0^2 & 0 \\ 0 & 0 & K_0^2 \end{pmatrix}, \quad \mathrm{Im}\left[\mathbb{G}_{EM0}\right] = \frac{1}{2q_0 a}\frac{K_0}{k}\begin{pmatrix} 0 & 0 & -1 \\ 0 & 0 & 0 \\ 1 & 0 & 0 \end{pmatrix}. \tag{A.17}$$

A.5 Fresnel amplitudes

The specular transmittance, T_0, of the lattice is:

$$T_0^{(p)} = \left|1 + \frac{i}{2ka\cos\theta_0} Z H_{x0}^{(T)}/E_{p_0}\right|^2, \tag{A.18a}$$

$$T_0^{(s)} = \left|1 + \frac{i}{2ka\cos\theta_0} E_{x0}^{(T)}/E_{s_0}\right|^2, \tag{A.18b}$$

where $H_{x0}^{(T)}$ and $E_{x0}^{(T)}$ are the fields scattered by the lattice to the transmitted region $z < 0$:

$$\begin{aligned} Z H_{x0}^{(T)}/E_{p_0} = k^2\gamma^{(p)}\Big(&\widetilde{\alpha}_x^{(M)} + \sin^2\theta_0\widetilde{\alpha}_z^{(E)} \\ &+ 2k^2\sin\theta_0 G_{bzx}\widetilde{\alpha}_x^{(M)}\widetilde{\alpha}_z^{(E)}\Big) + k^2\cos^2\theta_0\widetilde{\alpha}_y^{(E)}, \end{aligned} \tag{A.19a}$$

$$\begin{aligned} E_{x0}^{(T)}/E_{s_0} = k^2\gamma^{(s)}\Big(&\widetilde{\alpha}_x^{(E)} + \sin^2\theta_0\widetilde{\alpha}_z^{(M)} \\ &+ 2k^2\sin\theta_0 G_{bzx}\widetilde{\alpha}_x^{(E)}\widetilde{\alpha}_z^{(M)}\Big) + k^2\cos^2\theta_0\widetilde{\alpha}_y^{(M)}. \end{aligned} \tag{A.19b}$$

Finally, the reflectance for the diffracted order m (for $\Im\left[q_m\right] = 0$) is given by:

$$\begin{aligned} R_m^{(p)} = \left(\frac{1}{2ka\cos\theta_0}\right)^2 \Big|\gamma^{(p)}\Big(&k^2\widetilde{\alpha}_x^{(M)} + K_0 K_m\widetilde{\alpha}_z^{(E)} \\ &+k^3(K_0 + K_m)G_{bzx}\widetilde{\alpha}_x^{(M)}\widetilde{\alpha}_z^{(E)}\Big) - q_0 q_m\widetilde{\alpha}_y^{(E)}\Big|^2, \end{aligned} \tag{A.20a}$$

$$\begin{aligned} R_m^{(s)} = \left(\frac{1}{2ka\cos\theta_0}\right)^2 \Big|\gamma^{(s)}\Big(&k^2\widetilde{\alpha}_x^{(E)} + K_0 K_m\widetilde{\alpha}_z^{(M)} \\ &+k^3(K_0 + K_m)G_{bzx}\widetilde{\alpha}_x^{(E)}\widetilde{\alpha}_z^{(M)}\Big) - q_0 q_m\widetilde{\alpha}_y^{(M)}\Big|^2. \end{aligned} \tag{A.20b}$$

The transmittance follows the same expression, replacing $-q_0 q_m$ by $+q_0 q_m$.

Appendix B

Details of the lattice depolarization dyadic in 2D metasurfaces

B.1 Scattered field by a chain of particles

The scalar Green function (in 3D) is

$$g\left(\boldsymbol{r}-\boldsymbol{r}_n\right)=\frac{e^{\imath k|\boldsymbol{r}-\boldsymbol{r}_n|}}{4\pi|\boldsymbol{r}-\boldsymbol{r}_n|} \tag{B.1}$$
$$=\int\frac{\mathrm{d}Q_x\mathrm{d}Q_y}{4\pi^2}e^{\imath Q_x(x-x_n)}e^{\imath Q_y(y-y_n)}\frac{\imath}{2q}e^{\imath q|z-z_n|},\quad q=\sqrt{k^2-Q_x^2-Q_y^2},$$

where $\boldsymbol{r}$ is the observation point, $\boldsymbol{r}_n$ is the position of the emitter/source, and k is the wavevector in the media (In Section 1.3 the scalar Green Function was denoted by G_0 (Eq. 1.17) following the notation of Novotny and Hecht[3]). For a periodic chain of particles along the x axis, $\boldsymbol{r}$ and $\boldsymbol{r}_n$ are

$$\boldsymbol{r}=x\hat{x}+y\hat{y}+z\hat{z}, \tag{B.2}$$

$$\boldsymbol{r}_n=x_n\hat{x}=na\hat{x}, \tag{B.3}$$

being a the separation between particles. Upon the incidence of an external plane wave (with incident wavevector, $\mathbf{k^{(0)}}=k_x^{(0)}\hat{x}+k_y^{(0)}\hat{y}+k_z^{(0)}\hat{z}$), the response of the array can be defined by the next sum

$$\sum_{n=-\infty}^{\infty}g\left(\boldsymbol{r}-\boldsymbol{r}_n\right)e^{\imath k_x^{(0)}na}, \tag{B.4}$$

where $k_x^{(0)}$ is the projection of the incident wavevector along the x axis. After some algebraic manipulations, the sum in the real space can be rewritten in the reciprocal space as:

$$\sum_{n=-\infty}^{\infty}g\left(\boldsymbol{r}-\boldsymbol{r}_n\right)e^{\imath k_x^{(0)}na}=\sum_{l=-\infty}^{\infty}e^{\imath\left(k_x^{(0)}-\frac{2\pi}{a}l\right)x}\frac{\imath}{4a}H_0\left(k_{||}^{(l)}\rho\right), \tag{B.5}$$

where

$$\rho = \sqrt{y^2 + z^2}, \quad k_{||}^{(l)} = \sqrt{k^2 - \left(k_x^{(0)} - \frac{2\pi}{a} l\right)^2}. \tag{B.6}$$

The scalar Green function in 2D with translational symmetry along the x axis (i.e., for a infinitely long cylinder where the x axis is the cylinder axis), is

$$g_{2D}\left(\boldsymbol{r} - \boldsymbol{r}_n\right) = \frac{\imath}{4} H_0\left(\sqrt{k^2 - k_x^2}|\boldsymbol{r} - \boldsymbol{r}_n|\right) e^{\imath k_x x}. \tag{B.7}$$

Recall that for $k_x = 0$, Eq. B.7 is identical to Eq. A.1. Using the following association

$$k_x^{(l)} = \left(k_x^{(0)} - \frac{2\pi}{a} l\right), \tag{B.8}$$

Eq. B.5 can be written as:

$$\sum_{n=-\infty}^{\infty} g\left(k, \boldsymbol{r} - \boldsymbol{r}_n\right) e^{\imath k_x^0 n a} = \sum_{l=-\infty}^{\infty} \frac{1}{a} g_{2D}\left(k, k_x^{(l)}, \boldsymbol{r} - \boldsymbol{r}_n\right), \tag{B.9}$$

where we have explicitly added the wavevector as an argument in the scalar Green function (normally this is omitted).

Therefore, from Eq. B.9 we can infer that a chain of particles behaves effectively as an infinitely long cylinder that is excited by propagating and evanescent plane waves. There is always a propagating wave that coincides with an incident external plane wave, while the rest of propagating waves appears as a diffraction phenomenology when the lattice constant a exceed the incoming wavelength $\lambda = 2\pi/k$. Thus, at the far field only terms with $\mathrm{Im}\left[k_{||}^{(l)}\right] = 0$ survive, while in the near field there are contributions from all waves.

B.2 Lattice depolarization dyadic for rectangular 2D arrays

Now, we consider a two dimensional rectangular array of particles with lattice constants a and b illuminated by an an external plane wave $\mathbf{k}^{(\mathbf{0})}$. The position of the particle labeled as (n, m) is

$$\boldsymbol{r}_{nm} = x_n \hat{x} + y_n \hat{y} = na\hat{x} + mb\hat{y}, \tag{B.10}$$

The properties of the lattice are condensed in $\overleftrightarrow{\mathbb{G}}_{b-2D}$, the lattice 'depolarization' dyadic of the 2D array of particles,

$$\overleftrightarrow{\mathbb{G}}_{b-2D} \equiv \sum_{n\neq 0} \sum_{m\neq 0} \overleftrightarrow{\mathbf{G}}(-\boldsymbol{r}_{nm}) e^{\mathrm{i}k_x^{(0)} na} e^{\mathrm{i}k_y^{(0)} mb}. \tag{B.11}$$

From Eq. B.9, a 2D array of particles can be seen as a 1D array of chains of particles. Assuming that the chains are along the x axis, the effective cylinders (that the chains represent) are placed at

$\boldsymbol{r}_m = mb\hat{y}$. Within this convention, it is straightforward to show that

$$\overleftrightarrow{\mathbb{G}}_{b-2D} = \overleftrightarrow{\mathbb{G}}_{b-Ch} + \frac{1}{a}\left(\sum_{l=-\infty}^{\infty} \overleftrightarrow{\mathbb{G}}_{b-1D}^{(l)}\right), \tag{B.12}$$

where $\overleftrightarrow{\mathbb{G}}_{b-Ch}$ is the 'depolarization' dyadic of a chain of particles

$$\overleftrightarrow{\mathbb{G}}_{b-Ch}(a, k, k_x^{(0)}) \equiv \sum_{n\neq 0} \overleftrightarrow{\mathbf{G}}(-\boldsymbol{r}_n) e^{\mathrm{i}k_x^{(0)} na}, \tag{B.13}$$

and $\overleftrightarrow{\mathbb{G}}_{b-1D}^{(l)}$ is the 'depolarization' dyadic of a 1D array of cylinders (with their axis along the x axis)

$$\overleftrightarrow{\mathbb{G}}_{b-1D}^{(l)}(b, k, k_y^{(0)}, k_x^{(l)}, \boldsymbol{r}) = \sum_{m\neq 0} \overleftrightarrow{\mathbf{G}}_{2D}(k, k_x^{(l)}, -\boldsymbol{r}_m) e^{\mathrm{i}k_y^{(0)} mb}, \tag{B.14}$$

where $\overleftrightarrow{\mathbf{G}}_{2D}(k, k_x^{(l)}, -\boldsymbol{r}_m)$ is the Green function of a 2D system (with scalar Green function given by Eq. B.7). In both cases all arguments of the functions are shown explicitly. Analytical expression in the reciprocal space for Eq. B.13 and Eq. B.14 are shown below.

B.3 Lattice depolarization dyadic for arbitrary 2D arrays

Finally, let us consider a generic 2D array of particles defined by the lattice constants a and b with corresponding lattice vectors forming an angle θ between them. Then, if the primitive vector characterized by the lattice constant a is taken along the x axis, the position of the particle labeled as (n,m) becomes

$$\boldsymbol{r}_{nm} = (na + m\cos\theta)\hat{x} + m\sin\theta\hat{y}. \tag{B.15}$$

For example, the rectangular lattice is recovered for $\theta = \pi/2$, while $\theta = \pi/3$ and $a = b$ yield a triangular lattice. Using this description the lattice depolarization dyadic, $\overleftrightarrow{\mathbb{G}}_{b-2D}$, follows the same expression shown in Eq. B.12 but with some changes in the arguments of the functions:

$$b \to b\sin\theta, \tag{B.16}$$

$$k_y^{(0)} \to k_y^{(0)} - \frac{2\pi}{a} l \frac{\cos\theta}{\sin\theta}. \tag{B.17}$$

Thus, $\overleftrightarrow{\mathbb{G}}_{b-Ch}$ does not change

$$\overleftrightarrow{\mathbb{G}}_{Ch}\left(a, k, k_x^{(0)}\right) \to \overleftrightarrow{\mathbb{G}}_{Ch}\left(a, k, k_x^{(0)}\right), \tag{B.18}$$

while the arguments of $\overleftrightarrow{\mathbb{G}}_{b-1D}$ are modified

$$\overleftrightarrow{\mathbb{G}}^{(l)}_{b-1D}\left(b,k,k_y^{(0)},k_x^{(l)}\right)\rightarrow\overleftrightarrow{\mathbb{G}}^{(l)}_{b-1D}\left(b\sin\theta,k,k_y^{(0)}-\frac{2\pi}{a}l\frac{\cos\theta}{\sin\theta},k_x^{(l)}\right). \tag{B.19}$$

Alternatively, it is possible to define the chains of particles along the direction $\hat{u}=cos\theta\hat{x}+sin\theta\hat{y}$.

B.4 Generalization of the lattice depolarization dyadic for an array of cylinders

For $k_x=0$, Eq. B.14 is identical to Eq. A.4. Otherwise, if we write

$$\overleftrightarrow{\mathbb{G}}^{(l)}_{b-1D}(b,k,k_y,k_x)=\begin{pmatrix}\mathbb{G}_{b-1D} & \mathbb{G}^{(EM)}_{b-1D}\\ -\mathbb{G}^{(EM)}_{b-1D} & \mathbb{G}_{b-1D}\end{pmatrix}, \tag{B.20}$$

the expressions given by Eqs. A.5, A.6, A.7 and A.9 must be replaced by:

$$(\mathbb{G}_{b-1D})_{xx}=\frac{k_{||}^2}{k^2}\left(\mathrm{i}\left[\frac{1}{2q_0b}-\frac{1}{4}\right]+\frac{1}{2b}\sum_{m=1}^{\infty}\left(\frac{\mathrm{i}}{q_m}+\frac{\mathrm{i}}{q_{-m}}-\frac{2}{k_m}\right)+\frac{1}{2\pi}\left[\ln\frac{kb}{4\pi}+\gamma_e\right]\right), \tag{B.21}$$

$$\begin{aligned}(\mathbb{G}_{b-1D})_{yy}=\frac{k_{||}^2}{k^2}&\left(\frac{\mathrm{i}}{4}\left[\frac{2q_0}{k^2b}-\frac{1}{2}\right]+\frac{1}{2k^2b}\sum_{m=1}^{\infty}\left(\mathrm{i}q_m+\mathrm{i}q_{-m}+2k_m-\frac{k^2}{k_m}\right)\right.\\&\left.+\frac{1}{4\pi}\left[\ln\frac{kb}{4\pi}+\gamma_e-\frac{1}{2}\right]+\frac{K_0^2}{4k^2\pi}+\frac{1}{6}\frac{\pi}{k^2b^2}\right)\\&+\frac{k_x^2}{k^2}\left(\left[\frac{\mathrm{i}}{2q_0b}-\frac{1}{4}\right]+\frac{1}{2b}\sum_{m=1}^{\infty}\left(\frac{\mathrm{i}}{q_m}+\frac{\mathrm{i}}{q_{-m}}-\frac{2}{k_m}\right)+\frac{1}{2\pi}\left[\ln\frac{kb}{4\pi}+\gamma_e\right]\right),\end{aligned} \tag{B.22}$$

$$\begin{aligned}(\mathbb{G}_{b-1D})_{zz}=\frac{k_{||}^2}{k^2}&\left(\frac{\mathrm{i}}{4}\left[\frac{2K_0^2}{k^2q_0b}-\frac{1}{2}\right]+\frac{1}{2k^2b}\sum_{m=1}^{\infty}\left(i\frac{K_m^2}{q_m}+\mathrm{i}\frac{K_{-m}^2}{q_{-m}}-2k_m-\frac{k^2}{k_m}\right)\right.\\&\left.+\frac{1}{4\pi}\left[\ln\frac{kb}{4\pi}+\gamma_e-\frac{1}{2}\right]+\frac{q_0^2}{4k^2\pi}-\frac{1}{6}\frac{\pi}{k^2b^2}\right)\\&+\frac{k_x^2}{k^2}\left(\left[\frac{\mathrm{i}}{2q_0b}-\frac{1}{4}\right]+\frac{1}{2b}\sum_{m=1}^{\infty}\left(\frac{\mathrm{i}}{q_m}+\frac{\mathrm{i}}{q_{-m}}-\frac{2}{k_m}\right)+\frac{1}{2\pi}\left[\ln\frac{kb}{4\pi}+\gamma_e\right]\right),\end{aligned} \tag{B.23}$$

$$(\mathbb{G}_{b-1D})_{xy}=\frac{k_x}{k^2}\left(\mathrm{i}\frac{K_0}{2kq_0b}+\frac{\mathrm{i}}{2b}\sum_{m=1}^{\infty}\left(\frac{K_m}{q_m}+\frac{K_{-m}}{q_{-m}}\right)-\frac{1}{2\pi}K_0\right), \tag{B.24}$$

$$\begin{aligned}\left(\mathbb{G}^{(EM)}_{b-1D}\right)_{yz} &= -\left(\mathbb{G}^{(EM)}_{b-1D}\right)_{zy} \\ &= \frac{k_x}{k}\left(\mathrm{i}\left[\frac{1}{2q_0 b}-\frac{1}{4}\right]\right. \\ &+ \left.\frac{1}{2b}\sum_{m=1}^{\infty}\left(\frac{\mathrm{i}}{q_m}+\frac{\mathrm{i}}{q_{-m}}-\frac{2}{k_m}\right)+\frac{1}{2\pi}\left[\ln\frac{kb}{4\pi}+\gamma_e\right]\right),\end{aligned} \tag{B.25}$$

$$\begin{aligned}\left(\mathbb{G}^{(EM)}_{b-1D}\right)_{zx} &= -\left(\mathbb{G}^{(EM)}_{b-1D}\right)_{xz} \\ &= \mathrm{i}\frac{K_0}{2kq_0 b}+\frac{\mathrm{i}}{2kb}\sum_{m=1}^{\infty}\left(\frac{K_m}{q_m}+\frac{K_{-m}}{q_{-m}}\right)-\frac{1}{2\pi}\frac{K_0}{k},\end{aligned} \tag{B.26}$$

where

$$k_m=\frac{2m\pi}{b},\qquad K_m\equiv k_y-k_m,\qquad q_m=\sqrt{k_{||}^2-K_m^2},\qquad k_{||}^2=k^2-k_x^2. \tag{B.27}$$

The rest of the matrix elements are equal to zero. Note that a new term, $\left(\mathbb{G}^{(EM)}_{b-1D}\right)_{zx}$, arises.

B.5 Lattice depolarization dyadic for a chain of particles

When the lattice depolarization function of the chain of particles, $\overleftrightarrow{\mathbb{G}}_{b-Ch}$, is written as

$$\overleftrightarrow{\mathbb{G}}_{b-Ch}(a,k,k_x^{(0)})=\begin{pmatrix}\mathbb{G}_{b-Ch} & \mathbb{G}^{(EM)}_{b-Ch}\\ -\mathbb{G}^{(EM)}_{b-Ch} & \mathbb{G}_{b-Ch}\end{pmatrix}, \tag{B.28}$$

the matrix elements are:

$$\begin{aligned}(\mathbb{G}_{b-Ch})_{xx}=-\frac{\mathrm{i}}{2a^3k^2\pi}\{\ & ak\left[Li_2\left(e^{\mathrm{i}(k-k_x)a}\right)+Li_2\left(e^{\mathrm{i}(k+k_x)a}\right)\right] \\ & +\mathrm{i}\left[Li_3\left(e^{\mathrm{i}(k-k_x)a}\right)+Li_3\left(e^{\mathrm{i}(k+k_x)a}\right)\right]\},\end{aligned} \tag{B.29}$$

$$\begin{aligned}(\mathbb{G}_{b-Ch})_{yy}=-\frac{\mathrm{i}}{4a^3k^2\pi}\{\ & -\mathrm{i}a^2k^2\left[Li_1\left(e^{\mathrm{i}(k-k_x)a}\right)+Li_1\left(e^{\mathrm{i}(k+k_x)a}\right)\right] \\ & +ak\left[Li_2\left(e^{\mathrm{i}(k-k_x)a}\right)+Li_2\left(e^{\mathrm{i}(k+k_x)a}\right)\right] \\ & +\mathrm{i}\left[Li_3\left(e^{\mathrm{i}(k-k_x)a}\right)+Li_3\left(e^{\mathrm{i}(k+k_x)a}\right)\right]\},\end{aligned} \tag{B.30}$$

$$(\mathbb{G}_{b-Ch})_{zz}=(\mathbb{G}_{b-Ch})_{yy}, \tag{B.31}$$

$$(\mathbb{G}^{(EM)}_{b-Ch})_{yz} = -(\mathbb{G}^{(EM)}_{b-Ch})_{zy} = \frac{\mathrm{i}}{4a^3k^2\pi}\left\{ -\mathrm{i}a^2k^2\left[Li_1\left(e^{\mathrm{i}(k-k_x)a}\right) - Li_1\left(e^{\mathrm{i}(k+k_x)a}\right)\right]\right. \\ \left. +ak\left[Li_2\left(e^{\mathrm{i}(k-k_x)a}\right) - Li_2\left(e^{\mathrm{i}(k+k_x)a}\right)\right]\right\}, \tag{B.32}$$

being $Li_s(z)$ the polylogarithm function, also known as Jonquiére's function. For the special case of $s = 1$, the polylogarithm function is $Li_1(z) = -ln(1 - z)$. The rest of the matrix elements are equal to zero.

Appendix C

Details of the coupled detuned-dipole formulation

First of all, let us define the 3D scalar Green function, $G_0(\mathbf{r}-\mathbf{r_n})$, resulting from the Helmholtz equation with a point source located at $\mathbf{r} = \mathbf{r_n}$:

$$\nabla^2 G_0 + k^2 G_0 = -\delta(\mathbf{r} - \mathbf{r_n}), \tag{C.1}$$

whose solution is (also Eq. 1.17)

$$G_0(\mathbf{r} - \mathbf{r_n}) = \frac{e^{\imath k|\mathbf{r}-\mathbf{r_n}|}}{4\pi k|\mathbf{r} - \mathbf{r_n}|}k. \tag{C.2}$$

The Weyl expansion of the scalar Green function is

$$G_0(\mathbf{r} - \mathbf{r_n}) = \int_{-\infty}^{\infty}\int_{-\infty}^{\infty} \frac{dQ_x dQ_y}{4\pi^2} e^{\imath Q_x(x-x_n)} e^{\imath Q_y(y-y_n)} \frac{\imath}{2q} e^{\imath q|z-z_n|}, \quad q = \sqrt{k^2 - Q_x^2 - Q_y^2}. \tag{C.3}$$

The element yy of the (tensor) Green function, $G_{yy}(\mathbf{r} - \mathbf{r_n})$, is

$$\begin{aligned} G_{yy}(\mathbf{r} - \mathbf{r_n}) &= \left(1 + \frac{1}{k^2}\frac{\partial^2}{\partial y^2}\right) g(\mathbf{r} - \mathbf{r_n}) \\ &= \int_{-\infty}^{\infty}\int_{-\infty}^{\infty} \frac{dQ_x Q_y}{4\pi^2} \left(1 - \frac{Q_y^2}{k^2}\right) e^{\imath Q_x(x-x_n)} e^{\imath Q_y(y-y_n)} \frac{\imath}{2q} e^{\imath q|z-z_n|}. \end{aligned} \tag{C.4}$$

This element will be needed below.

Next, let us consider a 2D periodic lattice of two detuned dipoles per unit cell in the xy plane. The lattice has a rectangular symmetry with pitch a and b along the x and y axes, respectively, while the separation between the dipoles in the unit cell is d_x and d_y along the x and y-axis, respectively. The (parallel) dipoles are characterized by their polarizabilities along the y-axis, $\alpha_y^{(1)}$ and $\alpha_y^{(2)}$, where (1) and (2) account for each dipole in the unit cell. The array is excited by an

external plane wave, ψ_0, polarized along the y-axis and with wavevector $\mathbf{k} = k_z\hat{\mathbf{z}} + k_x\hat{\mathbf{x}}$. The dipole positions (1) and (2) are

$$\mathbf{r}^{(\mathbf{1})}_{\mathbf{nm}} = (-d_x/2 + na)\hat{\mathbf{x}} + (-d_y/2 + mb)\hat{\mathbf{y}}, \tag{C.5a}$$

$$\mathbf{r}^{(\mathbf{2})}_{\mathbf{nm}} = (d_x/2 + na)\hat{\mathbf{x}} + (d_y/2 + mb)\hat{\mathbf{y}}. \tag{C.5b}$$

From now on, we refer to the set of dipoles defined by $(n, m) = (0, 0)$ as the central dipoles, placed at $\mathbf{r}^{(\mathbf{i})}_{\mathbf{00}} \equiv \mathbf{r}^{(\mathbf{i})}$, with $i = 1, 2$. The y component of the field at the position of the central dipoles, $\psi^{(i)}_{loc}$, is the sum of the waves scattered from the rest of particles plus the external plane wave:

$$\begin{aligned}\psi^{(1)}_{loc}(\mathbf{r}^{(\mathbf{1})}) = \psi^{(1)}_0(\mathbf{r}^{(\mathbf{1})}) &+ k^2\alpha^{(1)}_y {\sum_{nm}}' \left[G_{yy}\left(\mathbf{r}^{(\mathbf{1})} - \mathbf{r}^{(\mathbf{1})}_{\mathbf{nm}}\right)\psi^{(1)}_{loc}(\mathbf{r}^{(\mathbf{1})}_{\mathbf{nm}})\right] \\ &+ k^2\alpha^{(2)}_y \sum_{nm}\left[G_{yy}\left(\mathbf{r}^{(\mathbf{1})} - \mathbf{r}^{(\mathbf{2})}_{\mathbf{nm}}\right)\psi^{(2)}_{loc}(\mathbf{r}^{(\mathbf{2})}_{\mathbf{nm}})\right], \end{aligned} \tag{C.6a}$$

$$\begin{aligned}\psi^{(2)}_{loc}(\mathbf{r}^{(\mathbf{2})}) = \psi^{(2)}_0(\mathbf{r}^{(\mathbf{2})}) &+ k^2\alpha^{(1)}_y \sum_{nm}\left[G_{yy}\left(\mathbf{r}^{(\mathbf{2})} - \mathbf{r}^{(\mathbf{1})}_{\mathbf{nm}}\right)\psi^{(1)}_{loc}(\mathbf{r}^{(\mathbf{1})}_{\mathbf{nm}})\right] \\ &+ k^2\alpha^{(2)}_y {\sum_{nm}}' \left[G_{yy}\left(\mathbf{r}^{(\mathbf{2})} - \mathbf{r}^{(\mathbf{2})}_{\mathbf{nm}}\right)\psi^{(2)}_{loc}(\mathbf{r}^{(\mathbf{2})}_{\mathbf{nm}})\right], \end{aligned} \tag{C.6b}$$

where $\sum_{nm}$ runs over n, m and $\sum_{nm}{}'$ means that the sum runs for all indices except for $(n, m) = (0, 0)$.

From Bloch's theorem, the local fields are related to the field at the central dipoles as

$$\psi^{(i)}_{loc}(\mathbf{r}^{(\mathbf{i})}_{\mathbf{nm}}) = \psi^{(i)}_{loc}(\mathbf{r}^{(\mathbf{i})})e^{\imath k_x na}. \tag{C.7}$$

Thus, Eqs. C.6 in matricial form reads

$$\begin{bmatrix}\psi^{(1)}_{loc}\\ \psi^{(2)}_{loc}\end{bmatrix} = \begin{bmatrix}\psi^{(1)}_0\\ \psi^{(2)}_0\end{bmatrix} + k^2\begin{bmatrix}G_{byy} & G^{(1-2)}_{yy}\\ G^{(2-1)}_{yy} & G_{byy}\end{bmatrix}\begin{bmatrix}\alpha^{(1)}_y & 0\\ 0 & \alpha^{(2)}_y\end{bmatrix}\begin{bmatrix}\psi^{(1)}_{loc}\\ \psi^{(2)}_{loc}\end{bmatrix}, \tag{C.8}$$

where the position dependence $(\mathbf{r}^{(\mathbf{i})})$ is assumed and suppressed, and

$$G_{byy} = {\sum_{nm}}' G_{yy}\left(\mathbf{r}^{(\mathbf{i})} - \mathbf{r}^{(\mathbf{i})}_{\mathbf{nm}}\right)e^{\imath k_x na}, \tag{C.9a}$$

$$G^{(1-2)}_{yy} = \sum_{nm} G_{yy}\left(\mathbf{r}^{(\mathbf{1})} - \mathbf{r}^{(\mathbf{2})}_{\mathbf{nm}}\right)e^{\imath k_x na}, \tag{C.9b}$$

$$G^{(2-1)}_{yy} = \sum_{nm} G_{yy}\left(\mathbf{r}^{(\mathbf{2})} - \mathbf{r}^{(\mathbf{1})}_{\mathbf{nm}}\right)e^{\imath k_x na}. \tag{C.9c}$$

From Eq. C.8 it is easy to solve for the local fields (Eq. C.7) once we determine the lattice green dyadic, as follows.

Combining the Poisson summation formula:

$$\frac{2\pi}{a}\sum_{l}\delta\left(K-\frac{2\pi l}{a}\right)=\sum_{n}e^{\imath Kan}, \tag{C.10}$$

with the Weyl expansion of the Green function, Eq. C.4, the term $G_{yy}^{(i-j)}$ can be rewritten as:

$$G_{yy}^{(1-2)}=\sum_{lp}\frac{\imath}{2k_{zlp}ab}\left(1-\frac{k_{yp}^2}{k^2}\right)e^{-\imath k_{xl}d_x}e^{-\imath k_{yp}d_y}, \tag{C.11a}$$

$$G_{yy}^{(2-1)}=\sum_{lp}\frac{\imath}{2k_{zlp}ab}\left(1-\frac{k_{yp}^2}{k^2}\right)e^{\imath k_{xl}d_x}e^{\imath k_{yp}d_y}, \tag{C.11b}$$

with

$$k_{xl}=k_x-\frac{2\pi l}{a},\qquad k_{yp}=-\frac{2\pi p}{b},\qquad k_{zlp}=\sqrt{k^2-k_{xl}^2-k_{yp}^2}. \tag{C.12}$$

At normal incidence, $k_x=0$ and $G_{yy}^{(1-2)}=G_{yy}^{(2-1)}$ reading as:

$$G_{yy}^{(1-2)}=\frac{\imath}{2k_zab}+4\sum_{l=1}^{\infty}\sum_{l=p}^{\infty}\frac{\imath}{2k_{zlp}ab}\left(1-\frac{k_{yp}^2}{k^2}\right)\cos\left(k_{xl}d_x\right)\cos\left(k_{yl}d_y\right). \tag{C.13}$$

Thus, in the absence of diffraction its imaginary part is

$$\Im\left[G_{yy}^{(1-2)}\right]=\frac{1}{2k_zab}. \tag{C.14}$$

Similarly, using the Weyl expansion the term G_{byy} can be written as:

$$G_{byy}=\lim_{z\to 0}\left[\sum_{lp}\frac{\imath}{2k_{zlp}ab}\left(1-\frac{k_{yp}^2}{k^2}\right)e^{\imath k_{zlp}|z|}-G_{yy}(z\hat{\mathbf{z}})\right], \tag{C.15}$$

where the term $(n,m)=(0,0)$ has been also included in the sum. Although the real part is intricate (the real parts of both terms in Eq. C.15 diverge), the imaginary part is well behaved

$$\Im\left[G_{byy}\right]=-\frac{k}{6\pi}+\sum_{lp}^{prop}\frac{1}{2k_{zlp}ab}\left(1-\frac{k_{yp}^2}{k^2}\right), \tag{C.16}$$

where the sum runs for all propagating orders ($\Im\left[k_{zlp}\right]=0$).

Finally, for lossless particles the imaginary part of the polarizability is

$$\Im\left[\frac{1}{k^2\alpha}\right]=-\frac{k}{6\pi}. \tag{C.17}$$

Therefore, for non-diffracting gratings at normal incidence

$$\Im\left[\frac{1}{\alpha_y}-G_{byy}+G_{yy}^{(1-2)}\right]=0, \tag{C.18}$$

where we have defined

$$\frac{2}{\alpha_y} = \frac{1}{k^2}\left(\frac{1}{\alpha_y^{(1)}} + \frac{1}{\alpha_y^{(2)}}\right). \tag{C.19}$$

The result given by Eq. C.18 is independent of the lattice parameters a, b, d_x and d_y as long as there are no diffraction orders

$$k < min\left(\frac{2\pi}{a}, \frac{2\pi}{b}\right) \quad \leftrightarrow \quad \Im\left[k_{zlp}\right] = 0. \tag{C.20}$$

Appendix D

Electromagnetic quantities for cylindrical waveguides

D.1 Energy, Poynting vector, and helicity densities in cylindrical waveguides

The energy density is defined as:

$$W = \frac{\epsilon}{4}|\mathbf{E}|^2 + \frac{\mu}{4}|\mathbf{H}|^2. \tag{C.1}$$

Upon introducing the electromagnetic fields of guided modes in a cylindrical lossless waveguide given by Eqs. 1.41 into Eq. C.1, the resulting total energy density reads:

$$\begin{aligned} W = \frac{1}{4}\Bigg\{ & \left(|a_m|^2\epsilon + |b_m|^2\mu\right)\Bigg[|Z_m(k_t r)|^2 \\ & + \frac{k_z^2 + k^2}{|k_t|^2}\left(\left|Z_n'(k_t r)\right|^2 + \frac{m^2}{|k_t|^2 r^2}|Z_m(k_t r)|^2\right)\Bigg] \\ & + \frac{8m}{|k_t|^2 r}\frac{k_z k}{k_t} Z_m(k_t r)\, Z_m'^{*}(k_t r)\, \Im\left[a_m b_m^*\right]\sqrt{\epsilon\mu}\Bigg\}. \end{aligned} \tag{C.2}$$

The Poynting vector density,

$$\mathbf{P} = \frac{1}{2c^2}\Re\left[\mathbf{E}^* \times \mathbf{H}\right] = \frac{1}{2c^2}\Re\left[\mathbf{E} \times \mathbf{H}^*\right], \tag{C.3}$$

yields:

$$P_r = 0, \tag{C.4a}$$

$$P_\theta = \frac{1}{2\omega}\frac{1}{\epsilon_r\mu_r}\Bigg\{\frac{m}{r}\frac{k^2}{k_t^2}|Z_m\left(k_t r\right)|^2\left(|a_m|^2\epsilon + |b_m|^2\mu\right) + 2\frac{k_z k}{k_t}Z_m^{'}\left(k_t r\right)Z_m^{*}\left(k_t r\right)\Im\left[a_m b_m^{*}\right]\sqrt{\epsilon\mu}\Bigg\}, \tag{C.4b}$$

$$P_z = \frac{1}{2\omega}\frac{1}{\epsilon_r\mu_r}\Bigg\{\frac{k^2}{|k_t|^2}k_z\left(|a_m|^2\epsilon + |b_m|^2\mu\right)\left[|Z_m^{'}\left(k_t r\right)|^2 + \frac{m^2}{|k_t^2|r^2}|Z_m\left(k_t r\right)|^2\right] + 2\frac{m}{r}\frac{k}{k_t}\frac{k_z^2+k^2}{|k_t|^2}Z_m\left(k_t r\right)Z_m^{'*}\left(k_t r\right)\Im\left[a_m b_m^{*}\right]\sqrt{\epsilon\mu}\Bigg\}. \tag{C.4c}$$

Finally, the helicity can be written as:

$$h = -\frac{\sqrt{\epsilon_0\mu_0}}{2\omega}\Im[\mathbf{E}^{*}\cdot\mathbf{H}]. \tag{C.5}$$

For an arbitrary guided mode in a cylindrical waveguide the helicity reads:

$$h = \frac{1}{2\omega n}\Bigg\{\frac{2m}{|k_t|^2 r}\frac{k_z k}{k_t}\left[|a_m|^2\epsilon + |b_m|^2\mu\right]Z_m\left(k_t r\right)Z_m^{'*}\left(k_t r\right) + \Bigg[|Z_m\left(k_t r\right)|^2 + \frac{k_z^2+k^2}{|k_t|^2}\Bigg(\left|Z_n^{'}\left(k_t r\right)\right|^2 + \frac{m^2}{|k_t|^2 r^2}\left|Z_m\left(k_t r\right)\right|^2\Bigg)\Bigg]\Im\left[a_m b_m^{*}\right]\sqrt{\epsilon\mu}\Bigg\}. \tag{C.6}$$

It can be shown that the energy and the helicity can be related as:

$$h = sign(m)\frac{W}{\omega n} - \frac{1}{4\omega n}\tilde{F}_{asy}(\mathbf{r})\left[|a_m|\sqrt{\epsilon} - |b_m|\sqrt{\mu}\right]^2, \tag{C.7}$$

where $\tilde{F}_{asy}(\mathbf{r})$ is

$$\tilde{F}_{asy}(\mathbf{r}) = |Z_m\left(k_t r\right)|^2 + \frac{k_z^2+k^2}{|k_t|^2}\left[\left|Z_n^{'}\left(k_t r\right)\right|^2 + \frac{m^2}{|k_t|^2 r^2}\left|Z_m\left(k_t r\right)\right|^2\right] - 4m\frac{k_z k}{|k_t|^2}\frac{Z_m\left(k_t r\right)Z_m^{'*}\left(k_t r\right)}{k_t r}. \tag{C.8}$$

Using the next inequalities

$$\left|Z_n^{'}\left(k_t r\right)\right|^2 + \frac{m^2}{|k_t|^2 r^2}\left|Z_m\left(k_t r\right)\right|^2 \geq 2\frac{Z_m\left(k_t r\right)Z_m^{'*}\left(k_t r\right)}{k_t r}, \tag{C.9}$$

$$k_z^2 + k^2 \geq 2k_z k, \tag{C.10}$$

it can be seen that $\tilde{F}_{asy}(\mathbf{r}) \geq 0$ and hence $|h| \leq W/(\omega n)$.

D.2 Spin density and momentum in cylindrical waveguides

The total spin density can be expressed as:

$$\mathbf{S} = \frac{\epsilon_0 \mu_r^{-1}}{4\omega} \Im \left[\mathbf{E}^* \times \mathbf{E}\right] + \frac{\mu_0 \epsilon_r^{-1}}{4\omega} \Im \left[\mathbf{H}^* \times \mathbf{H}\right]. \tag{C.11}$$

For arbitrary guided modes in a cylindrical waveguide with electromagnetic fields given by Eqs. 1.41, the spin density obeys the following expressions:

$$S_r = 0, \tag{C.12a}$$

$$S_\theta = \frac{1}{2\omega} \frac{1}{\epsilon_r \mu_r} \left[\frac{k_z}{k_t} Z_m^* \left(k_t r\right) Z_m^{'} \left(k_t r\right) \left(|a_m|^2 \epsilon + |b_m|^2 \mu\right) + \frac{2m}{k_t^2 r} k \left|Z_m \left(k_t r\right)\right|^2 \Im \left[a_m b_m^*\right] \sqrt{\epsilon\mu} \right], \tag{C.12b}$$

$$S_z = \frac{1}{2\omega} \frac{1}{\epsilon_r \mu_r} \frac{1}{|k_t|^2} \left\{ \frac{m}{k_t r} Z_m \left(k_t r\right) Z_m^{'*} \left(k_t\right) \left(k_z^2 + k^2\right) \left(|a_m|^2 \epsilon + |b_m|^2 \mu\right) + 2k_z k \left[\left| Z_m^{'} \left(k_t r\right) \right|^2 + \frac{m^2}{|k_t|^2 r^2} \left|Z_m \left(k_t r\right)\right|^2 \right] \Im \left[a_m b_m^*\right] \sqrt{\epsilon\mu} \right\}, \tag{C.12c}$$

The spin angular momentum,

$$\mathbf{P}^S = \frac{1}{2} \nabla \times \mathbf{S}, \tag{C.13}$$

yields:

$$P_r^S = 0, \tag{C.14a}$$

$$\begin{aligned} P_\theta^S = \frac{1}{4\omega}\frac{1}{\epsilon_r\mu_r}\Bigg\{ & \frac{m}{k_t^2 r}\left[|a_m|^2\epsilon + |b_m|^2\mu\right]\Bigg[k_z^2\Bigg(|Z_m(k_t r)|^2 - \frac{k_t^2}{|k_t|^2}\Big(|Z_m'(k_t r)|^2 \\ & + \frac{m^2}{|k_t|^2 r^2}|Z_m(k_t r)|^2 - \frac{2}{k_t r}Z_m(k_t r)\,Z_m'^*(k_t r)\Big)\Bigg) \\ & + k^2\left((k_t r)^{-1}Z_m(k_t r)\,Z_m'^*(k_t r) - Z_m(k_t r)\,Z_m''^*(k_t r) - \frac{k_t^2}{|k_t|^2}|Z_m'(k_t r)|^2\right)\Bigg] \\ & + 2k_z k\Im\left[a_m b_m^*\right]\sqrt{\epsilon\mu}\Bigg[\frac{1}{|k_t|^2 r}\left((m+1)\left|Z_m'(k_t r)\right|^2 + 2\frac{m^2}{|k_t|^2 r^2}|Z_m(k_t r)|^2\right) \\ & + k_t^{-1}\left(1 - \frac{m(3m+1)}{k_t^2 r^2}\right)Z_m^*(k_t r)\,Z_m'(k_t r) - k_t^{-1}Z_m'(k_t r)\,Z_{m-1}'^*(k_t r)\Bigg]\Bigg\}, \end{aligned} \tag{C.14b}$$

$$\begin{aligned} P_z^S = \frac{1}{4\omega}\frac{1}{\epsilon_r\mu_r}\Bigg\{ & k_z\left[\frac{k_t^2}{|k_t|^2}\left|Z_m'(k_t r)\right|^2 + \left(\frac{m^2}{k_t^2 r^2} - 1\right)|Z_m(k_t r)|^2\right]\left[|a_m|^2\epsilon + |b_m|^2\mu\right] \\ & + \frac{4mk}{k_t r}Z_m^*(k_t r)\,Z_m'(k_t r)\,\Im\left[a_m b_m^*\right]\sqrt{\epsilon\mu}\Bigg\}, \end{aligned} \tag{C.14c}$$

Finally, the canonical (orbital) part $\mathbf{P}^O$ of the momentum density can be expressed (in cartesians coordinates) as:

$$\mathbf{P}^O = \frac{\epsilon_0\mu_r^{-1}}{4\omega}\Im\left[\mathbf{E}^*\cdot(\nabla)\mathbf{E}\right] + \frac{\mu_0\epsilon_r^{-1}}{4\omega}\Im\left[\mathbf{H}^*\cdot(\nabla)\mathbf{H}\right], \tag{C.15}$$

where we use the notation

$$(\mathbf{X}^*\cdot(\nabla)\mathbf{Y})_i = \sum_i X_i^*\frac{\partial}{\partial x_i}Y_j. \tag{C.16}$$

Bear in mind that Eq. C.16 is only valid in cartesians coordinates. The direct replacement of the ∇ operator by its expression in other coordinate system is wrong. It is necessary to change the

expression accordingly. After some algebraic manipulation we arrive to:

$$P_r^O = 0, \tag{C.17a}$$

$$\begin{aligned} P_\theta^O = \frac{1}{4\omega}\frac{1}{\epsilon_r\mu_r}\frac{1}{r}\Bigg\{ & m\left|Z_m\left(k_t r\right)\right|^2\left[|a_m|^2\epsilon + |b_m|^2\mu\right] \\ & + \frac{2m(m-1)}{|k_t|^2 k_t r} Z_m\left(k_t r\right) Z_m'^*\left(k_t r\right)\left[\left(k_z^2+k^2\right)\left[|a_m|^2\epsilon + |b_m|^2\mu\right] + 4k_z k\Im\left[a_m b_m^*\right]\sqrt{\epsilon\mu}\right] \\ & + \left|Z_m'\left(k_t r\right) - \frac{m}{k_t r}Z_m\left(k_t r\right)\right|^2\left[m\frac{k_z^2+k^2}{|k_t|^2}\left[|a_m|^2\epsilon + |b_m|^2\mu\right] - 4\frac{k_z k}{|k_t|^2}\Im\left[a_m b_m^*\right]\sqrt{\epsilon\mu}\right]\Bigg\}, \end{aligned} \tag{C.17b}$$

$$\begin{aligned} P_z^O = \frac{1}{4\omega}\frac{1}{\epsilon_r\mu_r}k_z\Bigg\{ & \frac{8m}{|k_t|^2 r}\frac{k_z k}{k_t} Z_m\left(k_t r\right) Z_m'^*\left(k_t r\right)\Im\left[a_m b_m^*\right]\sqrt{\epsilon\mu} \\ & + \left[\left|Z_m\left(k_t r\right)\right|^2 + \left[\left|Z_m'\left(k_t r\right)\right|^2 + \frac{m^2}{|k_t|^2 r^2}\left|Z_m\left(k_t r\right)\right|^2\right]\frac{k_z^2+k^2}{|k_t|^2}\right]\left[|a_m|^2\epsilon + |b_m|^2\mu\right]\Bigg\}. \end{aligned} \tag{C.17c}$$

Upon comparing to the energy density Eq. C.2, it can be shown that the orbital momentum exhibits the expected dependence with the longitudinal wavevector k_z:

$$\frac{P^O}{W} = \frac{k_z}{\omega n^2}. \tag{C.18}$$

D.3 Orbital and Spin momenta in cylindrical waveguides for the hybrid HE$_{11}$ mode

We now turn to study the spin angular momentum of the HE$_{11}$ hybrid guided mode, which in fact exhibits strong intrinsic helicity given by:

$$\begin{aligned} h = \frac{1}{2\omega n}\Bigg\{ & \frac{2k_z k}{|k_t|^2 k_t r} Z_1\left(k_t r\right) Z_1'^*\left(k_t r\right)\left[|a_1|^2\epsilon + |b_1|^2\mu\right] \\ & + \left[\left|Z_1\left(k_t r\right)\right|^2 + \left(\left|Z_1'\left(k_t r\right)\right|^2 + \frac{\left|Z_1\left(k_t r\right)\right|^2}{|k_t|^2 r^2}\right)\frac{k_z^2+k^2}{|k_t|^2}\right]\Im\left[a_1 b_1^*\right]\sqrt{\epsilon\mu}\Bigg\}, \end{aligned} \tag{C.19}$$

the corresponding energy density from Eq. C.2 is:

$$\begin{aligned} W = \frac{1}{4}\Bigg\{ & \left[\left|Z_1\left(k_t r\right)\right|^2 + \left(\left|Z_1'\left(k_t r\right)\right|^2 + \frac{\left|Z_1\left(k_t r\right)\right|^2}{|k_t|^2 r^2}\right)\frac{k_z^2+k^2}{|k_t|^2}\right]\left[|a_1|^2\epsilon + |b_1|^2\mu\right] \\ & + \frac{8\sqrt{\epsilon\mu}}{|k_t|^2}\frac{k_z k}{k_t r} Z_1\left(k_t r\right) Z_1'^*\left(k_t r\right)\Im\left[a_1 b_1^*\right]\Bigg\}, \end{aligned} \tag{C.20}$$

and the spin density from Eq. C.12 is:

$$S_r = 0, \tag{C.21}$$

$$S_\theta = \frac{1}{2\omega\epsilon_r\mu_r}\left[\frac{k_z}{k_t}Z_1^*\left(k_t r\right)Z_1'\left(k_t r\right)\left[|a_1|^2\epsilon + |b_1|^2\mu\right] + \frac{2k}{k_t^2 r}\left|Z_1\left(k_t r\right)\right|^2\Im\left[a_1 b_1^*\right]\sqrt{\epsilon\mu}\right], \tag{C.22}$$

$$S_z = \frac{|k_t|^{-2}}{2\omega\epsilon_r\mu_r}\left\{\frac{k_z^2+k^2}{k_t r}Z_1\left(k_t r\right)Z_1'^*\left(k_t r\right)\left[|a_1|^2\epsilon + |b_1|^2\mu\right] + 2k_z k\left[\left|Z_1'\left(k_t r\right)\right|^2 + \frac{\left|Z_1\left(k_t r\right)\right|^2}{|k_t|^2 r^2}\right]\Im\left[a_1 b_1^*\right]\sqrt{\epsilon\mu}\right\}, \tag{C.23}$$

which becomes in this case very involved.

Finally, the orbital angular momentum from Eq. C.17 for the hybrid HE$_{11}$ mode reads:

$$P_r^O = 0 \tag{C.24a}$$

$$P_\theta^O = \frac{1}{4\omega}\frac{1}{\epsilon_r\mu_r}\frac{1}{r}\left\{\left|Z_1\left(k_t r\right)\right|^2\left[|a_1|^2\epsilon + |b_1|^2\mu\right] + \left|Z_1'\left(k_t r\right) - \frac{Z_1\left(k_t r\right)}{k_t r}\right|^2\left[\frac{k_z^2+k^2}{|k_t|^2}\left[|a_1|^2\epsilon + |b_1|^2\mu\right] - 4\frac{k_z k}{|k_t|^2}\Im\left[a_1 b_1^*\right]\sqrt{\epsilon\mu}\right]\right\}, \tag{C.24b}$$

$$P_z^O = \frac{1}{4\omega}\frac{1}{\epsilon_r\mu_r}k_z\left\{\frac{8}{|k_t|^2}k_z k\frac{Z_1\left(k_t r\right)Z_1'^*\left(k_t r\right)}{k_t r}\Im\left[a_1 b_1^*\right]\sqrt{\epsilon\mu} + \left[\left|Z_1\left(k_t r\right)\right|^2 + \left[\left|Z_1'\left(k_t r\right)\right|^2 + \frac{\left|Z_1\left(k_t r\right)\right|^2}{|k_t|^2 r^2}\right]\frac{k_z^2+k^2}{|k_t|^2}\right]\left[|a_1|^2\epsilon + |b_1|^2\mu\right]\right\}. \tag{C.24c}$$

And the spin momentum, from Eq. C.14:

$$P_r^S = 0,$$

$$P_\theta^S = \frac{1}{4\omega}\frac{1}{\epsilon_r\mu_r}\left\{\frac{1}{r}\left[\frac{\left|Z_1\left(k_t r\right)\right|^2}{k_t^2} - \frac{1}{|k_t|^2}\left|Z_1'\left(k_t r\right) - \frac{Z_1\left(k_t r\right)}{k_t r}\right|^2\right]\left(k_z^2+k^2\right)\left[|a_1|^2\epsilon + |b_1|^2\mu\right] + 4k_z k\left[\frac{1}{|k_t|^2 r}\left[\left|Z_1'\left(k_t r\right)\right|^2 + \frac{\left|Z_1\left(k_t r\right)\right|^2}{|k_t|^2 r^2}\right] + \left(1 - \frac{2}{k_t^2 r^2}\right)\frac{Z_1^*\left(k_t r\right)Z_1'\left(k_t r\right)}{k_t}\right]\Im\left[a_1 b_1^*\right]\sqrt{\epsilon\mu}\right\}, \tag{C.25a}$$

$$P_z^S = \frac{1}{4\omega}\frac{1}{\epsilon_r\mu_r}\left\{k_z\left[\frac{k_t^2}{|k_t|^2}\left|Z_1'\left(k_t r\right)\right|^2 + \left(\frac{1}{k_t^2 r^2} - 1\right)\left|Z_1\left(k_t r\right)\right|^2\right]\left[|a_1|^2\epsilon + |b_1|^2\mu\right] + \frac{4}{r}\frac{k}{k_t}Z_1^*\left(k_t r\right)Z_1'\left(k_t r\right)\Im\left[a_1 b_1^*\right]\sqrt{\epsilon\mu}\right\}. \tag{C.25b}$$

Appendix E

Resumen

El trabajo presentado en esta Tesis está dedicado al campo de la Nanofotónica, englobado en el amplio campo de la Nanociencia. Como Nanociencia nos referimos a la parte de la ciencia centrada en el estudio de los sistemas en la escala nanométrica (en la nanoescala, $\sim 10^{-9}$ m). Se puede decir que el comienzo de la Nanociencia data del año 1959, cuando Richard Feynman propuso desarrollar sistemas manipulando directamente de forma individual átomos y moléculas. No obstante, no fue hasta siglo XXI, y especialmente hasta comienzos de la presente década, cuando el campo experimentó un profundo avance. El desarrollo de nuevas técnicas experimentales nos ha permitido seguir las recomendaciones de Feynman, estando hoy en día al alcance de nuestra mano la manipulación precisa de átomos individuales. Todas las disciplinas experimentales (física, química, biología, medicina, etc.) se han beneficiado de estos avances tecnológicos, acercando a la sociedad nuevos descubrimientos que han cambiado por completo nuestra vida diaria. Además, el florecimiento de la Nanociencia sigue adelante, aumentando año a año el dinero invertido por los gobiernos. Hay todavía mucho por hacer.

En Nanofotónica estudiamos la emisión, propagación e interacción de la luz con la materia en la nanoescala, donde las frecuencia involucradas se encuentra usualmente entre el rango del ultravioleta y el infrarrojo cercano (longitudes de onda comparables con la escala de la materia). Sin embargo, las ecuaciones de Maxwell son invariantes respecto a la escala. Las ecuaciones son independientes del tamaño y, por ejemplo, no importa si estamos en la nanoescala o en la miliescala ($\sim 10^{-3}$ m). Esto significa que si escalamos un sistema (ya sea para hacerlo más grande o más pequeño) y escalamos en concordancia la longitud de onda, las soluciones siguen siendo las mismas. Por lo tanto, ¿qué hay de nuevo en la nanoescala?

La primera diferencia desde un punto de vista teórico es que las propiedades de los materiales sí dependen de la frecuencia. Por ejemplo, una antena de radio metálica es muy eficiente, pero el sistema no se puede escalar directamente porque los metales presentan pérdidas por absorción a frecuencias ópticas. Ahora necesitamos encontrar diferentes enfoques para el mismo problema que era bien conocido. Además, en la nanoescala los effectos cuánticos empiezan a emerger y aparecen nuevas reglas con las que jugar. También, en estas escalas nos encontramos por debajo del límite de difracción clásico, dado tradicionalmente por la luz visible, y nuevos fenómenos

interesantes aparecen como consecuencia del confinamiento del campo electromagnético. Por lo tanto hay nueva física que descubrir. Finalmente y sin ir más lejos, la Nanofotónica es un campo interesante per se porque la luz visible está en nuestro rango de visión, teniendo un impacto directo y amplio en nuestra vida diaria.

Si nos adentramos en el campo de la Nanofotónica, parte de esta Tesis está centrada en metasuperficies. Las metasuperficies son materiales artificiales compuestos por una ordenación periódica de partículas, típicamente en una superficie (en un mismo plano). Su respuesta a una excitación externa específica está regida por la geometría, ordenamiento y propiedades materiales de sus constituyentes básicos. Jugando con estos grados de libertad es posible diseñar prácticamente cualquier frente de onda y conseguir cualquier respuesta óptica. El campo de las metasuperficies ha sido ampliamente desarrollado en las radiofrecuencias, empleando partículas metálicas debido a sus propiedades en estas frecuencias y a la facilidad de manipular la materia a esta escala. De forma interesante, cuando bajamos a frecuencias ópticas los metales exhiben oscilaciones colectivas de los electrones en la banda de conducción denominados plasmones, que dio lugar a un rica fenomenología que fue denominada como Plasmónica, también investigados en el campo de las metasuperficies. Sin embargo, los metales empiezan a absorber en el régimen óptico, y con la llegada del mundo nano, el campo de la Nanofotónica basado en materiales dieléctricos ha surgido durante los últimos años como la alternativa a la plasmónica. Como las partículas dieléctricas presentan resonancias eléctricas y magnéticas, pueden ser empleadas para imitar la compleja fenomenología desarrollada para los metales, así como para explorar nuevos diseños.

En esta dirección, uno de los principales logros desarrollados en esta Tesis ha sido presentar de forma detallada un modelo analítico para describir las propiedades electromagnéticas de las metasuperficies en términos de dipolos eléctricos y magnéticos. El modelo (denominado formulación CEMD) ha sido detallado para un sistema periódico de cilindros/esferas, pero basándonos en este formalismo es sencillo extenderlo para sistemas más complejos. De este modo, en la Tesis también se han estudiado metasuperficies (redes 2D) con una y dos partículas en la celda unidad, aunque las posibilidades son mucho más amplias. Más allá de la Tesis y entre otros, con el formalismo CEMD seguiremos investigando temas interesantes como la generación de segundo armónico, sistemas con simetría paridad-tiempo, amplificación del dicroísmo circular, topología fotónica y láser de cavidades abiertas.

También, en conexión con las metasuperficies, hemos estudiado los denominados estados ligados en el continuo (BICs, de sus siglas en inglés). Si el campo de las metasuperficies ópticas es un campo relativamente nuevo, los BICs fotónicos son incluso más novedosos. En general, los BICs son modos localizados que no pueden emitir energía fuera del sistema que los soporta, en otras palabras, si conseguimos inyectar energía en uno de estos estados, la energía se mantendrá confinada dentro del sistema. La diferencia con un estado ligado común es que, espectralmente, los BICs están dentro del continuo de modos radiativos, coexistiendo con ondas propagantes. De forma concreta, para los BICs en electromagnetismo, esto significa que aunque no sea posible acoplar a estos estados, podemos explorar sus propiedades desde el campo lejano.

Las metasuperficies son una plataforma excelente para diseñar BICs. Debido a que el número de canales de radiación es en principio pequeño, jugando con las propiedades individuales y la

configuración de la celda unidad podemos suprimir por completo el acoplo a esos canales de radiación. Por lo tanto, podemos diseñar las condiciones físicas necesarias para tener un BIC. En metasuperficies ópticas, los BICs se caracterizan porque en el espectro de reflectancia aparecen resonancias estrechas que se desvanecen justo en la condición del BIC. Esto da lugar a una fuerte amplificación del campo electromagnético y a factores de calidad arbitrariamente altos, que pueden ser diseñados a partir de la composición de la celda unidad.

Otra de las contribuciones originales realizadas en esta Tesis es el estudio analítico, a través del formalismo CEMD, de BICs en dos sistemas diferentes. Además, los resultados han sido verificados por simulaciones numéricas y medidas experimentales. Estos resultados abren la puerta hacia nuevas estrategias para confinar la luz en sistemas ópticos con implicaciones en campos mencionados anteriormente en relación con las metasuperficies, como generación de segundo armónico y láser de cavidades abiertas.

El otro campo de la Nanofotónica explorado en la presente Tesis es el estudio de las propiedades fundamentales de nanohilos semiconductores (NWs, de sus siglas en inglés). Las propiedades de emisión (y por reciprocidad, de absorción) de un emisor no están únicamente determinadas por sus propiedades intrínsecas, si no que también dependen activamente de las propiedades del medio que le rodea. El entorno determina la densidad local de estados electromagnética y define los canales de radiación. Por ello, diseñando el entorno es posible amplificar o inhibir la emisión, controlar la polarización de la luz emitida y modificar la direccionalidad de la radiación.

De manera similar a otros campos, las primeras propuestas para modificar el entorno en la nanoescala estuvieron basadas en el uso de nanoestructuras metálicas. Su principal ventaja es que el campo electromagnético se amplifica fuertemente cerca de la superficie de los metales. No obstante, las pérdidas inherentes a frecuencias ópticas actúan en detrimento de su rendimiento, especialmente cuando se quiere reducir el decaimiento en canales no radiativos. De nuevo, para superar este problema podemos explorar nuevas estrategias basadas en estructuras dieléctricas. En este aspecto, las propiedades ópticas de los NWs semiconductores los hacen especialemente adecuados para guiar la luz de forma selectiva y amplificar la dispersión, la absorción y la fotoluminiscencia en la nanoescala. Para poder controlar con precisión todos estos procesos es necesario estudiar las propiedades fundamentales de la luz cuando se confina en los NWs.

Las contribuciones originales sobre estas propiedades fundamentales han sido desarrolladas en los últimos capítulos de la Tesis. Primero hemos estudiado las diferentes resonancias que presentan los NWs dielectricos, mostrando que existe una relación formal entre las denominadas resonancias de Mie y los modos guiados. Conviene recordar que en términos de estas resonancias podemos definir la densidad local de estados electromagnética. Después, basándonos en estos modos, hemos analizado sus propiedades globales (como la dispersión y la absorción) y las locales (como la densidad de energía y el momento angular). Por último, hemos explorado la posibilidad de alcanzar el régimen de acoplamiento fuerte utilizando NW dieléctricos. Aunque fundamental, estas propiedades son todavía un tema abierto y más esfuerzos se deben de realizar para seguir revelando su fenomenología asociada. Por ejemplo, sería interesante analizar qué contribuciones multipolares están asociadas a las resonancias Fano en cilindros finitos. O podemos seguir estudiando el momento angular de spin de la luz confinada en guías de ondas. Las posibilidades son

tan amplias como se pueda imaginar.

Appendix F

Summary

The work presented in this Thesis is devoted to the field of theoretical Nanophotonics, that is englobed in the extensive field of Nanoscience. As Nanoscience we refer to the part of science focused on the study of systems at the nanometer scales (nanoscale, $\sim 10^{-9}$ m). Some people clams that the beginning of Nanoscience dates back to 1959, when Richard Feynman proposed to built up systems via direct manipulations of atoms and molecules. However, it was not until the 21st century, and specially until the beginning of this decade, when the field experienced a more profound advance. The development of new experimental techniques allows us to follow the recommendations of Feynman, being within our grasp the precise manipulation of individual atoms. All experimental disciplines (physics, chemistry, biology, medicine and so on) have benefited from these technological advances, bringing to the society new discoveries that have completely changed our daily life. Moreover, the flourish of Nanoscience keeps growing, increasing year by year governments's investment. There is still much to be done.

In Nanophotonics we study the emission, propagation and interaction of light with matter at the nanoscale, where the involved frequency is usually between the ultraviolet and the near-infrared range (wavelength comparable with the matter scale). Nonetheless, Maxwell's equations are scale-invariant. They are the same independently of the size and, for example, no matter if at the nanoscale or at the miliscale ($\sim 10^{-3}$ m). If we scale a system (up or down), the solution is still the same by scaling in accordance the wavelength. Thus, what is new at the nanoscale?

A difference from the theoretical point of view is that material properties do depend on the frequency. For example, a metallic radio antenna is very efficient, but metals becomes lossy at optical frequencies and a direct scaling down is not possible. We need to find a different approach to the same well known problems. In addition, at nanoscale quantum effects start to arise and new rules come into play. Also, these sizes are even below the classical diffraction limit, arising new interesting phenomena as a consequence of the electromagnetic field confinement. Therefore there is new physics to discover. Finally and without going any further, Nanophotonics is an exciting field per se because visible light is within our range of vision, there is a direct and vast impact on our daily life.

Going deeper within the field of Nanophotonics, part of this Thesis is focused on metasur-

faces. They are artificial materials composed by a periodic arrangement of particles, typically in a surface. Its response to a given external excitation is governed by the geometry, arrangement, and material properties of its basic constituents. Playing with these degrees of freedom it is possible to practically engineer any wavefront and to achieve any optical response. The field of metasurfaces has been widely developed at radio frequencies for the easiness to manipulate metals at that spatial scale. In addition, recall that metals in the optical domain exhibit collective oscillations called plasmons that have given rise to a wealth of phenomenology termed Plasmonics. However, metals start to absorb at such optical frequencies, and with the advent of the Nano-world, the field of all-dielectric Nanophotonics has emerged during the last years as an alternative to Plamonics. Since dielectric particles present electric and magnetic resonances, they can be employed to mimic the complex phenomenology developed for metals, as well as in new designs.

On this wise, one of the main goals developed of this Thesis has been to present a detailed analytical model to describe the electromagnetic properties of metasurfaces in terms of electric and magnetic dipole contributions. The model (which we have called CEMD formulation) has been detailed for an array of cylinders/spheres, but based on the formalism it is straightforward to extend it for more complex arrangements. In the Thesis, metasurfaces (non-diffracting 2D arrays of particles) with one or two particles per unit cell have been studied too, but the possibilities are much wider. Beyond the thesis and among others, other interesting topics that will be investigated with the CEMD formulation are the second harmonic generation of light, parity-time symmetry systems, enhancement of circular dichroism, topological photonics, and open cavity lasing.

Also, in connection with metasurfaces we have studied the so called bound states in the continuum (BICs). If optical metasurfaces is a relative new field, BICs are even newer. In general, photonic BICs are localized modes that do not leak out energy outside the own system that supports them, i.e., if somehow we inject energy into one of these states, the energy keeps confined inside the system. The difference with a common bound state is that, spectrally, BICs lie inside the continuum of radiative modes, coexisting with extended waves. Specifically, for BICs in electromagnetism this means that, although it is not possible to couple to them, we can exploit their properties from the far field.

Metasurfaces are an excellent platform to design BICs. Since the number of radiation channels is in principle small, playing with the individual properties and the configuration of the unit cell we can totally suppress the coupling to these radiation channels. Therefore, we can engineer the physical conditions at which a BIC arises. For optical metasurfaces, BICs are characterized by a vanishing resonance in the reflectance spectra, leading to strong enhancement of the electromagnetic field and arbitrarily high Q-factors that can be tailored by the composition of the unit cell.

Another original contribution done in the Thesis has been the analytical study, through the CEMD formulation, of BICs in two different systems. In addition, the results have been supported by numerical simulations and experimental measurements. These results open the door toward new approaches to confine light in optical systems with implications in fields already mentioned in connection with metasurfaces, as second harmonic generation and open cavity lasing. No doubt we will keep studying BICs in connection with direct phenomena and applications.

The other field of Nanophotonics explored in the present Thesis is the study of fundamental properties of semiconductor nanowires (NWs). The emission (and by reciprocity the absorption) properties of a given emitter are not only determined by its intrinsic characteristics, but also strongly depend on its surrounding environment. The environment determines the electromagnetic local density of states and defines the radiation channels. Thus, by tailoring the environment it is possible to enhance or inhibit the emission, to control the polarization of the emitted light, and to modify the directionality of the radiation.

Similar to other fields, the first proposals to modify the environment at the nanoscale were based on the use of metallic nanostructures. The main advantage of metals is the high electromagnetic field enhancement close to the surfaces. However, their inherent losses at optical frequencies act to the detriment of their performance, specially when we want to reduce the non-radiative decay channels. Again, in order to overcome this issue we can explore new strategies based on dielectric structures. In this regard, the unique optical properties of semiconductor NWs make them specially suitable to selectively guide light and enhance the scattering, absorption and photoluminiscence at the nanoscale. Thus, in order to precisely control all these processes it is necessary to study the fundamental properties of light confined in NWs.

The original contributions about these fundamental properties have been shown in the last chapters of the Thesis. We have first studied the different resonances supported by dielectric NWs, showing formally the connection between the so called Mie resonances and leaky/guided modes. Remember that the total electromagnetic local density of states can be defined in terms of resonances. Later, based on these modes we have analyzed their global (as scattering and absorption) and local (as energy density and angular momentum) properties. Finally, we have explored the possibilities to achieve strong coupling with dielectric NWs. Although fundamental, this is still an open topic in which more efforts must be made to keep disclosing the phenomenology. For example, it would be interesting to analyze which multipole contributions are associated to Fano resonances in finite cylinders. Or we can keep studying the spin angular momentum of light in confined system. The possibilities are as broad as you can imagine.

Appendix G

List of publications

G.1 Publications on which the Thesis is based

P1 D. R. Abujetas, J. A. Sánchez-Gil, and J. J. Sáenz, "Generalized Brewster effect in high-refractive-index nanorod-based metasurfaces", Optics Express **26**, 31523 (2018),[37] **Chapter 2**.

P2 D. R. Abujetas, J. J. Sáenz, and J. A. Sánchez-Gil, "Narrow Fano resonances in Si nanocylinder metasurfaces: Refractive index sensing", Journal of Applied Physics **125**, 183103 (2019),[38] **Chapter 2**.

P3 D. R. Abujetas, A. Barreda, F. Moreno, J. J. Saenz, A. Litman, J.-M. Geffrin, and J. A. Sanchez-Gil, "Brewster quasi bound states in the continuum in all-dielectric metasurfaces from single magnetic-dipole resonance meta-atoms", Scientific Reports **9**, 16048 (2019),[59] **Chapter 3**

P4 D. R. Abujetas, N. van Hoof, S. ter Huurne, J. Gómez Rivas, and J. A. Sánchez-Gil, "Spectral and temporal evidence of robust photonic bound states in the continuum on terahertz metasurfaces", Optica **6**, 996 (2019),[64] **Chapter 3**

P5 D. R. Abujetas, R. Paniagua-Domínguez, and J. A. Sánchez-Gil, "Unraveling the Janus role of Mie resonances and leaky/guided modes in semiconductor nanowire absorption for enhanced light harvesting", ACS Photonics **2**, 921–929 (2015),[113] **Chapter 4**

P6 D. R. Abujetas, M. A. Mandujano, E. R. Méndez, and J. A. Sánchez-Gil, "High-contrast Fano resonances in single semiconductor nanorods", ACS Photonics **4**, 1814–1821 (2017),[49] **Chapter 4**

P7 D. R. Abujetas and J. A. Sánchez-Gil, "Spin angular momentum in planar and cylindrical waveguides induced by transverse confinement and intrinsic helicity of guided light", ACS Photonics **7**, 534–545 (2020),[167] **Chapter 5**

P8 D. R. Abujetas, J. Feist, F. J. García-Vidal, J. Gómez Rivas, and J. A. Sánchez-Gil, "Strong coupling between weakly guided semiconductor nanowire modes and an organic dye", Physical Review B **99**, 205409 (2019),[168] **Chapter 5**

G.2 Other publications

R1 R. Paniagua-Domínguez, D. R. Abujetas, and J. A. Sánchez-Gil, "Ultra low-loss, isotropic optical negative-index metamaterial based on hybrid metal-semiconductor nanowires", Scientific Reports **3**, 1507 (2013).[89]

R2 D. Van Dam, D. R. Abujetas, R. Paniagua-Domínguez, J. A. Sánchez-Gil, E. Bakkers, J. Haverkort, and J. Gómez Rivas, "Directional and polarized emission from nanowire arrays", Nano Letters **15**, 4557 (2015).[210]

R3 J. Olmos-Trigo, C. Sanz-Fernández, D. R. Abujetas, A. García-Etxarri, G. Molina-Terriza, J. A. Sánchez-Gil, F. S. Bergeret and J. J. Saenz, "Role of the absorption on the spin-orbit interactions of light with Si nano-particles", Journal of Applied Physics **126**, 033104 (2019).

R4 F. Dirnberger, D. R. Abujetas, J. König, M. Forsch, T. Koller, I. Gronwald, C. Lange, R. Huber, C. Schüller, T. Korn, J. A. Sánchez-Gil, and D. Bougeard, "Tuning spontaneous emission through waveguide cavity effects in semiconductor nanowires", Nano Letters **19**, 7287 (2019).

R5 J. Hu, D. R. Abujetas, D. Tsoutsi, L. Leggio, F. Rivero, E. M. Rodríguez, R. A. Torres, J. A. Sánchez-Gil, H. L. Ramírez, D. Gallego, H. L. Rivera, P. Rivera-Gil, F. Alonso, J. Garcá-Solé, and D. Jaque, "Invited Article: Experimental evaluation of gold nanoparticles as infrared scatterers for advanced cardiovascular optical imaging", APL Photonics **3**, 080803 (2018).

R6 D. R. Abujetas, R. Paniagua-Domínguez, and J. A. Sánchez-Gil, "Impedance-Matched, Double-Zero Optical Metamaterials Based on Weakly Resonant Metal Oxide NWs", Photonics **5**, 7 (2018).

R7 D. Van Dam, D. R. Abujetas, J. A. Sánchez-Gil, J. Haverkort, E. Bakkers, and J. Gómez Rivas, "Strong diameter-dependence of nanowire emission coupled to waveguide modes", Applied Physics Letters **108**, 121109 (2016).

R8 B. J. M. Brenny, D. R. Abujetas, D. Van Dam, J. A. Sánchez-Gil, J. Gómez Rivas, and A. Polman "Directional emission from leaky and guided modes in GaAs nanowires measured by cathodoluminescence", ACS Photonics **108**, 121109 (2016).

R9 D. R. Abujetas, R. Paniagua-Domínguez, M. Nieto-Vesperinas, and J. A. Sánchez-Gil, "Photonic band structure and effective medium properties of doubly-resonant core-shell metallodielectric nanowire arrays: low-loss, isotropic optical negative-index behavior", Journal of Optics **17**, 125104 (2015).

R10 R. Paniagua-Domínguez, D. R. Abujetas, L. F. Froufe-Pérez, J. J. Sáenz, and J. A. Sánchez-Gil, "Broadband telecom transparency of semiconductor-coated metal nanowires: more transparent than glass", Optics Express **21**, 22076 (2013).

Bibliography

[1] J. D. Jackson, *Classical Electrodynamics* (John Wiley & Son, New York, 1998).

[2] L. D. Landau and E. M. Lifshitz, *Electrodynamics of Continuous Media* (Pergamon, Press, 1984).

[3] L. Novotny and B. Hecht, *Principles of Nano-Optics* (Cambridge University Press, 2006).

[4] R. W. Boyd, *Nonlinear Optics* (Academic Press, 2007).

[5] C. F. Bohren and D. R. Huffman, *Absorption and scattering of light by small particles* (Wiley, N.Y., 1983).

[6] J. A. Stratton, *Electromagnetic Theory* (McGraw-Hill Book Company, New York and London, 1941).

[7] H. C. van de Hulst, *Light Scattering by Small Particles* (Dover Publications, New York, 1981).

[8] T. Setälä, M. Kaivola, and A. T. Friberg, "Decomposition of the point-dipole field into homogeneous and evanescent parts," Physical Review E **59**, 1200 (1999).

[9] E. E. Radescu and G. Vaman, "Exact calculation of the angular momentum loss, recoil force, and radiation intensity for an arbitrary source in terms of electric, magnetic, and toroid multipoles," Physical Review E **65** (2002).

[10] P. Grahn, A. Shevchenko, and V. Kaivole, "Electromagnetic multipole theory for optical nanomaterials," New Journal of Physics **14**, 093033 (2012).

[11] A. B. Evlyukhin, C. Reinhardt, E. Evlyukhin, and B. N. Chichkov, "Multipole analysis of light scattering by arbitrary-shaped nanoparticles on a plane surface," Journal of the Optical Society of America B **30**, 2589 (2013).

[12] R. Raab and O. L. de Lange, *Multipole Theory in Electromagnetism* (Clarendon Press, Oxford, 2005).

[13] C. Yeh, "The diffraction of waves by a penetrable ribbon," Journal of Mathematical Physics **4**, 65–71 (1963).

[14] S. Caorsi, M. Pastorino, and M. Raffetto, "Electromagnetic scattering by a multilayer elliptic cylinder under transverse-magnetic illumination: series solution in terms of mathieu functions," IEEE Transactions on Antennas and Propagation **45**, 926–935 (1997).

[15] E. Kallos, I. Chremmos, and V. Yannopapas, "Resonance properties of optical all-dielectric metamaterials using two-dimensional multipole expansion," Physical Review B **86**, 1–10 (2012).

[16] J. Hu and C. R. Menyuk, "Understanding leaky modes: slab waveguide revisited," Advances in Optics and Photonics **1**, 58 (2009).

[17] S. A. Ramakrishna, "Physics of negative refractive index materials," Reports on Progress in Physics **68**, 449–521 (2005).

[18] R. Marqués, F. Martín, and M. Sorolla, *Metamaterials with Negative Parameters: Theory, Design and Microwave Applications* (Wiley, 2007).

[19] S. Jahani and Z. Jacob, "All-dielectric metamaterials," Nature Nanotechnology **11**, 23–36 (2016).

[20] M. Kadic, G. W. Milton, M. van Hecke, and M. Wegener, "3D Metamaterials," Nature **1**, 198 (2019).

[21] A. I. Kuznetsov, A. E. Miroshnichenko, M. L. Brongersma, Y. S. Kivshar, and B. Luk'yanchuk, "Optically resonant dielectric nanostructures," Science **354** (2016).

[22] A. B. Evlyukhin, C. Reinhardt, A. Seidel, and B. N. Chichkov, "Optical response features of Si-nanoparticle arrays," Physical Review B **82**, 045404 (2010).

[23] A. García-Etxarri, R. Gómez-Medina, L. S. Froufe-Pérez, C. López, L. Chantada, F. Scheffold, J. Aizpurua, M. Nieto-Vesperinas, and J. J. Sáenz, "Strong magnetic response of submicron silicon particles in the infrared," Optics Express **19**, 4815–4826 (2011).

[24] M. Nieto-Vesperinas, R. Gómez-Medina, and J. J. Sáenz, "Angle-suppressed scattering and optical forces on submicrometer dielectric particles," Journal of the Optical Society of America A **28**, 54 (2010).

[25] R. Gómez-Medina, "Electric and magnetic dipolar response of germanium nanospheres: interference effects, scattering anisotropy, and optical forces," Journal of Nanophotonics **5**, 053512 (2011).

[26] N. Yu and F. Capasso, "Flat optics with designer metasurfaces." Nature materials **13**, 139–150 (2014).

[27] M. Khorasaninejad, P. Genevet, R. Devlin, F. Capasso, and F. Aieta, "Recent advances in planar optics: from plasmonic to dielectric metasurfaces," Optica **4**, 139 (2017).

[28] Y. Yang, W. Wang, P. Moitra, I. I. Kravchenko, D. P. Briggs, and J. Valentine, "Dielectric meta-reflectarray for broadband linear polarization conversion and optical vortex generation," Nano Letters **14**, 1394–1399 (2014).

[29] P. Moitra, B. A. Slovick, W. Li, I. I. Kravchencko, D. P. Briggs, S. Krishnamurthy, and J. Valentine, "Large-scale all-dielectric metamaterial perfect reflectors," ACS Photonics **2**, 692–698 (2015).

[30] W. Liu, "Generalized magnetic mirrors," Physical Review Letters **119**, 1–6 (2017).

[31] F. Aieta, M. A. Kats, P. Genevet, and F. Capasso, "Multiwavelength achromatic metasurfaces by dispersive phase compensation," Science **347**, 1342–1346 (2015).

[32] D. Sell, J. Yang, S. Doshay, K. Zhang, and J. A. Fan, "Visible light metasurfaces based on single-crystal silicon," ACS Photonics **3**, 1919–1925 (2016).

[33] M. Khorasaninejad, W. T. Chen, R. C. Devlin, J. Oh, A. Y. Zhu, and F. Capasso, "Metalenses at visible wavelengths: Diffraction-limited focusing and subwavelength resolution imaging Mohammadreza," Science **352**, 1190 (2016).

[34] Z. Zhou, J. Li, R. Su, B. Yao, H. Fang, K. Li, L. Zhou, J. Liu, D. Stellinga, C. P. Reardon, T. F. Krauss, and X. Wang, "Efficient silicon metasurfaces for visible light," ACS Photonics **4**, 544–551 (2017).

[35] P. Lalanne and P. Chavel, "Metalenses at visible wavelengths: past, present, perspectives," Laser and Photonics Reviews **11** (2017).

[36] W. Liu and A. E. Miroshnichenko, "Beam steering with dielectric metalattices," ACS Photonics **5**, 1733–1741 (2018).

[37] D. R. Abujetas, J. A. Sánchez-Gil, and J. J. Sáenz, "Generalized Brewster effect in high-refractive-index nanorod-based metasurfaces," Optics Express **26**, 31523 (2018).

[38] D. R. Abujetas, J. J. Sáenz, and J. A. Sánchez-Gil, "Narrow Fano resonances in Si nanocylinder metasurfaces: Refractive index sensing," Journal of Applied Physics **125**, 183103–1118 (2019).

[39] P. A. Belov, S. I. Maslovski, K. R. Simovski, and S. A. Tretyakov, "A condition imposed on the electromagnetic polarizability of a bianisotropic lossless scatterer," Technical Physics Letters **29**, 718–720 (2003).

[40] I. Sersic, C. Tuambilangana, T. Kampfrath, and A. F. Koenderink, "Magnetoelectric point scattering theory for metamaterial scatterers," Physical Review B **83**, 1–12 (2011).

[41] S. Albaladejo, R. Gómez-Medina, L. S. Froufe-Pérez, H. Marinchio, R. Carminati, J. F. Torrado, G. Armelles, A. García-Martín, and J. J. Sáenz, "Radiative corrections to the polarizability tensor of an electrically small anisotropic dielectric particle," Optics Express **18**, 3556 (2010).

[42] H. Marinchio, R. Carminati, A. García-Martín, and J. J. Sáenz, "Magneto-optical kerr effect in resonant subwavelength nanowire gratings," New Journal of Physics **16** (2014).

[43] V. Twersky, "On a multiple scattering theory of the finite grating and the wood anomalies," Journal of Applied Physics **23**, 1099–1118 (1952).

[44] G. Brönstrup, N. Jahr, C. Leiterer, A. Csáki, W. Fritzsche, and S. Christiansen, "Optical properties of individual silicon," ACS nano **4**, 7113–7122 (2010).

[45] R. Gómez-Medina, M. Laroche, and J. J. Sáenz, "Extraordinary optical reflection from subwavelength cylinder arrays," Optics Express **14**, 3730–3737 (2006).

[46] M. Laroche, S. Albaladejo, R. Gómez-Medina, and J. J. Sáenz, "Tuning the optical response of nanocylinder arrays: An analytical study," Physical Review B **74**, 1–5 (2006).

[47] B. García-Cámara, R. Gómez-Medina, and J. J. Sáenz, "Sensing with magnetic dipolar resonances in semiconductor nanospheres," Opt. Express **21**, 34–38 (2013).

[48] Y. Wang, B. Gao, K. Zhang, K. Yuan, Y. Wan, Z. Xie, X. Xu, H. Zhang, Q. Song, L. Yao, X. Fang, Y. Li, W. Xu, J. Zhang, and L. Dai, "Refractive index sensor based on leaky resonant scattering of single semiconductor nanowire," ACS Photonics **4**, 688–694 (2017).

[49] D. R. Abujetas, M. A. Mandujano, E. R. Méndez, and J. A. Sánchez-Gil, "High-contrast Fano resonances in single semiconductor nanorods," ACS Photonics **4**, 1814–1821 (2017).

[50] D. Visser, B. D. Choudhury, I. Krasovska, and S. Anand, "Refractive index sensing in the visible/NIR spectrum using silicon nanopillar arrays," Optics Express **25**, 12171 (2017).

[51] K. A. Willets and R. P. Van Duyne, "Localized surface plasmon resonance spectroscopy and sensing." Annual review of physical chemistry **58**, 267–297 (2007).

[52] K. M. Mayer and J. H. Hafner, "Localized surface plasmon resonance biosensors," Chemical Reviews **111**, 3828 (2011).

[53] I. M. Pryce, Y. A. Kelaita, K. Aydin, and H. A. Atwater, "Compliant metamaterials for resonantly enhanced infrared absorption spectroscopy and refractive index sensing," ACS Nano **5**, 8167–8174 (2011).

[54] F. López-Tejeira, R. Paniagua-Domínguez, and J. A. Sánchez-Gil, "High-performance nanosensors based on plasmonic Fano-like interference: Probing refractive index with individual nanorice and nanobelts," ACS Nano **6**, 8989–8996 (2012).

[55] R. Singh, W. Cao, I. Al-Naib, L. Cong, W. Withayachumnankul, and W. Zhang, "Ultrasensitive terahertz sensing with high- Q Fano resonances in metasurfaces," Applied Physics Letters **105** (2014).

[56] E. Baquedano, M. U. González, R. Paniagua-Domínguez, J. A. Sánchez-Gil, and P. A. Postigo, "Low-cost and large-size nanoplasmonic sensor based on Fano resonances with fast response and high sensitivity," Optics Express **25**, 15967 (2017).

[57] M. F. Limonov, M. V. Rybin, A. N. Poddubny, and Y. S. Kivshar, "Fano resonances in photonics," Nature Photonics **11**, 543–554 (2017).

[58] M. V. Rybin, D. S. Filonov, P. A. Belov, Y. S. Kivshar, and M. F. Limonov, "Switching from visibility to invisibility via fano resonances: Theory and experiment," Scientific Reports **5**, 1–6 (2015).

[59] D. R. Abujetas, A. Barreda, F. Moreno, J. J. Saenz, A. Litman, J.-M. Geffrin, and J. A. Sanchez-Gil, "Brewster quasi bound states in the continuum in all-dielectric metasurfaces from single magnetic-dipole resonance meta-atoms," arxiv:1902.07148 pp. 1–13 (2019).

[60] T. K. Fang and T. N. Chang, "Determination of profile parameters of a Fano resonance without an ultrahigh-energy resolution," Physical Review A **57**, 4407–4412 (1998).

[61] D. C. Marinica and A. G. Borisov, "Bound states in the continuum in photonics," Physical Review Letters **100**, 1–4 (2008).

[62] E. N. Bulgakov and A. F. Sadreev, "Bloch bound states in the radiation continuum in a periodic array of dielectric rods," Physical Review A **90**, 1–7 (2014).

[63] K. Koshelev, S. Lepeshov, M. Liu, A. Bogdanov, and Y. Kivshar, "Asymmetric metasurfaces with high-Q resonances governed by bound states in the continuum," Physical Review Letters **121**, 193903 (2018).

[64] D. R. Abujetas, N. van Hoof, S. ter Huurne, J. Gómez Rivas, and J. A. Sánchez-Gil, "From Fano resonances to bound states in the continuum in dipole arrays at THz frequencies," arxiv:1901.03122 pp. 1–6 (2019).

[65] J. van de Groep and A. Polman, "Designing dielectric resonators on substrates: Combining magnetic and electric resonances," Optics Express **21**, 26285 (2013).

[66] Z. J. Yang, Q. Zhao, and J. He, "Fano interferences of electromagnetic modes in dielectric nanoblock dimers," Journal of Applied Physics **125** (2019).

[67] S. Singh, W. F. Richards, J. R. Zinecker, and D. R. Wilton, "Accelerating the convergence of series representing the free space periodic Green's function," IEEE Transactions on Antennas and Propagation **38**, 1958–1962 (1990).

[68] R. Parker, "Resonance effects in wake shedding from parallel plates: Calculation of resonant frequencies," Journal of Sound and Vibration **5**, 330–343 (1967).

[69] F. H. Stillinger and D. R. Herrick, "Bound states in the continuum," Physical Review A **11**, 446–454 (1975).

[70] L. S. Cederbaum, R. S. Friedman, V. M. Ryaboy, and N. Moiseyev, "Conical Intersections and Bound Molecular States Embedded in the Continuum," Physical Review Letters **90**, 4 (2003).

[71] P. J. Cobelli, V. Pagneux, A. Maurel, and P. Petitjeans, "Experimental study on water-wave trapped modes," Journal of Fluid Mechanics **666**, 445–476 (2011).

[72] C. W. Hsu, B. Zhen, A. D. Stone, J. D. Joannopoulos, and M. Soljačić, "Bound states in the continuum," Nature Materials **1** (2016).

[73] C. W. Hsu, B. G. DeLacy, S. G. Johnson, J. D. Joannopoulos, and M. Soljačić, "Theoretical criteria for scattering dark states in nanostructured particles," Nano Letters **14**, 2783–2788 (2014).

[74] E. N. Bulgakov and D. N. Maksimov, "Topological Bound States in the Continuum in Arrays of Dielectric Spheres," Physical Review Letters **118**, 1–5 (2017).

[75] A. Taghizadeh and I. S. Chung, "Quasi bound states in the continuum with few unit cells of photonic crystal slab," Applied Physics Letters **111** (2017).

[76] A. Kodigala, T. Lepetit, Q. Gu, B. Bahari, Y. Fainman, and B. Kanté, "Lasing action from photonic bound states in continuum," Nature **541**, 196–199 (2017).

[77] J. Gomis-Bresco, D. Artigas, and L. Torner, "Anisotropy-induced photonic bound states in the continuum," Nature Photonics **11**, 232–236 (2017).

[78] H. M. Doeleman, F. Monticone, W. den Hollander, A. Alù, and A. F. Koenderink, "Experimental observation of a polarization vortex at an optical bound state in the continuum," Nature Photonics **12**, 397–401 (2018).

[79] S. T. Ha, Y. H. Fu, N. K. Emani, Z. Pan, R. M. Bakker, R. Paniagua-Dominguez, and A. I. Kuznetsov, "Directional lasing in resonant semiconductor nanoantenna arrays," Nature Nanotechnology **13** (2018).

[80] L. Carletti, K. Koshelev, C. de Angelis, and Y. Kivshar, "Giant nonlinear response at the nanoscale driven by bound states in the continuum," Physical Review Letters **121**, 33903 (2018).

[81] W. Zhang, A. Charous, M. Nagai, D. M. Mittleman, and R. Mendis, "Extraordinary optical reflection resonances and bound states in the continuum from a periodic array of thin metal plates," Optics Express **26**, 13195 (2018).

[82] S. I. Azzam, V. M. Shalaev, A. Boltasseva, and A. V. Kildishev, "Formation of bound states in the continuum in hybrid plasmonic-photonic systems," Physical Review Letters **121**, 253901 (2018).

[83] J. von Neumann and E. P. Wigner, "Über merkwürdige diskrete Eigenwerte," Physikalische Zeitschrift **30**, 465–466 (1929).

[84] Friedrich H and D. Wintgen, "Interfering resonances and BIC," Physical Review A **32**, 3231–3242 (1985).

[85] H. Friedrich and D. Wintgen, "Physical realization of bound states in the continuum," Physical Review A **31**, 3964–3966 (1985).

[86] J.-M. Geffrin, B. García-Cámara, R. Gómez-Medina, P. Albella, L. S. Froufe-Pérez, C. Eyraud, A. Litman, R. Vaillon, F. González, M. Nieto-Vesperinas, J. J. Sáenz, and F. Moreno, "Dielectric subwavelength sphere," Nature Communications **3**, 1171 (2012).

[87] A. B. Evlyukhin, S. M. Novikov, U. Zywietz, R. L. Eriksen, C. Reinhardt, S. I. Bozhevolnyi, and B. N. Chichkov, "Demonstration of magnetic dipole resonances of dielectric nanospheres in the visible region," Nano Letters **12**, 3749–3755 (2012).

[88] A. I. Kuznetsov, A. E. Miroshnichenko, Y. H. Fu, J. Zhang, and B. Luk'yanchuk, "Magnetic light," (2012).

[89] R. Paniagua-Domínguez, D. R. Abujetas, and J. A. Sánchez-Gil, "Ultra low-loss, isotropic optical negative-index metamaterial based on hybrid metal-semiconductor nanowires." Scientific Reports **3**, 1507 (2013).

[90] M. V. Rybin, K. L. Koshelev, Z. F. Sadrieva, K. B. Samusev, A. A. Bogdanov, M. F. Limonov, and Y. S. Kivshar, "High- Q supercavity modes in subwavelength dielectric resonators," Physical Review Letters **119**, 1–5 (2017).

[91] B. Zhen, C. W. Hsu, L. Lu, A. D. Stone, and M. Soljačić, "Topological nature of optical bound states in the continuum," Physical Review Letters **113**, 1–5 (2014).

[92] R. Paniagua-Domínguez, Y. F. Yu, A. E. Miroshnichenko, L. A. Krivitsky, Y. H. Fu, V. Valuckas, L. Gonzaga, Y. T. Toh, A. Y. S. Kay, B. S. Luk'yanchuk, and A. I. Kuznetsov, "Generalized Brewster effect in dielectric metasurfaces," Nature Communications **7**, 10362 (2016).

[93] W. Liu and Y. S. Kivshar, "Generalized Kerker effects in nanophotonics and meta-optics," Optics Express **284**, 274–284 (2017).

[94] F. J. García de Abajo, "Colloquium: Light scattering by particle and hole arrays," Reviews of Modern Physics **79**, 1267–1290 (2007).

[95] V. Giannini, G. Vecchi, and J. Gómez Rivas, "Lighting up multipolar surface plasmon polaritons by collective resonances in arrays of nanoantennas," Physical Review Letters **105**, 1–4 (2010).

[96] A. B. Evlyukhin, S. I. Bozhevolnyi, A. Pors, M. G. Nielsen, I. P. Radko, M. Willatzen, and O. Albrektsen, "Detuned electrical dipoles for plasmonic sensing," Nano Letters **10**, 4571–4577 (2010).

[97] S. R. Rodriguez, A. Abass, B. Maes, O. T. Janssen, G. Vecchi, and J. Gómez Rivas, "Coupling Bright and Dark Plasmonic Lattice Resonances," Physical Review X **1**, 1–7 (2011).

[98] N. Meinzer, W. L. Barnes, and I. R. Hooper, "Plasmonic meta-atoms and metasurfaces," Nature Publishing Group **8**, 889–898 (2014).

[99] S. Baur, S. Sanders, and A. Manjavacas, "Hybridization of Lattice Resonances," ACS Nano **12**, 1618–1629 (2018).

[100] M. Habib, M. Gokbayrak, E. Ozbay, and H. Caglayan, "Electrically controllable plasmon induced reflectance in hybrid metamaterials," Applied Physics Letters **113** (2018).

[101] S. Y. Chiam, R. Singh, C. Rockstuhl, F. Lederer, W. Zhang, and A. A. Bettiol, "Analogue of electromagnetically induced transparency in a terahertz metamaterial," Physical Review B **80**, 1–4 (2009).

[102] S. I. Bozhevolnyi, A. B. Evlyukhin, A. Pors, M. G. Nielsen, M. Willatzen, and O. Albrektsen, "Optical transparency by detuned electrical dipoles," New Journal of Physics **13** (2011).

[103] J. Gu, R. Singh, X. Liu, X. Zhang, Y. Ma, S. Zhang, S. A. Maier, Z. Tian, A. K. Azad, H. T. Chen, A. J. Taylor, J. Han, and W. Zhang, "Active control of electromagnetically induced transparency analogue in terahertz metamaterials," Nature Communications **3**, 1151–1156 (2012).

[104] S. R. K. Rodriguez, O. T. A. Janssen, G. Lozano, a. Omari, Z. Hens, and J. Gómez Rivas, "Near-field resonance at far-field-induced transparency in diffractive arrays of plasmonic nanorods," Optics Letters **38**, 1238 (2013).

[105] Z. Zhu, X. Yang, J. Gu, J. Jiang, W. Yue, Z. Tian, M. Tonouchi, J. Han, and W. Zhang, "Broadband plasmon induced transparency in terahertz metamaterials," Nanotechnology **24** (2013).

[106] M. C. Schaafsma, A. Bhattacharya, and J. Gómez Rivas, "Diffraction enhanced transparency and slow THz light in periodic arrays of detuned and displaced dipoles," ACS Photonics **3**, 1596–1603 (2016).

[107] A. Halpin, C. Mennes, A. Bhattacharya, and J. Gómez Rivas, "Visualizing near-field coupling in terahertz dolmens," Applied Physics Letters **110** (2017).

[108] A. Halpin, N. Van Hoof, A. Bhattacharya, C. Mennes, and J. Gomez Rivas, "Terahertz diffraction enhanced transparency probed in the near field," Physical Review B **96**, 1–6 (2017).

[109] M. Homer Reid and S. Johnson, "Efficient computation of power, force, and torque in BEM scattering calculations," arXiv:1307.2966 (2013).

[110] "M. Homer Reid," http://homerreid.github.io/scuff-em-documentation .

[111] R. Yu, L. M. Liz-Marzán, and F. J. García De Abajo, "Universal analytical modeling of plasmonic nanoparticles," Chemical Society Reviews **46**, 6710–6724 (2017).

[112] R. Yan, D. Gargas, and P. Yang, "Nanowire photonics," Nature Photonics **3**, 569–576 (2009).

[113] D. R. Abujetas, R. Paniagua-Domínguez, and J. A. Sánchez-Gil, "Unraveling the Janus role of Mie resonances and leaky/guided modes in semiconductor nanowire absorption for enhanced light harvesting," ACS Photonics **2**, 921–929 (2015).

[114] R. Paniagua-Domínguez, G. Grzela, J. Gómez Rivas, and J. A. Sánchez-Gil, "Enhanced and directional emission of semiconductor nanowires tailored through leaky/guided modes." Nanoscale **5**, 10582–90 (2013).

[115] B. Tian, T. J. Kempa, and C. M. Lieber, "Single nanowire photovoltaics," Chemical Society Reviews **38**, 165–184 (2009).

[116] J. Wang, M. S. Gudiksen, X. Duan, Y. Cui, and C. M. Lieber, "Highly polarized photoluminescence and photodetection from single indium phosphide nanowires." Science (New York, N.Y.) **293**, 1455–1457 (2001).

[117] O. L. Muskens, J. Gómez Rivas, R. E. Algra, E. P. A. M. Bakkers, and A. Lagendijk, "Design of light scattering in nanowire materials for photovoltaic applications," Nano Letters **8**, 2638–2642 (2008).

[118] L. Cao, J. S. White, J.-S. Park, J. A. Schuller, B. M. Clemens, and M. L. Brongersma, "Engineering light absorption in semiconductor nanowire devices." Nature Materials **8**, 643–647 (2009).

[119] P. M. Wu, N. Anttu, H. Q. Xu, L. Samuelson, and M.-E. Pistol, "Colorful InAs nanowire arrays: from strong to weak absorption with geometrical tuning." Nano Letters **12**, 1990–1995 (2012).

[120] G. Grzela, R. Paniagua-Domínguez, T. Barten, Y. Fontana, J. A. Sánchez-Gil, and J. Gómez Rivas, "Nanowire antenna emission," Nano Letters **12**, 5481–5486 (2012).

[121] M. H. Huang, S. Mao, H. Feick, H. Yan, Y. Wu, H. Kind, E. Weber, R. Russo, and P. Yang, "Room-temperature ultraviolet nanowire nanolasers." Science **292**, 1897–1899 (2001).

[122] T. M. Babinec, B. J. M. Hausmann, M. Khan, Y. Zhang, J. R. Maze, P. R. Hemmer, and M. Loncar, "A diamond nanowire single-photon source." Nature Nanotechnology **5**, 195–199 (2010).

[123] J. Claudon, J. Bleuse, N. S. Malik, M. Bazin, N. Gregersen, C. Sauvan, P. Lalanne, and J.-M. Gerard, "A highly efficient single-photon source based on a quantum dot in a photonic nanowire," Nature Photonics **4**, 174–177 (2010).

[124] M. Munsch, J. Claudon, J. Bleuse, N. Malik, E. Dupuy, J.-M. Gérard, Y. Chen, N. Gregersen, and J. Mørk, "Linearly polarized, single-mode spontaneous emission in a photonic nanowire," Physical Review Letters **108**, 1–5 (2012).

[125] M. D. Kelzenberg, S. W. Boettcher, J. A. Petykiewicz, D. B. Turner-Evans, M. C. Putnam, E. L. Warren, J. M. Spurgeon, R. M. Briggs, N. S. Lewis, and H. A. Atwater, "Enhanced absorption and carrier collection in Si wire arrays for photovoltaic applications," Nature Materials **9**, 239–244 (2010).

[126] L. Cao, P. Fan, A. P. Vasudev, J. S. White, Z. Yu, W. Cai, J. A. Schuller, S. Fan, and M. L. Brongersma, "Semiconductor nanowire optical antenna solar absorbers." Nano Letters **10**, 439–445 (2010).

[127] E. Garnett and P. Yang, "Light trapping in silicon nanowire solar cells." Nano Letters **10**, 1082–1087 (2010).

[128] S. L. Diedenhofen, O. T. A. Janssen, G. Grzela, E. P. A. M. Bakkers, and J. Gómez Rivas, "Strong geometrical dependence of the absorption of light in arrays of semiconductor nanowires." ACS Nano **5**, 2316–2323 (2011).

[129] J. Wallentin, N. Anttu, D. Asoli, M. Huffman, I. Aberg, B. Witzigmann, H. Q. Xu, L. Samuelson, K. Deppert, and M. T. Borgström, "InP nanowire array solar cells achieveing 13.8% efficiency by exceeding the ray optics limit," Science **339**, 1057 (2013).

[130] S. L. Diedenhofen, G. Vecchi, R. E. Algra, A. Hartsuiker, O. L. Muskens, G. Immink, E. P. A. M. Bakkers, W. L. Vos, and J. Gómez Rivas, "Broad-band and omnidirectional antireflection coatings based on semiconductor nanorods," Advanced Materials **21**, 973–978 (2009).

[131] L. Hu and G. Chen, "Analysis of optical absorption in silicon nanowire arrays for photovoltaic applications." Nano letters **7**, 3249–3252 (2007).

[132] N. Anttu and H. Q. Xu, "Efficient light management in vertical nanowire arrays for photovoltaics," Optics Express **18**, 27589–27605 (2013).

[133] N. Anttu, "Geometrical optics, electrostatics, and nanophotonic resonances in absorbing nanowire arrays." Optics Letters **38**, 730–732 (2013).

[134] B. Wang and P. W. Leu, "Tunable and selective resonant absorption in vertical nanowires." Optics Letters **37**, 3756–3758 (2012).

[135] K. T. Fountaine, C. G. Kendall, and H. A. Atwater, "Near-unity broadband absorption designs for semiconducting nanowire arrays via localized radial mode excitation," Optics Express **22**, A930—-A940 (2014).

[136] K. T. Fountaine, W. S. Whitney, and H. A. Atwater, "Resonant absorption in semiconductor nanowires and nanowire arrays: Relating leaky waveguide modes to Bloch photonic crystal modes," Journal of Applied Physics **116**, 153106 (2014).

[137] J. Arnbak, "Leaky waves on a dielectric rod," Electronics Letters **5**, 41–42 (1969).

[138] R. Sammut and A. W. Snyder, "Leaky modes on circular optical waveguides," Applied Optics **15**, 477–482 (1976).

[139] H. Ruda and A. Shik, "Polarization-sensitive optical phenomena in semiconducting and metallic nanowires," Physical Review B **72**, 1–11 (2005).

[140] H. E. Ruda and A. Shik, "Polarization-sensitive optical phenomena in thick semiconducting nanowires," Journal of Applied Physics **100** (2006).

[141] Y. Zhan, J. Zhao, C. Zhou, M. Alemayehu, Y. Li, and Y. Li, "Enhanced photon absorption of single nanowire α-Si solar cells modulated by silver core." Optics Express **20**, 11506–11516 (2012).

[142] S. A. Mann and E. C. Garnett, "Extreme light absorption in thin semiconductor films wrapped around metal nanowires." Nano Letters **13**, 3173–3178 (2013).

[143] G. Grzela, R. Paniagua-Domínguez, T. Barten, D. van Dam, J. A. Sánchez-Gil, and J. Gómez Rivas, "Nanowire antenna absorption probed with time-reversed fourier microscopy." Nano Letters (2014).

[144] E. D. Palik, *Handbook of Optical Constants of Solids*, vol. 3 (Academic Press, 1998).

[145] M. V. Rybin, K. B. Samusev, I. S. Sinev, G. Semouchkin, E. Semouchkina, Y. S. Kivshar, and M. F. Limonov, "Mie scattering as a cascade of Fano resonances," Opt. Express **21**, 825–828 (2013).

[146] R. Paniagua-Domínguez, G. Grzela, J. Gómez Rivas, and J. A. Sánchez-Gil, "Semiconductor nanowire photoluminescence: spatial/polarization averaged coupling into leaky modes," Active Photonic Materials V **8808**, 88080J (2013).

[147] Y. Yang, W. Wang, A. Boulesbaa, I. I. Kravchenko, D. P. Briggs, A. Puretzky, D. Geohegan, and J. Valentine, "Nonlinear Fano-resonant dielectric metasurfaces," Nano Letters **15**, 7388–7393 (2015).

[148] P. Fan, Z. Yu, S. Fan, and M. L. Brongersma, "Optical Fano resonance of an individual semiconductor nanostructure," Nature Materials **13**, 471–475 (2014).

[149] C. Wu, N. Arju, G. Kelp, J. a. Fan, J. Dominguez, E. Gonzales, E. Tutuc, I. Brener, and G. Shvets, "Spectrally selective chiral silicon metasurfaces based on infrared Fano resonances," Nature Communications **5**, 1–9 (2014).

[150] Y. Yang, I. I. Kravchenko, D. P. Briggs, and J. Valentine, "All-dielectric metasurface analogue of electromagnetically induced transparency," Nature Communications **5**, 1–7 (2014).

[151] B. Hopkins, D. S. Filonov, A. E. Miroshnichenko, F. Monticone, A. Alù, and Y. S. Kivshar, "Interplay of magnetic responses in all-dielectric oligomers to realize magnetic Fano resonances," ACS Photonics **2**, 724–729 (2015).

[152] J. Yan, P. Liu, Z. Lin, H. Wang, H. Chen, C. Wang, and G. Yang, "Directional fano resonance in a silicon nanosphere dimer," ACS Nano **9**, 2968–2980 (2015).

[153] Z. J. Yang, "Fano interference of electromagnetic modes in subwavelength dielectric nanocrosses," Journal of Physical Chemistry C **120**, 21843–21849 (2016).

[154] A. E. Miroshnichenko, S. Flach, and Y. S. Kivshar, "Fano resonances in nanoscale structures," Reviews of Modern Physics **82**, 2257–2298 (2010).

[155] B. Luk'yanchuk, N. I. Zheludev, S. a. Maier, N. J. Halas, P. Nordlander, H. Giessen, and C. T. Chong, "The Fano resonance in plasmonic nanostructures and metamaterials," Nature Materials **9**, 707–715 (2010).

[156] R. Paniagua-Domínguez, F. López-Tejeira, R. Marqués, and J. A. Sánchez-Gil, "Metallodielectric core-shell nanospheres as building blocks for optical three-dimensional isotropic negative-index metamaterials," New Journal of Physics **13**, 123017 (2011).

[157] H. Chen, L. Shao, T. Ming, K. C. Woo, Y. C. Man, J. Wang, and H.-Q. Lin, "Observation of the Fano resonance in gold nanorods supported on high-dielectric-constant substrates," Nano Letters **5**, 6754–6763 (2011).

[158] F. López-Tejeira, R. Paniagua-Domínguez, R. Rodríguez-Oliveros, and J. A. Sánchez-Gil, "Fano-like interference of plasmon resonances at a single rod-shaped nanoantenna," New Journal of Physics **14** (2012).

[159] N. Verellen, F. López-Tejeira, R. Paniagua-Domínguez, D. Vercruysse, D. Denkova, L. Lagae, P. van Dorpe, V. V. Moshchalkov, and J. A. Sánchez-Gil, "Mode parity-controlled fano- and lorentz-like line shapes arising in plasmonic nanorods," Nano Letters **14**, 2322–2329 (2014).

[160] N. Verellen, P. van Dorpe, C. Huang, K. Lodewijks, G. A. Vandenbosch, L. Lagae, and V. V. Moshchalkov, "Plasmon line shaping using nanocrosses for high sensitivity localized surface plasmon resonance sensing," Nano Letters **11**, 391–397 (2011).

[161] H.-S. Ee, J.-H. Kang, M. Brongersma, and M.-K. Seo, "Shape-dependent light scattering properties of subwavelength silicon nanoblocks," Nano Letters pp. 1759–1765 (2015).

[162] P. E. Landreman, H. Chalabi, J. Park, and M. L. Brongersma, "Fabry-Perot description for Mie resonances of rectangular dielectric nanowire optical resonators," Optics Express **24**, 29760 (2016).

[163] D. J. Traviss, M. K. Schmidt, J. Aizpurua, and O. L. Muskens, "Antenna resonances in low aspect ratio semiconductor nanowires," Optics Express **23**, 22771 (2015).

[164] J. Cambiasso, G. Grinblat, Y. Li, A. Rakovich, E. Cortés, and S. A. Maier, "Bridging the gap between dielectric nanophotonics and the visible regime with effectively lossless gallium phosphide antennas," Nano Letters **17**, 1219–1225 (2017).

[165] V. Giannini, Y. Francescato, H. Amrania, C. C. Phillips, and S. A. Maier, "Fano resonances in nanoscale plasmonic systems: A parameter-free modeling approach," Nano Letters **11**, 2835–2840 (2011).

[166] B. Gallinet and O. J. F. Martin, "Ab initio theory of Fano resonances in plasmonic nanostructures and metamaterials," Physical Review B **235427**, 1–6 (2011).

[167] D. R. Abujetas and J. A. Sánchez-Gil, "Spin angular momentum in planar and cylindrical waveguides induced by transverse confinement and intrinsic helicity of guided light," arxiv:1809.02406 pp. 1–19 (2019).

[168] D. R. Abujetas, J. Feist, F. J. García-Vidal, J. Gómez Rivas, and J. A. Sánchez-Gil, "Strong coupling between weakly guided semiconductor nanowire modes and an organic dye," Physical Review B **99**, 205409 (2019).

[169] D. M. Lipkin, "Existence of a new vonservation law in electromagnetic theory," Journal of Mathematical Physics **5**, 696–700 (1964).

[170] T. W. B. Kibble, "Conservation laws for free fields," Journal of Mathematical Physics **6**, 1022–1026 (1965).

[171] D. J. Candlin, "Analysis of the new conservation law in electromagnetic theory," Il Nuovo Cimento **37**, 1390–1395 (1965).

[172] T. A. Morgan, "Two classes of new conservation laws for the electromagnetic field and for other massless fields," Journal of Mathematical Physics **5**, 1659 (1964).

[173] W. I. Fushchich and A. G. Nikitin, "The complete sets of conservation laws for the electromagnetic field," Journal of Physics A **5**, L231–L233 (1992).

[174] R. P. Cameron, S. M. Barnett, and A. M. Yao, "Optical helicity, optical spin and related quantities in electromagnetic theory," New Journal of Physics **14**, 053050 (2012).

[175] M. G. Calkin, "An invariance property of the free electromagnetic field," American Journal of Physics **33**, 958 (1965).

[176] I. Fernandez-Corbaton, X. Zambrana-Puyalto, and G. Molina-Terriza, "Helicity and angular momentum: A symmetry-based framework for the study of light-matter interactions," Physical Review A **86**, 042103 (2012).

[177] K. Y. Bliokh, A. Y. Bekshaev, and F. Nori, "Optical helicity, optical spin and related quantities in electromagnetic theory," New Journal of Physics **15**, 033026 (2013).

[178] A. Aiello, P. Banzer, M. Neugebauer, and G. Leuchs, "From transverse angular momentum to photonic wheels," Nature Photonics **9**, 789–795 (2015).

[179] A. Y. Bekshaev, K. Y. Bliokh, and F. Nori, "Transverse spin and momentum in two-wave interference," Physical Review X **5**, 011039 (2015).

[180] K. Y. Bliokh, D. Smirnova, and F. Nori, "Quantum spin Hall effect of light," Science **3** (2015).

[181] K. Y. Bliokh and F. Nori, "Transverse and longitudinal angular momenta of light," Physics Reports **592**, 1–38 (2015).

[182] K. Y. Bliokh, F. J. Rodri, F. Nori, and A. V. Zayats, "Spin-orbit interactions of light," Nature Photonics **9**, 796 (2015).

[183] S.-H. Gong, F. Alpeggiani, B. Sciacca, E. C. Garnett, and L. Kuipers, "Nanoscale chiral valley-photon interface through optical spin-orbit coupling," Science **359**, 443–447 (2018).

[184] G. Li, G. Sartorello, S. Chen, L. H. Nicholls, K. F. Li, T. Zentgraf, S. Zhang, and A. V. Zayats, "Spin and Geometric Phase Control Four-Wave Mixing from Metasurfaces," Laser Photonics Rev. **12**, 1800034 (2018).

[185] G. Araneda, S. Walser, Y. Colombe, D. B. Higginbottom, J. Volz, R. Blatt, and A. Rauschenbeutel, "Wavelength-scale errors in optical localization due to spin-orbit coupling of light," Nat. Phys. **15**, 17 (2019).

[186] J. Olmos-Trigo, C. Sanz-Fernández, A. García-Etxarri, G. Molina-Terriza, F. Bergeret, and J. J. Sáenz, "Enhanced spin-orbit optical mirages from dual nanospheres," Phys. Rev. A **99**, 013852 (2019).

[187] J. Olmos-Trigo, C. Sanz-Fernández, F. S. Bergeret, and J. J. Sáenz, "Asymmetry and spin-orbit coupling of light scattered from subwavelength particles," Opt. Lett. **44**, 1762 (2019).

[188] K. Y. Bliokh, A. Y. Bekshaev, and F. Nori, "Extraordinary momentum and spin in evanescent waves," Nature Communications **5**, 1–8 (2014).

[189] K. Y. Bliokh, Y. S. Kivshar, and F. Nori, "Magnetoelectric effects in local light-matter interactions," Physical Review Letters **113**, 33601 (2014).

[190] D. O'Connor, P. Ginzburg, F. J. Rodríguez-Fortuño, G. A. Wurtz, and A. V. Zayats, "Spin-orbit coupling in surface plasmon scattering by nanostructures," Nature Communications **5**, 1–7 (2014).

[191] C. Sayrin, C. Junge, R. Mitsch, B. Albrecht, and D. O. Shea, "Nanophotonic optical isolator controlled by the internal state of cold atoms," Physical Review X **5**, 041036 (2015).

[192] T. Van Mechelen and Z. Jacob, "Universal spin-momentum locking of evanescent waves," Optica **3**, 118 (2016).

[193] M. Antognozzi, C. R. Bermingham, R. L. Harniman, S. Simpson, J. Senior, R. Hayward, H. Hoerber, M. R. Dennis, A. Y. Bekshaev, K. Y. Bliokh, and F. Nori, "Direct measurements of the extraordinary optical momentum and transverse spin-dependent force using a nanocantilever," Nature Physics **12**, 731–735 (2016).

[194] M. F. Picardi, A. Manjavacas, A. V. Zayats, and F. J. Rodríguez-Fortuño, "Unidirectional evanescent-wave coupling from circularly polarized electric and magnetic dipoles: An angular spectrum approach," Physical Review B **95**, 245416 (2017).

[195] M. F. Picardi, A. V. Zayats, and F. J. Rodríguez-Fortuño, "Janus and Huygens dipoles: Near-field directionality beyond spin-momentum locking," Physical Review Letters **120**, 117402 (2018).

[196] M. Neugebauer, J. S. Eismann, T. Bauer, and P. Banzer, "Magnetic and electric transverse spin density of spatially confined light," Physical Review X **8**, 21042 (2018).

[197] J. Petersen, J. Volz, and A. Rauschenbeutel, "Chiral nanophotonic waveguide interface based on spin-orbit interaction of light," Science **346**, 67–71 (2014).

[198] R. Mitsch, C. Sayrin, B. Albrecht, P. Schneeweiss, and A. Rauschenbeutel, "Quantum state-controlled directional spontaneous emission of photons into a nanophotonic waveguide," Nature Communications **5**, 1–5 (2014).

[199] B. Le Feber, N. Rotenberg, and L. Kuipers, "Nanophotonic control of circular dipole emission," Nature Communications **6**, 1–6 (2015).

[200] M. Alizadeh and B. M. Reinhard, "Emergence of transverse spin in optical modes of semiconductor nanowires," Optics Express **24**, 8471 (2016).

[201] R. J. Coles, D. M. Price, J. E. Dixon, B. Royall, E. Clarke, P. Kok, M. S. Skolnick, A. M. Fox, and M. N. Makhonin, "Chirality of nanophotonic waveguide with embedded quantum emitter for unidirectional spin transfer," Nature Communications **7**, 1–7 (2016).

[202] A. Andryieuski, S. M. Kuznetsova, S. V. Zhukovsky, Y. S. Kivshar, and A. V. Lavrinenko, "Water: Promising opportunities for tunable all-dielectric electromagnetic metamaterials," Scientific Reports **5**, 1–9 (2015).

[203] A. W. Snyder and J. D. Love, *Optical waveguide theory* (Chapman and Hall, London-New York, 1983).

[204] K. Y. Bliokh, A. Y. Bekshaev, and F. Nori, "Optical momentum, spin, and angular momentum in dispersive media," Physical Review Letters **119**, 073901 (2017).

[205] A. Espinosa-Soria and A. Martínez, "Transverse spin and spin-orbit coupling in silicon waveguides," IEEE Photonics Technology Letters **28**, 1561–1564 (2016).

[206] F. J. Rodríguez-Fortuño, I. Barber-Sanz, D. Puerto, A. Griol, and A. Martínez, "Resolving light handedness with an on-chip silicon microdisk," ACS Photonics **1**, 762–767 (2014).

[207] G. Maltese, Y. Halioua, A. Lemaître, C. Gomez-Carbonell, E. Karimi, P. Banzer, and S. Ducci, "Towards an integrated AlGaAs waveguide platform for phase and polarisation shaping," Journal of Optics **20** (2018).

[208] Z.-Y. Wang and C.-D. Xiong, "Photons inside a waveguide as massive particles," arXiv preprint pp. 1–14 (2007).

[209] X. Zang, J. Yang, R. Faggiani, C. Gill, P. G. Petrov, J. P. Hugonin, K. Vynck, S. Bernon, P. Bouyer, V. Boyer, and P. Lalanne, "Interaction between stoms and slow light: A study in waveguide Design," Physical Review Applied **5**, 1–8 (2016).

[210] D. Van Dam, D. Abujetas, R. Paniagua-Domínguez, J. Sánchez-Gil, E. Bakkers, J. Haverkort, and J. Gómez Rivas, "Directional and polarized emission from nanowire arrays," Nano Letters **15**, 4557 (2015).

[211] J. Yu, L. Wang, D. Yang, J. Zheng, Y. Xing, Z. Hao, Y. Luo, C. Sun, Y. Han, B. Xiong, J. Wang, and H. Li, "Study on spin and optical polarization in a coupled InGaN/GaN quantum well and quantum dots structure," Scientific Reports **6**, 1–8 (2016).

[212] Y. Shi, P. Duan, S. Huo, Y. Li, and M. Liu, "Endowing perovskite nanocrystals with circularly polarized luminescence," Advanced Materials **30**, 1–7 (2018).

[213] M. Naito, K. Iwahori, A. Miura, M. Yamane, and I. Yamashita, "Circularly polarized luminescent CDs quantum dots prepared in a protein nanocage," Angewandte Chemie - International Edition **49**, 7006–7009 (2010).

[214] S. Huo, P. Duan, T. Jiao, Q. Peng, and M. Liu, "Self-assembled luminescent quantum dots to generate full-color and white circularly polarized light," Angewandte Chemie - International Edition **56**, 12174–12178 (2017).

[215] T. H. Taminiau, S. Karaveli, N. F. Van Hulst, and R. Zia, "Quantifying the magnetic nature of light emission," Nature Communications **3**, 976–979 (2012).

[216] Y. Liu, D. Tu, H. Zhu, and X. Chen, "Lanthanide-doped luminescent nanoprobes: Controlled synthesis, optical spectroscopy, and bioapplications," Chemical Society Reviews **42**, 6924–6958 (2013).

[217] W. Lin, O. Yasutomo, S. Iwamoto, and Y. Arakawa, "Spin-dependent directional emission from a quantum dot ensemble embedded in an asymmetric waveguide," Opt. Lett. **44**, 3752 (2019).

[218] S. Parkin, G. Knöner, W. Singer, T. A. Nieminen, N. R. Heckenberg, and H. Rubinsztein-Dunlop, "Optical torque on microscopic objects," Methods in Cell Biology **82**, 525–561 (2007).

[219] M. Nieto-Vesperinas, J. J. Sáenz, R. Gómez-Medina, and L. Chantada, "Optical forces on small magnetodielectric particle," Optics Express **18**, 11428 (2010).

[220] J. R. Rodrigues and V. R. Almeida, "Tailoring Optical Forces Behavior in Nano-optomechanical Devices Immersed in Fluid Media," Scientific Reports **7**, 1–6 (2017).

[221] J. A. Hutchison, A. Liscio, T. Schwartz, A. Canaguier-durand, C. Genet, V. Palermo, P. Samorì, and T. W. Ebbesen, "Tuning the work-function via strong coupling," Advanced Materials **25**, 2481–2485 (2013).

[222] S. Ghosh, W. H. Wang, F. M. Mendoza, R. C. Myers, X. Li, N. Samarth, A. C. Gossard, and D. D. Awschalom, "Enhancement of spin coherence using Q-factor engineering in semiconductor microdisc lasers," Nature Materials **5**, 261–264 (2006).

[223] L. Novotny, "Strong coupling, energy splitting, and level crossings: A classical perspective," American Journal of Physics **78**, 1199 (2010).

[224] L. C. Andreani, G. Panzarini, and J.-M. Gérard, "Strong-coupling regime for quantum boxes in pillar microcavities: Theory," Physical Review B **60**, 276–279 (1999).

[225] Y. Zhu, J. D. Gauthier, S. E. Morin, Q. Wu, H. J. Carmichael, and T. W. Mossberg, "Vacuum Rabi splitting as a feature of linear-dispersion theory: Analysis and experimental observations," Physical Review Letters **21**, 2499–2502 (1990).

[226] G. Khitrova, H. M. Gibbs, M. Kira, S. W. Koch, and A. Scherer, "Vacuum Rabi splitting in semiconductors," Nature Physics **2**, 81–90 (2006).

[227] H. Walther, B. T. Varcoe, B. G. Englert, and T. Becker, "Cavity quantum electrodynamics," Reports on Progress in Physics **69**, 1325–1382 (2006).

[228] T. H. Taminiau, F. D. Stefani, and N. F. V. Hulst, "Enhanced directional excitation and emission of single emitters by a nano-optical Yagi-Uda antenna," Optics Express **16**, 858–866 (2008).

[229] S. Kühn, U. Hakanson, L. Rogobete, and V. Sandoghdar, "Enhancement of single-molecule fluorescence using a gold nanoparticle as an optical nanoantenna," Physical Review Letters **97**, 1–4 (2006).

[230] E. Yablonovitch, "Photonic band-gap structures," Journal of the Optical Society of America B **10**, 283 (2008).

[231] A. Wallraff, D. I. Schuster, A. Blais, L. Frunzio, R.-S. Huang, J. Majer, S. Kumar, S. M. Girvin, and R. J. Schoelkopf, "Strong coupling of a single photon to a superconducting qubit using circuit quantum electrodynamics." Nature **431**, 162–7 (2004).

[232] S. R. K. Rodriguez, Y. T. Chen, T. P. Steinbusch, M. A. Verschuuren, A. F. Koenderink, and J. Gómez-Rivas, "From weak to strong coupling of localized surface plasmons to guided modes in a luminescent slab," Physical Review B **90**, 1–9 (2014).

[233] S. Wang, S. Li, T. Chervy, A. Shalabney, S. Azzini, E. Orgiu, J. A. Hutchison, C. Genet, P. Samorì, and T. W. Ebbesen, "Coherent coupling of WS2 monolayers with metallic photonic nanostructures at room temperature," Nano Letters **16**, 4368–4374 (2016).

[234] I. Pockrand, A. Brillante, and D. Möbius, "Exciton-surface plasmon coupling : An experimental investigation," The Journal of Chemical Physics **77**, 6289–6295 (1982).

[235] R. Houdré, R. P. Stanley, and M. Ilegems, "Vacuum-field Rabi splitting in the presence of inhomogeneous broadening: Resolution of a homogeneous linewidth in an inhomogeneously broadened system," Physical Review A **53**, 2711–2715 (1996).

[236] J. Bellessa, C. Bonnand, J. C. Plenet, and J. Mugnier, "Strong coupling between surface plasmons and excitons in an organic semiconductor," Physical Review Letters **93**, 036404 (2004).

[237] J. Bellessa, C. Symonds, K. Vynck, A. Lemaitre, A. Brioude, L. Beaur, J. C. Plenet, P. Viste, D. Felbacq, E. Cambril, and P. Valvin, "Giant Rabi splitting between localized mixed plasmon-exciton states in a two-dimensional array of nanosize metallic disks in an organic semiconductor," Physical Review B **80**, 033303 (2009).

[238] A. González-Tudela, P. A. Huidobro, L. Martín-Moreno, C. Tejedor, and F. J. García-Vidal, "Theory of strong coupling between quantum emitters and propagating durface plasmons," Physical Review Letters **110**, 126801 (2013).

[239] L. Shi, T. K. Hakala, H. T. Rekola, J.-P. Martikainen, R. J. Moerland, and P. Törmä, "Spatial Coherence Properties of Organic Molecules Coupled to Plasmonic Surface Lattice Resonances in the Weak and Strong Coupling Regimes," Physical Review Letters **112**, 153002 (2014).

[240] P. Törmö and W. L. Barnes, "Strong coupling between surface plasmon polaritons and emitters: A review," Reports on Progress in Physics **78** (2015).

[241] J. P. Reithmaier, G. Sek, A. Löffler, C. Hofmann, S. Kuhn, S. Reitzenstein, L. V. Keldysh, V. D. Kulakovskii, T. L. Reinecke, and A. Forchel, "Strong coupling in a single quantum dot-semiconductor microcavity system," Nature **432**, 197–200 (2004).

[242] K. Hennessy, A. Badolato, M. Wigner, D. Gerace, M. Atatüre, S. Gulde, S. Fält, E. L. Hu, and A. Imamoglu, "Quantum nature of a strongly coupled single quantum dot-cavity system," Nature **445**, 896–899 (2007).

[243] L. K. V. Vugt, B. Piccione, C.-H. Cho, P. Nukala, and R. Agarwal, "Enhanced Coupling Strengths in Semiconductor Nanowires," Proceedings of the National Academy of Sciences of the United States of Americading og **108**, 10050–10055 (2011).

[244] Y. Ota, K. Kuruma, M. Kakuda, Y. Arakawa, D. Takamiya, and S. Iwamoto, "Position dependent optical coupling between single quantum dots and photonic crystal nanocavities," Applied Physics Letters **109**, 071110 (2016).

[245] A. A. High, E. E. Novitskaya, L. V. Butov, M. Hanson, and A. C. Gossard, "Control of Exciton Fluxes in an Excitonic Integrated Circuit," Science **321**, 229–231 (2008).

[246] S. M. Menke, W. A. Luhman, and R. J. Holmes, "Tailored exciton diffusion in organic photovoltaic cells for enhanced power conversion efficienc," Nature Materials **12**, 152–157 (2012).

[247] J. Feist and F. J. García-Vidal, "Extraordinary exciton conductance induced by strong coupling," Physical Review Letters **114**, 196402 (2015).

[248] C. Gonzalez-Ballestero, J. Feist, E. Moreno, and F. J. García-Vidal, "Harvesting excitons through plasmonic strong coupling," Physical Review B **92**, 121402 (2015).

[249] M. Ramezani, A. Halpin, A. I. Fernández-Domínguez, J. Feist, S. R.-K. Rodriguez, F. J. García-Vidal, and J. Gómez Rivas, "Plasmon-exciton-polariton lasing," Optica **4**, 22–27 (2017).

[250] M. Ramezani, A. Halpin, J. Feist, N. Van Hoof, A. I. Fernández-Domínguez, F. J. García-Vidal, and J. Gómez Rivas, "Dispersion anisotropy of plasmon-exciton-polaritons in lattices of metallic nanoparticles," ACS Photonics **5**, 233–239 (2018).

[251] C. Wolff, K. Busch, and N. A. Mortensen, "Modal expansions in periodic photonic systems with material loss and dispersion," Physical Review B **97**, 104203 (2018).

[252] J. Yuen-Zhou, S. K. Saikin, and V. M. Menon, "Molecular emission near metal interfaces: The polaritonic regime," Journal of Physical Chemistry Letters **9**, 6511–6516 (2018).

[253] C. Ciuti and I. Carusotto, "Input-output theory of cavities in the ultrastrong coupling regime: The case of time-independent cavity parameters," Physical Review A **74**, 1–13 (2006).

[254] S. de Liberato, "Virtual photons in the ground state of a dissipative system," Nature Communications **8**, 1–6 (2017).

[255] D. de Bernardis, T. Jaako, and P. Rabl, "Cavity quantum electrodynamics in the nonperturbative regime," Physical Review A **97**, 1–18 (2018).

[256] C. Schäfer, M. Ruggenthaler, and A. Rubio, "Ab initio nonrelativistic quantum electrodynamics: Bridging quantum chemistry and quantum optics from weak to strong coupling," Physical Review A **98** (2018).

[257] R. Loudon, "The propagation of electromagnetic energy through an absorbing dielectric," Journal of Physics A **3**, 515 (1970).

[258] K. E. Oughstun and S. Shen, "Velocity of energy transport for a time-harmonic field in a multiple-resonance Lorentz medium," Journal of the Optical Society of America B **5**, 2395–2398 (1988).

[259] J. E. Vázquez-Lozano and A. Martínez, "Optical chirality in dispersive and lossy media," Physical Review Letters **121**, 1–15 (2018).

[260] D. Ballarini, M. de Giorgi, E. Cancellieri, R. Houdre, E. Giacobino, R. Cingolani, A. Bramati, G. Gigli, and D. Sanvitto, "All-optical polariton transistor," Nature Communications **4** (2013).

[261] L. Brillouin, *Wave Propagation and Group Velocity* (Academic Press, London-New York, 1960).